

THE UNIVERSITY OF HULL

PHYSICAL CHARACTERISATION

OF THE GEOMETRY AND MICROFLUIDIC FLOW

WITHIN MICROREACTORS.

Being a Thesis submitted for the Degree of
Doctor of Philosophy

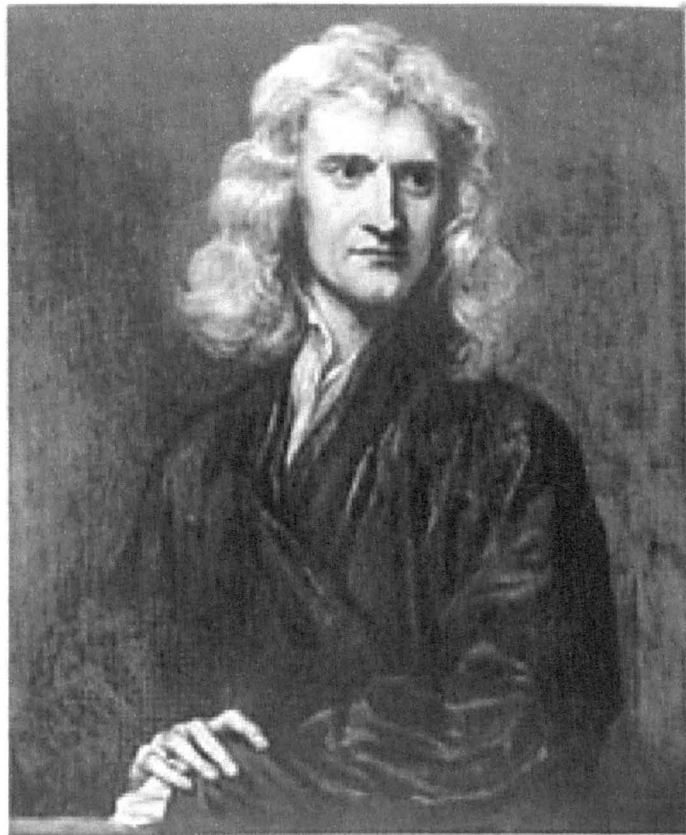
In the University of Hull

By

Ian Broadwell BSc (Special Hons).

(July 2003)

Sir Isaac Newton was possibly the greatest physicist.



As voted 6th by the British people in the BBC poll for the Greatest Britons (Oct 02).

**THIS THESIS IS DEDICATED TO SAM
WHO DIED EARLIER THIS YEAR. IN MY
CHILDHOOD HE TOOK THE PLACE OF
THE GRANDFATHER WHICH I WAS NOT
FORTUNATE ENOUGH TO HAVE AND MOST
OF ALL HE IGNITED THE FLAME OF
DISCOVERY WHICH I STILL HOLD TO THIS
DAY.**

GOD BLESS YOU SAM...

ACKNOWLEDGEMENTS.

After what seems like 4 years of very challenging academic work, I would like to express my sincere gratitude to Professor Paul Fletcher, who has been a friend as well as a supervisor and essentially made this PhD possible.

I will always be indebted to my parents Pauline and Norman for the emotional and financial support they provided in times of despair. I also wish to thank Hai Yan for being a close friend and an impartial adviser.

My final thanks go to the Engineering and Physical Sciences Research Council for funding this study and the additional financial contributions that the Institute of Applied Catalysis made.

I. Broadwell (12th July 2003)

N.B. It may be required in the future that other researchers need information about the experiments listed in this thesis. In this case the author can be reached on the following email: I_Broadwell@yahoo.com (October 2003)

ABSTRACT.

We have investigated the physical properties of glass microreactors. These devices contain a network of micron-sized channels and have application in chemical synthesis. To perform chemical reactions in a microreactor one requires an understanding of the microfluidics involved and this has been studied here.

A 3D profiling method has been developed to determine the internal microreactor channel dimensions to an accuracy of a few microns. This technique is based on optical imaging of a dye filled channel network. Its advantages over existing profiling techniques include that it is rapid, non-destructive and capable of profiling the covered interior channels.

A model has been developed to predict the voltage- (electroosmotic) and pressure-driven flows of different solvent systems in microreactor channels with known geometries, from measured electrical currents and driving voltages applied to the electrodes situated in each reservoir.

The model was validated using extensive experimental measurements of these variables for chips of different channel dimensions, to a level of experimental uncertainty of approximately 20 %. The model provides a useful quantitative tool, which enables the design of channel network dimensions required to achieve a desired set of flow characteristics prior to fabrication.

In the final investigation, we set out to understand the effects of voltage-driven mobilisation of charged and uncharged dye species and colloidal particles in a microreactor channel. Using absorbance-imaging to monitor the dye front velocities it was possible to determine: (1) a channel surface-solvent interface zeta potential and hence, characterise the flow properties of the solvent system and (2) calculate the diffusion coefficient for the charged dye species in the solvent. For the colloid sample with a Gaussian particle size distribution, a range of different velocities and mobilities were observed.

GLOSSARY

A list of the most common abbreviations used in this thesis are given below. Those which are not listed here are defined locally within the text.

ε	Molar extinction coefficient
ε_0	Permittivity of free space
ε_r	Relative permittivity
η	(Dynamic) viscosity of liquid
ρ	Density
g	Gravitational acceleration of Earth
C	Electrolyte concentration or circumference
ζ	Zeta potential
D	Diffusion coefficient
κ_s	Specific surface conductivity
κ_0	Bulk conductivity
E	Electric field strength
v_{eof}	Electroosmotic velocity
μ_{eof}	Electroosmotic mobility
F_{eof}	Electroosmotic volumetric flow rate
F_{press}	Pressure-driven volumetric flow rate
$P_{Laplace}$	Laplace pressure
P_{hydro}	Hydrostatic pressure
v_{eph}	Electrophoretic velocity
μ_{eph}	Electrophoretic mobility
A	Cross-sectional area or absorbance
L	Channel length
m	Apparent mask line width
d	Channel depth or optical path length
T	Absolute temperature
r_{cap}	Capillary radius

R_{elec}	Electrical resistance
R_{press}	Hydrodynamic resistance
R_{eof}	Electroosmotic resistance
R_{surf}	Electrical resistance of surface conduction path
R_{bulk}	Electrical resistance of bulk solution
I_{bulk}	Bulk current
I_{surf}	Surface current
I_{total}	Total current
I	Measured current or optical radiation intensity
n or R.I.	Refractive index
z	Integer charge number
e	Electronic charge
κ	Debye length
k	Boltzmann constant
N_A	Avogadro's number
[]	Solution concentration.
mM	Solution concentration = 10^{-3} mol dm ⁻³

CONTENTS

<u>CHAPTER</u>	<u>PAGE</u>
1. INTRODUCTION: MICROREACTORS AND MICROFLUIDICS.	1–65
1.1 Microreactors.	1
1.1.1 <i>What are microreactors?</i>	1
1.1.2 <i>The origin of microreactors.</i>	2
1.1.3 <i>The main operating features of microreactors.</i>	7
1.2 Microreactor fabrication techniques.	15
1.2.1 <i>Suitable fabrication materials for microreactors.</i>	15
1.2.2 <i>Existing methods used for fabricating channel networks.</i>	16
1.2.3 <i>The most suitable microreactor channel fabrication method.</i>	22
1.2.4 <i>Thermal bonding methods for microreactors.</i>	22
1.3 Microfluidics in channel networks.	24
1.3.1 <i>How are fluids moved around the microreactor channels?</i>	24
1.3.2 <i>The four kinds of electrokinetic phenomena.</i>	28
1.3.3 <i>The electric double layer and zeta potential.</i>	29
1.3.4 <i>The properties of electroosmotic flow.</i>	32
1.3.5 <i>Electrophoresis and diffusion.</i>	34
1.3.6 <i>How zeta potential varies with pH for glass-aqueous systems.</i>	35
1.3.7 <i>How zeta potential varies with salt concentration for different glass-aqueous electrolyte solutions.</i>	36
1.3.8 <i>Zeta potential for glass and non-aqueous systems.</i>	38
1.3.9 <i>The implications of specific surface conductivity in estimates of zeta potential.</i>	40
1.3.10 <i>Specific surface conductivity values for aqueous and non-aqueous solvents.</i>	42
1.3.11 <i>Flow profiles for combinations of electroosmotic and pressure-driven flow.</i>	44
1.3.12 <i>Methods for maximising pure EOF while minimising pressure-driven back-flow.</i>	49

1.3.13	<i>Joule heating and electrolysis within microreactor channel networks.</i>	52
1.4	Chemical detection methods.	53
1.4.1	<i>On-chip detector requirements.</i>	53
1.4.2	<i>Optical detection methods.</i>	56
1.4.3	<i>Electrochemical detection methods.</i>	57
1.5	Project objectives and thesis plan.	58
1.6	References.	61
2.	GENERAL EXPERIMENTAL PROCEDURES.	66–86
2.1	Methods.	66
2.1.1	<i>Microreactor fabrication.</i>	66
2.1.2	<i>Refractive index measurements.</i>	73
2.1.3	<i>UV-vis spectrophotometer measurements.</i>	73
2.1.4	<i>Determination of liquids flow rates and internal reservoir radii.</i>	74
2.1.5	<i>Determination of capillary dimensions.</i>	76
2.1.6	<i>Solutions and procedures used for cleaning equipment.</i>	78
2.1.7	<i>Solvent evaporation rates.</i>	79
2.1.8	<i>Voltage and current determination.</i>	80
2.1.9	<i>Conductivity and pH measurements.</i>	81
2.1.10	<i>Zeta sizing measurements of the colloidal catalysts.</i>	82
2.2	Materials.	84
2.3	References.	86
3.	CHANNEL PROFILING USING ABSORBANCE-IMAGING.	87–121
3.1	Introduction: <i>The problem of depth profiling bonded channels.</i>	87
3.2	Apparatus and theory.	88
3.3.1	<i>Description of microreactors used for absorbance-imaging study.</i>	88
3.2.2	<i>Microscope imaging theory.</i>	90
3.2.3	<i>Microscope configuration and experimental set up.</i>	91
3.2.4	<i>Dye solution requirements for absorbance-imaging.</i>	93
3.2.5	<i>Satisfactory dye solutions for absorbance-imaging.</i>	94

3.2.6	<i>Consideration of uncertainties.</i>	100
3.3	Results and discussion.	105
3.3.1	<i>3-dimensional profiles of channel networks.</i>	105
3.3.2	<i>Does the dye solution R.I. affect the apparent channel dimensions?</i>	107
3.3.3	<i>Fitting channel cross-sectional profiles and the effects of thermal bonding.</i>	110
3.3.4	<i>Time of etching and the effect on m, d and δ.</i>	115
3.4	Summary.	119
3.5	References	121
4.	COMBINED EOF AND PRESSURE-DRIVEN FLOW IN CYLINDRICAL CAPILLARIES.	122–145
4.1	Introduction: <i>The need for simple flow rate measurements.</i>	122
4.2	Apparatus and theory.	122
4.2.1	<i>U-tube apparatus and experimental set up.</i>	122
4.2.2	<i>Theory for flow rate modelling.</i>	125
4.2.3	<i>Optimum experimental conditions.</i>	127
4.3	Results and discussion.	130
4.3.1	<i>Determination of zeta potential and specific surface conductivity.</i>	130
4.3.2	<i>Steps in quality assurance for recorded data.</i>	132
4.3.3	<i>Flow rate reproducibility.</i>	136
4.4	Summary.	143
4.5	References.	145
5.	PURE ELECTROOSMOTIC FLOW IN CHANNEL NETWORKS.	146–179
5.1	Introduction: <i>Flow rate measurements on-chip.</i>	146
5.2	Apparatus and theory.	146
5.2.1	<i>Microreactor dimensions and reservoir arrangement.</i>	146
5.2.2	<i>Theory for microreactor current-voltage characteristics.</i>	149
5.3	Results and discussion.	154
5.3.1	<i>Verification that the pressure-driven flow is negligible within chip 004.</i>	154
5.3.2	<i>Characterisation results for different solvent systems in chip 004.</i>	156

5.3.3	<i>Choice of electrode material for on-chip flow rate measurements.</i>	171
5.4	Summary.	177
5.5	References.	179
6.	ABSORBANCE IMAGING OF REAGENT MOBILITIES.	180–216
6.1	Introduction: <i>The necessity to measure lower flow rates.</i>	180
6.2	Apparatus and theory.	180
6.2.1	<i>Microreactor dimensions, I-V characteristics and electrical set up.</i>	180
6.2.2	<i>Concentration-imaging theory.</i>	183
6.3	Results and discussion.	189
6.3.1	<i>The pK_a of PADA in solutions containing 80 vol. % DMA (aq) and 45 mM NaBr.</i>	189
6.3.2	<i>Time dependent changes of pH in the PADA dye solutions.</i>	191
6.3.3	<i>Concentration-imaging of PADA dye solutions.</i>	193
6.3.4	<i>PADA and $PADAH^+$ dye front velocities in 80 vol. % DMA (aq) with 45 mM NaBr as a function of applied voltage and pH.</i>	203
6.3.5	<i>Absorbance-imaging of colloidal catalyst in a microreactor.</i>	210
6.4	Summary.	214
6.5	References.	216
7.	COMBINED ELECTROOSMOTIC AND PRESSURE-DRIVEN FLOWS IN CHANNEL NETWORKS.	217–241
7.1	Introduction: <i>The necessity to model and measure combined flows on-chip.</i>	217
7.2	Apparatus and theory.	217
7.2.1	<i>Microreactor dimensions and reservoir arrangements.</i>	217
7.2.2	<i>The analogies between electrical and pressure-driven flows in microreactors.</i>	222
7.3	Results and discussion.	232
7.3.1	<i>Comparison of the combined flow theory with experiment.</i>	232
7.4	Summary.	238

7.5	References.	240
8.	CONCLUSIONS AND SUGGESTIONS FOR FUTURE WORK.	242
	APPENDIX (A): MATHEMATICAL TREATMENT OF ELECTRO-OSMOSIS.	246
	APPENDIX (B): DYE SPECIES ADSORPTION CALCULATIONS.	248
	APPENDIX (C): VISUAL BASIC CODE FOR ISOTROPIC ETCH PROFILES.	249
	APPENDIX (D): EOF CALCULATIONS 1.	250
	APPENDIX (E): EOF CALCULATIONS 2.	251
	APPENDIX (F): THE VISCOSITY OF 80 VOL.% DMA IN WATER.	252
	APPENDIX (G): THE RELATIVE PERMITTIVITY OF 80 VOL.% DMA IN WATER.	253
	APPENDIX (H): RESOLVING PADA ABSORBANCES AT 450 AND 550 NM.	254
	APPENDIX (I): CALCULATING THE pK_a FOR PADA IN 80 VOL. % DMA (AQ).	256
	APPENDIX (J): PADA ZETA POTENTIAL AND DIFFUSION COEFFICIENT CALCULATIONS.	257
	APPENDIX (K): PRESSURE EQUATIONS FOR CHIP 303.	258

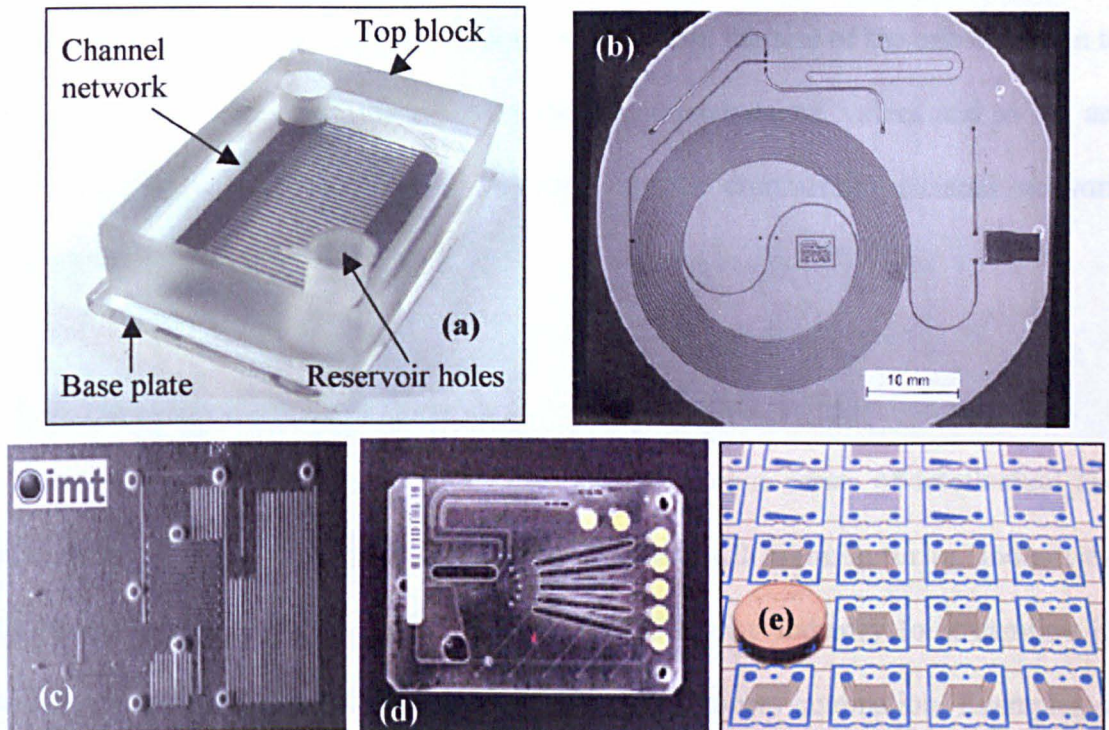
1. INTRODUCTION: MICROREACTORS AND MICROFLUIDICS.

1.1 Microreactors.

1.1.1 What are microreactors?

The simplest microreactors (chips) commonly occupy the volume of about a cubic inch. Their primary purpose is to perform chemical reactions for mainly analytical and synthetic applications. In the Hull group, the devices are fabricated from two pieces of glass: a top block containing a series of 3 mm diameter reservoir holes, which is thermally bonded to a base plate with an etched channel network. Thermal bonding seals the etched channel network and connects the reaction channels with the reservoirs. The channels are typically 200 μm wide by 50 to 100 μm deep. An assembled

Figure 1.1: (a) A Hull group bonded glass microreactor filled with ink to highlight the enclosed channel network. Overall, microreactor dimensions are 15 mm high x 25 mm wide x 34 mm long. (b) The original 1979 Stanford University gas chromatograph fabricated on to a silicon wafer [1]. (c) IMT chip made on a silicon wafer [2]. (d) Commercial Glass Micronics' T-Sensor[®] platform [3]. (e) Ehrfeld heat exchanger network on-chip [4].

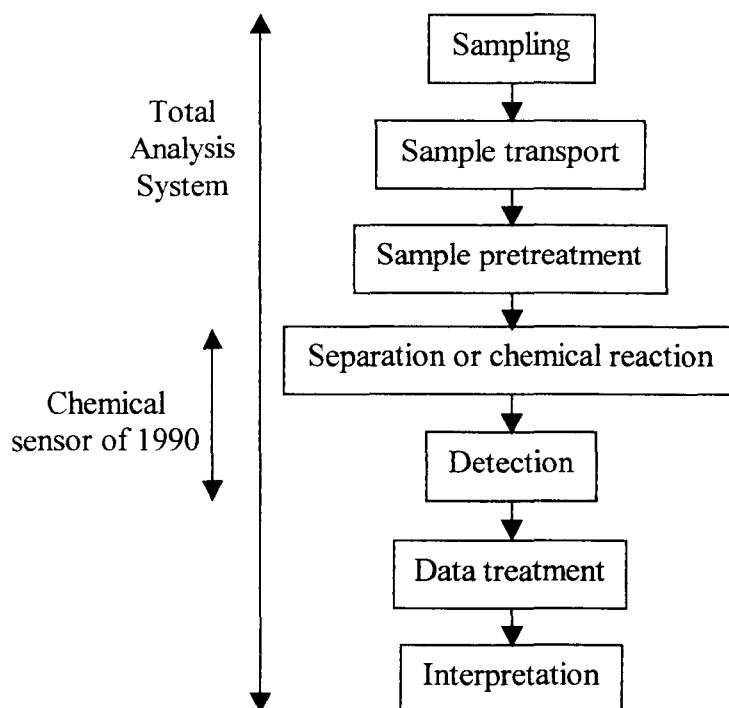


Hull microreactor can be seen in Figure 1.1 (a). The remaining examples of microreactors given in Figure 1.1 highlight the different range of devices currently in circulation. Figure 1.1 (b) is the original 1979 Stanford University gas chromatograph fabricated on a silicon wafer [1]. The significance of this device will become apparent later. The IMT chip, Figure 1.1 (c), is also fabricated on a silicon wafer. The wide range of materials from which microreactors can be fabricated, such as glass, silicon, numerous polymers and some metals, make them particularly useful and suited to a wide variety of applications. The Micronics T-sensor shown in Figure 1.1 (d) is available in both glass and a range of different polymers. The manufacturers describe it can be used for applications ranging from enzyme and protein analysis to process control and environmental research. Recently, scientific interest in microsystems technology has been more directed at producing fully integrated systems which calls for specialist components with reduced dimensions. The reasons for this interest will be discussed later. A typical microfabricated heat exchanger design is shown in Figure 1.1 (e). Actually, a fabricated plate of more than twenty devices can be seen. The heat exchangers are the hysteresis-loop shapes. Each is about the size of the one-euro coin to the lower left of the image. Structures such as heat exchangers, valves and so on, are now an integral feature of even the more simple commercial channel network geometries.

1.1.2 The origin of microreactors.

The idea of microreactors primarily originated from a series of intellectual and technological steps in analytical science. As with all manufacturing industries, particularly since the 1960's, there has been a drive by industry to streamline its workforce and introduce technology through greater process automation. Examples of

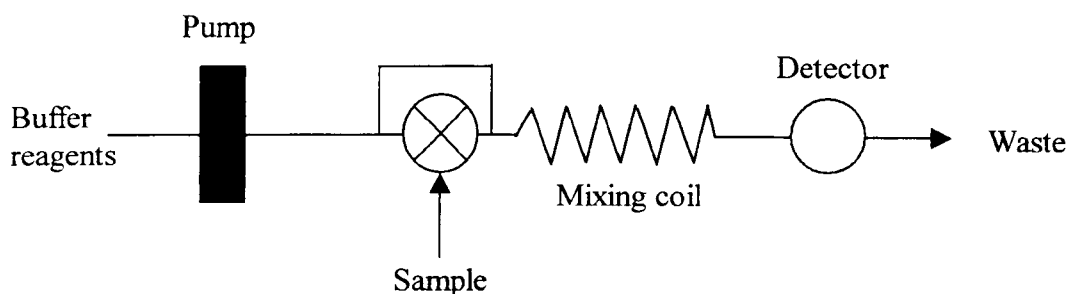
Figure 1.2: The steps of a chemical analysis procedure according to Widmer [7] *et al.*



this include: the automotive industry increasingly using robots and analytical laboratories using autotitrators to replace humans in their dedicated roles. In the proceeding paragraphs an account of the intellectual and technological steps necessary to arrive at microreactors is given.

In analytical science, there are two types of automated analytical systems: discrete analysers and continuous-flow analysers. Both perform most of the unit operations as listed in Figure 1.2 for a chemical analysis procedure, but fundamentally differ in the sample handling steps. In a discrete instrument, individual samples are maintained as separate entities, whereas in a continuous-flow system the sample becomes part of a flowing stream. This offers the unparalleled advantage of enhanced sample throughput via reduced sample analysis time. All of this is attributed to the ease of implementation and simplicity in manipulating flowing liquids in pipes.

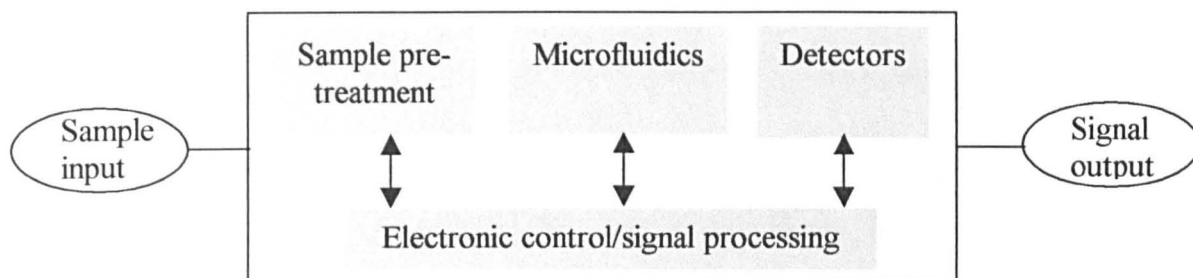
Figure 1.3: Method of producing serial assays in Flow Injection Analysis. The sample is injected into a moving carrier stream. The mixing coil helps blend the sample and reagents so they can chemically react and form a product that can be resolved by the detection system.



The first example of a continuous flow automatic analyser was introduced in 1975 by Ruzicka and Hansen [5]. Flow Injection Analysis or FIA is based on the injection of a liquid sample into an unbroken and moving carrier liquid. The injected sample mixes with the carrier reagents along the mixing coil as shown in Figure 1.3 and forms a zone of product that migrates toward the detector. The detector continuously monitors some physical parameter of the carrier liquid as the sample migrates along the column [6].

The advantages of continuous-flow automated systems remained largely underdeveloped and confined to the analytical arena in FIA type instruments until 1990. Widmer *et al.* [7] published work describing the use of chemical sensors in process control. They proposed that all the steps in chemical analysis from sample preparation to data interpretation could be achieved on one single device (Fig. 1.2). The concept was called Total Analysis System or TAS. In a pure TAS all of the unit operations of Figure 1.2, are performed without human intervention. In practice, due to the wide variety of sample matrices and compositions that are encountered in analytical laboratories, there is no universal TAS available.

Figure 1.4: Subcomponents of a Micro Total Analysis System (μ TAS) [9].



The Stanford University gas chromatograph designed by Terry and co-workers in 1979 (Fig. 1.1 b) goes some way towards demonstrating a practical TAS instrument. Their paper outlines the development of a miniature system, which allowed the separation of a mixture of hydrocarbons using a gas chromatograph design fabricated on a silicon wafer. The subcomponents to this device included a 1.5 m long column, injector valve and thermal conductivity detector allowing detection of the separated product within 10 s of injection. Since the device was the first of its kind to demonstrate this technology, it is now regarded as the pioneering device in microreactor circles.

It was Widmer, who again, saw the advantage of the increased separation speed over conventional GC systems, brought about by miniaturisation. He proposed a further concept. This was the miniaturised TAS or μ TAS (Micro TAS). In their definition Widmer *et al.* [8] state, “a TAS performing all sample handling steps extremely close to the place of measurement is called a miniaturised TAS.” The elements of a μ TAS according to van den Berg are shown in Figure 1.4. It can be seen to consist of four types of subsystems: a sampling unit, a microfluidic unit, a detector system and an electronic controller. The aspects of the electronic controller are too specific to be treated here. All other subsystems will be dealt with more fully, later in this Chapter. The terms “miniaturised TAS” and “micro TAS” are currently used interchangeably to

mean the same thing.

Since 1990, growing interest in the μ TAS concept has led to many starting points for developments particularly in biotechnology, environmental and medical sciences. Many instruments demonstrating this technology are in circulation. These include: Capillary Electrophoresis (CE) devices using micro-channels etched into planar glass substrates for their use in applied molecular genetics [10-12], systems for free-flow electrophoresis, gas and liquid chromatography [1,13,14], capillary electro-chromatography [15] and micellar electrokinetic capillary chromatography (MECC) [16]. Rapid and efficient capillary zone electrophoretic separations in micro-machined channels (i.e. open gel-filled or polyacrylamide-coated) on quartz substrates have also been shown [17,18,19]. Clearly, this multilateral development is way beyond 1990 expectations, especially when considering μ TAS was a system integration concept for rapid-response industrial sensors in process control.

In an attempt to keep up with the pace of development in the μ TAS field, new-dedicated conferences, such as the annual Micro Total Analysis Systems, were started in the mid-1990's. More recently, the first journal dedicated to miniaturisation in chemistry and biology was founded – Lab on a Chip (commenced Sept 2001). Its scope ranges from microfabrication to miniaturised chemical detection methods and encompasses all new developments in the field. One exciting and new area that is being given important coverage is that of microreactors. Whereas μ TAS is primarily an analytical concept, microreactors are not. The idea of a generalised μ TAS has been adopted to perform chemical synthesis [20-29]. The benefits that microreactors will potentially bring to chemical manufacture are similar to those that μ TAS has brought to

analytical science. These aspects will be discussed further in Section 1.1.3.

The term microreactor has actually been in use for a long time and (remarkably) precedes the period when microtechniques were first applied for microfluidic purposes [30]. Today, microreactors of increasing complexity have been developed with a whole range of on-chip chemical tools such as mixers, separators and injectors. This makes it possible to synthesize, analyse and characterise extremely small amounts of products in the pico-litre range [31]. These devices will become more useful for combinatorial synthesis and drug discovery where new procedures are being developed for the parallel synthesis and screening of large numbers of compounds. Several prototype microreactors for high speed DNA sequencing [32,33], immunoassay for serum cortisol in blood [34] and the possibility to detect high explosives at 1 ppm levels within 60 s on-chip [35] have already emerged.

1.1.3 The main operating features of microreactors.

A list of the main design features of microreactors relevant to performing chemical reactions is:

- Laminar liquid flow
- Small volumes
- High surface area to volume ratio
- High throughput: scale out not up
- Automation
- Spatial and temporal control of chemical reactions

Laminar flow

When fluid moves along a predefined path such as a microreactor channel network, the flow may be either laminar or turbulent. The flow type is defined by the Reynolds number Re . For developed flow within a tube of circular cross-section the Reynolds number is given by:

$$Re = \frac{ud_{hydro}\rho}{\eta} \quad (1.1)$$

where u is the mean flow velocity [ms^{-1}], d_{hydro} is the hydrodynamic diameter of the channel [m] (N.B. this is not restricted to circular tubes), ρ is the density [kg m^{-3}] and η is the viscosity [$\text{kg m}^{-1} \text{s}^{-1}$] of the fluid. Typically, a cylindrical microreactor channel 500 μm in diameter and supporting a water flow of 2 mm s^{-1} (having properties $\rho = 1000 \text{ kg m}^{-3}$ and $\eta = 0.000893 \text{ Pa s}$) has a Reynolds number of 1.13 [21]. The boundary between laminar and turbulent flow occurs at $Re \sim 2000$. Therefore, microreactors operate well within the laminar flow regime. It is always possible to produce laminar flow along a channel with miscible liquids, but is not possible for immiscible liquids [36].

Some benefits of laminar flow in microreactors have been demonstrated by Whitesides *et al.* [37]. They showed that if two parallel laminar flows of different solutions were brought together and allowed to flow side by side, the interface between them could be used to direct chemical reactions. Since laminar flows normally mix only by diffusion, chemical species meeting at the liquid-liquid interface would react along a very definite path. The width of this product zone was found to widen down stream of the flow, because of lateral diffusion. Whiteside *et al.* [37] fabricated small continuous

gold and silver wires by this technique, as well as etching a channel into the internal surface of the cylindrical glass capillary carrying the solutions. The structures produced had feature sizes of less than 5 μm and exhibited spatial resolution to within 5 μm . This spatial resolution was maintained over lengths of approximately a few cm. It indicates that conditions can be set such that diffusive broadening across the moving interface is not very significant over this distance.

Sometimes it is required that chemicals are rapidly mixed to produce fast results, particularly in analytical applications such as process monitoring. This dictates that long mixing by diffusion is not the best method to achieve the desired state. Fortunately, rapid mixing systems have been demonstrated which overcome the laminar flow properties of microreactors. One such device, produced by Manz *et al.* [21], relies on the division and recombination of two laminar flowing streams. The flows are divided in such a way to increase the overall diffusional interface between the streams and thus decrease overall diffusional mixing time. The advantage with such a device is that it can be applied to a particular microreactor channel section and mix the flows directly where this is required on-chip.

Alongside the possibility of performing chemical reactions using molecular interfacial diffusion in laminar flows, there also exists the opportunity to produce diffusion based separation and detection systems. Weigl and Yager [38] were the first to demonstrate the viability of a μTAS T-Sensor device to separate a particle sample based on their diffusion coefficients. Essentially, three parallel laminar flows were joined at a channel inlet node. These were the reference solution, sample and detection streams. Large particles such as blood cells do not diffuse significantly within the time the

flowing streams are in contact. Thus, the smaller particles diffuse more rapidly into the detection stream before being carried to the fluorescence detector. The diffusion-based aspects of microreactors are only possible because of their small channel dimensions.

Small volumes

The average time t taken for a molecule to diffuse over a distance x in one dimension is given by:

$$t = \frac{x^2}{2D} \quad (1.2)$$

where D is the diffusion coefficient [$\text{m}^2 \text{s}^{-1}$]. A large molecule with $D = 10^{-10} \text{ m}^2 \text{ s}^{-1}$ requires 20 min to cross a distance of 500 μm [21]. That means in a systems where mass transport is governed by diffusion, a reduction in system dimensions to 1/10 of the original size reduces the required transport time by a factor of 1/100 [8]. This is the basis for rapid analytical separations, particularly in biotechnology. DNA and other charged macromolecules are usually separated using capillary electrophoresis since no other technique can offer the same resolution. In the past, DNA separation use to take hours but now is routinely performed in minutes [33].

The very nature of small volume microreactor channels limited to a few nano-litres of reagent containment, suggests reduced chemical consumption, lower wastage, power usage and laboratory space. The significance of increased efficiency in sample usage is nowhere as marked as in clinical diagnostics. Consider a blood test for determining the blood glucose concentration of a diabetes sufferer. Traditionally, the medical practitioner typically removes 10 ml of blood, whereas now a single 50 μl drop is sufficient for the individual to perform the analysis on their own personal instrument;

purchased on the High Street.

In addition to increased sample efficiency, microreactors have been shown to give increased chemical yields for a number of reactions. Haswell and Skelton [22, 24] report results for heterogeneous catalysis in a modified Suzuki synthesis and homogeneous reactions based on Wittig chemistry. For the Suzuki synthesis, reagent solutions (0.1 M 4-bromobenzonitrile and 0.1 M phenylboronic acid both in 75 % THF (aq)) were flowed over an immobilised heterogeneous palladium catalyst bed (1.8 % Pd on silica). The synthesis of 4-cyanobiphenyl was achieved at room temperature in a microreactor to give a yield of 67 ± 7 % in 25 min. This is in comparison to the conventional laboratory batch method performed under the same conditions of solution concentration and temperature but involving reflux for 8 hrs, which gave a non-optimised product of 10%. The Wittig reaction, involving reactions of 2-nitrobenzyltriphenylphosphonium bromide with a selection of aldehydes, produced an optimised yield 10 % greater in a microreactor than by the traditional methodology for the same conditions. McCreedy and Wilson [28] demonstrated the use of sulphated zirconia catalyst in a microreactor for the dehydration of hexanol. Reported conversion efficiencies close to 100 % were obtained compared with the industrial process that only gives a 30 % conversion for the dehydration of hexanol to hexene. Besides this academic interest in microreactors, there has also been growing commercial interest, particularly from a product yield standpoint. Merck (Germany) carried out their own investigations in the Suzuki reaction between 3-bromobenzaldehyde and 4-fluorophenylboronic acid using five continuous-flow microreactors for industrial scale synthesis. Yields of 90 % were reported for the microreactors compared with 50 % in stirred flasks [39].

High surface area to volume ratio

The small geometries of microreactor channels give them a very high surface area to internal volume ratio. Typically, this ranges from 10,000 to 50,000 $\text{m}^2 \text{m}^{-3}$ compared to 1000 $\text{m}^2 \text{m}^{-3}$ in conventional laboratory vessels [24]. This gives microreactors a greater thermal dissipation capacity for performing exothermic chemical reactions. Very high heat transfer rates associated with microreactor heat exchangers have been noted on devices made by Pacific Northwest National Laboratories (PNNL, Richland, USA). For instance, heat transfer coefficients of 10,000 $\text{W m}^{-2} \text{K}^{-1}$ in liquid-liquid interactions were obtained for substrate metals like pure copper, compared with 1,700 $\text{W m}^{-2} \text{K}^{-1}$ for standard heat exchangers [40]. This increased thermal dissipation of microreactors has allowed direct fluorination of aromatic compounds to take place safely [41]. Jensen *et al.* [42] have also shown that the synthesis of organic peroxides from acid chlorides and hydrogen peroxide may even be carried out beyond the “explosion limit,” as the transfer of heat away from the reaction area is enough to prevent explosion. This effective handling of highly exothermic chemical reactions opens up the possibility for manufacturing dangerous products on a mobile microreactor production platform at the point of requirement. Dangers of transporting large volumes of hazardous chemicals could be significantly reduced.

High throughput: scale out not up

Individual microreactors typically produce nano-litres of products over a series of minutes. They have been envisaged to replace “centralized world-scale chemical plants” [43]. For this to happen the output of microreactors must be significantly increased. Increasing the channel dimensions for greater throughput alters the small-scale chemistry benefits of reduced channel dimensions. Klavs Jensen suggests a scaling out

of microreactor devices as an alternative to a scaling up. Microreactors are very good at being multiplexed on single microfabricated substrates. This is not the case for the larger numbers of individual devices needed for parallel synthesis. An industrial scale production set up would require optimised microreactors to be successfully interfaced together and also with the outside world. The traditional intermediate scale up production step of the pilot plant, used to accommodate the changing chemistry scale, would be unnecessary.

The problem of interfacing microreactors for parallel chemical production is not a simple problem for chemical engineers to solve. The small channel geometries are easily blocked by particulate matter. Typical sample pretreatment techniques for μ TAS devices (Fig. 1.4) include: (1) sample filtering through fine membrane filters, and (2) fabricated structures produced directly on the device's substrate [44]. Clearly, the possibilities of (1) and (2) can also be used on a more elaborate scale for microreactors.

The automatic chemical plant

In a lot of manufacturing processes, the key to maximising profits is to automate as many systems as possible. The scaled out production platform of microreactors described in the previous Section, could be fully automated and controlled by a central computer (Fig. 1.4). The chemical plant could be set up at the point of demand, switched on and left to run without human supervision. The flexibility and advantages of such a manufacturing system are self-explanatory. Microreactors are possibly more versatile than traditional chemical production methodologies, since each individual device can either operate in batch or continuous-flow mode [45]. To achieve the goal of realising a mobile microreactor production platform, much research and device

characterisation is required. The work presented here, and in later Chapters, goes some way in exploring this.

Spatial and temporal control of chemical reactions

The small dimensions of microreactor channels bring them close to the size of biological cells (10 – 100 μm). Gradients in the properties of solutions are important in many processes such as chemotaxis [46] and crystal growth [47]. Traditional methods for generating concentration gradients in solutions use a pipet tip or a reservoir in a gel. These methods have limitations in the shape of the gradients created and are limited to a spatial resolution of the order of several millimetres [47]. Whitesides *et al.* [48] fabricated a microfluidic gradient generator on a polymer microreactor with three inlets. A solution of 100 μM fluorescein isothiocyanate (FITC) in aqueous sodium bicarbonate buffer was introduced in the centre inlet while two outer inlets comprised only buffer solution with no FITC present. Using a laminar flow regime with repeated separation and recombination of the flows, a concentration gradient with a resolution of 25 μm was produced across a 375 μm wide channel. The resolution of the dynamic concentration gradient was easily changed by using narrower channels. Typically, 30 % changes in FITC concentration were noted over a 100 μm distance perpendicular to the flow. This is comparable with changes in concentration gradient of 2 – 20 % per 100 μm for living cells.

The spatial control of reagents in a channel allows direct manipulation of a chemical reaction and the possibility to steer it (i.e. reaction equilibrium and kinetics) in a particular direction. Whilst the ability to manipulate reactions is not a new concept in chemistry, the ease and selectivity with which it can be achieved is a unique feature of

the microreactor environment [49]. Ehrfeld *et al.* [50] prepared hydrogen cyanide in a microreactor via the Andrussow route. The rapid cooling of the products using a micro heat exchanger prevented hydrolysis of the HCN to ammonia. The Wittig reaction, mentioned earlier, between 2-nitrobenzyltriphenylphosphonium bromide and methyl 4-formylbenzoate in dry methanol, which was reported by Haswell *et al.* [26] gives the first example of stereoselective control of a chemical reaction in a microreactor by varying the applied electric fields in particular channel section. At a 1 to 1 stoichiometry in the traditional batch synthesis, the kinetically favoured *cis* stereoisomer is produced with a typical *Z/E* (molecular charge to electric field) ratio of 2.8 – 3.0. Using the same starting conditions of reaction time, reagent concentrations, solvent and stoichiometry in a microreactor, the *Z/E* ratio could be changed between 0.6 and 5.2 simply by altering driving voltages. This is rationalised in terms of the localised concentrations of reagents within the microreactor channel network and more specifically, the changes in the aldehyde concentration with applied voltage. This extra degree of control over the spatial and temporal evolution of the chemical reactions relative to a conventional stirred reactor in which concentrations are generally uniform, is what makes microreactors truly novel.

1.2 Microreactor fabrication techniques.

1.2.1 Suitable fabrication materials for microreactors.

For a microreactor to work reliably and to meet the needs of our investigations, the material from which it is made should meet certain criteria. These are:

- Optically transparent
- Electrically insulating
- Inert to the reagents

- Forms a rigid channel structure
- Low temperature bonding with minimum channel distortion
- Low auto-fluorescence

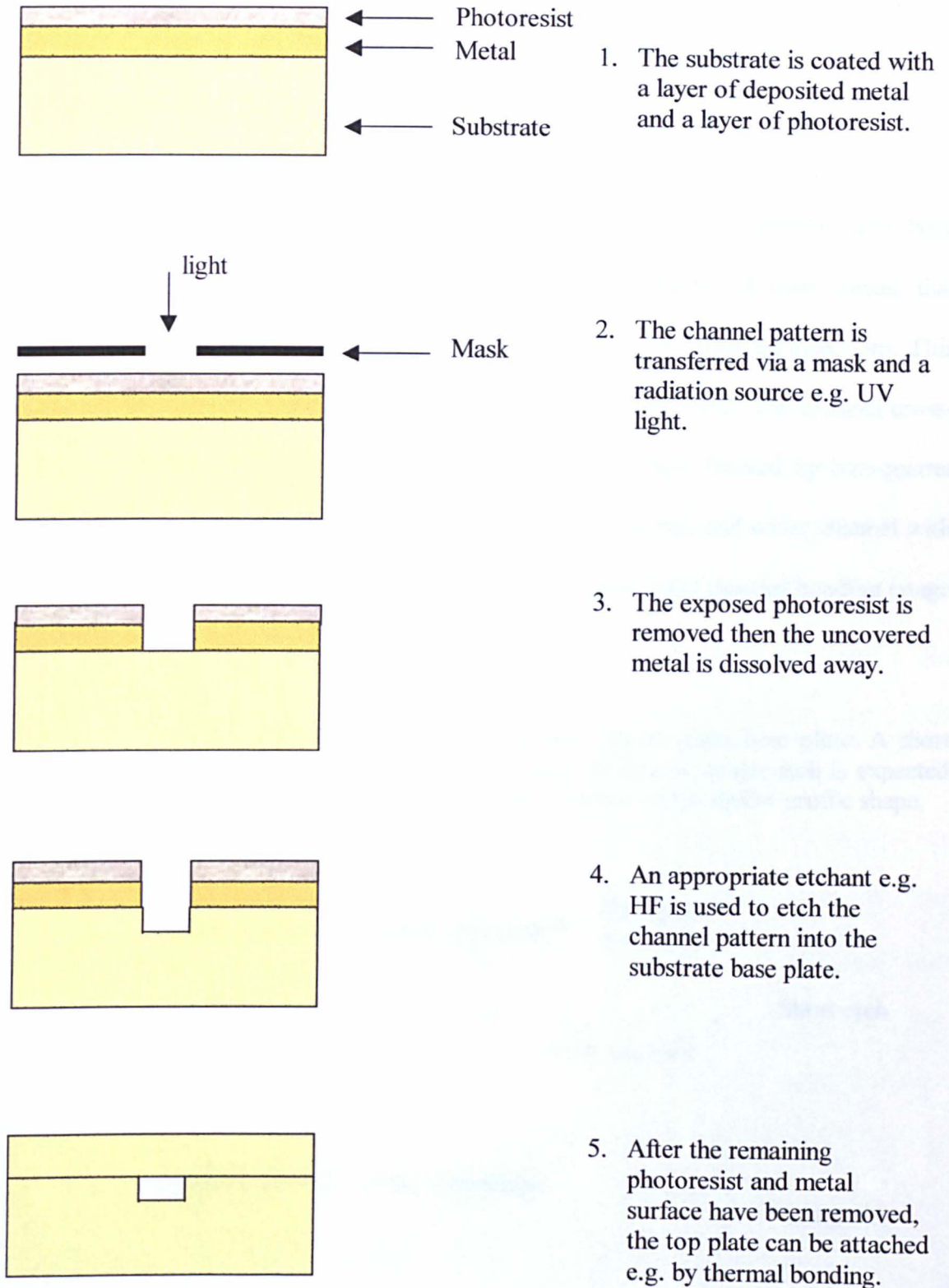
Microreactors have been fabricated from materials such as silicon, glass, metals and polymers [51], but only glass and certain polymers satisfy the criteria noted above.

1.2.2 Existing methods used for fabricating channel networks.

The commonly available fabrication methods which can be used to form micron-sized channel networks on glass and polymers are: (1) photolithography with wet chemical etching; (2) photoetchable glasses; (3) hot embossing and injection moulding; (4) LIGA – Lithography, Galvaforming and Abforming; (5) Ion beam etching; (6) Laser microforming.

By far the most commonly described method of microreactor base plate fabrication in the literature is photolithography with wet chemical etching. Lithography is the technique used to transfer copies of a master pattern onto the solid surface of a target material (or substrate). The term photolithography indicates the use of some form of electromagnetic radiation to transfer the master pattern. Photolithography has been the cornerstone and fabrication benchmark of the electronics industry particularly for the production of integrated circuits [52]. The generic process of microreactor production by photolithography is summarised by McCreedy [51] and is shown in Figure 1.5. The initial steps to arrive at stage 1 (Fig. 1.5) are outlined in his review and involve vapour depositing a chromium layer a few hundred angstroms deep, followed by spin-coating a photoresist layer from 0.5 to 2.0 μm thick. The commercial availability of substrates pretreated with Cr and photoresist at realistic prices, does not warrant in-house

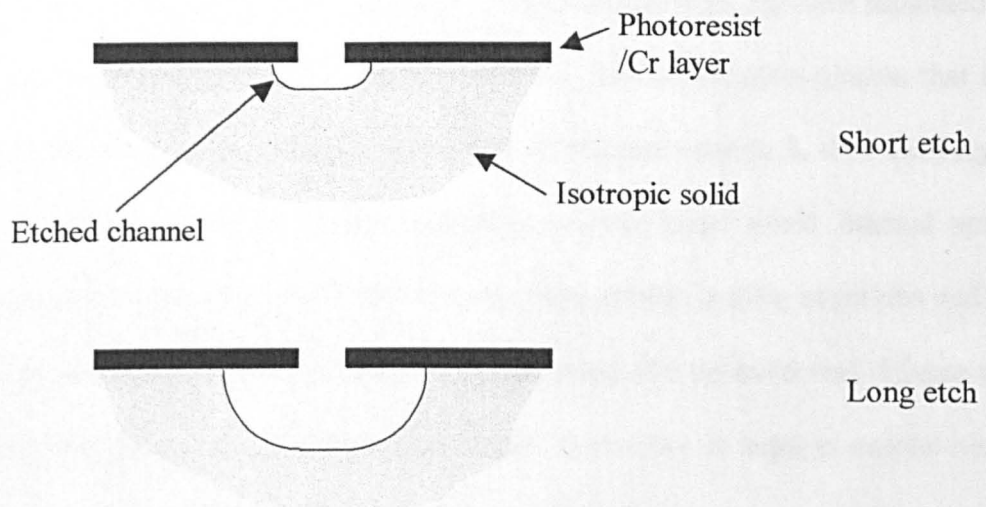
Figure 1.5: The generic process for microreactor fabrication by photolithography, wet chemical etching and thermal bonding. Drawings are not to scale.



production. Mask templates of the desired channel network designs are generated using CAD software [53]. After printing a hard copy of the photographically reduced negative mask, the pattern is transferred using UV light (stage 2) to the photoresist. This is then developed (stage 3) and the baked in an oven to harden the photoresist before etching (stage 4).

Typical wet chemical etchant mixtures consisting of HF / NH₄F solutions have been used to etch channels into glass [17]. The amorphous nature of glass means that chemical etchants such as HF attack the glass at the same rate from all directions. This gives an isotropic etch shape to the channel cross-sectional profile. The channel cross-sectional profile is characterised in Figure 1.6 by a rectangle flanked by two-quarter circle shapes. A longer etch in the solution should give a deeper and wider channel with a similar shape. The final stage of microreactor production is the thermal bonding (stage 5) outlined in Section 2.1.1.

Figure 1.6: Schematic diagram of an isotropically etched glass base plate. A short etch gives a small cross-section area, whereas a longer etch is expected to give a larger cross-sectional area channel with a similar profile shape.



Photoetchable glasses rely on the differential exposure of UV light to alter the solubility of the material dissolved in acid. Glasses from the basic $\text{Li}_2\text{O} / \text{SiO}_2$ family containing traces of Noble metals, will partially crystallize after exposure to UV light and subsequent heat treatment. The crystalline phase is lithium silicate, which is much more soluble in hydrofluoric acid than the surrounding unexposed glass. This makes the production of intricate and high precision components possible via an etching process [54]. Its use has been explored for microfluidic applications but is generally considered too expensive. In addition, it produces surfaces that are unacceptable rough for many chemical applications. The use of photo-curable materials is not just limited to glass. Indeed, photoplastics are gaining popularity for the fabrication of micro-moulds as a cheaper alternative to X-ray based LIGA techniques [55].

Hot embossing is a technique used to fabricate high precision structures in polymers [56]. A polymeric material is stamped with a master to produce a final design. The master moulds can be made from silicon, glass or nickel and these are usually laser machined [51,57]. The embossing tool and the polymer substrate are heated to just above the polymer's glass transition temperature, brought together in a controlled way, cooled to just below the polymer's glass transition temperature and then separated. Hot embossing has the reputation for being a slow and labour intensive process that is not very attractive for the commercial fabrication of microstructures. A slow delivery rate of the fabrication medium in the moulding process helps avoid internal stresses developing and allows the fabrication of very high optical quality structures and even more delicate pieces of artwork, such as freestanding thin columns and oblique walls. Although the procedure is theoretically simple, in practice it requires careful control. Any small lateral movements can destroy the moulded structure.

Injection moulding is the ideal process for mass manufacture of microstructures. Yao and Kim [58] report replication of 576 high aspect ratio micro-wells (400 μm deep by 40 μm thick walls) in a total cycle time of 15 sec. The replication process of injection moulding usually involves a polymer (replicate fabrication medium) being injected into a nickel mould. The most common fabrication materials are polycarbonate, poly(ether-ether-ketone) (PEEK), poly(methyl-methacrylate) (PMMA) and polysulphone. The use of ceramics, metals and hybrid composites are increasingly being reported. In the Hull group, poly(dimethyl-siloxane) or PDMS polymer microstructures are fabricated in a similar manner to injection moulding. McCreedy, for example, describes how a positive relief chip is etched in glass and this forms the base of the mould. The mould is then filled with PDMS and allowed to cure in the oven [59].

LIGA, derived from the German acronym “Lithography, Galvaforming and Abformung”, is a three stage process which involves lithography, electroplating and moulding to produce high aspect ratio 3D microstructures in a wide range of materials such as metals, polymers and ceramics [60,61]. The fabrication of the LIGA mould first begins with irradiation of a polymer photoresist (usually PMMA) with a laser or other ionising radiation source. Typically high intensity X-rays from a synchrotron are used. The shorter wavelengths (corresponding to higher energies) of the X-rays (20 \AA) cause the photons to penetrate deeper into the PMMA photoresist. The LIGA photoresist is about 15-20 μm deep whereas, the equivalent for optical photolithography is about 0.5-2 μm deep. The shorter wavelengths ensure a greater depth of focus and resolution than is achievable with optical photolithography. Optical photolithography is typically limited to structures larger than 0.5 μm (i.e wavelength of visible light). When the mask image is transferred to the photoresist it is developed and results in a 3D replication of

the pattern. Using electroplating, a metallic master mould is produced which can be used for injection moulding or as a hot embossing tool. LIGA is a relatively cheap fabrication process that is capable of achieving high precision in a wide range of materials.

Deep reactive ion etching (DRIE) is a specialised process that falls into the category of ion beam etching. In principle, ion beam etching involves bombarding a surface with heavy Noble ions, which have enough surplus kinetic energy to cause the ballistic mass ejection of surface atoms from the target. Such ion etching methods exhibit etch rates in the range of 10 – 300 nm / min for silicon, oxides, nitrides and photoresists when these materials are bombarded with ions having energies of the order of 1 keV [Ref. 53 pg. 63]. DRIE is able to achieve similar etch rates, but the aspect ratios produced are somewhat greater than unity. DRIE involves the formation of reactive ions which are produced when gases, such as CHF_3 / CF_4 and Ar are subjected to plasma confinement. The reactive ions so formed, interact both physically and chemically with the target surface. The maintenance of correct acceleration potentials, magnetic confinement and high vacuum equipment, requires the skills of specialist staff to operate. The use of DRIE is a costly operation, which is usually justifiable only when the outstanding precision of 10 nm resolution is required. Such high etch precision is not normally needed for microreactor fabrication.

Laser micro-forming using laser ablation to directly remove material is an emerging technology [57]. UV Excimer lasers using pulse lengths of 20 ns duration can break molecular bonds in the exposed material and form channels. With typical spot sizes of 10 μm , high aspect ratio channels are possible [51]. Very recently, a 157 nm VUV F_2

laser has been used to ablate glass to sub-micron resolutions with an effective spot size of 80 nm. This spot size estimate was based on how far the heat flow would diffuse during 11 ns pulse length [62]. The spatial coherence of the beam at the mask was also estimated to be about 7 μm . Clearly, this minimum sample heating is another plus for laser microfabrication and is extremely useful for vaporising polymers. Lasers also offer a rapid turn around time from drawing to prototype in only a few days. The technique is applicable to any material that will allow molecular bonds to be broken by high peak energy UV radiation.

1.2.3 The most suitable microreactor channel fabrication method.

The main features of the common fabrication techniques are summarised in Table 1.1. Although glass and polymers fulfil nearly all the criteria specified in Section 1.2.1, glass had marginally better material properties for forming rigid channels, being chemically inert and impervious to solvents. Having decided on glass as the substrate, consideration of cost plus ease of use leads to the choice of optical photolithography with wet chemical etching.

1.2.4 Thermal bonding methods for microreactors.

The process of thermal bonding of the etched base plate to the top block should result in a sealed channel network that is less prone to external particulate contamination than an open channel and sustains a fluid flow without leakage. The chemical bond formed between the two pieces of glass comprising the microreactor, should remain intact when routinely handled. There are a number of different methods for chemically fusing two pieces of glass that fall under the definition of thermal bonding. These include: (1) low temperature thermal bonding; (2) conventional annealing.

Table 1.1: Comparison of the different types of fabrication techniques used to produce microdevices. For the investigations of this thesis, certain criteria have been specified. Each technique has been assessed against these criteria as listed in the first row of the table. The most suitable and cost effective technique was found to be photolithography with wet chemical etching.

FABRICATION METHOD	Can the method etch glass and polymer?	Can the method be set up for less than £1000?	Does the method give adequate channel quality and minimum surface roughness?	Does the technique require specialist training and chemical handling techniques?	Does the fabrication method have a rapid turn around time i.e. less than 3 days to produce a prototype?
OPTICAL PHOTOLITHOGRAPHY	Glass only	Yes	Yes, 1 μm roughness [63]	Yes, requires hydrofluoric acid for wet chemical etching	Yes
PHOTOGLASSES	Glass only	Yes	Yes, 1-3 μm roughness [54]	Yes, requires hydrofluoric acid for wet chemical etching	Yes
HOT EMBOSsing AND INJECTION MOULDING	Polymer only	No	Yes, similar to LIGA in fact use Ni moulds from LIGA process [56]	Yes, slow labour intensive process demanding skilled technicians	Yes
LIGA	Polymer only	No	Yes, roughness averages 50 nm for Ni moulds [60]	Yes, complex 3 stage process requires specialist training	No
DEEP REACTIVE ION ETCHING	Polymer and glass	No	Yes, produce structures with 10 nm resolution [Ref. 53 pg. 63]	Yes, complex vacuum chamber and sampling preparation	Yes
LASER MICROMACHINING	Polymer and glass	No	Yes, roughness below 100 nm [57]	Yes, hazards or laser light need trained technician to operate and use computer	Yes

Low temperature thermal bonding as described by Ramsey [64] involves using a spin coated sodium silicate layer between the base plate and top block layers of glass to act as an adhesive. The supersaturated solution of sodium silicate allows low temperature condensation reactions between Si-OH groups to form Si-O-Si bonds, hence the short curing time of 1 hr at 90 °C.

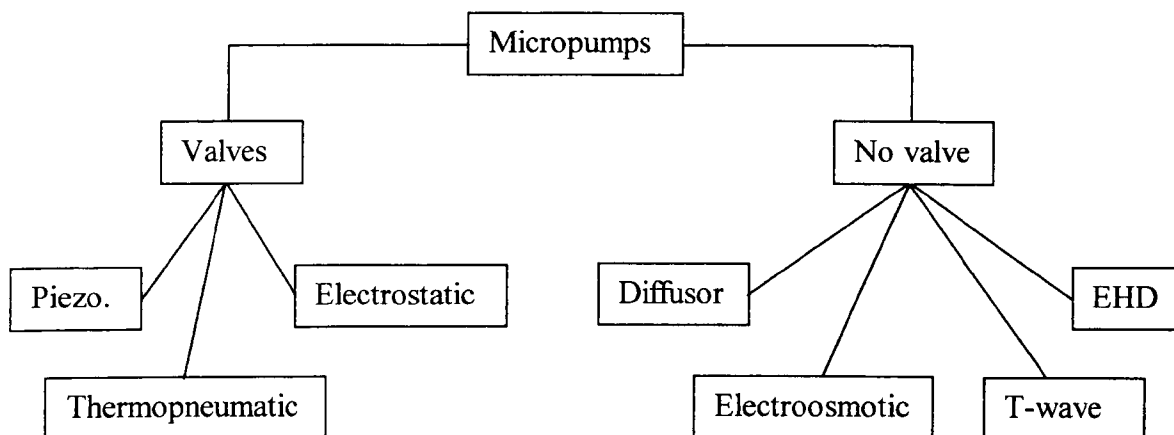
Conventional annealing in a muffle furnace involves elevating the glasses' temperature to the fusion or softening point and maintaining it at this temperature in prolonged contact, before return through natural cooling to room temperature. By ensuring that the thermal expansion coefficients of the glasses to be bonded do not differ by more than $1 \mu\text{m K}^{-1}$ [65] and that the surfaces to be fused are clean and not too rough, bonding should be successful. The typical surface roughness for fired or mechanically polished glass is between 50 and 70 Å [66]. Common thermal bonding regimes for microreactors, involve using a muffle furnace at 500 to 600 °C for 6 hr [67]. Indeed, this is similar to the method used in the Hull group for microreactor bonding [59]. With the recent advent of various new glasses with low melting points such as boron-doped glass that melts at 450 °C [64], the possibility of reduced channel distortion through the use of lower bonding temperatures becomes a realistic possibility.

1.3 Microfluidics in channel networks.

1.3.1 How are fluids moved around the microreactor channels?

There are a number of different pumping methods available for driving fluids around microreactor channel networks. These include: indirect pumping, such as (1) piezoelectric, thermopneumatic, electrostatic and direct pumping such as (2) diffusor, electroosmotic, travelling-wave (T-wave), electrohydrodynamic (EDH). Each pumping

Figure 1.7: Classification of different types of micropumps used in microreactors.



method can be classified according to its actuation principle and whether it involves a valve. A summary of the different micropumps available using the actuation principles described above, is shown in Figure 1.7 [Ref. 9 pg. 29]. This classification of micropumps is based on the presence of a valve. Group 1 (valved micropumps) indirectly mobilise the fluid, whereas group 2 (valveless micropumps) directly mobilise the liquid.

Group 1 micropumps, which include piezoelectric, thermoelectric and electrostatic actuation methods, cause fluid mobilisation by inducing a movement of a membrane usually located in the roof of an otherwise rigid cavity. The change in volume of the cavity due to movement of the membrane, coupled with a series of one-way inlet and outlet valves, gates the fluid flow in one direction. The creation of a hydrodynamic pressure gradient between the inlet and outlet of the pump is very similar to the method which larger piston pumps use to generate pressure driven flow.

Group 2 micropumps, which include diffusor, electroosmotic, travelling-wave

(T-wave), electrohydrodynamic (EDH) actuation methods, utilise the properties of the fluid and material that form the system. This allows them to be free of mechanical moving parts and eliminates potential mechanical failure of the pumping diaphragm associated with the valved micropumps.

There are a number of disadvantage associated with both group 1 and 2 micropumps. Firstly, for group 1 devices, hydrodynamic pressure requirements increase rapidly with decreasing channel cross-section. Secondly, group 2 devices may experience undesired hydrostatic back-flow through the micropump when the primary pumping force is removed.

The first point of high hydrodynamic pressure requirements for small channel microreactors can be understood from Poiseuille's equation. For a liquid of viscosity η , flowing through a cylindrical capillary of radius r_{cap} and of length L , the pressure driven volumetric flow rate F_{press} is give by:

$$F_{press} = \frac{\pi P r_{cap}^4}{8\eta L} \quad (1.3)$$

where P is the hydrostatic pressure difference between the ends of the capillary [Ref. 68 pg. 64]. From equation 1.3, it can be deduced that maintaining a set flow rate through a cylindrical channel when the radius is reduced 10 X will require a 10,000 fold increase in pressure [8].

The second point, about group 2 micropumps suffering from undesired back-flow will be discussed shortly. From the list of group 2 micropumps, the diffusor system is a

hybrid and belongs to essentially both groups. A typical diffusor micropump employs two group 1 pumps in a push-pull arrangement to mobilise fluid. Instead of having actual one-way valves, a series of check valves are used instead. Check valves take the form of a cone shaped tube, which allows liquid to flow more easily in one direction than the other. With this system, when the pump is switched off, pressure-driven back-flow can leak back through the pump. The back-flow leakage is generally much less than that for the other group 2 micropumps.

A summary of the remaining features of the group 2 micropumps and pressure-driven pumps such as peristaltic and syringe pumps, are shown in Table 1.2. *Electroosmotic flow* (EOF) utilises the surface charges on the glass surface and an applied electric field to drive the fluid in the microreactor channel forwards. This fluid mobilisation technique forms an important part of the work discussed in this thesis and will be considered later in Section 1.3.4. *Travelling wave* or ultrasonic pumps induce fluid motion by flexural travelling waves. These consist of a series of phase shifted square waves being applied to an electrode array. Frequencies of typically 1 MHz are used. Liquid can move in the direction of the wave propagation with a speed proportional to the square of the acoustic amplitude [Ref. 9 pg. 184]. *Electrohydrodynamic* pumping is based on the use of large electric fields, which are applied to metallic electrode grids located orthogonal to the flow direction. The high electric fields generate ions at one grid and these migrate by Coulombic forces and drag the fluid in the migration direction. With such induction pumping, gradients in the permittivity or conductivity of the liquid are required [Ref. 9 pg. 32]. The absence of valves and the presence of large open channels, gives some indication why back-flow leakage can present a problem for the remaining group 2 micropumps listed in Table 1.2.

Table 1.2: A short summary of the important microfluidic fluid mobilisation mechanisms currently in use. This information was taken from Verpoorte [2].

Pumping mechanism	Fluid mobilised	Some pros and cons
Pressure	Aqueous and non-aqueous	Independent of solution composition, but dependent on viscosity and channel geometry.
Electroosmotic	Mostly aqueous (non-aqueous reported but is uncommon).	Very dependent on buffer composition (e.g. ionic strength, pH) and requires high electric fields.
T-wave	Aqueous and non-aqueous	Requires complex integrated structure
Electrohydrodynamic	Low conductivity liquids (non-aqueous)	Requires high electric fields

1.3.2 The four kinds of electrokinetic phenomena.

The four kinds of electrokinetic phenomena are:

- Electroosmosis
- Electrophoresis
- Streaming potential
- Sedimentation potential

Electroosmosis is the movement of a liquid relative to a stationary charged surface under the influence of an electric field. Electrophoresis is the movement of a charged particle relative to a stationary liquid under an applied electric field. Streaming potential is the voltage created when a liquid is made to flow along a stationary charged surface. This is the opposite phenomenon of electroosmosis. Finally, sedimentation potential is the potential created when charged particles move relative to a stationary liquid. This is

the opposite phenomenon of electrophoresis. These paired phenomena are examples of, and subject to Onsager's principle of reciprocity of irreversible phenomena [69].

All the electrokinetic phenomena above rely on the properties of the electric double layer (EDL), which is formed between the charged solid surface and the bulk liquid interface. In the work of this thesis, we are primarily interested in electroosmosis and electrophoresis. These two electrokinetic phenomena will be considered in-detail following a discussion of the structure of the EDL.

1.3.3 The electric double layer and zeta potential.

Both electroosmosis and particle electrophoresis are controlled by the forces that are applied to the double layer. The formation of a double layer requires the development of either a positive or a negatively charged surface. There are several methods of spontaneous charge development at a surface: ionisation, ion adsorption, ion dissolution and adsorption / orientation of dipoles. For the amorphous tetravalent silica matrix of glass (i.e. SiO_2), de-protonation of the surface silanol groups (i.e. $-\text{SiOH} \rightarrow -\text{SiO}^- + \text{H}^+$) is the main mechanism for charge development. Any ions that are in the bulk solution are either attracted, or repelled by, the surface charge.

Consider a flat infinite solid surface of uniformly distributed positive charge. Anions (negative ions) in solution will migrate to the charged solid surface and attempt to neutralise this excess positive charge through adsorption. Cations (positive ions) remain in the bulk solution. Hence, concentration gradients of negative and positive ions are set up between the solid-liquid interface and the bulk. In 1853 Helmholtz proposed a simple model that attempted to describe the EDL surrounding an electrode by balancing

the charges in solution with the electron excess or deficiency in the electrode surface. This model was developed further by Gouy (1910) and Chapman (1913), who provided the simplest quantitative treatment and introduced the idea of Brownian motion creating a diffuse part to the EDL. The final part of the theory of the EDL was due to Stern in 1924. He proposed that the double layer was divided into two parts separated by a plane (Stern plane) located at about one hydrated ion radius from the solid surface. He also considered the possibility of specific ion adsorption.

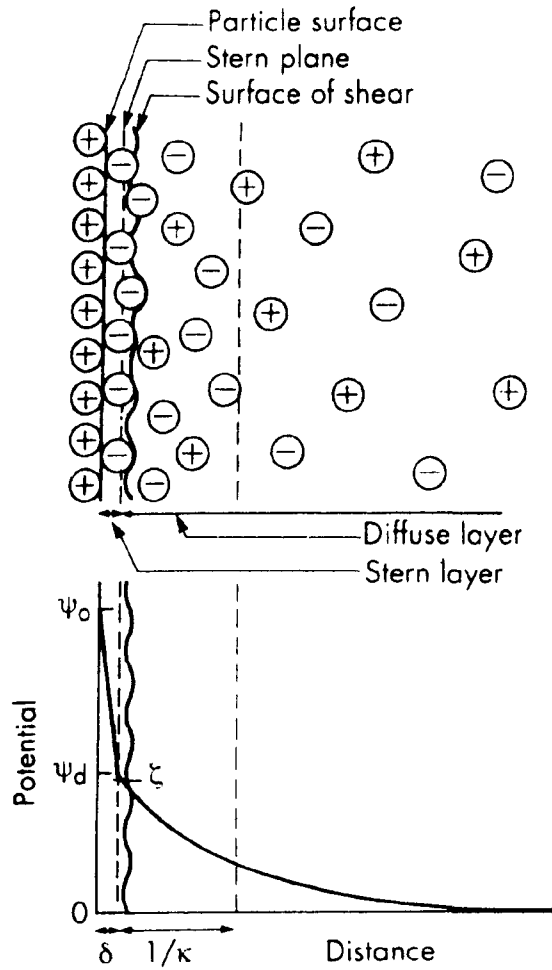
Specifically adsorbed ions are those which are bound directly to the solid surface strongly enough to overcome thermal agitation. It is possible for specifically adsorbed ions to be at least partly dehydrated in the direction of the surface (i.e. lost part of solvation shell). The Stern plane in Figure 1.8 is defined by the centres of these ions. Ions with centres located beyond the Stern plane form the diffuse part of the double layer. The potential of the solid surface ψ_o decreases sharply to ψ_d at the start of the diffuse or outer double layer. The decrease in potential ψ in the diffuse double layer with increasing distance x from the surface is given by:

$$\psi = \frac{2kT}{ze} \ln \left(\frac{1 + \gamma \exp[-\kappa x]}{1 - \gamma \exp[-\kappa x]} \right) \quad (1.4)$$

in accordance with the Gouy-Chapman treatment. In equation 1.4, k is the Boltzmann constant, T is the thermodynamic temperature, z is the integer charge number of the particle and e is the electronic charge. γ is given by:

$$\gamma = \frac{\exp[ze\psi_d / 2kT] - 1}{\exp[ze\psi_d / 2kT] + 1} \quad (1.5)$$

Figure 1.8: The structure of the electric double layer according to Stern theory [70].



and

$$\kappa^{-1} = \sqrt{\left(\frac{\epsilon_r kT}{2e^2 N_A c z^2}\right)} \quad (\text{Debye length}) \quad (1.6)$$

where N_A is Avogadro's number, ϵ_r is the relative permittivity and c is the electrolyte concentration. The thickness of the Stern layer is defined by the distance δ and that of the diffuse double layer by $1/\kappa$. The diffuse double layer is many times thicker than the Stern layer and depends on the electrolyte concentration, thermodynamic temperature, relative permittivity and charge number (Eqn. 1.6).

Electrokinetic behaviour such as EOF and electrophoresis depends on the potential at the surface of shear between the charged surface and the electrolyte solution. This potential is called the ζ (zeta) potential. The exact location of the shear plane is an unknown feature of the electric double layer. For this reason a distinction is made between ψ_d the potential at the Stern plane and ζ the potential at the plane of shear. It is, however, reasonable to assume that the surface of shear lies just beyond the Stern plane and that ζ is always marginally smaller than ψ_d . Experimental evidence suggests that the customary assumption of $\psi_d = \zeta$ usually introduces only small errors [Ref. 70 pg 185].

1.3.4 The properties of electroosmotic flow.

Electroosmotic flow (EOF) was discovered by Reuss in 1809. In the original experiments, a lump of moist clay was inserted between two vertical reservoirs of a glass U-tube filled with distilled water. On the application of a potential difference between a pair of submerged platinum electrodes, a change in the water levels in each reservoir were noted after about 20 minutes. It was clear that water had been transferred through the porous clay diaphragm. At the cathode, the water level went up, whereas at the anode, the level went down and turbidity developed in the solution. This turbidity arose from the simultaneous electrophoretic migration of some detached clay particles (naturally occurring silica and alumina). These observations indicated that the two electrokinetic effects of electroosmosis and electrophoresis were occurring simultaneously [71]. Today, the discovery of EOF has had far reaching implications in fields as diverse as engineering geology where it is used to drain foundations [72] and even reduce soil contamination [73].

The clay silica particles that Reuss noticed moving in his experiments are chemically almost identical to the glasses used to fabricate glass capillaries and microreactors. The atomic structure of glass gives it a local surface charge, which forms an EDL in the presence of a salt solution. When there exists a non-zero zeta potential, mobile charges within the diffuse double layer can be made to move along the channel walls within a microreactor, through the application of an external electric field applied to the ends of the channel. The resulting ion migration along the channel wall drags the bulk solvent along, this is known as EOF. Through the zeta potential, EOF depends strongly on pH and naturally varies between different surfaces and solvent systems.

The first mathematical treatment of EOF theory was given by Von Smoluchowski (1921), who considered the movement of a liquid under the influence of an electric field E applied parallel to a charged flat surface. The derivation of the Smoluchowski equation is given in Appendix A [Ref. 68 pg 61]. The electroosmotic liquid velocity v_{eof} is given by:

$$v_{eof} = -\mu_{eof} E \quad (1.7)$$

where μ_{eof} is the electroosmotic mobility and E is the electric field strength. Since $\mu_{eof} = (\epsilon_0 \epsilon_r \zeta / \eta)$, the more common form of the Smoluchowski equation is usually written:

$$v_{eof} = -\frac{E \epsilon_0 \epsilon_r \zeta}{\eta} \quad \text{Smoluchowski's formula} \quad (1.8)$$

where ϵ_0 is the permittivity of free space, ϵ_r is the relative permittivity of the liquid, ζ is the zeta potential of the solid-liquid interface and η is the liquid viscosity. For pure

water in a glass tube v_{eof} is of the order of mm s^{-1} , based on $\mu_{eof} = 7.6 \times 10^{-8} \text{ m}^2 \text{ V}^{-1} \text{ s}^{-1}$ at $25 \text{ }^\circ\text{C}$ and $E \sim 10^4 \text{ V m}^{-1}$ [75].

The electroosmotic volumetric flow rate F_{eof} , for a liquid flowing through a capillary tube of constant cross-sectional area A is given by the product of $v_{eof}A$. Hence:

$$F_{eof} = A \frac{E \epsilon_0 \epsilon_r \zeta}{\eta} \quad (1.9)$$

With the aim of producing greatest microreactor throughput, it is desirable to maximise the electroosmotic flow rate. This can be achieved by (1) choosing a solvent with low viscosity and high relative permittivity to obtain a high zeta potential (2) modifying the surface properties of the channel wall e.g. coating it with a different material. Through changes in the surface coating or modification of the surface charges, it is possible to either enhance or retard the electroosmotic flow rate [74]. Using a different solid material to form the double layer allows direct manipulation of the zeta potential and thereby the liquid flow rate. The same effect on zeta potential can be produced by varying the concentration of dissolved electrolyte in the channel solution at fixed pH. From this discussion, it is clear that the zeta potentials for different solvent systems are central to the work presented here and therefore, will be given further detailed coverage.

1.3.5 Electrophoresis and diffusion.

Consider when there is an applied electric field across the ends of a glass microreactor channel. The bulk liquid, if it is water at pH 7, will move toward the cathode with an electroosmotic velocity v_{eof} . If an uncharged particle exists within the water, it will be free to diffuse through the water via Brownian motion, but will still be

dragged along the channel with the solvent bulk at v_{eof} . If a charge of $+ze$ was now assigned to the particle, it would then also be influenced by any applied electric fields along the channel. The total velocity v_{tot} with which the particle would move, is the vector sum of the bulk solvent velocity and its own electrophoretic velocity v_{eph} in the solvent (i.e. $v_{eof} + v_{eph}$). The direction of the electrophoretic velocity of the particle depends on the charge of the species. If a particle's charge is positive, then it would move with the electric field toward the cathode. The electrophoretic mobility of the particle is given by the Einstein relation $\mu_{eph} = (zeD / kT)$, where z is the integer charge number, e is the electronic charge, D is the diffusion coefficient, k is the Boltzmann constant and T is the absolute temperature [Ref. 76 pg 765]. The electrophoretic velocity is related to electrophoretic mobility through:

$$v_{eph} = \mu_{eph} E \quad (1.10)$$

where E is the applied electric field. The more complete form of this equation is:

$$v_{eph} = \frac{zeED}{kT} \quad (1.11)$$

The magnitude of v_{eph} is typically in the order of mm s^{-1} that is generally comparable to v_{eof} [77].

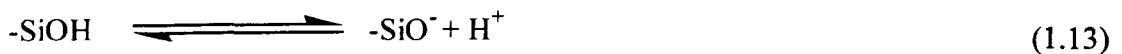
1.3.6 How zeta potential varies with pH for glass-aqueous systems.

Given that electroosmotic flow rate depends on zeta potential, it is now relevant to note a few properties of zeta potentials. Consider a solid surface such as a microreactor channel wall that is terminated by silanol groups. These groups are able to be protonated and de-protonated. From the results published by Pravdic *et al.* [78] listed in Table 1.3,

it can be deduced that the zeta potential for an aqueous solution of 10^{-3} M NaCl in a quartz capillary at pH ~ 2.5 is about zero mV. At this point, the ionic charges in solution are effectively neutralising the charged groups on the surface. At pH ≤ 2.5 the excess protons create a positive zeta potential through the equilibrium reaction:



whereas at pH ≥ 2.5 the silanol groups become de-protonated according to:



and give a negative zeta potential. Both of these equilibrium reactions have different pK_a 's. The first reaction has a pK_a below pH 2.5 whereas the second reaction lies somewhere between pH 5 – 7 for glass-water interfaces. This therefore demonstrates zeta potential and EOF both strongly depend on pH and that the usable electroosmotic flow rates are confined to a pH range of between > 2.5 and ~ 8 [80].

Table 1.3: Reported zeta potentials vs. pH for 10^{-3} M NaCl (aq) in quartz tube [78].

pH	ζ / mV
2.32	+ 12.5
3.29	- 10.4
4.11	- 35.4
5.13	- 72.9
6.29	- 89.6

1.3.7 How zeta potential varies with salt concentration for different glass-aqueous electrolyte solutions.

Electrolyte concentration strongly affects the zeta potential because of the changes brought about in surface charge density. Table 1.4 shows how zeta potential varies with

Table 1.4: Published zeta potentials from a range of authors for aqueous electrolyte solutions with quartz and glass surfaces. N. – Value not stated.

Author(s)	Aqueous-solid interface	Salt conc. / M	pH	ζ / mV
Pravdic <i>et al.</i> [78]	Silica glass (50 ppm Al ₂ O ₃) as cylindrical capillaries	10 ⁻⁴ NaCl	7	- 159
		10 ⁻³ NaCl	7	- 137
		10 ⁻² NaCl	7	- 86
Johnson [80]	Granular quartz sand grains	10 ⁻⁵ KCl	7	- 48
		10 ⁻⁴ KCl	7	- 54
		10 ⁻³ KCl	7	- 47
		10 ⁻² KCl	7	- 30
		10 ⁻¹ KCl	7	- 16
		10 ⁻² KCl	7.4	- 93 ± 3
Van Wagenen & Andrade [81]	Borosilicate glass capillaries and slides	10 ⁻² KCl	7.4	- 93 ± 3
Rutgers & De Smet [82]	Glass capillaries	10 ⁻⁶ KI	≈ 7	- 165
		10 ⁻⁵ KI	≈ 7	- 150
		10 ⁻⁴ KI	≈ 7	- 125
		10 ⁻³ KI	≈ 7	- 93
		Pure water	≈ 7	- 148
Riekkola <i>et al.</i> [75]	Fused silica capillaries	Pure water	N.	- 97.8
Fairbrother and Balkin [83]	<i>Quartz capillaries</i>	Pure water	N.	- 55.4

concentration for a range of different salts in aqueous solution. For all the 1-1 binary electrolytes systems shown, the observed zeta potential decreases with increasing concentration. This is because increasing the electrolyte concentration (Eqn. 1.6), leads to a compression of the double layer ($1/\kappa$). The zeta potential for pure water in theory should be the limiting case where the highest zeta potential is obtained. In practice, however, this is determined by the concentration of impurities and the extent of solvent autoprotolysis [79].

Zeta potential being a surface phenomena, is very sensitive to surface contamination. Consequently, a certain degree of natural variability between published data from similar systems can be found. Consider the results listed in Table 1.4 for pure water. Riekkola *et al.* [75] reported a $\zeta = - 97.8$ mV for fused silica capillaries, whereas

Fairbrother and Balkin [83] reported a $\zeta = -55.4$ mV for quartz capillaries. Both these systems show a 50 – 100 % relative error. It should be noted that the terms silica and quartz are synonymous and regularly used interchangeably in the literature [Ref 65, pg 209]. The natural variability between similar experiments has been attributed to surface cleaning procedures and solution contamination [84].

1.3.8 Zeta potential for glass and non-aqueous systems.

An important requirement of the Hull group for efficient on-chip chemical synthesis is to use solvents that are capable of dissolving a large range of different compounds. Many organic reagents will not dissolve in water and require organic solvents. It is useful to have some knowledge of the trends in zeta potential for some non-aqueous solvent / glass systems. Table 1.5 goes some way to addressing this.

It can be seen from De Smet and Delfosses' data in Table 1.5 that for solutions containing KI in both methanol and n-propanol, zeta potential becomes progressively more positive with increasing KI concentration. For the pure solvents reported by Riekkola *et al.* it appears that zeta potential depends on relative permittivity. Solvents with $\epsilon_r > 35$ in Table 1.5, have a high negative zeta potential of – 100 mV or more. Formamide appears to be the only exception with a $\epsilon_r = 109.5$ and a $\zeta = -45.6$ mV. The formamide data reported by Fairbrother and Balkin also shows some natural variability compared to that of Riekkola *et al.*.

Hidalgo-Alvarez *et al.* [85] offer one possible explanation to why low relative permittivity solvents tend to give a low zeta potential with glass. They reported that decreasing the dielectric constant of the solvent leads to a decrease of the surface charge

Table 1.5: The zeta potentials for several non-aqueous solvent systems of interest. All solvents are pure unless otherwise stated and values reported are for 25 °C.

Author(s)	Solvent-solid interface	$\mu_{eof} / \text{m}^2 \text{s}^{-1} \text{V}^{-1}$	ζ / mV	ϵ_r
Riekkola <i>et al.</i> [75]	<i>Fused silica (qz) capillaries</i>			
	Acetonitrile	1.81×10^{-7}	- 195.2	37.4
	N,N-dimethylformamide	5.86×10^{-8}	- 144.7	37.1
	Methanol	4.46×10^{-8}	- 84.0	32.6
	Ethanol	1.46×10^{-8}	- 72.6	24.3
	1-Propanol	4.13×10^{-8}	- 46.7	20.1
	Formamide	1.34×10^{-8}	- 45.6	109.5
Fairbrother and Balkin [83]	<i>Quartz capillaries</i>			
	Formamide		- 59.1	84.0
	Ether		+ 13.6	4.4
De Smet and Delfosse [Ref 69 pg 230]	<i>Porous silica glass</i>			
	0.01 mM KI in methanol		- 115.0	
	0.1 mM KI in methanol		- 96.0	
	1 mM KI in methanol		- 65.0	
	0.1 mM KI in n-propanol		- 19.0	
	1 mM KI in n-propanol		+ 5.0	

density. When the EDL is considered as a parallel plate capacitor, it is easy to understand that a lower zeta potential and surface charge will be obtained because of lowering the relative permittivity of the dielectric material.

The observed trends in zeta potential from Tables 1.4 and 1.5 can be summarised as follows:

- Zeta potential generally decreases in magnitude with increasing added electrolyte concentration.
- Zeta potential is predominantly negative for pHs greater than 2.5 for glass / water surfaces.
- Generally, high relative permittivity solvents have the highest magnitude of zeta potential.

1.3.9 The implications of specific surface conductivity in estimates of zeta potential.

In a microreactor channel filled with conducting liquid, the normal electrical conduction path is through the liquid bulk. Sometimes because of the accumulation of ions in the double layer, an additional electrical conduction path exists along the channel surface. This has the effect of dividing the total current I_{total} flowing through the channel into two components: the surface current I_{surf} and the bulk conduction current I_{bulk} . In some cases, I_{surf} can be of the same order of magnitude as I_{bulk} , especially at low electrolyte concentrations and in small dimension channels. Gu and Li [86] indicate that zeta potentials can be underestimated by one order of magnitude if specific surface conductivity is not taken into account. A detailed description of this phenomenon will now be given.

For a capillary of constant cross-sectional area A , filled with a solution of bulk conductivity κ_o the associated electroosmotic current I_{eof} for a given electric field is:

$$I_{eof} = \frac{V}{R_{elec}} = \kappa_o AE \quad \text{Ohm's law} \quad (1.14)$$

where V is potential difference applied to the electrodes, set across the channel of resistance R_{elec} . Ohm's law can be used to recast equation 1.9 in terms of the electroosmotic current:

$$F_{eof} = \frac{\epsilon_o \epsilon_r \zeta}{\eta \kappa_o} I_{eof} \quad \text{Wiedemann's formula [90]} \quad (1.15)$$

where ϵ_o is the permittivity of free space, ϵ_r is the relative permittivity of the liquid, ζ is the solid-liquid interface zeta potential, η is the liquid viscosity and κ_o is the bulk electrical conductivity. An important feature of equation 1.15 is that electroosmotic

volumetric flow rate is directly proportional to I_{eof} and ζ . This is only true if the surface currents are negligible relative to the total current. For a zeta potential to be calculated using experimentally determined flow rates and electrical currents, the measured current (I_{total}) requires proper separation into I_{eof} and I_{surf} .

In the case that a significant proportion of the total current I_{total} flowing through the channel is carried by surface conduction, it is necessary to then consider specific surface conductivity κ_s . Considering that $I_{total} = I_{bulk} + I_{surf}$, this requires Ohm's law (Eqn. 1.14) to be amended to include this extra surface conduction term. For a cylindrical capillary of radius r_{cap} this yields:

$$\frac{I_{total}}{E} = \pi r_{cap}^2 \kappa_o + 2\pi r_{cap} \kappa_s \quad (1.16)$$

where κ_o is the solution bulk conductivity and has the units $S\ m^{-1}$ and κ_s is the specific surface conductivity which is measured in Siemens. κ_s refers to the conductance of a square sheet of material of unit area and constant, negligible thickness, measured along the length of the square. Equation 1.16 can be generalised for any channel shape with cross-sectional area A and circumference C :

$$\frac{I_{total}}{E} = \kappa_o A + \kappa_s C \quad (1.17)$$

This can also be expressed in terms of the electrical resistance R_{elec} :

$$R_{elec} = \left(\frac{L}{\kappa_o A + \kappa_s C} \right) \quad (1.18)$$

where L is the channel length.

An important requirement for the minimisation of specific surface conductivity in zeta potential measurements is that the capillary diameter is sufficiently large in comparison to the EDL. Werner *et al.* [87] points out that the thickness of the EDL can extend up to a few micrometers for both pure water and pure organic liquids. Consider equation 1.16, $I_{bulk} \propto r_{cap}^2$ whereas $I_{surf} \propto r_{cap}$. That means as surface current increases with increasing capillary radius, but overall becomes less significant to the total contribution of current flow I_{total} . Therefore, in practice, κ_s is made less significant by using larger bore capillaries and higher electrolyte concentrations ($I_{surf} \propto \sqrt{\text{concentration}}$ whereas $I_{bulk} \propto c$ [Ref. 69 pg 237]).

1.3.10 Specific surface conductivity values for aqueous and non-aqueous solvents.

Hunter [Ref. 68 pg 63] reports that specific surface conductivities are of the order of 10^{-8} or 10^{-9} S for water in glass capillaries and that non-negligible surface currents can be expected in 1 mm diameter capillaries at electrolyte concentration below about $10^{-3.5}$ M. Some values of specific surface conductivity for aqueous KCl solutions in glass capillaries are reported by Overbeek (in Table 4, pg 236 of ref. 69) and are reproduced here in Table 1.6. The κ_s values given by Urban *et al.* [69] indicate that, for increasing KCl concentration, the specific surface conductivity also increases. A comparison of the three different authors' (McBain and Foster, Urban *et al.* and Fricke and Curtis) results for fixed KCl concentration (0.001 M) shows a variation of approximately two orders of magnitude for the same aqueous solutions. Theoretical specific surface conductivities for solutions of 5×10^{-4} M KCl (aq) with a $\zeta = -120$ mV lie in the range 1 – 10 nS. This result is somewhat lower than the mid-range of reported experimental values (1 – 95 nS) for 5×10^{-4} M KCl (aq) with glass surfaces [Ref. 69 pg 237].

Specific surface conductivity data for non-aqueous solvents is scarce in the literature. The limited datasets that were found are shown in the last 4 columns of Table 1.6. Given these limited values it is difficult to judge what is really an average result. For formamide and ether it is impossible to say if these results are consistent with other published work. Martin and Gortner [88] report $\kappa_s = 8.8 \mu\text{S}$ for pure water-cellulose and $\kappa_s = 8.1 \mu\text{S}$ for methanol-cellulose. Clearly, these values show the more erratic nature of specific surface conductivity associated with pure solvents and low electrolyte concentrations.

Table 1.6: The specific surface conductivities for several aqueous and non-aqueous solvent systems. N.B. indicates that no buffer was present in the solvent.
* Indicates the data taken from Overbeek [Ref. 69 pg 236].

Author(s)	Solid-solution interface	Salt conc. / mol dm ⁻³	$\kappa_s / 10^{-9} \text{ S}$
McBain and Foster*	Pyrex glass-KCl (aq)	10 ⁻³ M	100
	Urban <i>et al.</i> *	0.0005 M	4.3
Fricke and Curtis*	Pyrex glass-KCl (aq)	10 ⁻³ M	8.2
		10 ⁻² M	35
		10 ⁻³ M	0.6
		N.B.	63
Gu and Li [86]	glass-pure water	N.B.	63
Fairbrother and Balkin [83]	glass-NaCl (aq)	10 ⁻³ M	322
	<i>Quartz capillaries</i>		
	Formamide	(N.B.)	1.2 x 10 ⁻⁵ S
	Ether	(N.B.)	< 10 ⁻⁸ S
	Pure water	(N.B.)	1.7 x 10 ⁻⁶ S

The irreproducible nature of reported specific surface conductivities may arise from the use of different cleaning techniques. It is well known that such surface phenomena are particularly sensitive airborne contaminants. Overbeek [Ref. 69 pg 238] further suggests that an additional conduction or adsorption may exist that is completely independent of electrokinetic phenomena and has not yet been taken into account. It should be noted that electrokinetic experiments performed using different

radii capillaries have yield variable values of κ_s . I_{surf} is proportional to r_{cap} , but κ_s is not proportional to r_{cap} . Therefore, specific surface conductivity should be independent of capillary radius at fixed electrolyte concentration.

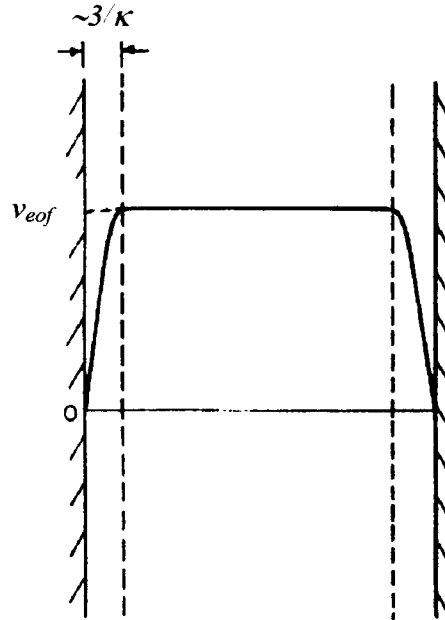
The observed trends in specific surface conductivity from Table 1.6 can be summarised as follows:

- Specific surface conductivity generally increases with increasing salt concentration for aqueous solutions.
- Specific surface conductivity becomes less important in larger bore capillaries and at higher electrolyte concentrations.
- The wide variability in specific surface conductivities particularly for aqueous solutions makes it difficult to judge what is an average result. This can possibly be attributed to the different cleaning methods used by various authors.

1.3.11 Flow profiles for combinations of electroosmotic and pressure-driven flow.

Both electroosmotic and pressure-driven flows have specific advantages that distinguish them in their choice of application. One advantage of EOF over pressure-driven flow, is that its plug-type flow does not cause band broadening in analytical separations where the resolution is limited by the degree of sample dispersion on the separating column. Figure 1.9 shows the typical plug-type flow profile for pure EOF. This boundary layer is the region where the stationary liquid changes to the bulk liquid flow velocity v_{eof} at approximately $3/\kappa$ from the channel wall. From equation 1.6, the double layer thickness is about 1 nm for a 0.1 M solution and 10 nm for a 1 mM solution [Ref. 70 pg 181]. Clearly, the thickness of the boundary layer is also of the order of nanometres and is generally negligible relative to the typical channel

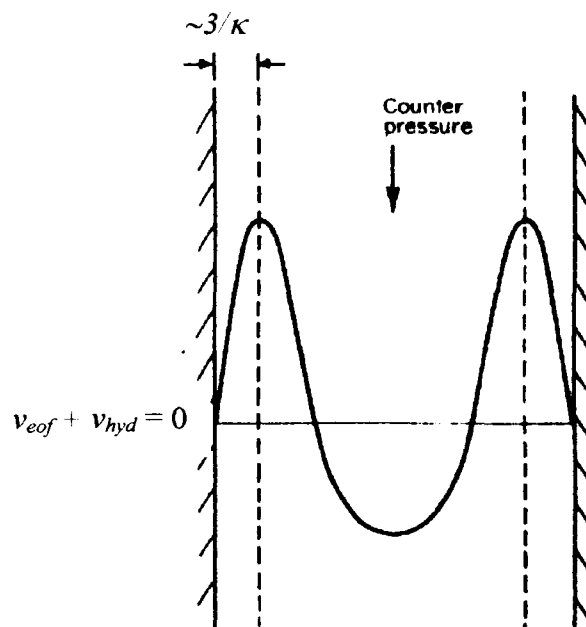
Figure 1.9: The flow profile for a liquid being mobilised in a smooth microreactor channel under pure EOF conditions. The liquid is stationary at the channel wall but moves with v_{eof} at approximately $3/\kappa$ from the channel wall [Ref. 68 pg 62]. The thickness of this layer has been greatly exaggerated.



dimensions of a microreactor.

For EOF under non-zero hydrostatic back-pressure condition, a distorted flow profile exists which differs from the pure EOF profile shown in Figure 1.9, by the superimposition of a reverse parabolic flow. The parabolic flow profile is the signature of a pressure-driven flow. The flow in the middle of the channel, shown in Figure 1.10, is faster along the centre than at the channel wall. This changing velocity across the channel gives rise to dispersion in separation systems and subsequent loss of resolution. Although the electroosmotic pressure is producing a flow in the direction toward the top of the page in Figure 1.10, the greater hydrostatic counter pressure causes the flow to move in the opposite direction with a maximum speed down the page of v_{hyd} . Garguilo *et al.* [89] elegantly verified the velocity profiles of the types shown schematically in

Figure 1.10: The flow profile for a liquid being mobilised in a smooth microreactor channel under EOF conditions with a non-zero opposing hydrostatic back-pressure. The bold solid line across the channel indicates the combined electroosmotic v_{eof} and pressure-driven v_{hyd} flow velocity [Ref. 68 pg 62].



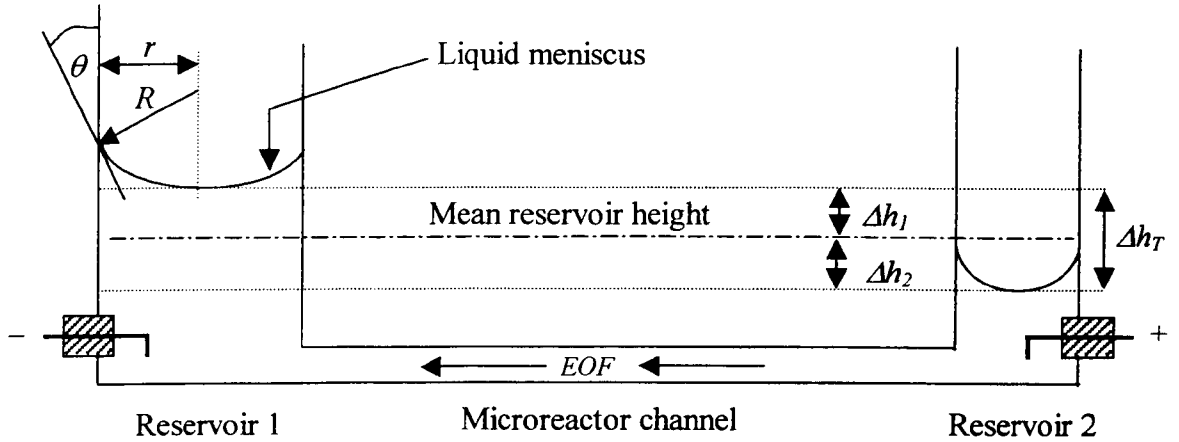
Figures 1.9 and 1.10 for electroosmotic and pressure driven flows using a caged dye method.

Two situations exist where such a flow profile as shown in Figure 1.10 will be generated within a microreactor. These are: (1) when non-zero hydrostatic pressure heads and (2) non-zero Laplace pressure differences exist between reservoirs.

Non-zero hydrostatic pressures

Non-zero hydrostatic pressures naturally occur because of liquid being displaced from one reservoir to another as occurs with EOF. Consider the reservoir arrangement shown in Figure 1.11. When the reservoirs are filled to different initial heights with zero applied voltage, the liquid flows to a mean level where the combined reservoir liquid

Figure 1.11: Schematic representation of the liquid such as water in a typical microreactor with two reservoirs connected by a narrow channel. The Laplace pressure in each reservoir is a function of the radius of meniscus curvature, whereas hydrostatic pressure is a function of the relative height differences between the liquids in each reservoir. Reservoir 1 has a cross-sectional area A_1 and reservoir 2 a cross-sectional area A_2 .



level height difference $\Delta h_T = 0$. The reverse scenario happens when voltage is applied to individual electrodes situated in each reservoir. Forward electroosmotic pressure causes a displacement of liquid from reservoir 2 toward reservoir 1. The liquid level in reservoir 1 of cross-sectional area A_1 increases by Δh_1 , whereas the liquid level in reservoir 2 of cross-sectional A_2 is depressed by Δh_2 . The combined reservoir liquid level height difference $\Delta h_T = \Delta h_1 + \Delta h_2$, gives rise to a reverse hydrostatic counter pressure:

$$P_{hydro} = \Delta h_T \Delta \rho g \quad (1.19)$$

where $\Delta \rho$ is the density difference between the liquid and air; and g is the acceleration due to gravity.

From the previous discussions it has been shown that varying degrees of “pure” EOF can exist. To give a quantitative description of what is and what is not pure, it is

necessary to consider when the pressure-driven flow component of the total flow can be considered negligible relative to that from EOF. In the case that Laplace pressures and channel obstruction effects are absent, i.e. pressure driven flow arises only from differences in hydrostatic liquid levels; Fletcher *et al.* [77] calculated that, for the pressure-driven volumetric flow rate to be equal to or less than 10 % of the total flow in an EOF system, Δh_T must satisfy:

$$\Delta h_T \leq \frac{4V\varepsilon_r\varepsilon_0\zeta}{5\Delta\rho gr_{eff}^2} \quad (1.21)$$

where V is the potential difference applied between the reservoir electrodes and r_{eff} is the “effective” flow radius of the cylindrical channel. N.B. equation 1.21 is the correctly derived form that is misquoted in Ref. 77.

Non-zero Laplace pressure differences

The Laplace pressure change $P_{Laplace}$ that exists across the liquid meniscus within a single reservoir is given by:

$$P_{Laplace} = \frac{2\gamma}{R} \quad \text{Laplace's equation} \quad (1.19)$$

where R is the radius of meniscus curvature, and γ the surface tension of the liquid (N m^{-1}). As in capillary rise phenomena [90], the radius of curvature of the liquid meniscus depends on both the radius of the reservoir containing the liquid r and the contact angle θ made by the liquid with the reservoir wall according to $R = r / \cos \theta$, represented in Figure 1.11. For pure water of $\gamma = 72 \text{ mN m}^{-1}$ making a contact angle of 0° within a 1 mm radius cylindrical reservoir, the Laplace pressure is approximately 140 Pa. The magnitude of this Laplace pressure is equivalent to the hydrostatic pressure

exerted by a column of water 14 mm high. Clearly, this can have significant implications for flowing liquids within microreactor channel networks.

1.3.12 Methods for maximising pure EOF while minimising pressure-driven back-flow.

Pressure-driven flow can be minimised in a number of ways such as:

- Ensuring liquid level height differences are zero
- Porous channel restrictions
- Matching the reservoir radii and hence Laplace pressure differences
- Matched or 90° contact angles in each reservoir
- Large bore reservoirs, such that $P_{Laplace} \sim 0$ Pa

Ensuring $\Delta h_T = 0$ and porous channel restrictions

In a sealed microreactor system that has a fixed mass of fluid, there is no way that the liquid can flow between reservoirs without the liquid levels in each reservoir changing. If the liquid level height difference between reservoirs Δh_T was zero, such as at the equilibrium level in Figure 1.11, then the liquid flow profile would not be distorted by pressure-driven flow. This condition could only be realised in a working microreactor, if fluid was added to the system from an external source. The solution to this problem of interfacing and getting reagents into and out of microreactors is does not form part of the work presented here.

As a need to control pressure-driven flow F_{Press} in a microreactor with a fixed liquid / fluid mass, the notion of reducing the channel cross-section has been reported and implemented in several cases. Those methods outlined include: fabricating smaller channels [91] or deposition of a porous plug in the flow path [24, 26, 28, 92]. The idea

of fabricating smaller channels to control F_{press} is a topic discussed further in proceeding Chapters. The deposition of porous silica plugs (known as frits) into the microreactor channels has been investigated by McCreedy *et al.* [92] with some limited success. They reported fabricating silica frits from the reaction between 10 % w/w formamide and potassium silicate (21 % SiO₂ and 9 % K₂O) followed by dehydration in an oven at 100 °C. These basic hydrodynamic restrictions became the basis for controlling pressure-driven flow in the Hull group. In performing experiments, it was noticed that frits degraded with chemical exposure and could not be fabricated to a given reproducible porosity. An additional problem with silica frits was that the high pressures needed to force liquid through them to produce a conducting and air free channel, often removed the restriction. Both methods of creating porous channel restrictions break up the total flow in the single channel and effectively replace it with many parallel finer channels. This does not conserve the pure electroosmotic flow profile because of the different flow path lengths encountered.

Matching the reservoir radii and hence Laplace pressure differences

Choosing reservoirs with matching internal radii will significantly reduce Laplace pressure differences occurring between inlet and outlet reservoirs.

Matched or 90° contact angles in each reservoir

Consider reservoir 1 in Figure 1.11; when the contact angle $\theta = 90^\circ$ the Laplace pressure is zero. Such a contact angle for water in a glass tube can be almost achieved by adding a surfactant that lowers the surface tension. Unfortunately, this method has implications for the conductivity of the solution and can cause problems with zeta potential measurements. An uncompromising alternative, which gives approximately

the same result for Laplace pressure differences, is to match the contact angles between reservoirs. The easiest contact angle to approach for an air-water interface in a glass tube, is that of zero degrees. Conveniently, this is produced by thorough chemical cleaning and solution wetting of the glass reservoirs.

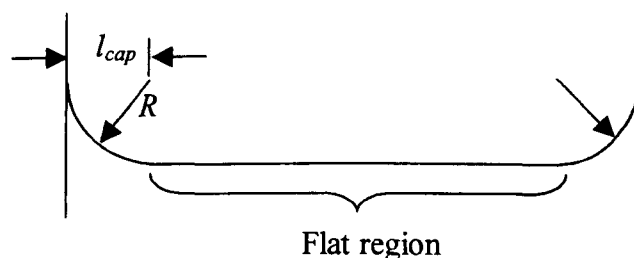
Large bore reservoirs, such that $P_{Laplace} \sim 0$ Pa

A Laplace pressure of zero can be attained in a single reservoir if it has an internal radius sufficiently large, such that a flat region exists in the centre of the meniscus cap, when the reservoir is filled with liquid. Consider Figure 1.12, the distance over which the liquid curves up the reservoir wall is known as the capillary length l_{cap} and is defined by the equation:

$$l_{cap} = \sqrt{\frac{2\gamma}{\Delta\rho g}} \quad (1.22)$$

where γ is the liquid surface tension $\Delta\rho$ is the density difference between the liquid and air; and g is the acceleration due to gravity. The capillary length for pure water is about 3.8 mm; hence, a reservoir must be larger than about 8 mm in diameter to contain a flat region.

Figure 1.12: Schematic representation of meniscus in a wide bore reservoir. Liquid curvature only exists at the edge extremities where the container meets the liquid-air interface [90].



Generally, large reservoirs of matched internal radii will give the minimum possible Laplace pressure differences. It is worth noting that, as one reservoir is emptying and another is filling, a dynamic contact angle hysteresis can exist between reservoirs which makes a non-zero Laplace pressure differences.

1.3.13 Joule heating and electrolysis within microreactor channel networks.

Considerations of the electric field strength that will be used in a microreactor are a very important design aspect for the device. As the electric field increases between different reservoir electrodes a number of different conduction phenomena such as solvent and glass breakdown can occur. The usable range of electric fields required for EOF purposes usually lies far below this threshold. In the Hull group, we typically employ 100 V cm^{-1} and obtain satisfactory EOF, using both aqueous and non-aqueous solvent systems. Harrison *et al.* [93] reported using electric field strengths in excess of 1000 V cm^{-1} for mobilising reagents in methanol and acetonitrile. This was for performing organic phase reactions. This high value is not outside the normal range for analytical electrophoretic separations such as in capillary electrophoresis, where typical electric field strengths of the order $200 - 1000 \text{ V cm}^{-1}$ are routinely used [84, 87]. The high field strengths used in capillary electrophoresis account for the speed and efficiency that this technique can separate mixtures.

High electric field strengths usually incur problems of solution Joule heating and electrolysis. Arulanandam and Li [94] made a conservative estimate of Joule heating. They calculate that for a $100 \text{ }\mu\text{m}$ internal diameter silica glass capillary operating under pure EOF conditions and filled with; $\sim 10^{-4} \text{ M KCl (aq)}$ ($\rho \sim 10^3 \text{ kg m}^{-3}$, $\kappa_0 \sim 10^{-2} \text{ S m}^{-1}$ specific heat capacity $\sim 10^3 \text{ J kg}^{-1} \text{ K}^{-1}$) at $E \sim 10^4 \text{ V m}^{-1}$, a $0.12 \text{ }^\circ\text{C}$ temperature rise

could be expected for a 120 s switch on time. The implication of this is that for a Hull group microreactor operating under the same conditions of 100 V cm^{-1} and left on for 1200 s the expected temperature rise would be $1.2 \text{ }^\circ\text{C}$. This is much less, than the natural day-to-day temperature variation in many laboratories and can be regarded as insignificant.

Gas evolution, because of electrolysis at the reservoir electrodes, can seriously impede microreactor performance. The gas pockets formed in the reservoirs are able to migrate into the main channels of the microreactor and completely cut the electrical conduction path. In this case the device abruptly stops working. To avoid these problems, it is important that electrolysis is minimised as much as practically possible. Faraday's law states that the amount of chemical reaction occurring at an electrode is proportional to the "Faradaic currents" between the electrode surface and the bulk solution [95]. When electrolysis is desired, such as in the manufacture of chlorine, high solution conductivities ensure a high chemical reaction rate at the electrode surfaces. For the purposes of EOF, low electrolyte concentrations and solution conductivities are used to avoid electrolysis. This reduces the number of available charge carriers and conduction current for electrolysis at the electrodes.

1.4 Chemical detection methods.

1.4.1 On-chip detector requirements.

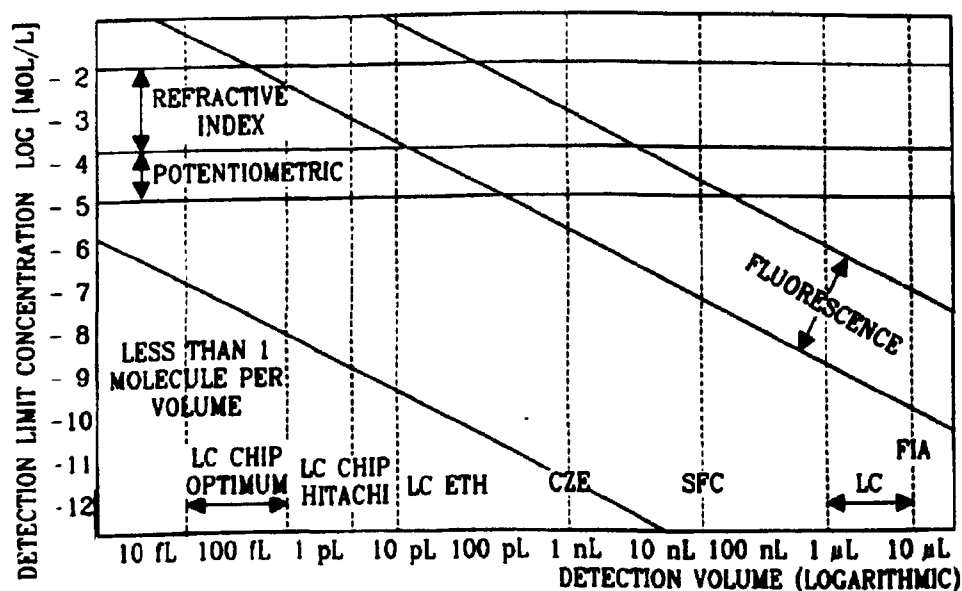
The penultimate Section of this Chapter is assigned to a discussion of the requirements for chemical detection. The design features of an on-chip detector are addressed and current examples of working systems described, concentrating on optical and electrochemical methods.

The requirements for on-chip detection are different from those on the macro-scale. Miniaturisation has pushed detection technology to a new limit. Three areas have to be considered to produce on-chip detectors:

- Small volumes mean fewer analyte molecules in the detection volume so a lower limit of detection is needed.
- Rapid detection system response time is required if fast moving molecules are to be detected (i.e. a sample in the small detection volume remains there only for a short time before being replaced by fresh solution in the flowing channel).
- The detection system must be easy to implement on a microreactor.

For any detection system the fundamental limit of detection occurs when there exists only one molecule in the detection volume within the microreactor channel. Consider

Figure 1.13: Published theoretical detection limits as a function of detection volume for refractive index, potentiometric and fluorescent detectors as reported by Widmer *et al.* [8]. FIA is flow injection analysis, LC: normal liquid chromatography, SFC: capillary supercritical fluid chromatography, CZE: capillary zone electrophoresis.



when light passes through a channel of absorbing species, the absorbance of the solution may give a large signal output compared to a smaller path length channel where the absolute concentration of the absorbing species is less. The relationship between the detector signal output and the size of the detection volume is of critical importance in the successful implementation of micro-detectors. Widmer *et al.* [8] have studied this aspect of detectors from a theoretical standpoint. Their reported graph for detection limit concentration as a function of detection volume is reproduced in Figure 1.13. If s is the characteristic length in a given detection system, the fluorescence detector signal is proportional to s^3 and an amperometric signal to s^2 . From Figure 1.13 it is seen that refractive index (R.I.) and potentiometric detectors are almost totally insensitive to volume changes. Electrochemical detection methods exhibit superior lower limits of detection to optical methods such as fluorescence at low detection volumes. R.I. detectors are the exception to this rule.

A discussion of detection limits cannot be fully elaborated without a mention of system response (i.e. detection and integration) time in the context of small volumes. Consider a single molecule with $D = 10^{-9} \text{ m}^2 \text{ s}^{-1}$ diffusing along the axis of a microreactor channel. If the lower detection limit of the detector is set as one molecule in the given detection volume, then there will be an associated time that the molecule must be in that volume in order to be detected. It can be seen from Table 1.7, that for a 1 nl detection volume when no applied flow exists, the minimum detector response time would have to be 10 s for the molecule to diffuse across 100 μm . For a 1 pl volume the time required becomes 0.1 s. Clearly if an applied flow was given to the molecule the detector system response time would have to be much faster. Application of a slow 500

Table 1.7: Theoretical times that a single molecule with $D = 10^{-9} \text{ m}^2 \text{ s}^{-1}$ will be in the detection volume of an on-chip detector. The third column is based on straight diffusion from one side of the detection volume to the other. The fourth column is calculated for flow-induced movement of $500 \text{ } \mu\text{m s}^{-1}$ across the detection volume.

Detection volume	s / microns	Detector response diffusion only / s	Detector response with a $500 \text{ } \mu\text{m s}^{-1}$ flow applied / s
nl	100	10	0.2
pl	10	0.1	0.02

$\mu\text{m s}^{-1}$ flow for a 1 nl detection volume, decreases the required response time to 1/50 th of the original value. This example highlights the trade-off between detector response time and sample detection volume. Response time is dependent on and indeed limited by, the channel geometry, reagent concentration and detection method used.

1.4.2 Optical detection methods.

Optical detection methods are the most widely used detection systems in microreactors because of their simplicity [96]. They include fluorescence [97], absorbance [13,98], refractive index [2], scattering [Ref. 95 pg 639] and microscopy [99]. Those techniques that are of direct relevance to us are absorbance and microscopy. Absorbance detectors are similar in principle to fluorescent detectors, since they rely on the selective absorption of specific electromagnetic wavelengths by molecules. The difference arises in that absorbance detection relies on the reduced intensity of particular wavelengths of electromagnetic radiation arriving at a photoelectric detector. A commonly employed method of on-chip absorbance detection uses fibre optics to connect the external transducers to the detection cavity. The absorbance A of a species in channel depth d , is given by the Beer-Lambert law:

$$A = Cd\varepsilon \quad (1.23)$$

where C is the molar concentration (mol dm^{-3}) and ε the molar extinction coefficient ($\text{mol}^{-1} \text{dm}^3 \text{cm}^{-1}$).

In practice, to evaluate the absorbance of a dissolved species in a sample cuvette, it is necessary to consider the substantial attenuation of the signal from reflection losses at the interfaces and scattering in the cell. To compensate for these effects, the power of a transmitted beam by the analyte solution I_{species} is ordinarily compared with the power of the beam transmitted by an identical cell containing only solvent I_{solvent} [Ref. 95 pg 125]. An expression relating the absorbance of the species to the experimental transmitted intensities in solvent, species and background intensity $I_{\text{background}}$ is:

$$A = \log \left\{ \frac{I_{\text{solvent}} - I_{\text{background}}}{I_{\text{species}} - I_{\text{background}}} \right\} \quad (1.24)$$

It is interesting to note that Fletcher *et al.* [99] have recently demonstrated the viability of monitoring chemical reactions on-chip using a transmission microscope fitted with a CCD camera to form a spectrophotometer (see Chapter 6). They used equation 1.24 to determine the concentrations of the chemical species from their absorbances.

1.4.3 *Electrochemical detection methods.*

The different methods which fall into this group are conductivity, amperometry, voltammetry and to a lesser degree polarography. All of these techniques were originally used as detection methods in capillary electrophoresis. Gilman *et al.* [100] demonstrate the use of current and conductivity monitoring to measure the EOF in a T-chip. Girault *et al.* show, using a PDMS chip with carbon microelectrodes and a 120 pl detection volume, that a lower detection limit of one fmol is possible with cyclic

voltammetry and chronoamperometry (monitoring current over time) for ferrocenecarboxylic acid. The work introduces a novel fabrication technique and the design of microfabricated electrodes within a polymer microchannel element. The integration of carbon ink electrodes is shown to be an advantageous design for detection in small-volume devices [101].

Electrochemical detection is successful in macro-scale separations because of its ease of implementation and ability to selectively detect analytes at low concentrations. On the micro-scale it also proves a strong competitor with other miniaturised detection systems [8,102]. The one major drawback with electrochemical detectors is their high selectivity generally limits their use in analysis to easily oxidized or reduced species. Optical absorbance detection has a lower selectivity than electrochemical systems, but a generally higher sensitivity to a broader range of analyte species. The advantageous features of both optical and electrochemical detection have been combined by Manica *et. al.* in their “dual electrochemical and optical detection on a microfabricated electrophoresis chip” [103].

Other detection methods such as mass spectrometry (MS) exist, but do not involve direct on-chip analysis. Separations are performed on-chip and samples are ported from the microreactor directly into a MS, via a coupling tube for analysis [104]. These descriptions cover the most common methods used for “on-chip” analysis and give the necessary background to understand the work that follows in this thesis.

1.5 Project objectives and thesis plan.

The main objectives of the work described in this thesis can be summarised as follows:

- To develop a rapid, accurate and non-destructive technique to determine the dimensions of the internal channel network of any optically transparent microreactor.
- To predict voltage- and pressure-driven flows in any glass microreactor from the measured electrical currents, channel dimensions and applied voltages.
- To accurately model and predict the current-voltage profiles for any glass microreactor, from measured electrical currents, bulk conductivity and the applied voltages.
- To gain a greater understanding of the effects of voltage-driven mobilisation of charged and uncharged dye species and colloidal particles in a microreactor channel.

Following this Introduction, Chapter 2 describes the general experimental procedures and the specifications of reagents used. Chapter 3 discusses the development of an absorbance imaging technique, based on optical microscopy, to determine the full 3D microreactor channel network profile and therefore the channel dimensions. Chapter 4 outlines a simple model for preliminary voltage- and pressure-driven flow measurements made in cylindrical capillaries, which were used to eliminate the relatively complex microreactor channel geometries. Chapter 5 discusses modelling the microreactor current-voltage characteristics and the use of measured electrical currents to predict the voltage-driven flow in a microreactor channel of known dimensions. Chapter 6 outlines the use of the absorbance-imaging technique developed in Chapter 3, to investigate the mobilities of charged and uncharged dye species, as well as colloidal particles in a microreactor channel where the fluid is propelled by voltage-driven flow. Chapter 7 outlines and experimentally verifies a final sophisticated model that unifies

all voltage- and pressure-driven flows, electrical currents, applied voltages, resistances and channel dimensions. Chapter 8 summarises all the conclusions and discusses possible areas of future work.

1.6 References.

- [1] S. C. Terry, J. H. Jerman & J. B. Angell, *IEEE Trans. Electron Devices*, 1979, ED-26, 1880.
- [2] S. Verpoorte, Workshop on MicroChemical Systems, University of Hull, July 01.
- [3] <http://www.micronics.net/products/cas.php> (Jan 02).
- [4] http://www.ehrfeld.com/page_e/frames_e.html (Jan 02).
- [5] J. Ruzika & E. H. Hansen, *Anal. Chim. Acta*, 1975, 78, 145.
- [6] J. Ruzika & E. H. Hansen, *Flow Injection Analysis* (1988) 2nd Edn., John Wiley, New York, p15.
- [7] N. Graber, H. Ludi & H. M. Widmer, *Sensors and Actuators B*, 1990, 239.
- [8] A. Manz, N. Graber & H. M. Widmer, *Sensors and Actuators B*, 1990, 244.
- [9] Diagram redrawn from Fig. 2, A. Manz & H. Becker, *Microsystem Technology in Chemistry and Life Sciences* (1999) Springer, Ch.1, p25.
- [10] D. J. Harrison, K. Fluri, K. Seiler, Z. Fan, C. S. Effenhauser & A. Manz, *Science*, 1993 261, 895.
- [11] S. C. Jacobson, A. W. Moore, & J. M. Ramsey, *Anal. Chem.*, 1995, 67, 2059.
- [12] A. J. Tomlinson, N. A. Guzman, *J. Capillary Electrophoresis*, 1995, 2, 247.
- [13] G. Ocvirk, E. Verpoorte, A. Manz, M. Grasserbauer & H. M. Widmer, *Anal. Methods Instrum.*, 1995, 2, 74.
- [14] A. Manz, Y. Miyahara, J. Miura, Y. Watanabe, H. Miyagi & K. Sato, *Sensors & Actuators B*, 1990, 1, 249.
- [15] S. C. Jacobson, R. Hergenroder, L. B. Koutny & J. M. Ramsey, *Anal. Chem.*, 1994, 66, 2369.
- [16] F. Heeren, E. Verpoorte, A. Manz & W. Thormann, *Anal. Chem.*, 1996, 68, 2044.
- [17] S. C. Jacobson, R. Hergenroder, L. B. Koutny & J. M. Ramsey, *Anal. Chem.*, 1994, 66, 1107.
- [18] C. S. Effenhauser, A. Paulus, A. Manz & H. M. Widmer, *Anal. Chem.*, 1994, 66, 2949.
- [19] C. S. Effenhauser, A. Manz & H. M. Widmer, *Anal. Chem.*, 1993, 65, 2637.

- [20] Y. Murakami, M. Suda, K. Yokoyama, T. Takeuchi, E. Tamiya & I. Karube, *Microchemical Journal*, 1994, 49, 319.
- [21] C. Erbacher, F. G. Bessoth, M. Busch, E. Verpoorte & A. Manz, *Mikrochim. Acta*, 1999, 131, 19.
- [22] S. J. Haswell & V. Skelton, *TrAC*, 2000, 19, 389.
- [23] T. McCreedy & N. G. Wilson, *Chem. Commun.*, 2000, 733.
- [24] S. J. Haswell, R. J. Middleton, B. O'Sullivan, V. Skelton, P. Watts & P. Styring, *Chem. Commun.*, 2001, 391. *Gives a clear account of current work on synthesis in microreactors.*
- [25] V. Skelton, G. M. Greenway, S. J. Haswell, P. Styring, D. O. Morgan, B. H. Warrington & S. Y. F. Wong, *Analyst*, 2001, 126, 7.
- [26] V. Skelton, G. M. Greenway, S. J. Haswell, P. Styring, D. O. Morgan, B. H. Warrington & S. Y. F. Wong, *Analyst*, 2001, 126, 11. *First demonstration of the control of stereoselective product formation in a microreactor.*
- [27] G. N. Doku, S. J. Haswell, T. McCreedy & G. M. Greenway, *Analyst*, 2001, 126, 14.
- [28] T. McCreedy & N. G. Wilson, *Analyst*, 2001, 126, 21.
- [29] M. C. Mitchell, V. Spikemans & A. J. de Mello, *Analyst*, 2001, 126, 24.
- [30] K. Kochloefl, *Chimie-Technik*, 1975, 4, 443.
- [31] R. A. Clark, P. B. Hietpas & A. G. Ewing, *Anal. Chem.*, 1997, 69, 259.
- [32] R. M. McCormick, R. J. Nelson, M. G. Alonso-Smigo, D. J. Benvegna & H. H. Hooper, *Anal. Chem.*, 1997, 69, 2626.
- [33] S. Liu, Y. Shi, W. W. Ja & R. A. Mathies, *Anal. Chem.*, 1999, 71, 566.
- [34] L. B. Koutny, D. Schmaizing, T. A. Taylor & M. Fuchs, *Anal. Chem.*, 1996, 68, 18.
- [35] S. R. Wallenborg & C. G. Bailey, *Anal. Chem.*, 2000, 72, 1872.
- [36] Whitesides' lecture notes, http://web.mit.edu/10.491/ICEmF_Lecture021201.pdf (April 03).
- [37] P. J. A. Kenis, R. F. Ismagilov & G. M. Whitesides, *Microfabrication inside capillaries using multiphase laminar flow patterning.*, *Science*, 1999, 285, 83.

- [38] B. H. Weigl & P. Yager, *Microfluidic diffusion-based separation and detection.*, Science, 1999, 283, 346.
- [39] E. Dietzsch, D. Honicke, M Fichtner, K. Schubert & G. Weibmeier, *IMRET 4: 4th International Conference of Micro Reaction Technology, topical conference proceedings, AIChE Spring national meeting March 5-9, 2000, p89.*
- [40] A. Shanley, *Chemical Engineering*, March 1997, 30.
- [41] K. Jahnisch, M. Baerns, V. Hessel, W. Ehrfeld, V. Haverkamp, H. Lowe, C. Wille & A. Guber, *Journal of Fluorine Chemistry*, 2000, 105, 117.
- [42] T. M. Floyd, M. W. Losey, S. L. Firebaugh, K. F. Jensen & M. A. Schmidt, *Proceedings of the 3rd International Conference on Microreaction Technology*, Frankfurt, Germany, 1999, p171.
- [43] P. Fairley, *Chemical Week*, 16th Dec 1998, 37.
- [44] D. E. Raymond, A. Manz & H. M. Widmer, *Anal. Chem.* 1994, 66, 2858.
- [45] E. B. van Akker, M. Bos & W. E. van der Linden, *Analytica Chimica Acta*, 1999, 378, 111.
- [46] C. A. Parent & P. N. Devreotes, *Science*, 1999, 284, 765.
- [47] B. S. Gallardo, V. K. Gupta, F. D. Eagerton, L. I. Jong, V. S. Crag, R. R. Shah & N. L. Abbott, *Science*, 1999, 283, 57.
- [48] N. L. Jeon, S. K. W. Dertinger, D. T. Chui, I. S. Choi, A. D. Stroock & G. M. Whitesides, *Langmuir*, 2000, 16, 8311.
- [49] <http://www.open2.net/bluesky/lab.htm> (Jan 02).
- [50] W. Ehrfeld, V. Hessel, S. Kiese-walter, H. Lowe, T. Richter & J. Schiewe, *Proceedings of the 3rd International Conference on Microreaction Technology*, Frankfurt, Germany, 1999, p14.
- [51] T. McCree-dy, *Special Edition of TrAC*, 2000, 19, 396.
- [52] W. M. Moreau, *Semiconductor lithography: principles and materials* (1988) Plenum, New York.
- [53] M. Madou, *Fundamentals of Microfabrication* (1997) CRC Press, London.
- [54] T. R. Dietrich, W. Ehrfeld, M. Lacher, M. Kramer & B. Speit, *Microelectronic Engineering*, 1996, 30, 497.
- [55] H. Lorentz, M. Despont, P. Vettiger & P. Renaud, *Microsystems Technologies*, 1998, 4, 143.

- [56] M. Hecke, W. Bacher & K. D. Muller, *Microsystems Technologies*, 1998, 4, 122.
- [57] R. A. Laws, A. S. Holmes & F. N. Goodall, *Microsystems Technologies*, 1997, 3, 17.
- [58] D. Yao & B. Kin, *Micro Total Analysis Systems 2001*, Ed. J. M. Ramsey & A. van den Berg (2001) Kluwer Academic Press, Netherlands, p413.
- [59] T. McCree, *Analytica Chimica Acta*, 2001, 427, 39.
- [60] W. Ehrfeld & H. Lehr, *Radiat. Phys. Chem.*, 1995, 45, 349.
- [61] W. Bacher, K. Bade, B. Matthis, M. Saumer & R. Schwarz, *Microsystems Technology*, 1998, 4, 117.
- [62] P. E. Dyer, M. Ersoz, P. D. I. Fletcher, S. M. Maswadi, V. N. Paunov & C. D. Walton, *Appl. Phys. A: J. Materials Sci. & Processing*, 2003, DOI 10.1007/s00339-002-1936-0
- [63] A. Manz, J. C. Fetting, E. Verpootre, H. Ludi, H. M. Widmer & D. J. Harrison, *TrAC*, 1991, 10, 144.
- [64] H. Y. Wang, R. S. Foote, S. C. Jacobson, J. H. Schneibel & J. M. Ramsey, *Sensors and Actuators B*, 1997, 45, 199.
- [65] M. Hart, *Manual of Scientific Glass Blowing* (1992) Sturdy Print, Skelmersdale, Lancs, p20.
- [66] N. Chiem, L. Lockyear-Shultz, P. Andersson, C. Skinner & D. J. Harrison, *Sensors and Actuators B*, 2000, 63, 147.
- [67] Z. H. Fan & D. J. Harrison, *Anal. Chem.*, 1994, 66, 177.
- [68] R. J. Hunter, *Zeta Potential in Colloid Science* (1981) Academic Press, London.
- [69] J. Th. G. Overbeek, in *Colloid Science*, Ed. H. R. Kruyt (1952) Elsevier, Amsterdam, Vol. 1, Ch. V, p206.
- [70] D. J. Shaw, *Introduction to Colloid and Surface Chemistry* (1992) Butterworth-Heinemann Ltd, p183.
- [71] F. F. Reuss, *Memoires de la Societe Imperiales de Naturalistes de Moskou*, 1809, 2, 327. (printed in French)
- [72] D. P. Krynine & W. R. Judd, *Principles of Engineering Geology and Geotechnics* (1957) McGraw-Hill Book Company, London, p205.
- [73] L. M. Vane & G. M. Zang, *J. Hazardous Materials*, 1997, 55, 1.

- [74] M. J. Sepaniak, A. Craig Powell, D. F. Swaile & R. O. Cole, *Capillary Electrophoresis Theory and Practice*, Ed. P. D. Grossman & J. C. Colburn (1992) Academic Press, London, p176.
- [75] I. E. Valko, H. Siren & M. Riekkola, *J. Microcolumn Separations*, 1999, 11, 199.
- [76] P. W. Atkins, *Physical Chemistry* (1990) Oxford University Press, p225.
- [77] P. D. I. Fletcher, S. J. Haswell & V. N. Paunov, *Analyst*, 1999, 124, 1273.
- [78] J. Jednacak, V. Pravdic & W. Haller, *J. Colloid Interface Sci.*, 1974, 49, 16.
- [79] R. Aveyard, B. P. Binks, P. D. I. Fletcher, C. E. Rutherford, P. J. Dowding & B. Vincent, *Phys. Chem. Chem. Phys.*, 1999, 1, 1971.
- [80] P. R. Johnson, *J. Colloid Interface Sci.*, 1999, 209, 264.
- [81] R. A. van Wagenen & J. D. Andrade, *J. Colloid Interface Sci.*, 1980, 76, 305.
- [82] A. J. Rutgers & M. De Smet, *Trans. Faraday Soc.*, 1945, 41, 764.
- [83] F. Fairbrother & M. Balkin, *Chemical Society Journal*, 1931, IV, 389.
- [84] A. Vernhet, M. N. Bellon-Fontaine & A. Doren, *J. Chim. Phys.*, 1994, 91,1728.
- [85] O. El-Gholabzouri, M. A. Cabrerizo & R. Hidalgo-Alvarez, *J. Colloid Interface Sci.*, 1999, 214, 243.
- [86] Y. Gu & D. Li, *J. Colloid Interface Sci.*, 2000, 226, 328.
- [87] D. Erickson, D. Li & C. Werner, *J. Colloid Interface Sci.*, 2000, 232, 186.
- [88] W. M. Martin & R. A. Gortner, *J. Phys. Chem.*, 1930, 34, 1509.
- [89] P. H. Paul, M. G. Garguilo & D. J. Rakestraw, *Anal. Chem.*, 1998, 70, 2459.
- [90] A. W. Adamson A. P. Gast, *Physical Chemistry of Surfaces* (1967) John Wiley and Sons, New York, p11.
- [91] P. D. I. Fletcher, S. J. Haswell & X. Zhang, *Lab on a Chip*, 2001, 1, 115.
- [92] P. D. Christensen, S. W. P. Johnson, T. McCreedy, V. Skelton & N. G. Wilson, *Chem. Commun.*, 1998, 35, 341. *Reports first use in Hull group of silica as a hydrodynamic restriction.*
- [93] H. Salimi-Moosavi, T. Tang & D. J. Harrison, *J. Amer. Chem. Soc.*, 1997, 119, 8716.

2. GENERAL EXPERIMENTAL PROCEDURES.

2.1 Methods.

2.1.1 Microreactor fabrication.

The microreactors used for the investigations presented in subsequent Chapters were fabricated using the methods reported by McCreedy [1]. The top blocks were made from 12 mm thick Crown white glass (B 270 – Superwite, Instrument Glasses Ltd., Enfield, Middlesex) and the base plates from 3 mm thick White Crown soda lime glass. The choice for these two glasses was determined by their low temperature thermal bonding properties, close thermal expansion coefficients and broad wavelength range of optical transmission:

- White Crown soda lime glass, because of its high soda content of approximately 13 % has a relatively low softening temperature of 585 °C, which is similar to Crown white glass.
- Crown white glass has a thermal expansion coefficient of $9.5 \times 10^{-6} \text{ K}^{-1}$, whereas White Crown soda lime glass is $9.3 \times 10^{-6} \text{ K}^{-1}$.
- Crown white glass has a transmission of 90 – 92 % over a wavelength range of 0.36 – 1.4 μm for a 2 mm thick sample. This allowed “on-chip” experiments to be carried out while optically monitoring the interior channel network.

A further reason for the choice of glass type used in the base plates was that prefabricated sheets were available already prepared for wet chemical etching i.e. the glass came with a deposited chrome and spun-coated photoresist layer. Standard 6 in. x 6 in. sheets of 3 mm thickness were purchased from Alignrite Ltd (Bridgend, Mid Glamorgan, Wales) and cut into either 25 mm squares or 25 x 34 mm rectangles. Glass

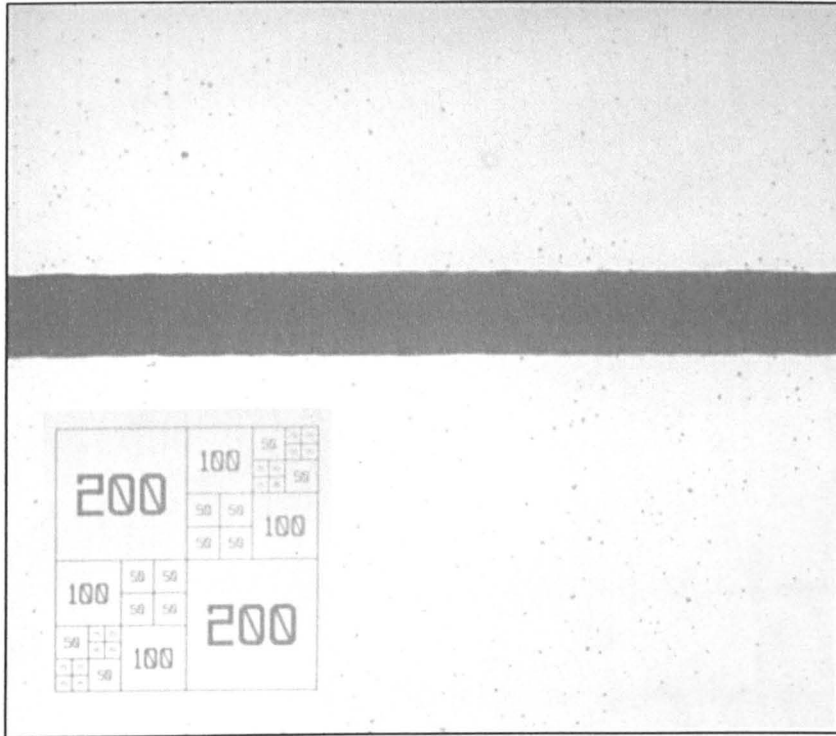
cutting was performed manually by scoring on the reverse side to the photoresist with a diamond knife and then snapping. Care was taken to avoid touching or scratching the photoresist and exposing it to light, as three actions would damage the surface. It was however, safe to handle the optically sensitive photoresist at red-yellow wavelengths where the surface photochemistry of the photoresist remains inactive.

There are five stages for producing microreactors these include:

- Producing a final optical mask
- Photolithographic pattern transfer
- Base plate etching
- Top block polishing
- Microreactor bonding

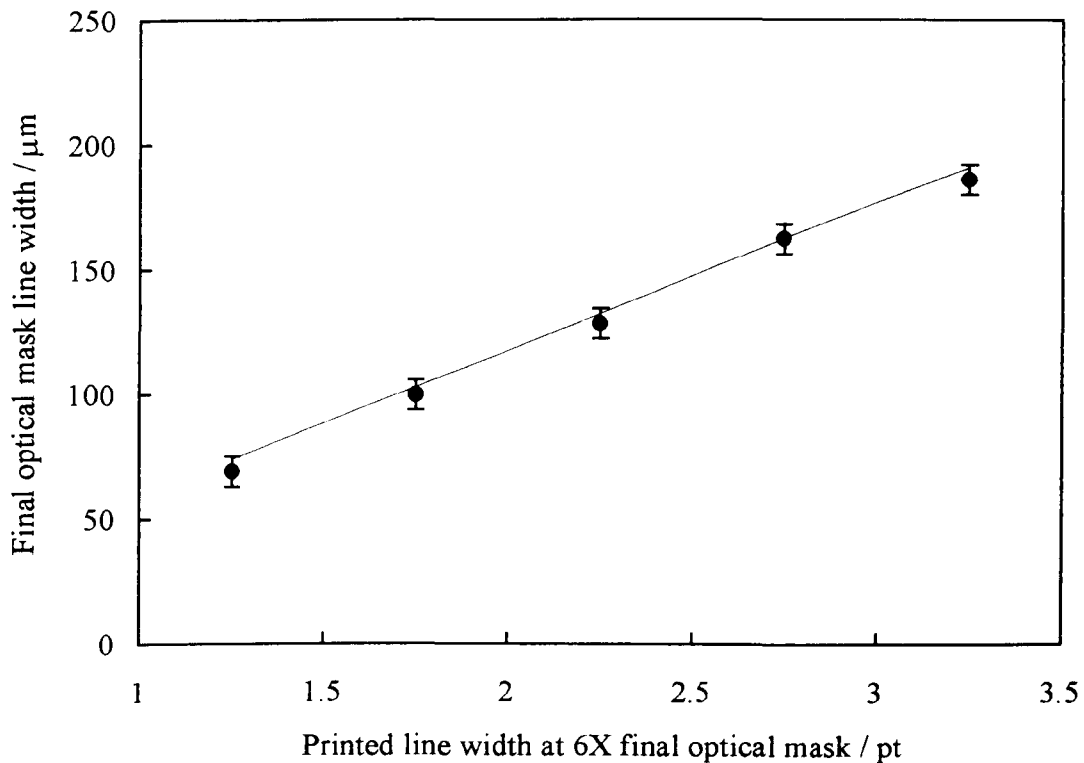
Final optical masks of the channel networks that were used in the photolithography, consisted of photographic negatives, produced by photoreduction of printed images of the channel network designs. The first stage in the process was to produce a channel network design at 6X the final size required using the drawing tools within Microsoft Word. The design was printed onto white A4 paper using a HP 850 inkjet printer with a resolution of 600 dots per inch (dpi). The channel width in the final optical mask was set by variation of the point size of the line widths in Word and the extent of photoreduction. One point in Word corresponds to a line width of 0.3528 mm. This coupled with a photoreduction of 6X gives a line width of 1 point corresponding to 58.8 μm in the final optical mask. The photoreduction was done by Hull University Photographic Service using KodaLith Orthofilm type 3 (Kodak Professional).

Figure 2.1: Optical micrograph of a 2.25 pt final optical mask line width as produced on the original photographic negative used for etching. The edges of the solid black line are still clearly defined at this width. The National Physics Laboratory scale graticule is 400 x 400 μm .



For the set up used in this work, the relationship between the printed line width (point size) and line width on the final optical mask was investigated using a Navitar optical microscope. The M Plan Apo 5X objective lens and X2.5 macro zoom of the Pixera PVC100C digital camera (Mitutoyo), allowed the final optical mask to be studied in sufficient detail to measure the line widths to about $\pm 2 \mu\text{m}$. Figure 2.1 shows a captured image of the line width on a (positive) final optical mask produced from an original printed line width of 2.25 pt after photoreduction. The dominant uncertainties in the final optical mask line widths arise from the random errors in measuring the line width on the final optical mask (line edge uncertainty), and the random errors in the printing process. A random uncertainty in the printing of ± 1 dpi for a 600 dpi printer

Figure 2.2: Plot of final optical mask line width versus the printed line width point size produced on A4 paper at 6X the required size. The line corresponds to the expected final optical mask line width. The filled circles are for the measured final optical mask line widths and have error bars of $\pm 6 \mu\text{m}$.

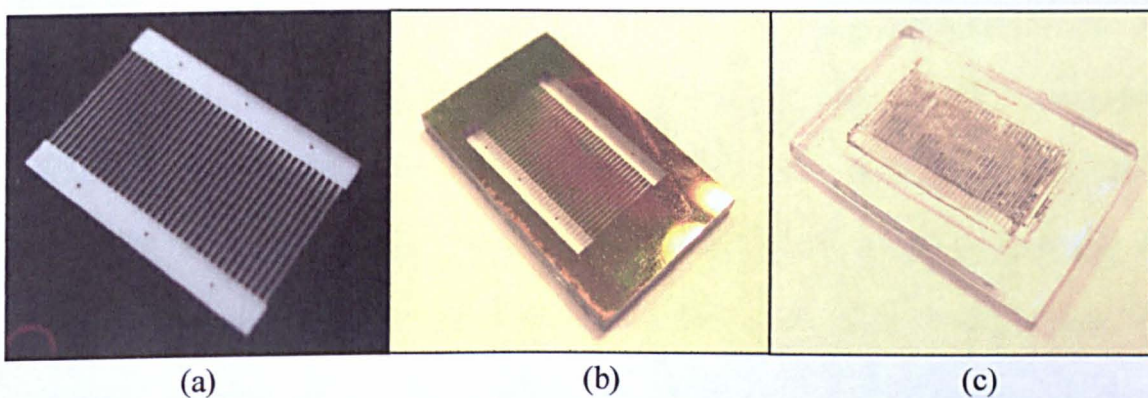


(coupled with a 6X photo reduction) corresponds to an uncertainty in the final optical mask line width of $\pm 4 \mu\text{m}$. Addition of the measurement uncertainties gives a combined uncertainty of $\pm 6 \mu\text{m}$. The actual and expected final optical mask line widths clearly agree within this margin of uncertainty as shown in Figure 2.2. The combination of a 600 dpi printer and a 6X photoreduction is therefore of adequate precision (i.e. within a few percent) to produce final optical mask line widths greater than $50 \mu\text{m}$.

A typical (negative) final optical mask of the channel network design is shown in Figure 2.3 (a). The channel network design on the final optical mask was transferred to the base plate photoresist layer using a standard UV exposure unit (Mega Electronics, Cambridge, UK). A 70 s exposure gave consistent line widths, with no measured

broadening when two 8 W UV tubes were used. After exposure, the glass was left in contact with the final optical mask without disturbance for 3 min before placing in the developer solution. This was found to give the sharpest pattern transfer, in comparison to immediate removal. The developer solution comprised 50 % Microposit developer mixed with 50 % pure water. A 20 s contact time with the developer solution sufficiently removed all the exposed photoresist to give a visible positive channel network imprint in the photoresist layer. After the glass was rinsed with pure water and dried, it was immersed in neat solution of Shipley Chrometch solution. This removed all unprotected chrome down to the glass surface. The base plate was then rinsed with water again and oven baked for 24 hrs at 140 °C. This oven baking was used to harden the unexposed photoresist and increases its resistance to the etchant solution (see Fig. 2.3 b).

Figure 2.3: (a) Negative final optical mask with channel network design (overall dimensions 25 x 17 mm) consisting of 35 parallel channels each 128 μm wide. (b) Base plate after photolithographic pattern transfer, development and pattern baking in oven for 24 hrs at 140°C. (c) Etched base plate stained with ink after all photoresist and chrome layer has been removed.



All glass used a common etch solution, which consisted of 250 ml of water, 12.5 g ammonium fluoride and 7 ml of 40 % hydrofluoric acid in aqueous solution. The newly baked base plates were placed on a support in the etch solution with pattern side facing

downwards and heated within an ultrasonic bath (Ultrawave Scientific Supplies, Nottingham, UK). The bath temperature and the solution agitation methods used to fabricate the different base plates are listed in Table 2.1. After the base plates have been etched for the desired length of time, they were removed from the etch solution to the Chrometch, once again, where the remaining chrome and photoresist was removed. An example of an etched and fully fabricated base plate is shown in Figure 2.3 (c).

Table 2.1: Summary of the procedures used for the wet chemical etching of the base plates described in later Chapters.

Procedure	T / °C	Agitation method	Base plate made
1	65	1 min ultrasound at 5 min intervals.	Chip 1
2	60	Stirred with a plastic rod for 1 min in every 5 min	Chip 2
3	60	1 min ultrasound at 10 min intervals	Chips 3 – 7
4	65	Base plate 10 min continuous ultrasound Middle plate 1 min continuous ultrasound	Chips 004 and 301
5	65	Continuous ultrasound	Chips 6M, 12M
6	65	Base plate 15 min continuous ultrasound Middle plate 3 min continuous ultrasound	Chip 303

The success of thermally bonding each base plate to the corresponding top block required that the two glass surfaces were sufficiently close so chemical bonds could be formed during the glass bonding process. Newly manufactured White Crown glass according to the manufacturer's specifications should have no scratches greater than 1 μm and no pitting greater than 10 μm . Surface scratches arise from routine handling. To produce a successful channel network in a sealed microreactor, it was frequently necessary to polish the top block using successively finer grinding pastes. The three required stages to polish a chip (microreactor) to optical quality were: to start with a coarse polish such as silicon carbide (Carborundum Company, Manchester), followed

by intermediate polishing with Cerium Oxide (Gemtek) then finishing off with Jeweller's Rouge.

Freshly etched base plates and polished top blocks were cleaned in a 5 vol. % aqueous solution of Hellmanex II, then presented for thermal bonding. The method of thermal bonding described by Daykin and Haswell [2] involved heating the base plate and top block configuration in a muffle furnace at 575 °C for 96 hrs and allowing it to cool for 24 hrs. Maintaining the partially bonded microreactor at this elevated temperature for a longer period resulted in no extra benefit to the bonding process. McCreeedy has shown [1] that the bonding quality achieved using a microreactor with a 45 g quartz weight placed on top of it and a muffle furnace temperature of 570 °C for 3 hrs of bonding, gave a failure rate of less than 10 %. This thermal bonding procedure formed the central method used in this work. It was necessary to fine-tune some of the variables, such as the furnace temperature and mass of the quartz weight, so investigations could be made into their effects on channel shape. These slight variations of McCreeedy's procedure are listed in Table 2.2. The furnace temperatures and quartz block masses listed in Table 2.2 were found not to produce significant channel distortion, as occurred at slightly higher temperatures and higher masses. It should be noted that chips 004, 301 and 303 were thermally bonded in 2 steps because of the

Table 2.2: List of thermal bonding procedures used to fabricate microreactors.

Procedure	Temperature / °C	Bonding time / hrs	Mass of quartz block	Chip produced
1	575	3	70	Chip 1
2	570	3	28	Chip 2
3	570	3	70	Chips 004, 301, 303, 6M & 12M

additional middle plate present. The base plate and middle plate were first thermally bonded according to procedure 3 in Table 2.2 and left to cool naturally. These chips were then completed by thermal bonding of the top block using the same procedure.

2.1.2 Refractive index measurements.

To satisfy the requirements of a non-volatile, refractive index (R.I.) matched and low absorbance solvent (at 647 nm) for the experiments described in Chapter 3, a solution was prepared by mixing glycerol (R.I. = 1.4740) and m-cresol (R.I. = 1.5424) at room temperature. The m-cresol was titrated into the glycerol containing a submerged base plate and top block. At a solution composition of between 29 – 31 wt. % glycerol in m-cresol, the two glass specimen were seen to become invisible at slightly different compositions. This indicated a difference in R.I. of the base plate and top block. An Abbe 60 refractometer (Bellingham & Stanley) was used to determine the exact R.I. of these, as listed in Table 2.3. The best average solution composition resulting from the titration-mixing procedure and the Refractometer analysis was 30.2 wt. % glycerol in m-cresol.

Table 2.3: Abbe Refractometer data for a series of samples illuminated with filtered light of wavelength 647 nm (Edmund Scientific N43-136 filter) from a 12V 70W tungsten halogen lamp and thermostatted at 20.0 ± 0.2 °C.

Sample	Refractive index
Base plate	1.5225
Top block	1.5215
30.2 wt.% glycerol in m-cresol	1.5239
pure water	1.3320

2.1.3 UV-vis spectrophotometer measurements.

Absorbance measurements were made using a Unicam UV3 dual beam

spectrophotometer operating over the wavelength range 190 – 900 nm. Instrument initialisation was performed without sample and reference cuvettes present. Lamp switch over between the deuterium (190 – 325 nm) and tungsten (326 – 900 nm) lamps was automatic. The sample cuvette was supported in a copper block that was temperature regulated by a circulating thermostat unit (Grant LTD6). All measurements were made using a single cuvette with air in the reference beam. Baseline measurements were made separately using the same cuvette filled with solvent. All cuvettes were cleaned with a 5 vol. % aqueous solution of Hellmanex II before measurements were made.

2.1.4 Determination of liquids flow rates and internal reservoir radii.

Liquid flow rates were determined by measuring the position of a moving meniscus in an extended glass reservoir tube. A 2202D cathetometer (Precision Tool & Instrument Co., Sussex) equipped with a digital clock gauge having 1 μm resolution (Mitutoyo) and a X10 magnification telescope was used to measure changes in meniscus position. In the XY plane (parallel to the lab floor), the telescope was able to rotate on a cast iron base. Adjustable feet and on-board spirit levels ensured a completely level baseline. The telescope was free to move in the Z plane through a rack and pinion mechanism. This allowed the fine movements necessary to track the moving meniscus.

Extended reservoirs were chosen for the following reasons:

- Longer tubes allow the liquid menisci to be tracked over larger distances, thereby reducing the relative uncertainty in the measurement.
- Easy fitting and replacement of reservoirs with different internal radii allowed more convenient control of Laplace pressures.

- Glass reservoirs are easier to clean than transparent plastic ones and are not so easily attacked by harsh cleaning regimes.
- Electrodes positioned through the sides of the extended reservoirs did not distort the shapes of the liquid menisci and hence alter Laplace pressures.

The procedure used to measure flow rates in the U-tube apparatus and the extended transparent glass reservoirs was as follows: At the start of the experiment the selected reservoir and meniscus cap was positioned into the field of view and the crosshairs fixed on the chosen reference point, which was usually the lowest point in the meniscus cap. The rack and pinion system was positioned to the mid-range of allowed movement in the Z plane (± 6 mm) and the digital clock gauge zeroed. Any meniscus movement was recorded by noting the time and the new position with the telescope crosshairs and reading the number directly off the clock gauge.

Table 2.4: Internal reservoir radii of the U-tube apparatus.

Apparatus	Reservoir 1 radius / mm	Reservoir 2 radius / mm
U-tube 1	1.91 ± 0.01	1.92 ± 0.01
U-tube 2	2.98 ± 0.02	2.98 ± 0.02
U-tube 3	3.97 ± 0.02	3.98 ± 0.02

The internal radii of the extended reservoirs given in Tables 2.4 and 2.5 were measured by injecting a known volume of liquid and then determining the length of the slug formed with the cathetometer. The accuracy of the cathetometer, via the digital clock gauge, was found through repeated measurements on a stationary meniscus to be $\pm 17 \mu\text{m}$ for a 96 % confidence limit. This uncertainty is somewhat larger than the uncertainty of the digital clock gauge and resulted from random alignment errors. The

absolute error specified for each value of reservoir radius in Tables 2.4 and 2.5 arises from the combination of these random alignment errors in measuring the meniscus position and the absolute error in measured liquid volumes.

For the flow rate measurements on chip, the extended reservoirs were mounted directly into the 3 mm diameter reservoir holes drilled into the top block (see pg 1). The extended reservoirs were heated and drawn to a point by the glassblower and their tips chamfered to make a ground glass joint with the top block holes. Due to the difficulty of making such small ground glass fittings, it was necessary to use glue to complete the sealing. Loctite 403 cyanoacrylate ester gave good results with water and methanol after 24 hrs oven curing at 80 °C. For other organic solvents leaks rapidly appeared. A range of glues was tried, including Norland optical adhesive 61 UV curing glue, Araldite GY 250 BD and silicone rubber compound (RS 555 – 588). All showed leakage with DMA (N,N-Dimethylacetamide) except Araldite 2014 (Sil-Mid, England), which was found to solve the leakage problems when organic solvents were used.

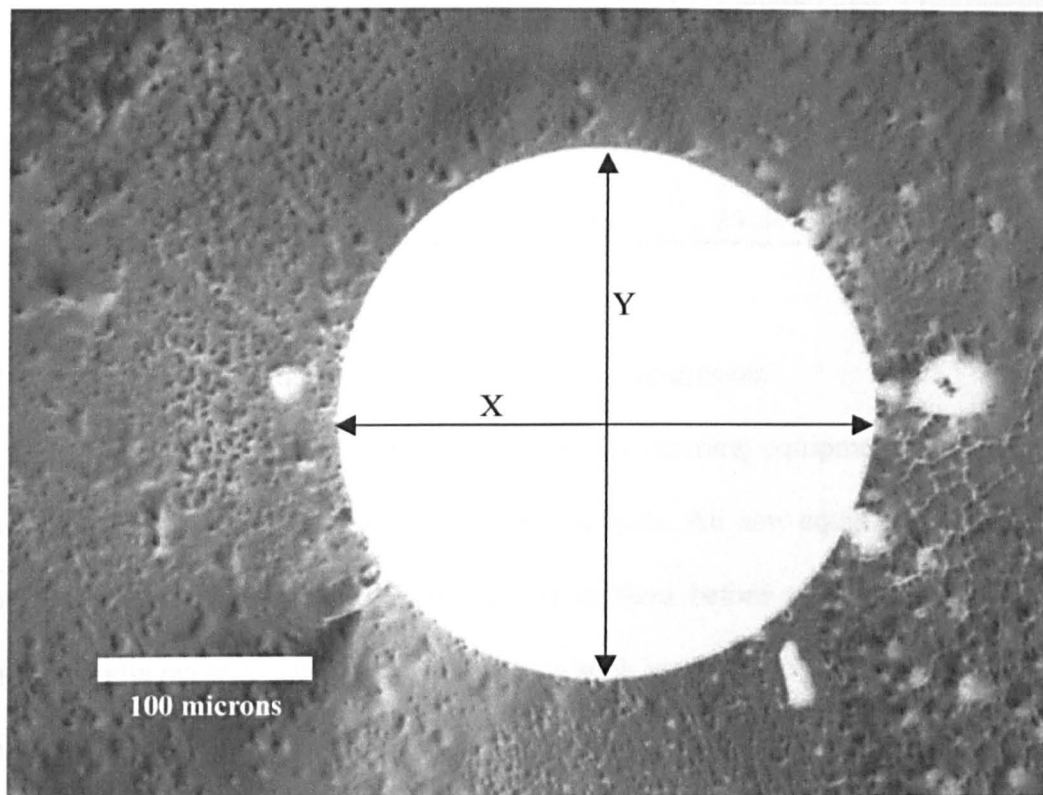
Table 2.5: Internal radii of extended reservoirs used for “on-chip” flow rate measurements. These reservoirs consisted of either 20 ml glass syringe barrels or 1 ml grade A glass pipettes.

Reservoir set	reservoir 1 / mm	reservoir 2 / mm	reservoir 3 / mm
20 ml syringe barrels	9.88 ± 0.05	9.77 ± 0.05	9.81 ± 0.05
1	1.21 ± 0.01	1.20 ± 0.01	1.22 ± 0.01
2	1.50 ± 0.01	1.50 ± 0.01	1.50 ± 0.01
3	1.21 ± 0.01	1.22 ± 0.01	1.22 ± 0.01

2.1.5 Determination of capillary dimensions.

Different samples of capillary tubing with varying bore and glass chemical composition required accurate characterisation for use in preliminary liquid flow rate experiments. Optical micrographs were made of both ends of each capillary using a

Figure 2.4: Optical micrograph of QZ1B quartz glass capillary in cross-section. Slight irregularity in the circular cross-section between the X and Y dimensions required the average radius to be calculated for experiments.



Navitar microscope. This was equipped with an M Plan Apo 5X objective lens, X2 – X4 macro zoom and a Pixera PVC100C digital camera (Mitutoyo). The optical magnification of the lenses coupled with the software and printer setting gave an overall capillary sample to printout magnification of approximately 420X. A typical cross-sectional micrograph of a capillary sample is shown in Figure 2.4. The slight oblate shape of some capillary samples required the average internal radius to be calculated.

The internal radii for the other capillary samples used for the preliminary flow rate experiments are listed in Table 2.6 along with their lengths. Capillary lengths were measured with a pair of Mitutoyo Vernier gauge callipers with a precision of ± 0.02 mm.

Table 2.6: The internal radii and lengths of capillary samples used in the U-tube apparatus. QZ denotes quartz glass and BORO denotes borosilicate glass.

Capillary sample	Radius / μm	Length / mm
QZ1A	129 ± 2	41.53 ± 0.02
QZ1B	124 ± 6	42.30 ± 0.02
QZ2B	234 ± 3	39.50 ± 0.02
QZ2D	238 ± 3	39.92 ± 0.02
BORO1	136 ± 4	39.84 ± 0.02

2.1.6 Solutions and procedures used for cleaning equipment.

There were two general procedures adopted for cleaning equipment and glassware, these included the lightly and heavily soiled methods. All new equipment was given a thorough initial clean by the heavily soiled method before either first use or after prolonged idle periods. This involved a 30 min soak in alcoholic KOH, scrubbing with a fine nylon brush and rinsing with pure water. Following this, the equipment was dried and put in conc. sulphuric acid for a further 5 min, rinsed with pure water until no acid remained and then stored in pure water until required. Storing in this way was found to be the best method of keeping the equipment clean for extended periods. Maintenance degreasing using the lightly soiled method was used regularly to clean equipment usually before each new run. It was found to be sufficient to give zero degree contact angles on the wetted glass surface. A typical cleaning regime by the lightly soiled method involved a 5 min soak in concentrated sulphuric acid, Alcoholic KOH or 5 vol. % Hellmanex II solution.

Alcoholic KOH

This consisted of 2 M potassium hydroxide dissolved in pure ethanol. The solution degraded after about 1 week to brown sludge and could, given exposure to direct

sunlight, even degrade within two days. Photodegradation was reduced, by storing the alcoholic KOH in a dark cupboard. Alcoholic KOH was very effective at degreasing oily residues such as squalene.

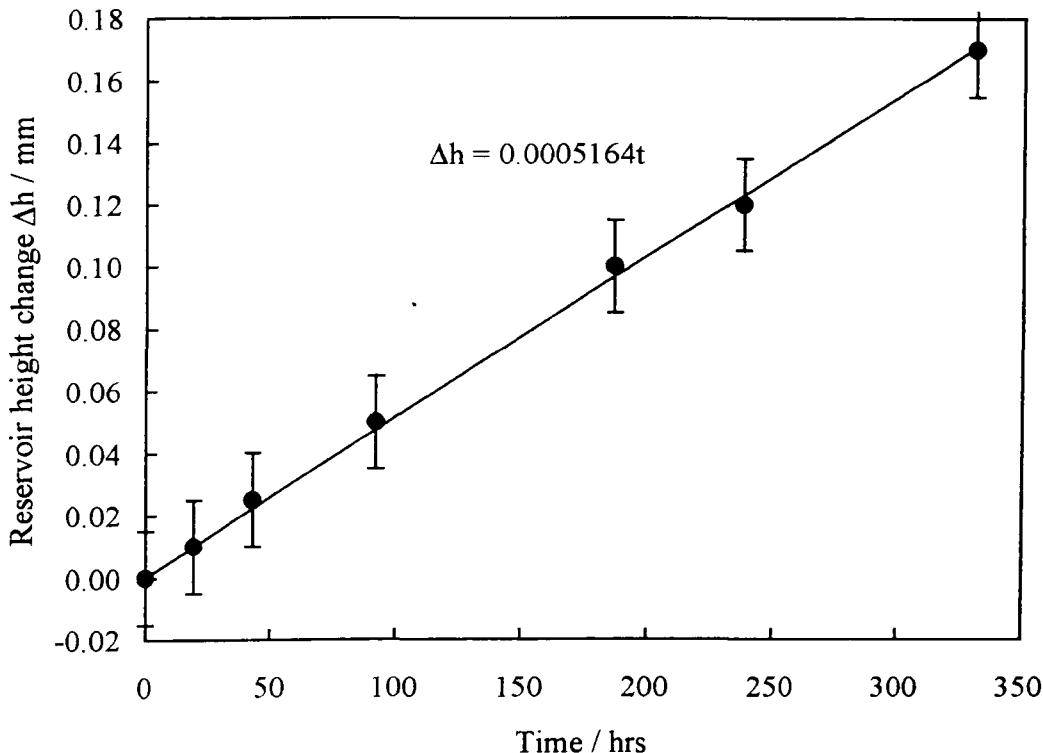
Hellmanex II cuvette cleaner

A 5 vol. % Hellmanex II solution in pure water was probably the most effective cleaner. Dried-on dye residue within a 50 μm path length cuvette was removed using a two hr soaking. This Hellmanex II solution formed the standard cuvette cleaning procedure that was quickly extended to washing the extended reservoirs for on-chip flow rate measurements. Hellmanex II being a surfactant based solution offered the advantages over the other cleaning solutions that it did not degrade the glue seals used to stick the extended reservoirs into the microreactors like sulphuric acid, nor did it leave any hard to remove residue like alcoholic KOH. A 5 min soak in 5 vol. % Hellmanex II was a more than enough for lightly soiled cleaning applications.

2.1.7 Solvent evaporation rates.

To determine whether the evaporation of solvent from the extended reservoirs was having a significant effect on measured flow rates, a 1 ml grade A pipette was taken and the tip sealed in a Bunsen flame. It was then cleaned with concentrated sulphuric acid, rinsed with water and dried. After mounting in a retort stand, the pipette was filled with ultrasonically degassed AnalaR methanol from a syringe. A 5 ml Pyrex beaker placed over the open end of the reservoir reduced airflow and evaporation. The meniscus position was recorded over time using the cathetometer. As seen from Figure 2.5, $d\Delta h / dt = 0.5 \mu\text{m hr}^{-1}$ for evaporation. Typically $d\Delta h / dt$ for a flow rate experiment is very much greater than $17 \mu\text{m hr}^{-1}$ (see Section 2.1.4). Hence, $d\Delta h / dt$ for evaporation is

Figure 2.5: Methanol evaporation rate from a 1 ml glass pipette covered with a 5 ml beaker. Measurements were made in a room set at constant humidity with an average temperature of 23.1 °C. Rate of evaporation = 509 nl hr⁻¹ and error bars are ± 17 μm.



very much less than $d\Delta h / dt$ for flow rate. Therefore, evaporation of methanol from the extended reservoirs has a negligible effect on measured liquid flow rates. Since methanol was the most volatile solvent system investigated in this work [3], it can be assumed evaporation for all other solvent is also negligible. The change in reservoir methanol level resulting from evaporation over a 2 hr period was approximately 1 μm.

2.1.8 Voltage and current determination.

Currents and voltages were monitored during the flow rate experiments using a Thurlby-Thandar 1906 digital multimeter. This had a nominal input impedance (Z) of 10 MΩ, a usable current range from 1 nA to 10 A and an AC / DC voltage range from 1 mV to 1 kV. A special function allowed a $Z = 1000$ MΩ to be selected on the 1 V and

100 mV DC ranges. The accuracy of the instrument (quoted as a percentage of full scale deflection) was better than 0.5 % across all resistance ranges, 0.3 % for DC currents below 100 mA and 0.06 % or less, across all DC voltage ranges [4]. Direct current was supplied from a one of two variable voltage photomultiplier power supplies: the lower voltage 0 – 1 kV (Advanced Hivolt, Farnell, England) supply and the 0 – 2.5 kV (Wallis Hivolt, Farnell, England).

Further into the microreactor project, electrokinetic control of reagents in the microreactors and associated current-voltage measurements were directly controlled from a computer. A home designed power supply (the Paragon), constructed by Kingfield Electronics, UK had four separate outputs where the voltage could be independently varied on each. Delivered electrical currents and voltages were monitored by sensory channels linking the Paragon to the computer. Programmed control of the timed voltage sequences applied to each output along with current and voltage logging, was made using LabVIEW software and a PCI-6031E/6703 data acquisition card (National Instruments).

2.1.9 Conductivity and pH measurements.

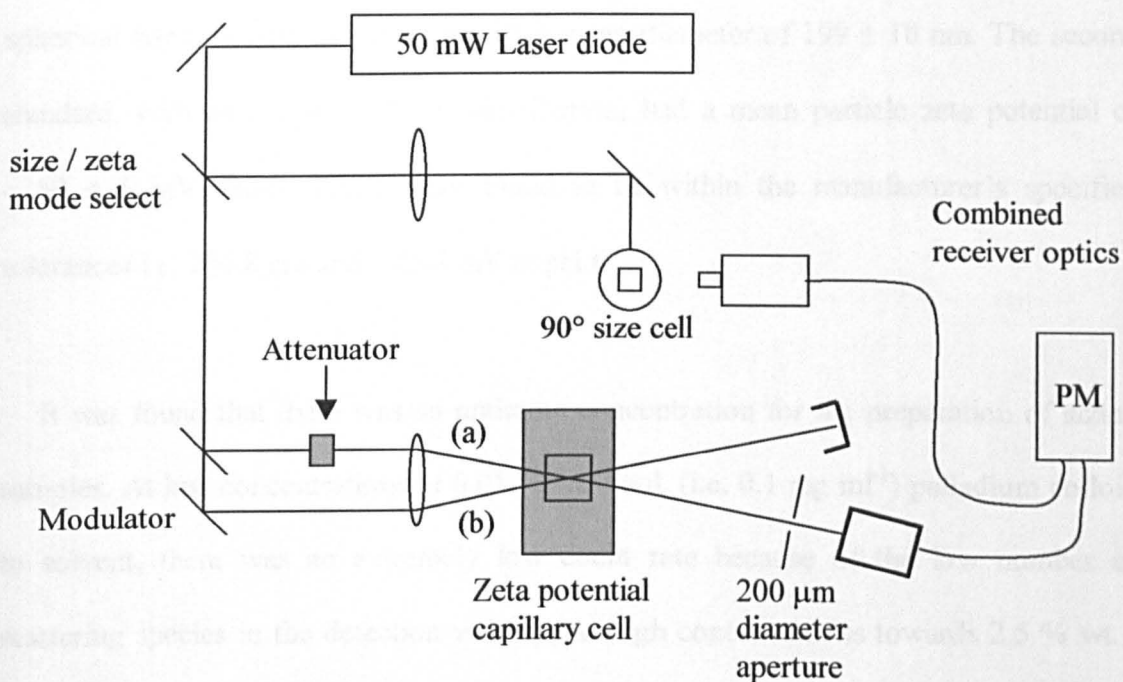
Liquid conductivities were measured using a WTW GmbH model LF340 AC conductivity bridge operating at 1000 Hz and equipped with a graphite electrode dip cell with cell constant equal to 0.475 cm^{-1} . Resistance measurements of microreactor channel sections connecting two reservoirs were made using a Wayne-Kerr 6430A impedance bridge operating at 200 Hz. It was checked that the operating frequency was sufficiently low such that the resistance values corresponded to the DC limit. All measurements were made at room temperature equal to 22 – 25 °C.

The pH of solutions was measured using a Jenway PHM6 pH meter with glass electrode (Jenway Ltd, Essex, UK) accurate to ± 0.01 pH. For each new series of measurements, the probe was calibrated at pH 4 and 7 using standard laboratory buffer solutions at room temperature.

2.1.10 Zeta sizing measurements of the colloidal catalysts.

A Malvern 3000HS Zetasizer (Malvern Instruments, Suffolk) fitted with a 50 mW 532 nm laser diode was used to measure particle size distributions and the zeta potential of solutions containing different concentrations of 2.11 wt. % colloidal palladium stabilised with polyvinylpyrrolidone (PVP) in (1) 80 vol.% DMA (aq) with 45 mM

Figure 2.6: The optical set up of Zetasizer 3000HS [5]. Sizing cell and capillary (electrophoresis) cells are shown. This instrument incorporates heterodyne detection. (a) Reference beam and (b) scattering beam.



NaBr and (2) methanol with 10 mM NaBr. Mode selection for zeta / sizing mode was selected automatically by the computer through the software settings. As seen from the

internal instrument configuration of the Malvern 3000HS Zetasizer shown in Figure 2.6, zeta potential and sizing measurements are completely independent of each other. About 10 ml of solution was necessary to run a zeta potential measurement, whereas 5 ml was adequate to fill a 1 cm path length quartz cuvette for the sizing measurement.

Samples were prepared according to the guidelines given in the Malvern Zetasizer manual [5]. Particular attention was paid to avoiding dust contamination of the samples as this would lead to a poor signal to noise ratio. All samples as a precaution were filtered through 200 nm Anotop 10 inorganic membrane filter (Whatman, Maidstone, England).

A system check of the sizing and zeta modes was made with two spherical latex standards (Duke Scientific Corporation, CA, USA). The first standard consisted of a spherical latex particle distribution with a mean diameter of 199 ± 10 nm. The second standard, with an unspecified size distribution, had a mean particle zeta potential of -50 ± 5 mV. Both checks were found to be within the manufacturer's specified tolerances i.e. 206.8 nm and -45.8 mV at pH 6.

It was found that there was an optimum concentration for the preparation of sizing samples. At low concentrations of 0.01 % wt. / vol. (i.e. 0.1 mg ml^{-1}) palladium colloid to solvent, there was an extremely low count rate because of the low number of scattering species in the detection volume. At high concentrations towards 2.5 % wt. / vol. (i.e. 25 mg ml^{-1}) colloidal to solvent, the absorption and dispersion also accounted for low count rates. Samples prepared in the mid-range between these two concentrations gave the best signal to noise ratio.

2.2 Materials.

The materials used for the microreactor experiments described in this thesis are listed in the Tables below. Dyes are given in Table 2.7; salts, acids and cleaners in Table 2.8; general-purpose solvents and reagents in Table 2.9 and miscellaneous consumables in Table 2.10. The use of the term “pure water” in this thesis, refers to milli Q reverse osmosis water from an Elgastat Prima which was filtered for particulates with a 0.22 μm carbon filter (CDFC01204 Carbon, Millistack-GS, England) and had a bulk liquid conductivity of 0.8 $\mu\text{S cm}^{-1}$ at 20.3 $^{\circ}\text{C}$. In addition, all compounds listed were used without further purification.

Table 2.7: Listing of the dyes used particularly in Chapters 3 and 6.

Compound	Supplier	Purity
Rose Bengal	Aldrich	95 %
Patent Blue	Fluka	standard reagent
PADA	Sigma	99 %
Black Indian ink	Chemistry Stores	-

Table 2.8: Listing of all salts, acids and cleaners used.

Compound	Supplier	Purity
AnalaR Potassium hydroxide	BDH	> 99.5 %
AnalaR Potassium chloride	BDH	99.5 %
Sodium hydroxide	Prolab	> 98.0 %
AnalaR Sodium chloride	Prolab	99.9 %
Sodium bromide	Aldrich	99+ %
0.5 M Sodium methoxide in methanol	Fluka	> 97.0 %
Sodium bicarbonate	Fisher	99.8 %
Concentrated H_2SO_4 (1.84 g cm^{-3})	Aldrich	97.5+ %
Concentrated HNO_3 (1.40 g cm^{-3})	Aldrich	99+ %
AnalaR HCl (1.18 g cm^{-3})	Prolab	> 99.99 %
Hydrofluoric acid in water (40 wt. %)	BDH Merck	99 %
Ammonium fluoride	Lancaster	98 %
Hellmanex II cuvette cleaner	Hellma GmbH	-

Table 2.9: Listing of all solvents and general-purpose reagents used.

Compound	Supplier	Purity
m-Cresol	Lancaster	99 %
glycerol	Lancaster	> 99 %
AnalaR methanol	Aldrich	99.8 %
Acetone	Lancaster	99+ %
AnalaR ethanol	Fisher	99.99 %
Propan-2-ol	Fisher	> 99.5 %
α -bromonaphthalene	Lancaster	97 %
Dodecane	Avocado	> 99 %
Squalene	Fluka	> 97.0 %
N,N-Dimethylacetamide	Fluka	> 99.8 %

Table 2.10: Miscellaneous consumables.

Compound	Supplier	Purity
Pt, Ag, Au, wire	Scientific Wire Co.	> 99 %
Cu wire	R.S. stores	> 99 %
Tungsten 1 mm dia. rod	Glass Blowers	-
Photoresist coated glass	Alignrite Ltd.	-
Microposit developer	Alignrite Ltd.	Not available
Shipley Chrometch	Shipley, Coventry	
KodaLith orthofilm	Kodak	-
Araldite 2017	Sil-Mid	-
PTFE septa	F. Leu, Houston, TX	-

The colloid palladium samples used in the imaging studies of Chapter 6, were kindly provided by Prof D. G. Blackmond of the Catalysis group at the University of Hull. The Chemistry Stores at the University of Hull, provided syringes, pipettes and other reservoirs materials. All cleaning and chemical preparation was carried out in specially designated areas. All experiments were performed in a safe manner following the in-house code of general laboratory practices and procedures.

2.3 References.

- [1] T. McCreedy, *Anal. Chim. Act.*, 2001, 427, 39.
- [2] R. N. C. Daykin & S. J. Haswell, *Anal. Chim. Act.*, 1995, 313, 155.
- [3] K.J. Beverley, J. H. Clint and P.D.I. Fletcher, *Phys. Chem. Chem. Phys.*, 1999, 1, 149-153.
- [4] <http://www.tti-test.com/products-tti/pdf-brochure/prec-1906-4p.pdf> (March 02).
- [5] Malvern Zetasizer notes (Sept. 1998).

3. CHANNEL PROFILING USING ABSORBANCE-IMAGING.

3.1 Introduction: *The problem of depth profiling bonded channels.*

In order to quantitatively predict and control the electrokinetic movement of reagents within microreactors (chips), it is necessary to determine the full 3-dimensional profile of the channel network in the assembled devices. Any such profiling technique must be able to adequately and accurately map the channel surfaces. For open etched base plates before bonding, 3D profiles can be obtained using mechanical, stylus-based techniques [1]. For such methods, care must be taken to avoid errors in reported channel geometries arising from imperfections in shape of the stylus tip when drawn across a near vertical channel edge. Although this method is acceptable to determine maximum channel depth, from our experience this technique proved inadequate to determine the profiles near the channel edges. For the closed, bonded base plates, it is possible to obtain the channel profile by cutting the bonded device perpendicular to the channel axis followed by microscopically imaging the channel profile. This procedure has a number of disadvantages. Firstly, the device is destroyed by the measurement. Secondly, the channel profile is only obtained at a single point where the cut is made. Lastly, it is not a trivial matter to obtain the channel cross-section accurately without “chipping” of the channel edges arising from the cutting process.

As a consequence of the clear need for a rapid, accurate and non-destructive method for 3D profiling of both open and closed etched channel networks, we have developed a technique (patent pending) based on digital microscope imaging of the channel network filled with an optically absorbing dye solution (Figure 3.2). The method is generally applicable for the quantitative 3D profiling of any voids fillable with an optically

absorbing dye solution, which are present in a transparent solid [2]. In this Chapter, we describe the application of the method for the profiling of channel networks within a range of bonded and non-bonded microreactor devices.

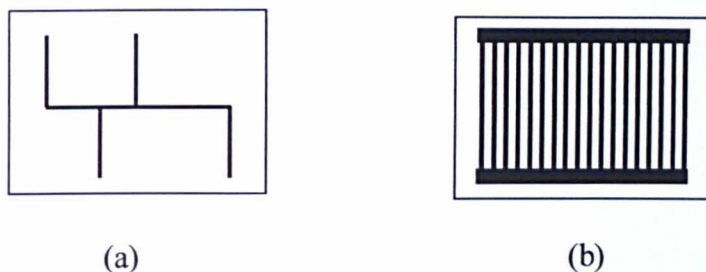
The method described here is similar to a range of generally more complex spectroscopic imaging techniques that have been developed for particular applications and utilise UV-vis (absorbance and fluorescence), IR or Raman [3-9]. In addition, acoustic microscopy poses a viable alternative to absorbance-imaging with some added advantages. Since ultrasound can penetrate optically opaque materials and the reflection of acoustic waves is determined by the mechanical properties of the material, acoustic reflections provide a potentially quantitative measure of these properties [10]. Although resolutions of $< 1 \mu\text{m}$ are possible by using ultrasound frequencies of 1 GHz, there is a trade off between probing depth and resolution. A specimen area of typically $0.25 \text{ mm} \times 0.25 \text{ mm}$ scanned at this frequency, can be sampled to depths of up to $50 \mu\text{m}$. Reducing the ultrasound frequency to 10 MHz increases the scanning area to $15 \text{ cm} \times 15 \text{ cm}$ and the penetration depth to 5 cm, but is accompanied by a significant reduction in resolution. This result coupled with the advantage of the low cost of optical light microscopes and its superior resolution (about 250 nm with a similar depth of field [11]), suggests only one imaging method – optical microscopy. Since microreactors are not made of opaque material, there is no problem in using light. The absorbance-imaging method described here is simple to implement and provides absolute values of the channel depths without the complicating factors associated with acoustic microscopy.

3.2 Apparatus and theory.

3.3.1 Description of microreactors used for absorbance-imaging study.

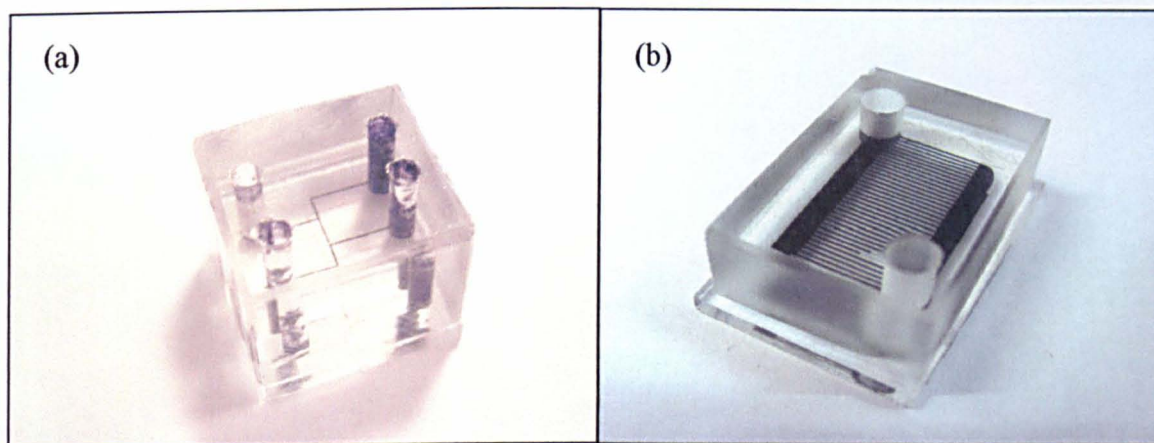
The microreactors used in this study were based on two channel network designs. These were the “double T” (chip 1) shown in Figure 3.1 (a) and the multi-channel network (chip 2 and base plates 3 – 7) consisting of 35 parallel channels as shown in Figure 3.1 (b).

Figure 3.1: (a) The “double T” chip 1, channel network design. (b) Chip 2 and base plate’s 3 – 7 channel network design, consisting of 35 parallel channels. Designs are not to scale.



The base plates of chips 1 and 2 were etched according to procedures 1 and 2, described in Table 2.1, pg 72. The base plates 3 – 7 were etched according to the third procedure in Table 2.1. Chips 1 and 2 were thermally bonded according to procedures 1 and 2 described in Table 2.2, pg 73. Examples of the thermally bonded microreactors (chips 1 and 2) are show in Figure 3.2.

Figure 3.2: Fully assembled and bonded microreactors filled with ink. (a) Chip 1 is about the size of a 25 mm cube. (b) Chip 2 is 15 mm high x 25 mm wide x 34 mm long.



3.2.2 Microscope imaging theory.

The optical absorbance of a solution is given by the Beer-Lambert law:

$$A_M = \log \left\{ \frac{I_{\text{solvent}} - I_{\text{dark}}}{I_{\text{dye}} - I_{\text{dark}}} \right\} = Cd_M \varepsilon \quad (3.1)$$

A_M is the absorbance of the dye solution in the channel network, I_{solvent} and I_{dye} are the transmitted light intensities recorded through the solvent and the dye solution respectively. I_{dark} is the detector signal recorded in the absence of incident light. For a given concentration C of the absorbing species in solution and molar absorption coefficient, ε the product $C\varepsilon$ can be determined for a given wavelength using a conventional spectrophotometer. Using a cell of known path length d_S for this measurement, a spectrophotometer absorbance A_S can be measured independently:

$$A_S = Cd_S \varepsilon \quad (3.2)$$

The ratio the absorbances A_M and A_S , multiplied by d_S , yields microreactor channel depth, d_M :

$$d_M = \frac{A_M}{A_S} \cdot d_S \quad (3.3)$$

d_M is obtained for each pixel of a microscope CCD imaging system. This requires that the following series of images have to be captured using the apparatus shown schematically in Figure 3.3.

- Image of the channels with zero incident illumination to obtain the array of I_{dark} intensities.
- Images of the channels filled with solvent giving the array of I_{solvent} intensities.

- Images of the channels filled with dye solution giving the array of I_{dye} intensities.

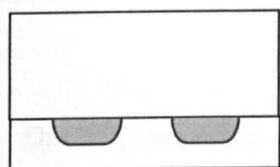
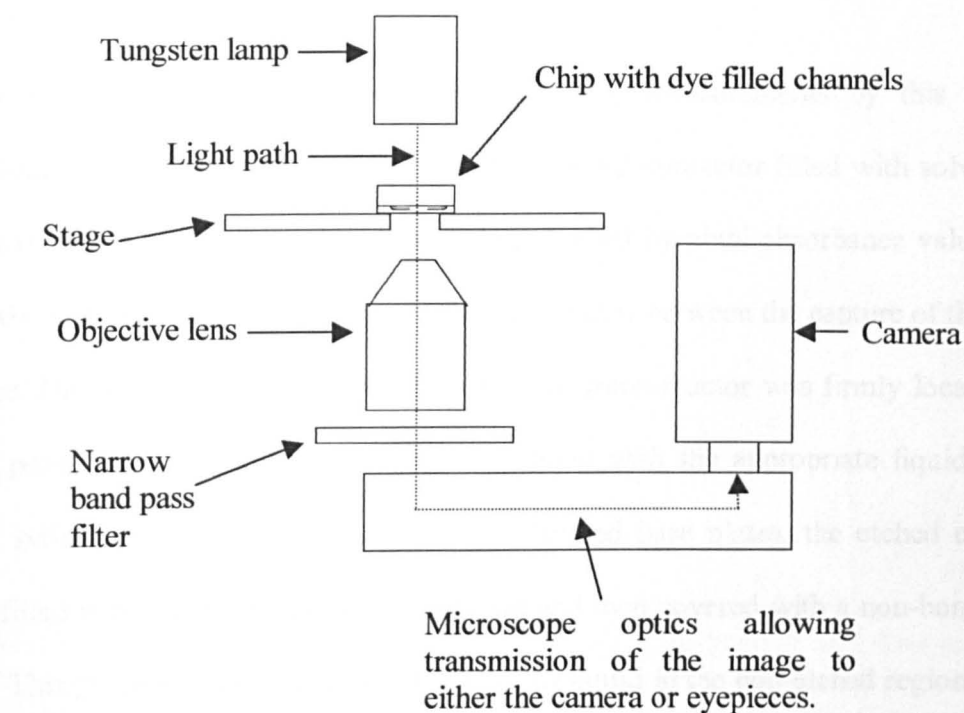
For each measurement set, the incident light intensities and the camera gain were adjusted so that the maximum intensities in the $I_{solvent}$ array were close to the maximum integer value of 4095 allowed by the 12 bit resolution of the camera. It was found that, under these conditions, the array of I_{dark} values did not exceed about 200. This procedure ensured that the full dynamic range of intensities allowed by the 12-bit camera was used.

3.2.3 Microscope configuration and experimental set up.

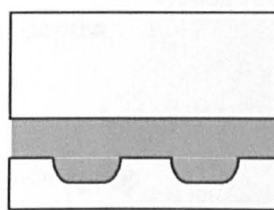
An Axiovert S100 inverted microscope (Carl Zeiss) using transmission optics was employed to obtain digital micrographic images of the microreactors filled with either solvent or dye solutions. The light source was a tungsten lamp emitting over the wavelength range from approximately 400 to 800 nm. Wavelength selection appropriate to the particular dye solution used was achieved by incorporating an appropriate narrow band-pass filter of the correct maximum transmission wavelength (i.e. matching the wavelength of maximum absorbance of the dye solution) between the microscope objective and the camera (Fig 3.3). Transmittance spectra of the two filters used here (Chroma 11002, with peak transmission at 546 nm and a full width at half maximum of 10 nm and Edmund Scientific N43-136, peak 649 nm, full width at half maximum 11 nm) are given in Figure 3.6. Stray ambient light was reduced to negligible levels by the use of an opaque hood, which enclosed the entire apparatus.

Microscope images were collected using a digital monochrome CCD camera (Hamamatsu C4742-95-12NRB) giving a digital output of a maximum of 1024 x 1024 pixels with 12 bit resolution of the light intensity in each pixel. The camera was

Figure 3.3: Schematic diagram of the inverted optical microscope arrangement used for the 3D profiling of microreactor channel networks. The lower diagrams show side views of dye filled channels (shaded grey) in a bonded chip and in a non-bonded chip covered with a non-bonded top block.



Bonded chip with dye filled channels



Non-bonded chip base with channels filled with dye and covered with a top block. A thin layer of dye remains in the non-etched regions (its thickness is greatly exaggerated here)

connected to a PC and controlled by the digital image recording and analysis software AQM from Kinetic Imaging Ltd. Averaging of pixel intensities over 4×4 groups of pixels ("4 x 4 binning") was used to yield a 256×256 array of intensity values. This procedure was found to provide the best compromise between rapid data acquisition,

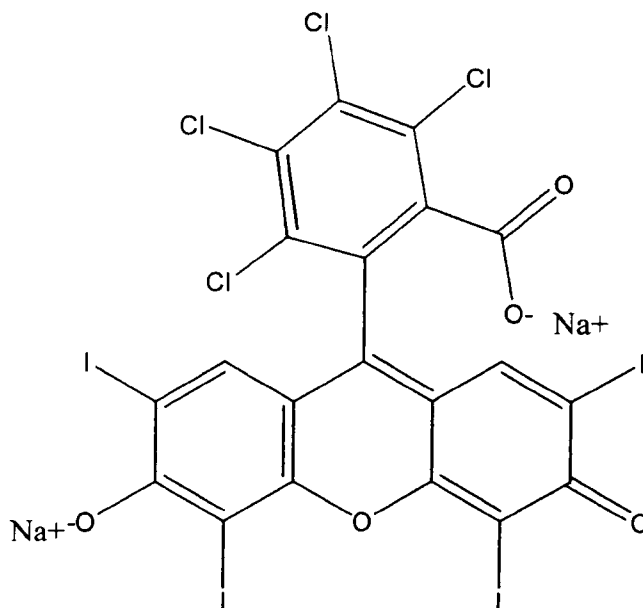
signal-to-noise ratio, spatial resolution and data file size. Scion Image software (Scion Corporation) was used to transfer the numerical image data into Microsoft Excel for subsequent conversion into absorbance values and hence pixel-by-pixel depth values.

As explained in detail below for the profiling measurements by this imaging technique, it is necessary to capture images of the microreactor filled with solvent and then dye solution. For the proper calculation of pixel-by-pixel absorbance values, it is essential that there is no movement of the microreactor between the capture of these two images. Hence, care was taken to ensure that the microreactor was firmly located in a fixed position on the microscope stage and filled with the appropriate liquid *in situ* using syringes. For 3D profiling of the non-bonded base plates, the etched channels were filled with either solvent or dye solution and then covered with a non-bonded top plate. This procedure always gave a thin layer of liquid in the non-etched regions of the base plate (see detail in Figure 3.3). This small depth of dye solution was subtracted from the derived values to obtain the true channel depths.

3.2.4 *Dye solution requirements for absorbance-imaging.*

For the absorbance-imaging to be a rapid and accurate technique for depth profiling microreactor channels, it is necessary for the dye solution and carrier solvent to be easily made and that it is known how light refraction may affect the apparent channel dimensions. Since the greater the mismatch in refractive indexes between solvent and microreactor glass, the greater the theoretical error in the apparent channel dimensions, it is a relatively simple matter to quantitatively analyse this effect. Two dye solutions with differing refractive indexes were made up and were based on Rose Bengal (RB) and Patent Blue (PB). The structures of these two dye species are shown in

Figure 3.4: Chemical structure of Rose Bengal dye molecule. It has the chemical formula $C_{20}H_2Cl_4I_4Na_2O_5$ and a molecular weight $1017.64 \text{ g mol}^{-1}$.



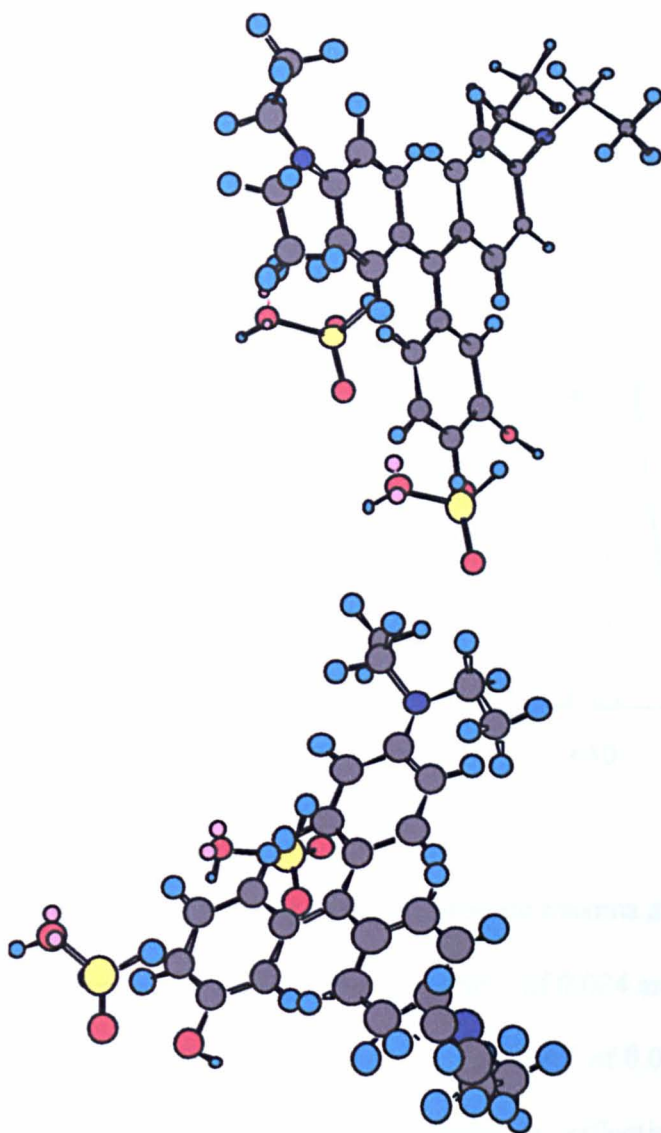
Figures 3.4 and 3.5. In order to optimise the 3D profiling method, it was considered that dye solutions should meet the following criteria:

- The absorbance of the solvent is negligible compared to that of the dye solution at the optimum wavelength.
- The dye solution must be involatile and highly soluble in the solvent so that sufficiently high absorbances (~ 0.6) for small channel depths ($100 \mu\text{m}$ or less) can be accessed.
- That the spectrum of the dye is stable in the solvent system and does not change over the time frame in which the measurement is being made.

3.2.5 Satisfactory dye solutions for absorbance-imaging.

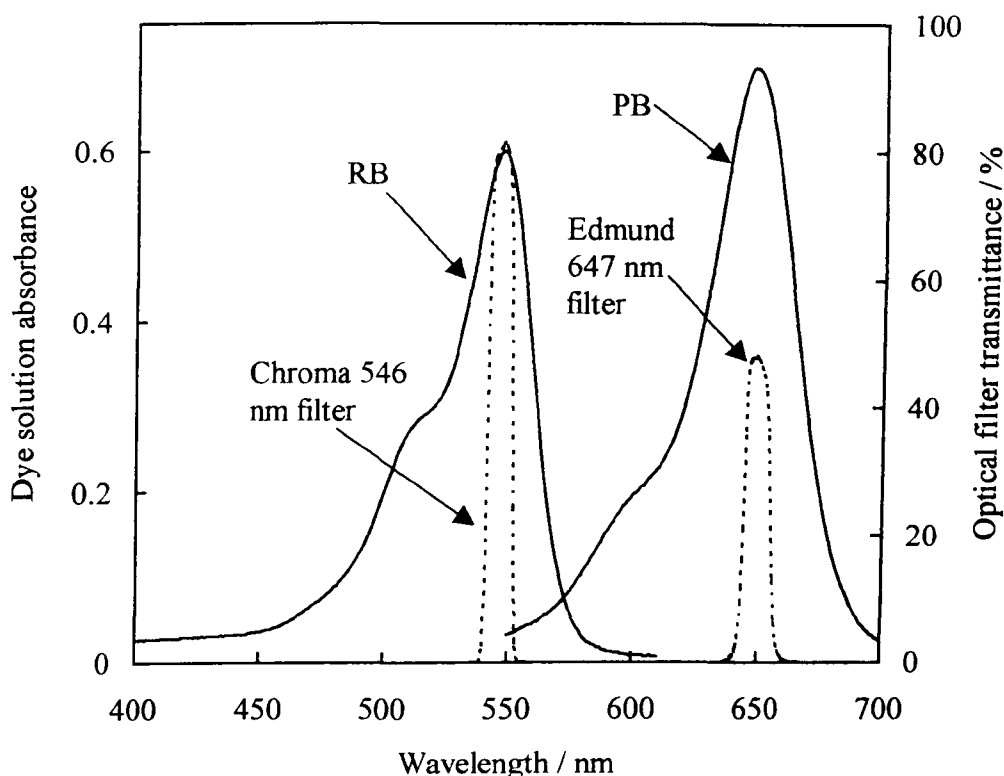
The chosen solvent for RB was water and for PB 30.2 wt. % glycerol in m-cresol. This latter solvent was selected to match the R.I. of the glass to the microreactors. Their

Figure 3.5: 3D representation of Patent Blue molecule. It is 1.75 nm long, 1.1 nm wide and 0.94 nm deep (into page). Light blue colouring represents H, green-C, yellow-S, dark blue-N, red-O). It has a molecular weight of $1159.45 \text{ g mol}^{-1}$.



refractive indexes were found using an Abbe refractometer (see Section 2.1.2) to be 1.3320 for the RB and 1.5239 for the PB solutions. The corresponding spectra of these dye solutions, recorded using a conventional spectrophotometer as described in Section 2.1.3 for a range of accurate path length cuvettes (Hellma 50 – 10,000 μm) along with the transmittance of the narrow band-pass filters used in the absorbance-imaging, are shown in Figure 3.6. The related absorbances of the solutions in a 100 μm path length

Figure 3.6: Absorbance spectra of RB (1.06 mM in water, $\lambda_{max} = 547$ nm) and PB solutions (0.828 mM in 30.2 wt. % glycerol in m-cresol, $\lambda_{max} = 647$ nm). The path length was 100 μm . The dashed lines show the transmittance curves for the two narrow band-pass filters used in conjunction with different dye solutions.



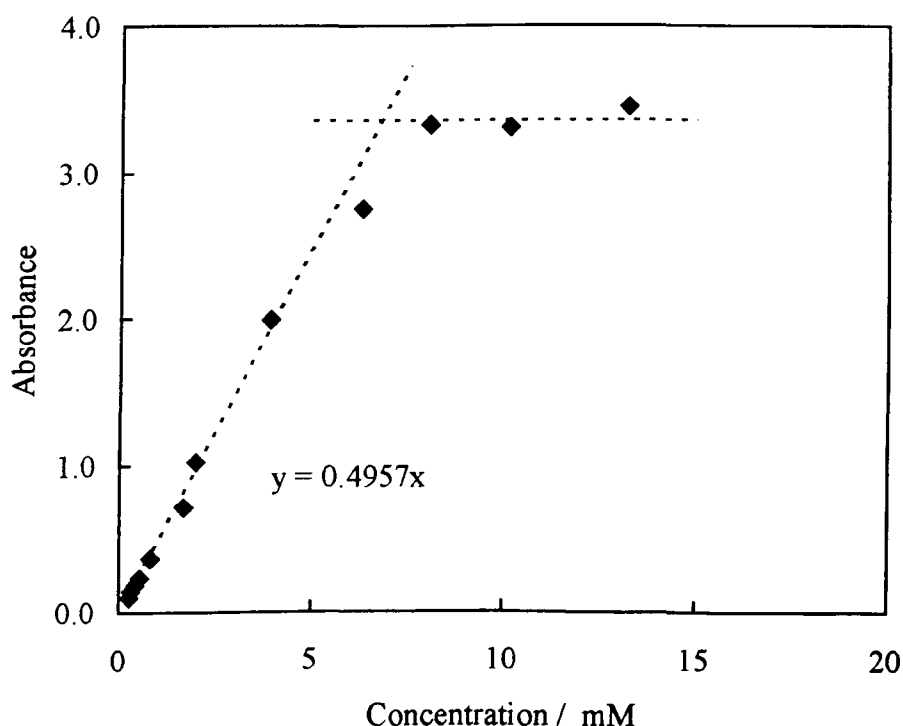
cuvette at the wavelengths corresponding to the absorbance maxima at 20 ± 1 °C were: 0.600 for the RB dye solution compared to the pure water of 0.024 and 0.697 for the PB dye solution compared to the 30.2 wt. % glycerol in m-cresol of 0.066. The maximum absorbance of the solvent solutions has been corrected for reflection losses from the cuvette by assuming a 10 % drop in transmitted light intensity. This allows the absorbance of each solvent solution to be directly compared with the corresponding dye solution absorbance. Clearly given the above analysis, the absorbance of each solvent is insignificant when compared to that of the dye solution at the optimum wavelength.

Absorbance-imaging measurements were expected to be routinely carried out at

room temperature. Preliminary measurements made with RB solutions dissolved in toluene were problematic due to significant evaporation. The newer dye solutions, based on water and 30.2 wt. % glycerol in m-cresol with their lower volatility and higher boiling points, were comparatively problem free.

An important requirement for achieving a good signal to noise ratio in the absorbance-imaging technique, was to ensure that each dye species was sufficiently soluble to give an absorbance ~ 0.6 in a path length equal to the minimum microreactor channel depth to be measured. From previous experience of using aqueous RB solutions and the result shown in Figure 3.6, it was evident that RB would give a good signal to noise ratio.

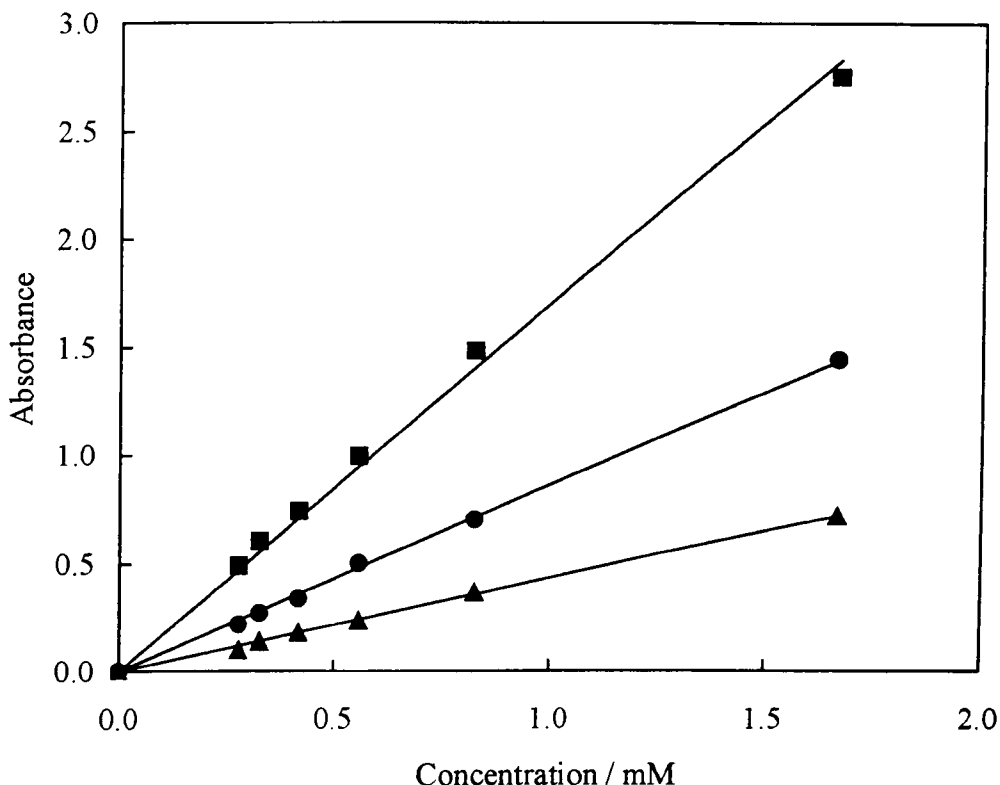
Figure 3.7: Plot of all PB solution absorbances after 1 week aging of the dye solutions at 20 ± 1 °C. Data recorded at 647 nm in a 50 μm path length cuvette. From the intersection, the solubility of PB in this mixture is 6.78 mM. From the slope of the dotted line starting at the origin the molar absorption coefficient for PB in 30.2 wt. % glycerol in m-cresol was calculated to be $9.91 \times 10^4 \text{ M}^{-1} \text{ cm}^{-1}$.



To investigate the solubility of PB in 30.2 wt. % glycerol in m-cresol, a series of different PB solutions were made up covering the concentration range 0 – 15 mM. At increasing PB concentrations, it was found that up to two hours ultrasonication was necessary to dissolve all crystals visible to the naked eye. This was difficult to judge due to the opacity of the solutions even when a sample was pressed between two microscope slides. The absorbances of these solutions determined using a conventional spectrophotometer (Section 2.1.3) in a 50 μm path length cuvette are shown in Figure 3.7. Between 0 and 5 mM the absorbance of each PB solution can be seen to increase linearly and thereafter, beyond the solubility of approximately 5 mM to level off. Clearly, the reasonably high solubility of PB in 30.2 wt. % glycerol in m-cresol gives sufficiently high absorbances to achieve a usable signal to noise ratio in low depth channels.

The spectrum of the dye solutions should not change over the time frame of the experiment. The stability of a freshly prepared solution of RB gave an absorbance of 1.549 at 547 nm in a 50 μm path length cuvette. After 6 months, the spectrum of the original solution showed no spectral shift and the absorbance had changed only by + 0.096 for the same path length cuvette. The PB dye solutions at concentrations below 5 mM were stable enough to be used for experiments. At concentrations above 5 mM, there was an observed trend of slightly increasing absorbance over a period of about 7 weeks. This was attributed to the final solvation of the remaining suspended (microscopic) PB crystals. As a matter of developing an accurate procedure for depth profiling, calibration of the dye solution was performed before and after the absorbance-imaging measurement using a conventional spectrophotometer. This procedure ruled out any possible variation in solution absorbance over the period of the measurement.

Figure 3.8: Absorbance at 647 nm of PB dye solution vs. PB concentration in glycerol-cresol mixed solvent, measured using a conventional spectrophotometer at 50 (filled triangles), 100 (filled circles) and 200 (filled squares) μm path lengths.



For the absorbance-imaging technique outlined here, it was also considered advantageous if the absorbances of the dye solutions were proportional to concentration. This would facilitate the optimisation of dye concentrations necessary to minimise experimental uncertainties for different channel depths. It was not essential that the dye solution obeys Beer's law (i.e. that absorbance is proportional to concentration), only that the absorbance of the actual dye solution be accurately known. Of course, it was essential that Lambert's law, stating that absorbance is proportional to path length, be obeyed. From Figure 3.8 we see that sufficiently high absorbance values can be obtained with the Patent Blue dye solution and that both Beer's and Lambert's laws are obeyed with reasonable precision.

3.2.6 Consideration of uncertainties.

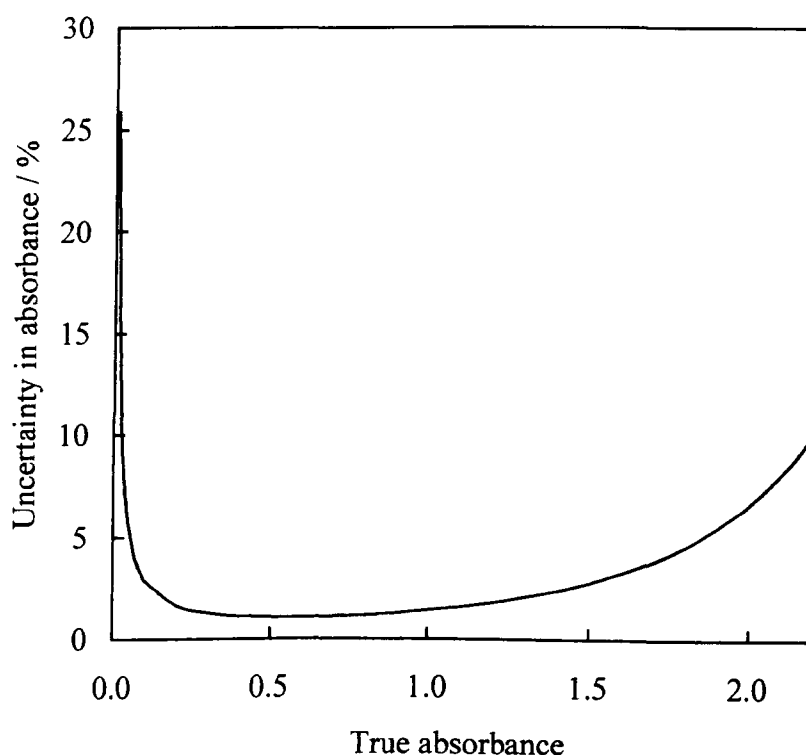
As this absorbance-imaging method is a new technique to determine 3D profiles of channel networks, some understanding of the associated systematic and random uncertainties needs to be taken into account. Considerations that are of paramount importance in optimising the accuracy of this technique are listed below:

- Optimum absorbance
- Numerical aperture of microscope objective lens
- Possible complications due to dye adsorption at the channel walls
- Non-linearity of response of the digital camera

Optimum absorbance

The accuracy with which d_M , the channel depth for a given pixel, can be determined for each image array value (corresponding to a single ‘binned’ pixel group) depends on the

Figure 3.9: Variation of percentage uncertainty in the measured absorbance with true absorbance for $I_{dark} = 100$ and $I_{solvent} = 3500$. Uncertainties of ± 5 in each of the intensities I_{dark} , $I_{solvent}$ and I_{dye} were assumed.



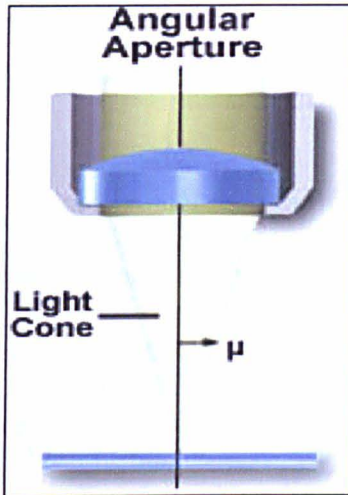
value of the absorbance. For the set up used here, the typical experimental uncertainty in each of the intensity values $I_{solvent}$, I_{dye} and I_{dark} was estimated from the measured variation in arrays of intensity values to be approximately ± 5 . The values for I_{dark} and $I_{solvent}$ using optimised settings for the incident light intensity and camera gain was typically 100 and 3500 respectively. Conversion of the uncertainties in the individual (binned) pixel intensities to the uncertainties in derived absorbance yields the plot shown in Figure 3.9. The uncertainty in absorbance, and hence in depth d_M , is minimum for absorbance values of around 0.6 and is approximately 2 %. Since absorbance is proportional to channel depth, the dye concentration used must be adjusted in order to achieve the optimum absorbance of 0.6 for the particular channel depth under study and an acceptable uncertainty of 2 % in d_M .

Numerical aperture of microscope objective lens

A possible source of systematic error in d_M , may occur when the microscope objective has a significant numerical aperture NA , meaning that light rays passing through the sample take on a variety of paths with different angles. The numerical aperture of a microscope objective is a measure of its ability to gather light and resolve fine specimen detail at a fixed object distance. Image-forming light waves pass through the specimen and enter the objective in an inverted cone as illustrated in Figure 3.10. A longitudinal slice through the central axis of the cone of light shows the angular aperture. The maximum angular deviation for light rays entering the objective is $\pm \mu$ relative to the perpendicular. For an air objective where $n \approx 1$, $NA = \sin \mu$. Hence the average path length experienced by a light ray will be the intensity weighted average for all angles between 0 and $\pm \mu$. The maximum error in the channel depth measurement can be estimated by calculation of the ratio:

$$x_{max} = \left(\frac{\text{true perpendicular path length}}{\text{max light path length}} \right) \quad (3.4)$$

Figure 3.10: Schematic showing the light paths through an objective lens [12].



The angle μ is one-half the angular aperture and is related to the numerical aperture through the following Equation:

$$\text{Numerical Aperture (NA)} = n(\sin \mu) \quad (3.5)$$

Where n is the refractive index of the imaging medium between the front lens of the objective and the specimen.

The maximum light path length occurs for light rays at the maximum acceptance angle μ and is equal to $\cos(\sin^{-1}NA)$ for air objectives where $n = 1$. The effective path length measured will differ from the true (perpendicular) value by an intensity distribution weighted average factor $\langle x \rangle$, which will be intermediate between 1 and x_{max} . As an approximate estimate of this effect, we take $\langle x \rangle$ to be $(1 + x_{max})/2$. For the objective lenses used the values of NA and $\langle x \rangle$ are shown respectively in Table 3.1. It is apparent that the errors in channel depth introduced by this effect are negligible (i.e. $\langle x \rangle$ deviates from unity by less than 2 %) so long as objectives of magnification X 10 or less are used. Proper correction for the effect would be required when using objectives of higher magnification.

Possible complications due to dye adsorption at the channel walls

The adsorption of a positive dye species such as PB onto the negatively charged glass surface within the channel network may affect the overall uncertainty in d_M . When

Table 3.1: The microscope objectives used and the manufacturer's numerical apertures specifications. As a measure of uncertainty in path length which is dependant on NA , $\langle x \rangle$ is calculated. This has a value between 0 and 1 (see text).

Lens magnification	Numerical Aperture	$\langle x \rangle$
1.25	0.035	0.9997
2.5	0.075	0.9986
4	0.1	0.9975
10	0.3	0.9770

a clean channel is used for absorbance-imaging, there should be no dye molecules adsorbed onto the surface of the glass. Filling the channel with solvent to obtain $I_{solvent}$ and I_{dark} intensity values also does not put dye molecules onto the channel wall. To fill the channel with dye, dye solution is flushed through the channel that fills the mid-channel region with a known concentration of dye. As migration of the dye molecules takes place and they adsorb onto the channel wall, the bulk dye concentration is reduced. Further flushing with new dye solution through the channel replenishes the depleted bulk. The final situation during the absorbance-imaging is that there is a slightly higher overall concentration of dye in the imaged region due to the dye adsorption at the channel wall. The question is, does this different concentration significantly affect the apparent channel depth as determined by absorbance-imaging?

If we consider two square parallel plates of equal dimensions $100 \mu\text{m} \times 100 \mu\text{m}$ and separated by a known path length, the concentration change brought about by the adsorption of 2 monolayers of PB molecules can be easily calculated. The dimensions of a single Patent Blue molecule, shown in Figure 3.5, were determined using CS Chem 3D Pro (CambridgeSoft Corp., Massachusetts USA) software and found to be approximately $1.75 \times 1.10 \times 0.94 \text{ nm}$. Assuming that the molecules all lie with one end touching the channel wall and are as tightly packed as possible into the monolayer, the

maximum number of molecules adsorbed onto both plates can be found by dividing the area of the monolayer by the cross-sectional area of one molecule end on. Results based on this model were calculated in Microsoft Excel (a typical worksheet is shown in Appendix B). For each channel depth value, the solution dye concentration was adjusted to obtain the optimum absorbance of 0.6 for that particular channel depth. The dye concentration required was inversely proportional to the path length for a fixed optimum absorbance. The number of dye molecules forming the monolayer was assumed constant at saturation coverage to give the greatest possible concentration difference. For a series of different path lengths, the apparent path length for each case was calculated along with the associated uncertainty arising from dye adsorption, as are shown in Table 3.2. Clearly, the maximum error in d_M resulting from dye adsorption is insignificant at approximately 0.05 % and is independent of channel depth. This value is for the molecules being adsorbed end on. If they were orientated flat on the surface the maximum relative error would be approximately 0.03 %.

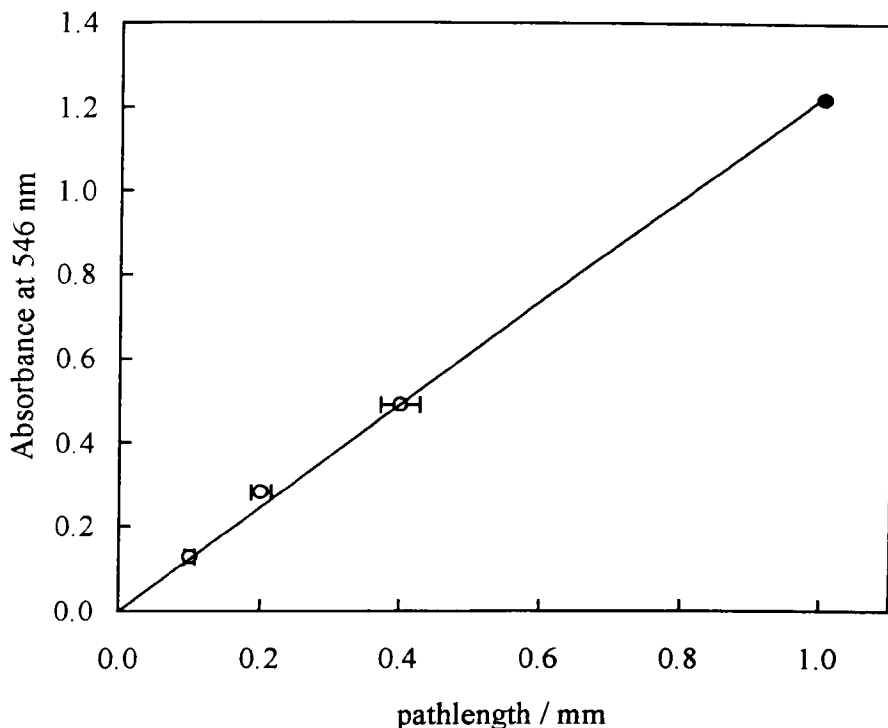
Table 3.2: The maximum calculated error in apparent channel depth arising from dye molecule adsorption onto the channel wall.

True path length / μm	Apparent path length / μm	% error in measurement
5	5.002	0.05
20	20.010	0.05
50	50.026	0.05
100	100.053	0.05
250	250.133	0.05

Non-linearity of the digital camera response

The final source of uncertainty in the absorbance-imaging method lies in the possible non-linear response of the digital camera, when acting as a spectrophotometric detector of light intensity. This was checked by comparing absorbance values derived from

Figure 3.11: Absorbance (546 nm, measured using the microscope-imaging method) vs. path lengths for RB dye filled capillaries or rectangular cross-section (open circles) and a 1 mm path length cuvette (filled circle).



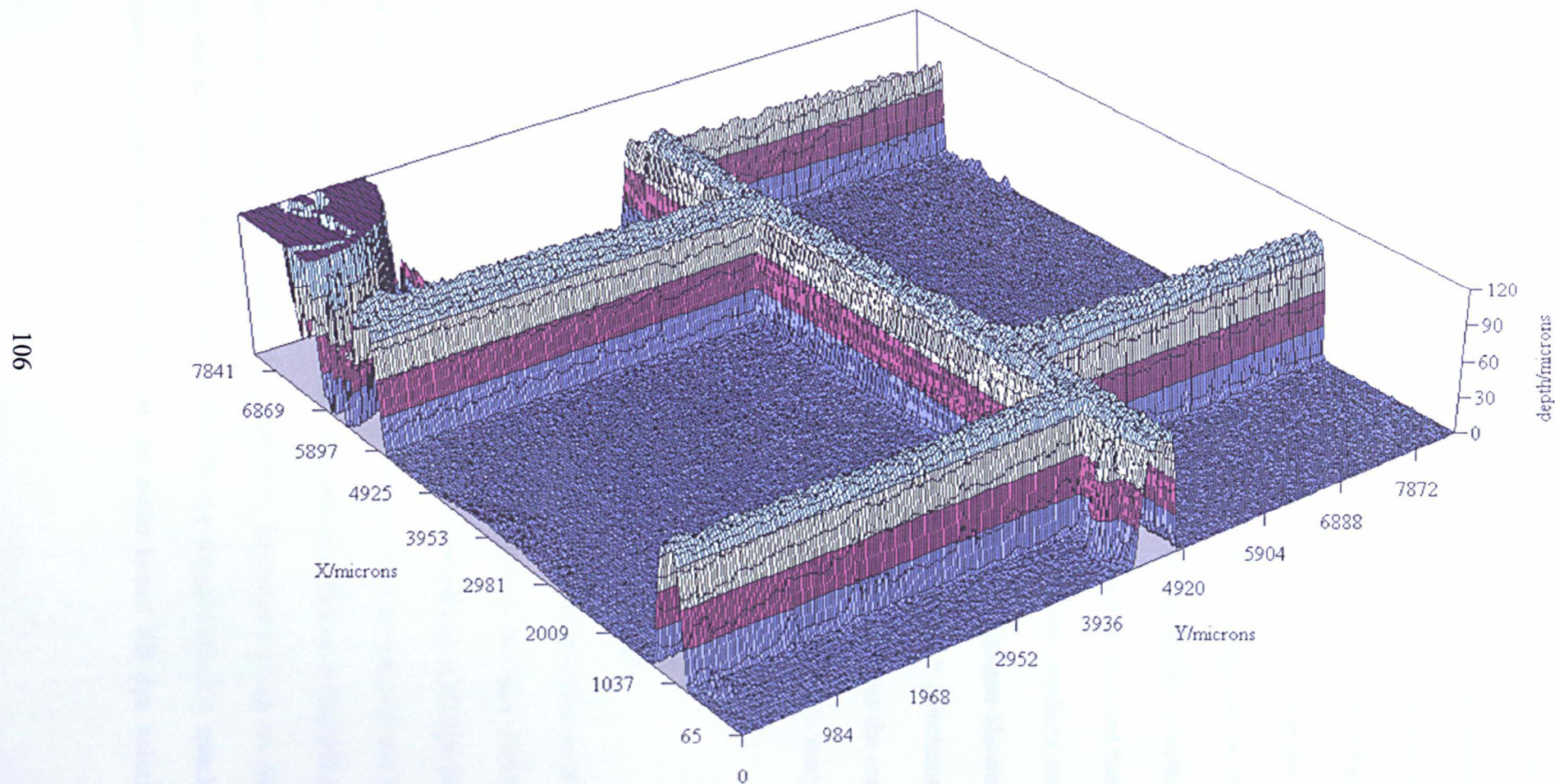
camera measurements with values determined using a conventional spectrophotometer. Images of dye filled rectangular capillaries of different path lengths (obtained from Camlab, UK) and a 1 mm cuvette were recorded and converted to absorbance. The absorbance of the 1 mm cuvette sample was also measured using a conventional spectrophotometer. The results, plotted in Figure 3.11, show that the microscope absorbance values agree within the experimental uncertainties. These uncertainties mainly arise from the uncertainties ($\pm 7\%$, estimated microscopically) in the path lengths of the capillaries.

3.3 Results and discussion.

3.3.1 3-dimensional profiles of channel networks.

Figure 3.12 shows a 3D profile image of 7 x 7 mm area of chip 1 recorded using the

Figure 3.12: 3D profile images of a 7 x 7 mm area of the channel network of chip 1. The image was recorded using RB as the dye (non-R.I. matched dye).

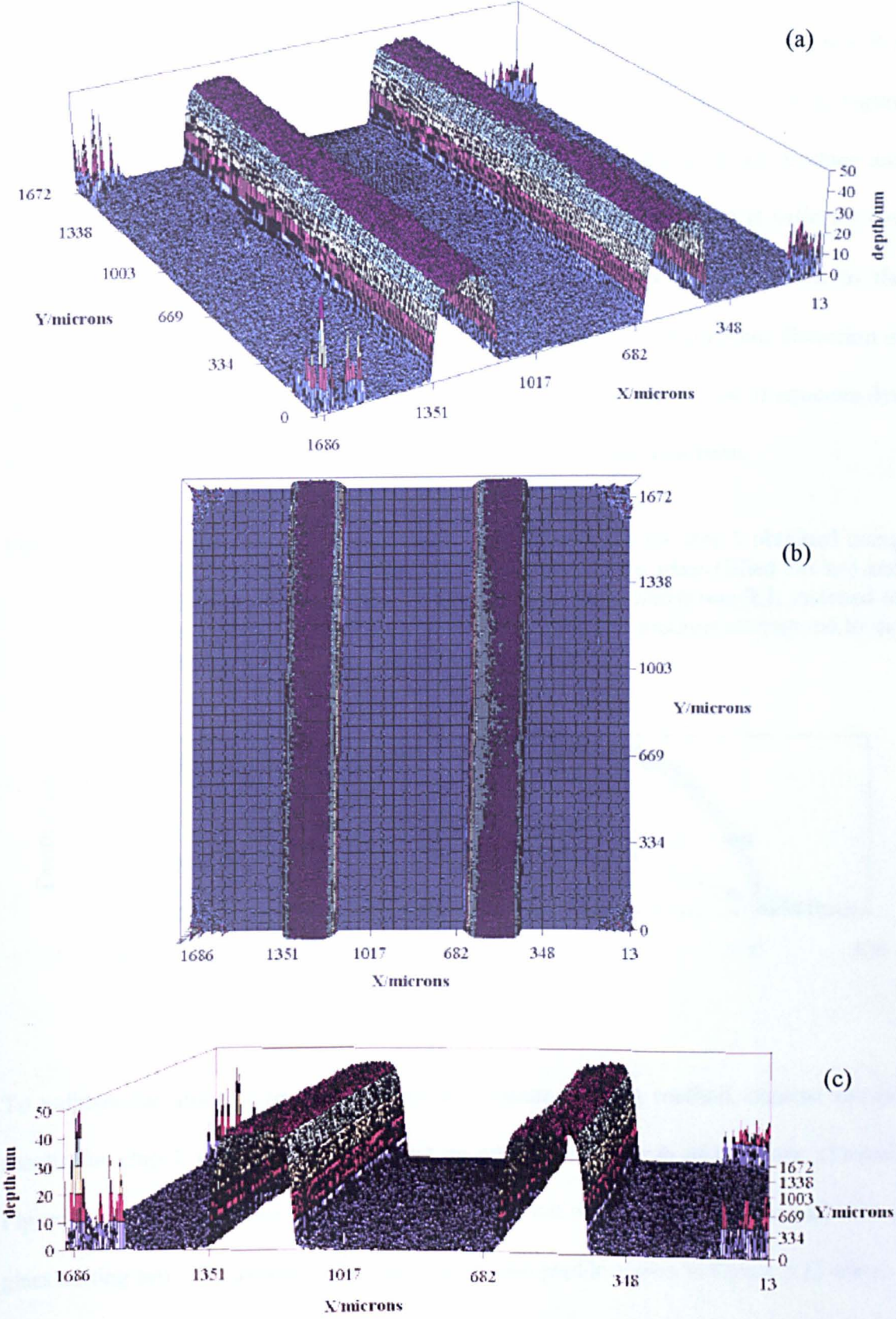


set up shown in Figure 3.3 with a X1.5 objective lens. Even at this low magnification (required to image a large area), the spatial resolution is sufficient to allow details of the channel profiles and intersections to be seen clearly. The deep circular shape at $X = 7800$, $Y = 0$ mm corresponds to one of the reservoirs on the microreactor. The time required for acquisition of the image set and subsequent data analysis to produce Figure 3.12 was about 1 hr. One of the useful aspects of this technique is that when the 3D profiles are displayed on a computer screen using Microsoft Excel, they can be fully rotated in 3D allowing examination from all angles. To illustrate this feature, a series of images made of the bonded chip 2 are shown in Figure 3.13. It should be noted that in the corners of Figure 3.13 (a) there are a series of “spikes”. These artefacts occur because of the circular field of view in the microscope. Since the images shown in Figure 3.13 are constructed from 256 data slices in each of the X and the Y directions, it is quite straightforward to plot a slice of data along a single channel or across the entire channel network. In the next Section the use of such slices will be employed to analyse the isotropic etch shape of etched channels.

3.3.2 Does the dye solution R.I. affect the apparent channel dimensions?

This experiment was designed to check whether any significant differences in apparent channel dimensions, arose from the use of dye solutions that had different refractive indexes to the microreactor glass. It was expected that refraction of light from the edges of the channels would occur when the R.I. values were not matched and this might affect the channel dimension measurements. The refractive indexes of the RB and PB dye solutions along with the microreactor glass were determined using an Abbe refractometer and are listed in Table 2.3, pg 74. The PB dye solution was R.I. matched to the microreactor glass, whereas the R.I. of the water based RB dye solution

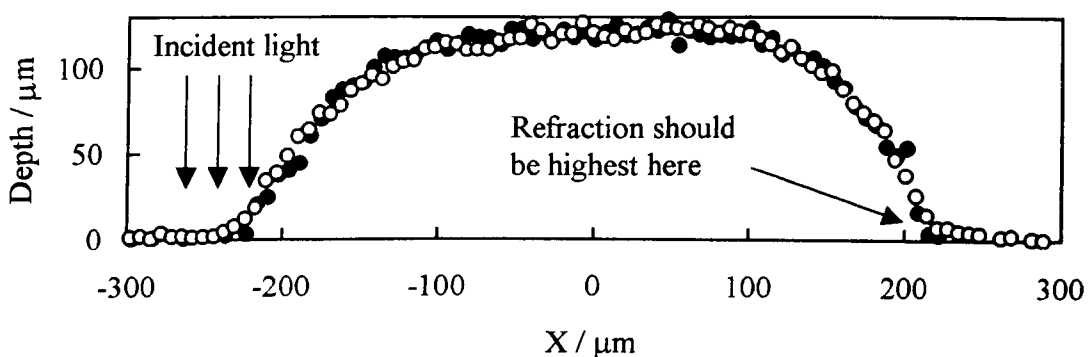
Figure 3.13: Series of 3D profile images of a 1.7 x 1.7 mm area of chip 2 after thermal bonding. The images show how the profile is fully rotatable (a) oblique projection (b) plan view (c) cross-sectional view of channels. The images were recorded using PB as the dye (R.I. matched).



differed by approximately 0.2.

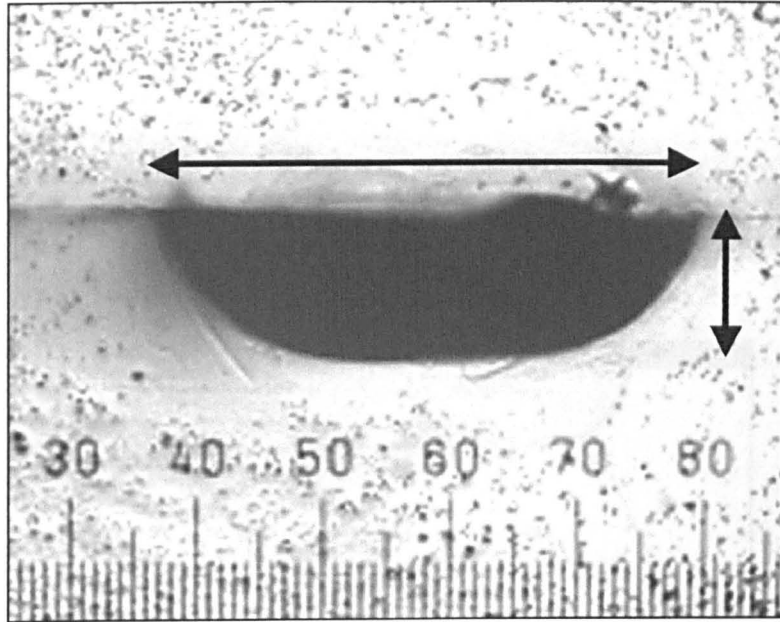
Images using the X10 objective were made of a sub-area of chip 1, as shown in Figure 3.12. Slices through the 3D images taken using both aqueous RB (non-R.I. matched) and glycerol / cresol PB dye (R.I. matched) solutions are shown in Figure 3.14. It can be seen that use of a non-R.I. matched dye solution does not produce any significant distortion of the measured channel profiles. This conclusion is valid for dye solutions having an R.I. that differs by no more than ± 0.2 in comparison to the microreactor glass. Higher levels of R.I. mismatch may produce significant distortion of the channel profiles. The important result established here is that the use of aqueous dye solutions to image glass microreactors does not give significant distortion.

Figure 3.14: Comparison of channel cross-sectional profiles for chip 1 obtained using RB aqueous dye solution not R.I. matched to the glass (filled circles) and PB solution in glycerol / cresol mixed solvent which was R.I. matched to the glass (open circles). The two channel cross-sections correspond to the same position in the channel network of chip 1.



To validate the absolute precision of the absorbance-imaging method, channel profile results for chip 1 were compared against an optical micrograph of the same channel. Figure 3.15 shows the open channel that was the result of cutting the chip in half with a glass cutting saw. The dimensions of the channel end profile shown in Figure 3.15 show

Figure 3.15: Optical micrograph of a side view of a channel end in chip 1. The horizontal arrow length (409 μm) corresponds to the channel top width measured in Fig. 3.14. The vertical arrow length (119 μm) corresponds to the channel depth measured in Fig. 3.14.

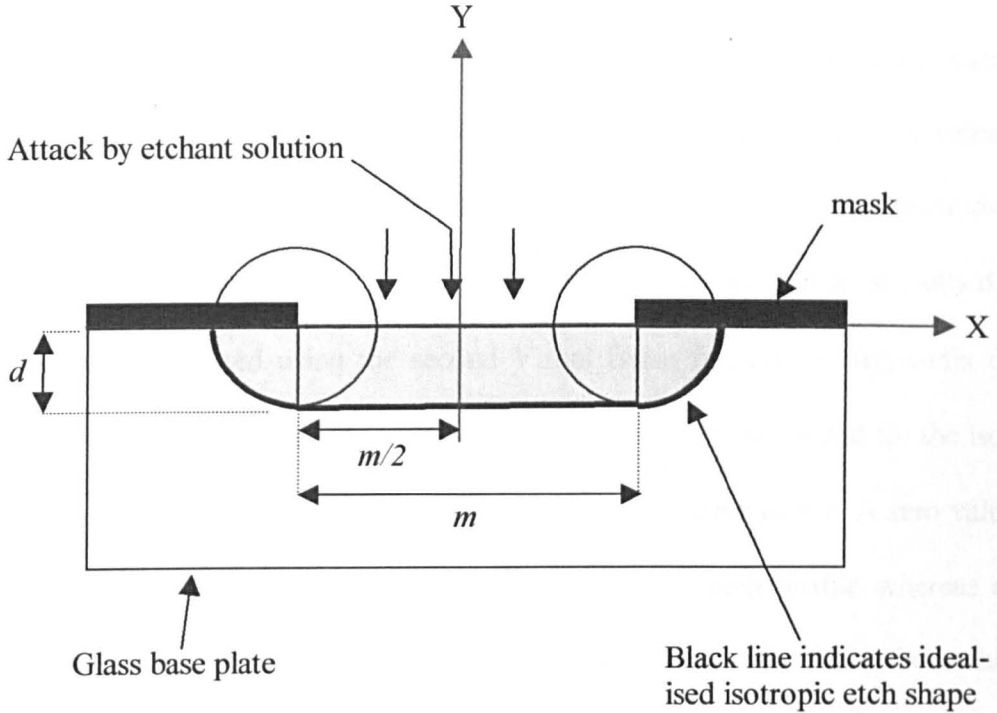


good agreement with those determined from the absorbance-imaging measurements of Figure 3.14.

3.3.3 *Fitting channel cross-sectional profiles and the effects of thermal bonding.*

The profile produced by isotropic etching of glass was briefly discussed in Figure 1.6, pg 18. This can be extended to include a quantitative description. Consider Figure 3.16, as the etchant encounters the newly prepared base plate; it is presented with a uniform flat surface. In those regions that are free of masking material, the etching proceeds at an equal rate in all directions (i.e. isotropically). Hence, the channel cross-sectional shape formed by wet chemical etching of glass consists of a rectangle of mask line width m flanked by two-quarter circles of radius and channel depth d . The total width of the etched channel at the base plate glass surface is equal to the sum of the mask line width plus twice the channel depth (i.e. $m + 2d$).

Figure 3.16: Simple quantitative illustration of how wet chemical etching produces an isotropic shape in a glass base plate. The width of the etched channel is equal to the mask line width m plus twice the channel depth d . The etched channel cross-section (grey shaded region) can be represented by a rectangle plus two quarter circles.



In order to model how effective the wet chemical etching process had been at producing a channel network with the idealised isotropic cross-sectional shape shown in Figure 3.16, it was necessary to derive the mathematical equations which define it. If isotropic etch shape is defined in terms of an XY coordinate system, where X denotes a distance on the base plate surface measured from the centre of the channel and the Y denotes a given depth on the isotropically etched channel surface, it is possible to represent the position of each point on the channel surface mathematically. At the origin, the channel is of depth d over a range $X = \pm m / 2$ and $Y = d$. At the base plate surface, $Y = 0$. At the two-quarter circles, Y is given by the equation:

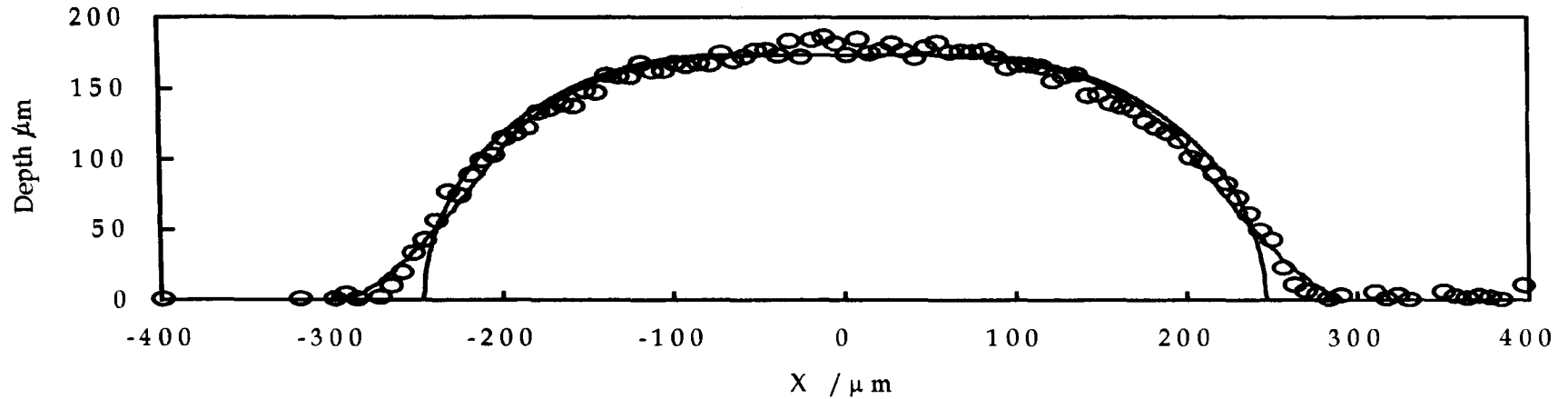
$$Y = \sqrt{d^2 - \left(X \pm \frac{m}{2}\right)^2} \quad (3.6)$$

Calculation of the ideal channel profiles was implemented as a Visual Basic (VB) function in Excel. The VB code for this is given as the first function in Appendix C.

In practice, either prolonged etching or thermal bonding may produce a “smoothing” of the channel edges away from the idealised quarter circle shape. In order to model this extra effect, we must first calculate the ideal isotropic etch profile using the values of m and d . The “smoothing” of the profile was parameterised by incorporation of a smoothing length δ into the model. The channel cross-sectional profile, smoothed over a length δ , was calculated using the second Visual Basic function in Appendix C. The channel depth at each X value is obtained by taking the depth calculated for the isotropic etch profile averaged over the range of X values corresponding to $\pm \delta$. A zero value of δ corresponds to no distortion from the idealised isotropic etch profile whereas a high value indicates that significant smoothing has occurred during either the etching or thermal bonding processes.

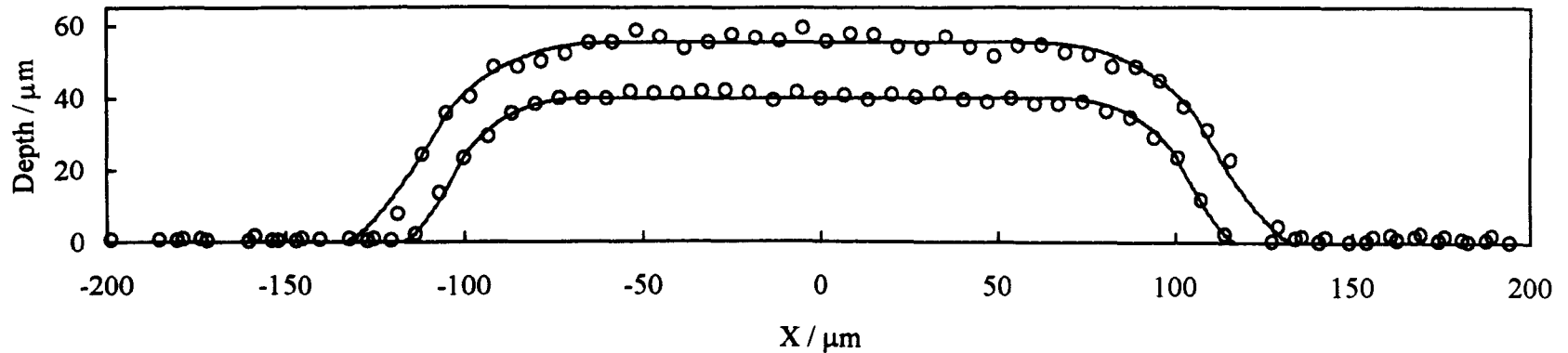
A slice of data taken from the 3D absorbance image plot for the 96 min etched base plate (No. 6, Table 3.3) shows a typical channel cross-sectional profile. The open circles shown in Figure 3.17 indicate the measured channel cross-sectional profile. The black solid line represents the best two-parameter fit obtained by floating m and d in the Excel worksheet. The red solid line is for the 3 parameter fit obtained by floating m , d and δ together. It can be seen from Figure 3.17 that the 3 parameter fit gives the best estimate of the isotropic etch shape for an actual channel. The difference between the two and three parameter fit is most distinct at the channel edges. Whereas the black solid line representing the calculated ideal isotropic etch shape for this chip ($m = 145.2 \mu\text{m}$ and $d = 173.4 \mu\text{m}$) does not consider the smoothing due to etching, it correspondingly does

Figure 3.17: Channel cross-section profile for 96 min etched and un-bonded base plate. Filled circles are experimental data. The solid black line shows the ideal isotropic etch model with $m = 145.2 \mu\text{m}$ and $d = 173.4 \mu\text{m}$ (best-fit). The red solid line is the fitted line incorporating the smoothing parameter, $\delta = 88 \mu\text{m}$.



113

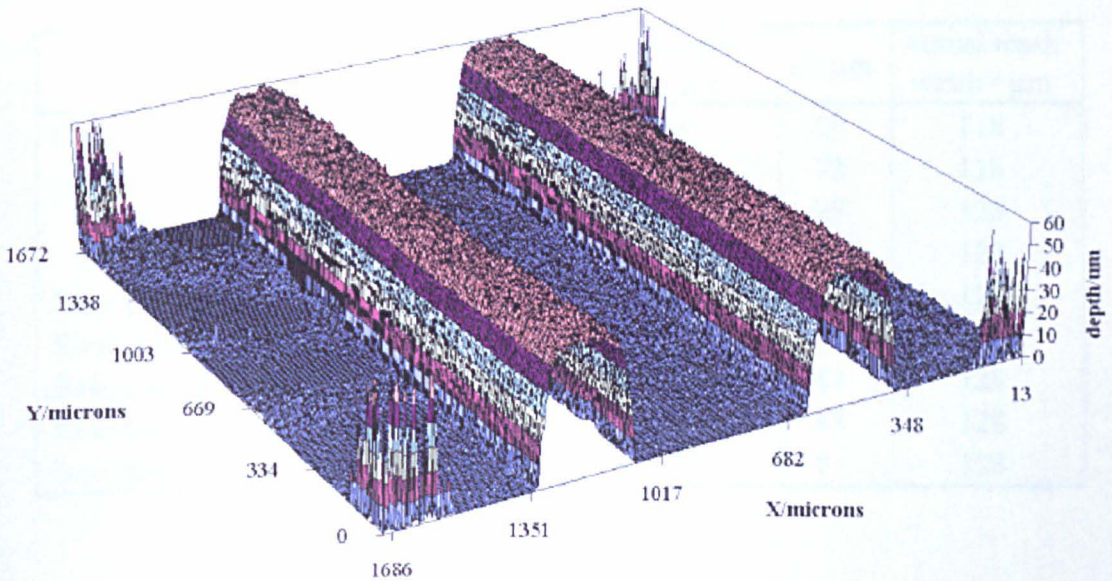
Figure 3.18: Channel cross-section profiles for chip 2 before (larger depth) and after thermal bonding (smaller depth) of the base plate and top block. The solid curves are best fits to the model based on m , d and δ listed in Table 3.3.



not achieve the excellent fit shown by the red solid line ($m = 145.2 \mu\text{m}$, $d = 173.4 \mu\text{m}$ and $\delta = 88 \mu\text{m}$).

We now consider the effects of thermal bonding. Chip 2 was profiled before (Figure 3.19) and after thermal bonding (Figure 3.13 a) and the cross-section profiles compared as shown in Figure 3.18. Absorbance-imaging reveals that thermal bonding has decreased the channel width and depth. This is a consequence of the thermal bonding process where the glass is hot enough to flow.

Figure 3.19: 3D profile image of a 1.7 x 1.7 mm area of chip 2 before thermal bonding. This is included to complement the bonded chip 2 profile shown in Figure 3.13 (a).



The derived parameters for chip 2 (shown in Table 3.3) show relatively low values of δ indicating there is little or no distortion from the idealised isotropic etch profile. Thermal bonding in this case apparently reduced δ slightly. However, it can be seen in Figure 3.18, that the difference in channel profile shapes corresponding to the best-fit

values for δ of 25 and 15 μm (for the non-bonded and bonded chip respectively) are rather small. In contrast to chip 2, the δ values for chip 1 (Table 3.3, where similar values are seen for non-R.I. and R.I. matching) are high, indicating that significant smoothing of the channels occurred during the fabrication process. It is relevant to note here that chip 1 was bonded using a higher temperature and a larger top mass (added to aid bonding) than chip 2. Both factors might be expected to increase channel profile distortion during bonding. These examples serve to demonstrate the utility of the 3D profiling method coupled with the channel profile modelling for characterisation of microreactor channel networks and the optimisation of their fabrication.

Table 3.3: Summary of measured channel profile parameters. Chip 1 (non-R.I. matched) was profiled using a RB solution in water. All other chips were profiled using PB solutions in glycerol-cresol mixed solvent which was R.I. matched to the glass of the chip.

Microreactor	Depth / μm	Apparent mask width / μm	δ / μm	Actual mask width / μm
Chip 1 (non-R.I. matched)	119.4	170.9	59	118
Chip 1 (R.I. matched)	119.2	173.8	72	118
Chip 2 (non-bonded)	55.3	129.0	25	128
Chip 2 (bonded)	39.9	138.2	15	128
Base plate 3 (24 min etch)	50.1	126.0	17	128
Base plate 4 (36 min etch)	62.8	137.1	11	128
Base plate 5 (48 min etch)	85.7	157.3	41	128
Base plate 6 (96 min etch)	173.4	145.2	88	128
Base plate 7 (120 min etch)	189.8	126.9	57	128

3.3.4 Time of etching and the effect on m , d and δ

For the routine fabrication of channels of different depths, it is helpful to know the etch rate. To acquire this information, chip base plates 3 – 7 were taken in their non-bonded state and depth profiled using absorbance-imaging. The best fit values of m , d and δ for the channels of these base plates are given in Table 3.3 and some examples of

Figure 3.20: Channel cross-section profiles for base plates 3, 5 and 7 are shown. The shallower plot corresponds to 24, then 48 and finally 120 min etch time. The solid curves are best fits to the model incorporating m , d and δ as described previously. The parameters listed in Table 3.3.

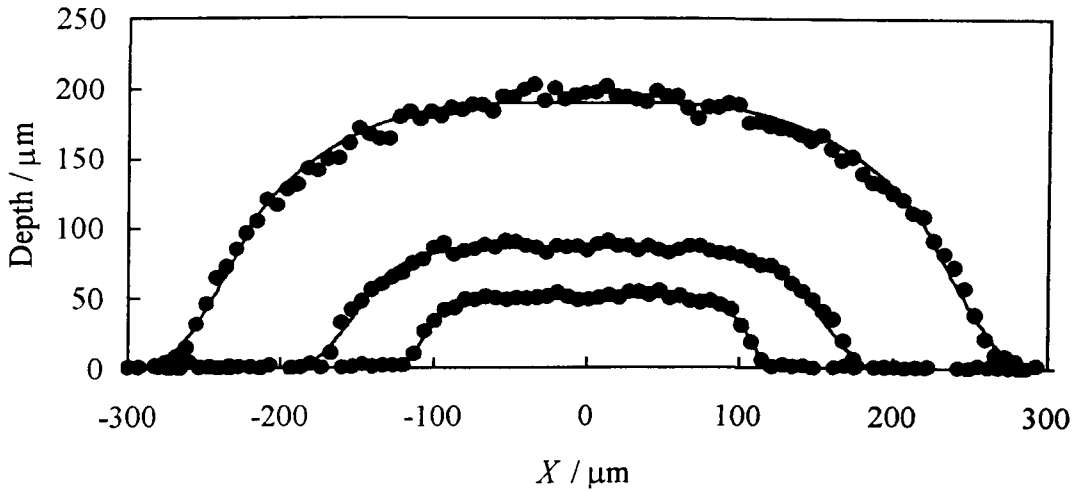
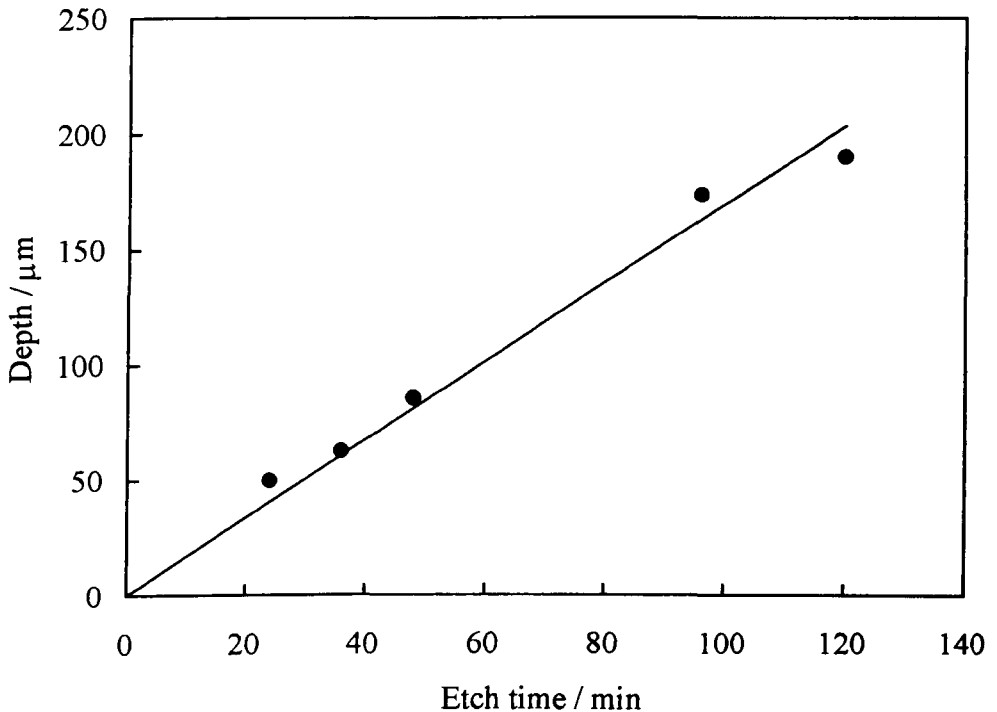


Figure 3.21: Variation of channel depth with etch time under the conditions set in Section 2.1.1. The solid line corresponds to a mean etch rate of $1.7 \mu\text{m min}^{-1}$.



the smoothed isotropic etch profiles are shown in Figure 3.20. As shown in Figure 3.21, the plot of depth versus etch time is linear i.e. the etch rate is approximately constant

and equal to $1.7 \mu\text{m min}^{-1}$. It was hoped that this etch rate could be compared against other authors' findings for buffered hydrofluoric acid etchant systems in the literature. Given that etch rates vary significantly with temperature and those values found in the literature do not specify any temperature, their data cannot be quantitatively compared. However, some illustrative literature values are noted here. Harrison [13] reported etch rates for Paragon Pyrex and Corning 7059 Pyrex glass of $0.5 - 0.8 \mu\text{m min}^{-1}$ and $5.0 \mu\text{m min}^{-1}$ using HF-HNO₃ etchant. Madou [14] reported etch rates for Corning 7740 Pyrex glass of $1.9 \mu\text{m min}^{-1}$ using HNA (HF/HNO₃/CH₃COOH). Pyrex is the American brand name for borosilicate glass, which is very similar in composition to the Crown glass used by the Hull group to fabricate their microreactors.

The apparent mask line widths m derived from the fits to the measured channel profiles (Table 3.3) are reasonably close to the actual mask width of $128 \mu\text{m}$. The origin of the small differences between fitted and actual mask widths observed for some of the samples is unclear at present. In addition, as expected, the m values in Table 3.3 do not vary significantly with etch time.

The pixel-to-pixel variation in channel depth across “flat” regions of the channels can result from two causes. Firstly, variation can result from the random uncertainty in the microscope absorbance measurements and hence in the measured depths. Secondly, the channel surfaces may actually be rough giving a real point-to-point variation in depth. Figure 3.22 shows a plot of the standard deviation in depth vs. actual channel depth. The slope of the best-fit straight line (solid line) to this plot corresponds to an uncertainty to 2.3 % of the measured depth (i.e. one standard deviation in channel depth). This level of uncertainty is reasonably consistent with the value expected from

Figure 3.22: Standard deviation in channel depth versus depth. The solid line corresponds to an uncertainty (one standard deviation) of 2.3% of the channel depth plus an intrinsic depth variability of $0.7 \mu\text{m}$ given by the intercept of the plot.

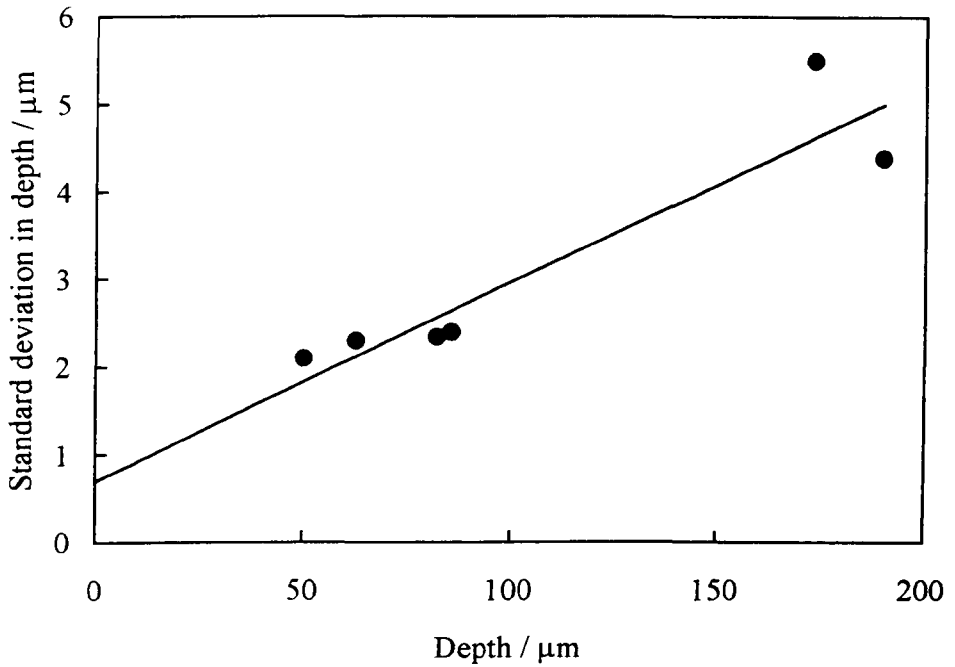
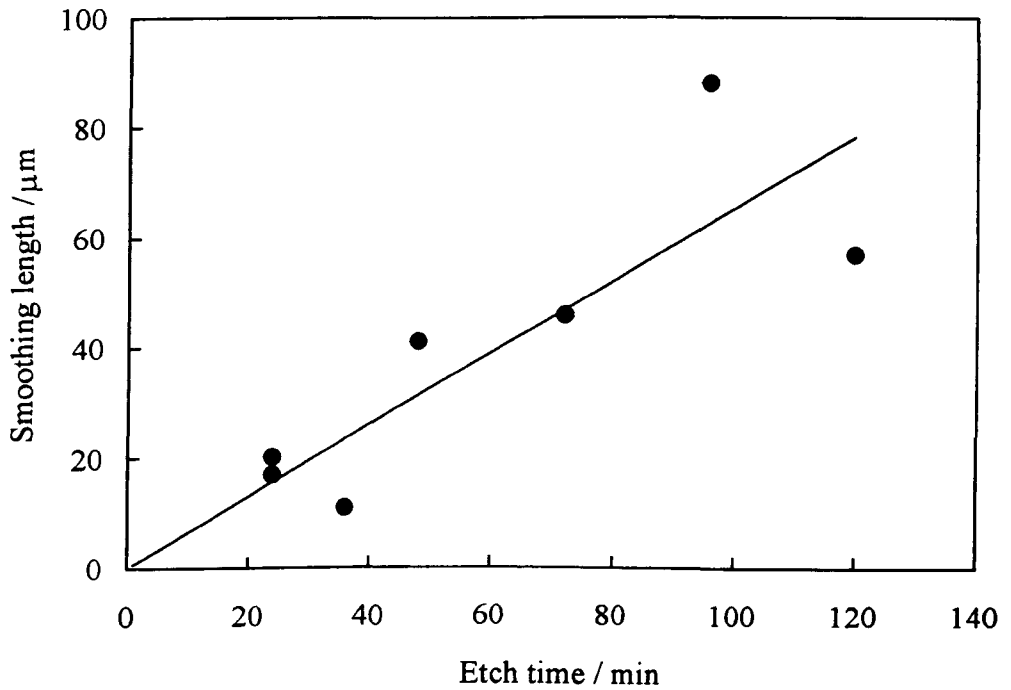


Figure 3.23: Variation of fitted smoothing length δ with etch time.



the analysis shown in Figure 3.9. The intercept of Figure 3.22 suggests that the actual roughness of the channel surface is of the order of 0.7 μm . Although plausible, the “scatter” of the data (Fig. 3.22), makes this estimate rather uncertain.

It can be seen from Figure 3.23, that there is an approximately linear correlation between δ and etch time. This suggests that the extent of profile smoothing from the ideal isotropic etch shape is determined (at least in part) by the etch process (and not solely due to thermal bonding). Originally a deviation from the isotropic etch shape was not expected to arise from the etching procedure. The scatter of the data in Figure 3.23 may partly arise due to the way etchant solution is replaced at the glass surface and whether reactant transport in the solution became rate limiting.

3.4 Summary.

We have developed a rapid, accurate and non-destructive technique to determine the 3D profiles of microreactor channel networks based on optical imaging of dye filled channels. The method is capable of measuring channel depths from 10 to 500 μm (and probably smaller depths) with an accuracy of a few percent and a spatial resolution of less than 1 μm . It has been established that distortion effects of the measured profiles resulting from a mismatch of ± 0.2 in refractive index between the dye solution and the glass of the microreactors are insignificant. The method has been successfully used to investigate the effects of thermal bonding and etch time on channel profiles. Channel cross-section profiles determined by absorbance-imaging show good agreement to those independently measured using optical microscopy.

The imaging method developed here could be applied to profile any solution-fillable

voids within transparent solids. Furthermore, for microreactor channels where the depth (path length) has been measured, the technique may also be applied to determine the concentration profiles of either absorbing or fluorescent species in the channels with a time resolution of greater than 10 frames per second. This aspect will be discussed further in later Chapters of this thesis.

3.5 References.

- [1] http://www.veeco.com/html/product_bymarket_proddetail.asp?TypeID=2&MarketID=&FamilyID=1&ProductID=190 (Sept 02).
- [2] I. Broadwell, P. D. I. Fletcher, S. J. Haswell, T. McCreedy and X. Zhang, *Lab on a Chip*, 2001, 1, 66-71.
- [3] P. J. Treado, A. Govil, M. D. Morris, K. D. Steernitzke & R. J. McCreery, *Appl. Spectrosc.*, 1990, 44, 1270.
- [4] S. C. Jacobson, R. Hergenroder, L. B. Koutny, R. J. Warmack & J. M. Ramsey, *Anal. Chem.*, 1994, 66, 1107.
- [5] J. Wu & J. Pawliszyn, *Anal. Chem.*, 1994, 66, 867.
- [6] E. N. Lewis, P. J. Treado, R. C. Reeder, G. M. Story, A. E. Dowrey, C. Marcott & I. W. Levin, *Anal. Chem.*, 1995, 67, 3377.
- [7] Z. Wang & D. Scherson, *J. Electrochem. Soc.*, 1995, 142, 4225.
- [8] E. T. Bergstrom, D. M. Goodal, B. Porkric & N. M. Allinson, *Anal. Chem.*, 1999, 71, 4376.
- [9] B. L. McClain, J. Ma & D. Ben-Amotz, *Appl. Spectrosc.*, 1999, 53, 1118.
- [10] P. E. J. Flewitt & R. K. Wild, *Physical methods for material characterisation*, (1994) IOP Publishing: Bristol, p196-200.
- [11] P. E. J. Flewitt & R. K. Wild, *Physical methods for material characterisation*, (1994) IOP Publishing: Bristol, p169.
- [12] <http://www.microscopy.fsu.edu/primer/anatomy/numaperture.html>
- [13] Z. H. Fan & D. J. Harrison, *Anal. Chem.*, 1994, 66, 177.
- [14] M. Madou, *Fundamentals of Microfabrication*, (1997) CRC Press, p167.

4. COMBINED EOF AND PRESSURE-DRIVEN FLOW IN CYLINDRICAL CAPILLARIES.

4.1 Introduction: *The need for simple flow rate measurements.*

The object of the work outlined in this Chapter was to establish a better understanding of some aspects of electroosmotic and pressure-driven flows using a U-tube arrangement of reservoirs interconnected by a cylindrical glass capillary. The main benefit of such a set up was that it substantially simplified flow rate modelling by eliminating the complex microreactor channel network geometry.

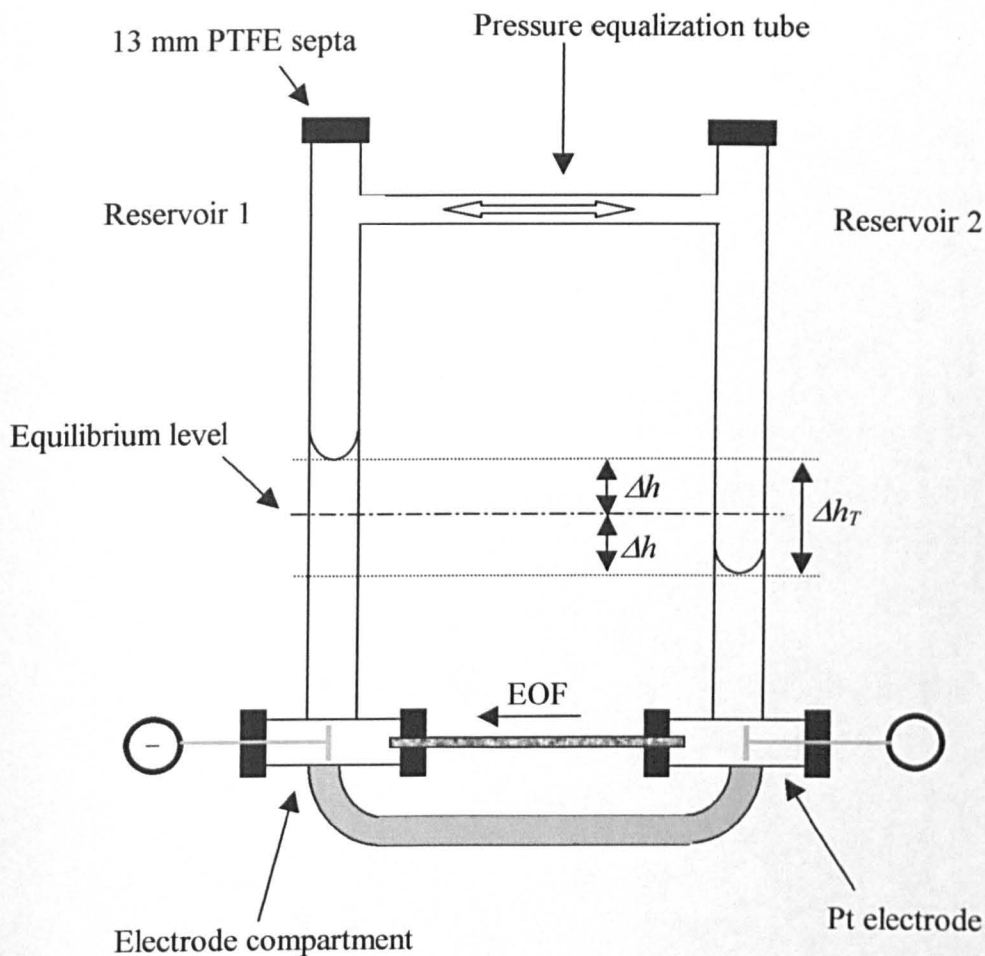
4.2 Apparatus and theory.

4.2.1 U-tube apparatus and experimental set up.

The experimental apparatus used here had some similarities to that used by McCreedy *et al.* [1] to record solvent volumetric flow rates. A schematic representation of the new apparatus (U-tube) can be seen in Figure 4.1. The rubber seals McCreedy's apparatus used to secure the capillary tube and prevent leakage were replaced by 13 mm diameter PTFE septa (Frank Leu, Houston, TX). These did not decay when organic solvents were used. Adjustable 0.75 mm diameter platinum wire electrodes allowed separations of 5 – 11 cm to be selected to give varying electric field strengths. The pressure equalisation tube, coupled with the PTFE septa capping the reservoirs, allowed reservoir liquid levels to change in response to EOF while forming a completely sealed system to the surroundings. This prevented liquid loss through evaporation. As shown in Figure 4.2, a key difference between this apparatus and McCreedy's was that this could be accurately temperature controlled by immersion in a thermostat tank.

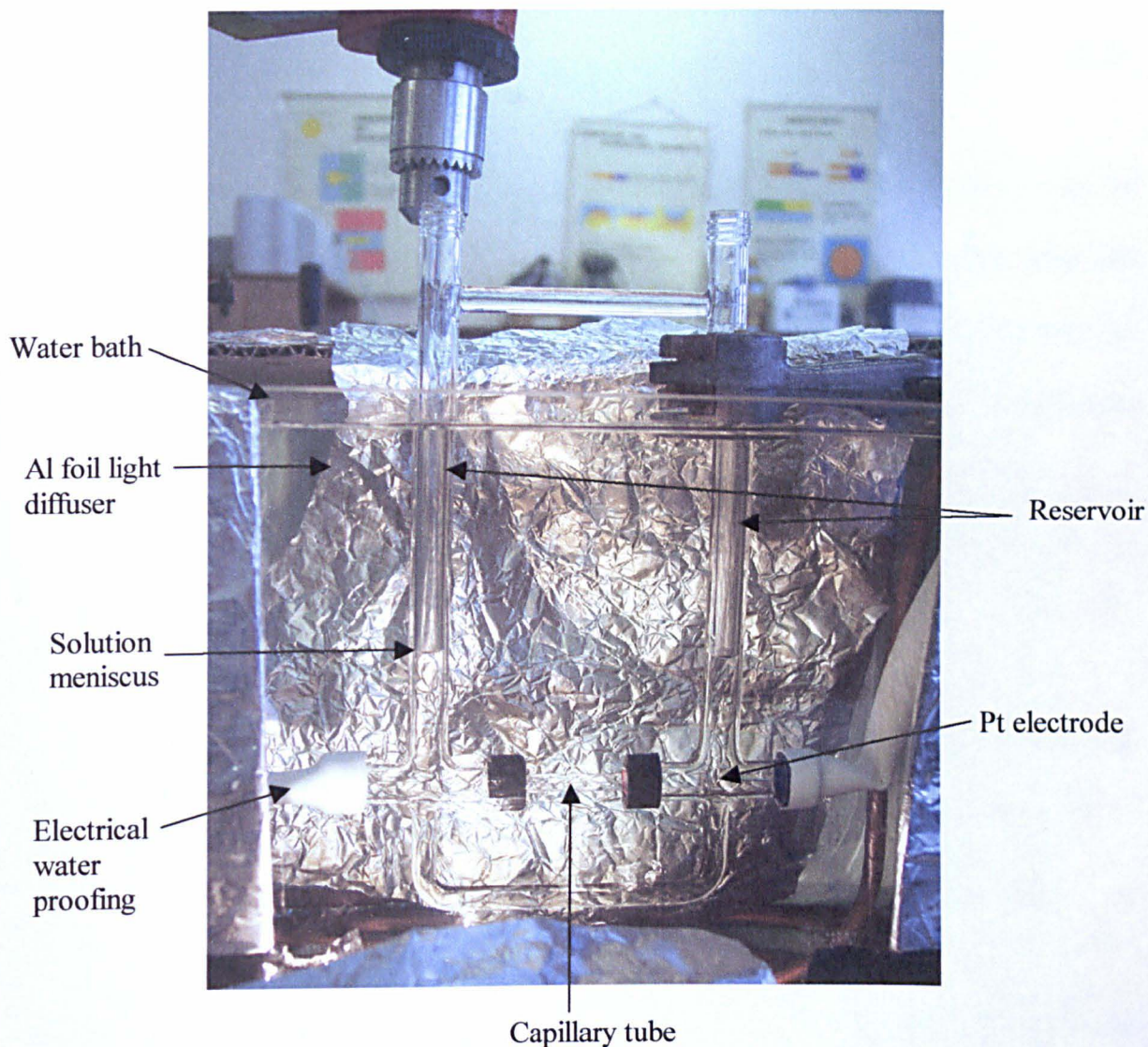
The actual U-tube (No 1) apparatus made by Hull University Glass Blowers is shown

Figure 4.1: Schematic representation of glass U-tube apparatus used to make preliminary flow rate measurements. The reservoirs are of equal cross-sectional area A_{res} and the liquid is sealed in by PTFE septa secured with screw on caps. EOF causes liquid flow from reservoir 2 to reservoir 1. A corresponding displacement in the liquid levels of $\pm \Delta h$ is observed in each reservoir from the equilibrium position.



in Figure 4.2. After cleaning the apparatus with alcoholic KOH (Section 2.1.6) and filling with an ultrasonically degassed solution of 0.1 mM KCl (aq), the U-tube was securely mounted in a water bath, which received circulating coolant at 25 ± 1 °C from a Thermo Haake open-bath circulator (C10-V15, Sigma-Aldrich, Dorset). The bath was stirred for about 10 min at a constant 300 rpm then switched off. After zeroing the cathetometer and waiting for about an additional 20 minutes, the reservoir liquid levels usually appeared fixed. When this condition was observed, 500 V was then applied to

Figure 4.2: Actual U-tube No 1 experimental set up. High voltage is delivered to electrodes via white waterproof plastic sleeving. Any leakage into these areas was minimal and electrical conduction insignificant, due to the pure water used ($0.8 \mu\text{S cm}^{-1}$ at $20.3 \text{ }^\circ\text{C}$) as the coolant. The aluminium foil helped illuminate the meniscus cap better and reduce glare.



the reservoir electrodes through wires located within the waterproof white plastic sleeving (Fig. 4.2). Both menisci positions were then recorded simultaneously as a function of time (outlined in Section 2.1.4). At the beginning and the end of the experiment, the bath temperature was noted and the average run temperature used in the modelling calculations.

4.2.2 Theory for flow rate modelling.

The electroosmotic flow rate F_{eof} of a liquid through a capillary tube of circular cross-section and internal radius r_{cap} is given by:

$$F_{eof} = \pi \cdot r_{cap}^2 \cdot \frac{E \varepsilon_0 \varepsilon_r \zeta}{\eta} \quad (4.1)$$

where r_{cap} is the radius of the capillary, E is the electric field strength, ε_0 is the permittivity of free space, ε_r is the relative permittivity of the solution filling the capillary, ζ is the capillary glass-solution interface zeta potential and η is the solution viscosity. The equivalent expression for pressure-driven flow F_{press} through a cylindrical capillary is derived from Poiseuille's equation (Eqn. 1.3, pg 26) and is given by:

$$F_{press} = \frac{\pi \Delta h_T \Delta \rho g r_{cap}^4}{8 \eta L} \quad (4.2)$$

where Δh_T is the combined reservoir liquid height difference between reservoirs (see Fig 4.1), $\Delta \rho$ is the density difference between air and the liquid, g is the acceleration due to gravity, η is the liquid viscosity, r_{cap} is the radius and L is the length of the capillary.

The total volumetric flow rate F_{total} is equal to the difference between the electroosmotic flow rate and the pressure-driven flow rate:

$$F_{total} = F_{eof} - F_{press} = \left(\frac{d\Delta h_1}{dt} \right) \cdot A_1 = \left(\frac{d\Delta h_2}{dt} \right) \cdot A_2 \quad (4.3)$$

where Δh_1 is the liquid level height above the equilibrium position in reservoir 1 of cross-sectional area A_1 and Δh_2 is the liquid level height below the equilibrium position

in reservoir 2 of cross-sectional area A_2 (Fig. 1.11, pg 47). Since liquid volume and mass is conserved, what flows out of reservoir 2 will flow into reservoir 1. Given that the measured internal radii of the U-tube apparatus are the same within the error (Table 2.4, pg 76), $A_{res} = A_1 = A_2$ and $\Delta h = \Delta h_1 = \Delta h_2$. This helps to simplify the modelling by eliminating unused variables as shown in Figure 4.1. Hence, given $\Delta h_T = 2\Delta h$, equation 4.3 can be recast:

$$\frac{d\Delta h}{dt} = \frac{E\varepsilon_o\varepsilon_r\zeta.A_{cap}}{\eta.A_{res}} - \frac{\pi.\Delta\rho.g.r_{cap}^4}{4.\eta.L.A_{res}} \Delta h \quad (4.4)$$

$\underbrace{\hspace{10em}}$
 X

$\underbrace{\hspace{10em}}$
 Y

where Δh is the change in liquid level height at any time for any given reservoir of cross-sectional area A_{res} (Fig. 4.1).

Integration of equation 4.4 yields an expression for the time t required for a given liquid level height change Δh to occur in a single reservoir, as shown in Appendix D:

$$t = -\frac{1}{Y} \ln(X - Y.\Delta h) + \frac{1}{Y} \ln X \quad (4.5)$$

Similarly

$$\Delta h = \Delta h_{max} [1 - \exp(-Yt)] \quad (4.6)$$

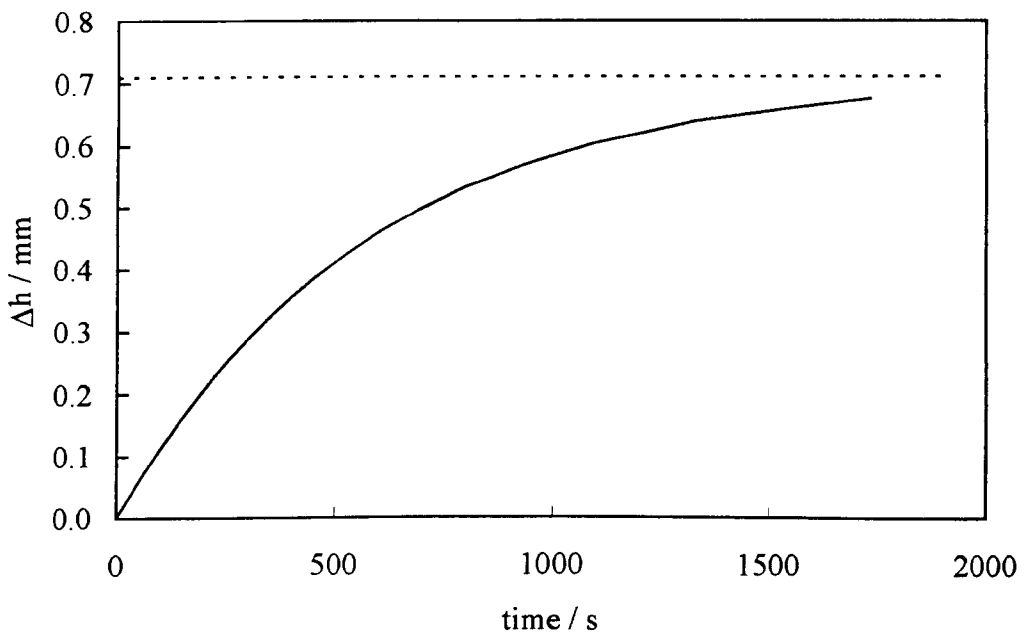
where $\Delta h_{max} = X / Y$ as given in Appendix E and represents the largest possible liquid level height change in a single reservoir achievable before electroosmotic and pressure-driven flows are balanced. Equations 4.5 and 4.6 were evaluated using a Microsoft

Excel worksheet and the parameter values listed in Table 4.1. The predicted liquid level height change for a single reservoir over time is represented in the height-time ($\Delta h-t$) graph shown in Figure 4.3.

Table 4.1: Parameter values used in model to predict Δh as a function of time.

The U-tube reservoirs both had an internal radius of 2.0 mm and were connected by a quartz capillary of internal radius $100 \pm 5 \mu\text{m}$ and length $50 \pm 1 \text{ mm}$.
500 V was applied across the platinum electrodes, set 10 cm apart in each reservoir.
All hydrodynamic and electrical resistances were predominantly across the capillary.
The liquid used was 1 mM NaCl (aq) solution at pH 6 with an assumed zeta potential of -80 mV as given by Jednacak and Pravdic [2]. The parameters ϵ_r , η and ρ are taken as for pure water at $25 \text{ }^\circ\text{C}$.
Other parameters included: $g = 9.81 \text{ N kg}^{-1}$ and $\epsilon_0 = 8.845 \times 10^{-12} \text{ F m}^{-1}$.

Figure 4.3: Theoretical liquid level height changes occurring in a reservoir containing a cathode and a solution fitting the above bullet pointed assumptions (solid line). Δh_{max} is represented by the dotted line.



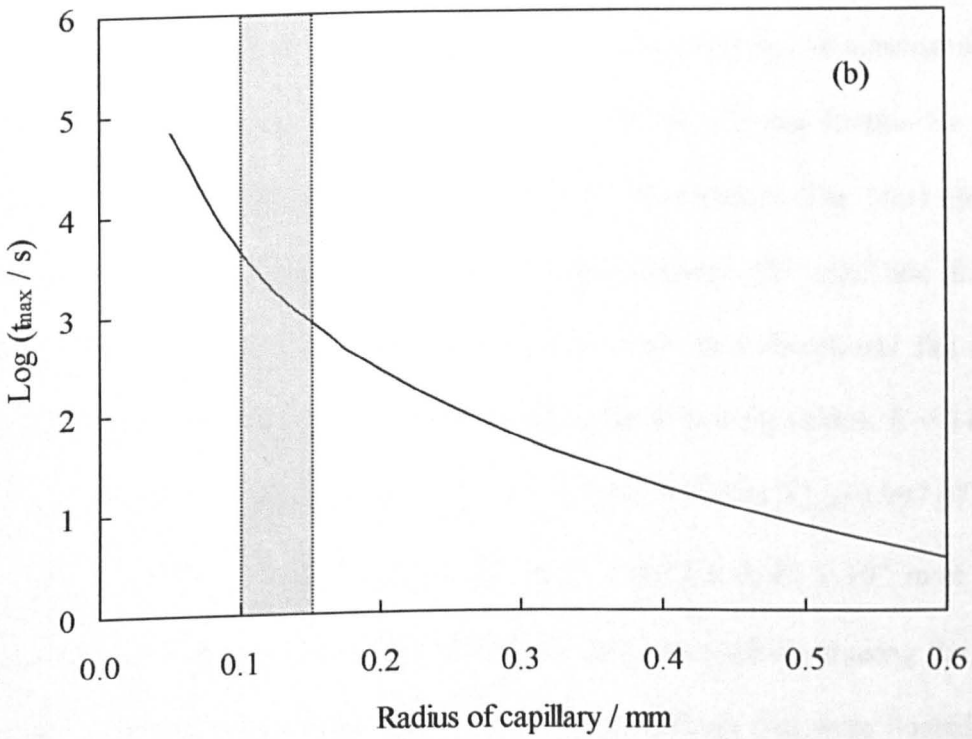
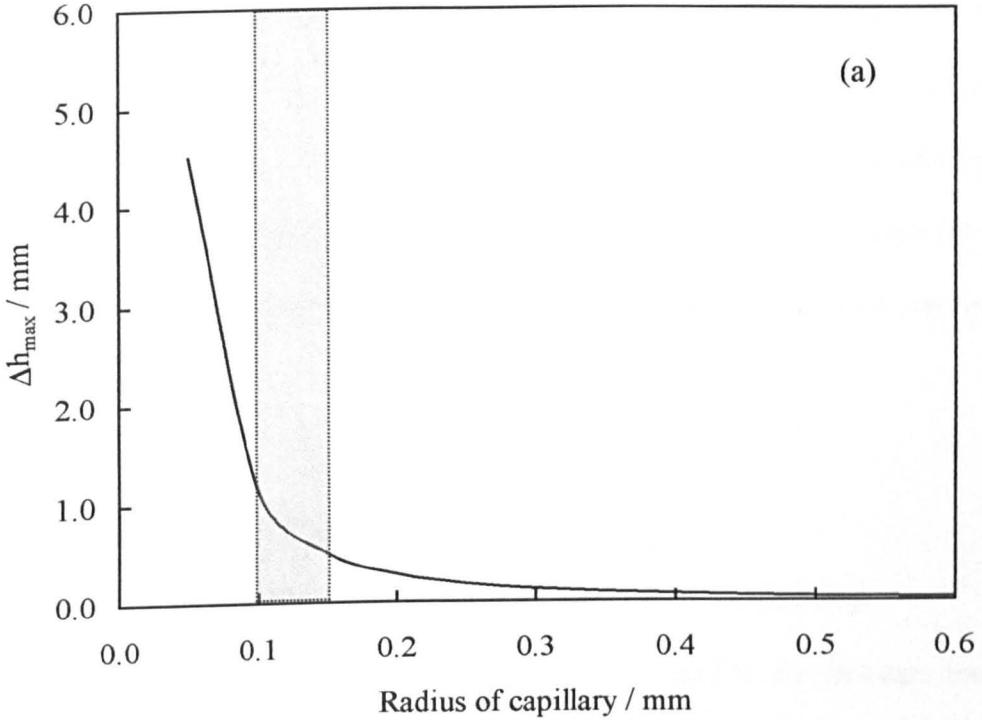
4.2.3 Optimum experimental conditions.

It was possible to interactively change individual variables and to study their theoretical effects on the $\Delta h-t$ graph. Varying the internal radius and length of the

capillary; the applied voltage and the solution conductivity in the model, showed that the experiment was feasible (i.e. conditions such that $\Delta h_{max} \gg$ error in Δh were achievable). The variable found to have the greatest effect on the $\Delta h-t$ graph was the capillary radius. The model outlined above was used to determine the optimum experimental conditions for the determination of e.g. zeta potential using flow rate measurements. It can be seen from Figure 4.4 that there is a trade off between Δh_{max} and the time required to reach this liquid level height change. With all the conditions as set out in Table 4.1, r_{cap} typically of 0.05 mm, gives a time t_{max} to reach Δh_{max} (4.51 mm) of approximately 70,000 s. At larger r_{cap} (0.4 mm), Δh_{max} reaches 0.07 mm in 17 s. This low value of Δh_{max} is rather small compared to the experimental error in measuring Δh (approx ± 0.04 mm). Clearly, somewhere in between these two extremes there is a radius that gives a reasonable Δh_{max} that is approached in a realistic time frame. For the conditions of Table 2.1, the best value of r_{cap} would be somewhere in between 100 – 150 μm .

Each meniscus in the two reservoirs of the U-tube apparatus has a Laplace pressure $P_{Laplace}$ associated with it (Eqn 1.17). This may give rise to Laplace pressure differences $\Delta P_{Laplace}$ across the capillary, and can be a significant source of uncertainty in the overall pressured difference and hence liquid levels and flow rates. As calculated by Fletcher *et al.* [3], for a cylindrical reservoir of radius 1 mm, filled with pure water having a surface tension of 72 mN m^{-1} and making a contact angle with the reservoir wall of zero degrees, the Laplace pressure is approximately 140 Pa. The magnitude of this Laplace pressure is equivalent to a reservoir filled with water to a height of 14 mm. Clearly, if Δh_{max} is no greater than 1 mm at the optimum experimental conditions, then the presence of unequal Laplace pressures could have a huge effect on the accuracy of

Figure 4.4: (a) Δh_{max} versus capillary radius and (b) time t_{max} take to reach Δh_{max} for a given capillary radius. The grey shaded areas on both graphs indicate the optimum predicted theoretical conditions for Δh_{max} and t_{max} , based on a capillary radius of 100 – 150 μm and the parameters listed in Table 4.1.



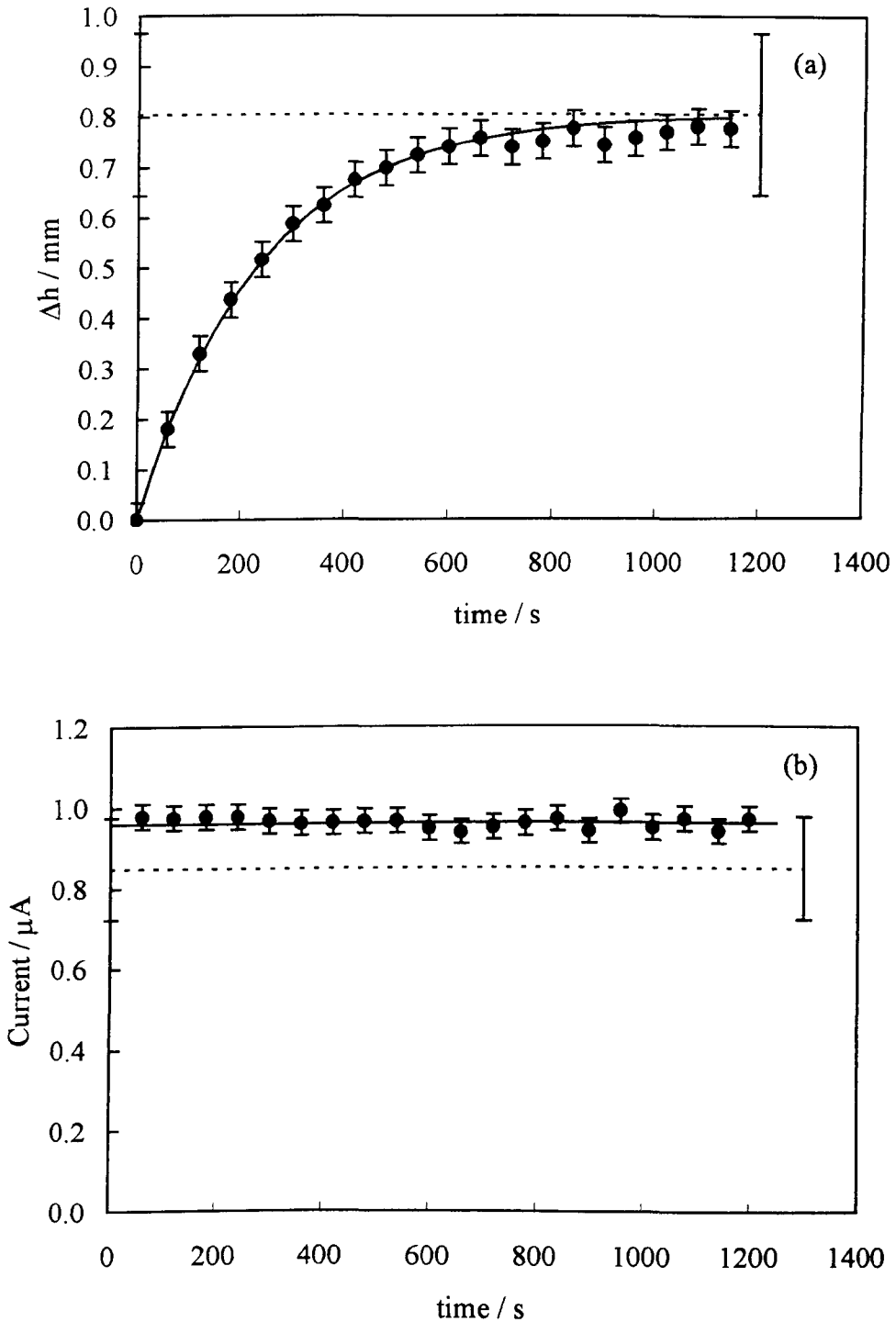
the recorded data. From Table 2.4 (pg. 76), the reservoir radii of each U-tube apparatus are essentially the same within the error of ± 0.02 mm. Given that two Laplace pressures are involved and that $P_{Laplace}$ is inversely proportional to the internal reservoir radius, the corresponding minimum calculated difference in Laplace pressure between the reservoirs is 0.8 Pa. This is equivalent to an estimated uncertainty in Δh of ± 40 μm , which is very similar to the expected uncertainty arising from the cathetometer in measuring two liquid levels. The series of different U-tubes listed in Table 2.4 (with a range of different internal radii) was made to test whether Laplace pressures presented problems.

4.3 Results and discussion.

4.3.1 Determination of zeta potential and specific surface conductivity.

The Excel model described in the last Section was used to fit $\Delta h-t$ data (collected using the cathetometer) and electrical currents (measured using a Thurlby-Thandar digital multimeter as described in Section 2.1.8) at 1 min intervals. An aqueous solution of 0.1 mM KCl (bulk conductivity $\kappa_o = 1.4889 \times 10^{-3} \text{ S m}^{-1}$) and U-tube No 1 with QZ1B quartz capillary was set up and used for this investigation. The filled circles in Figure 4.5 (a) show the measured liquid level height changes. The solid line in Figure 4.5 (a) and the solid line in Figure 4.5 (b) indicate the best theoretical fits for the experimental data sets. They were calculated using the following values: $E = 11820 \text{ V m}^{-1}$, $\epsilon_r = 78.304$ [4], $\epsilon_o = 8.854 \times 10^{-12} \text{ F m}^{-1}$, $\eta = 8.93 \times 10^{-4} \text{ Pa s}$ [4], $\rho = 997.07 \text{ kg m}^{-3}$ [4], $g = 9.81 \text{ m s}^{-2}$, $r_{cap} = 1.24 \pm 0.06 \times 10^{-4} \text{ m}$, $L = 4.23 \pm 0.002 \times 10^{-2} \text{ m}$ at 25 °C. Fitting of the theory lines to the experimental data sets was performed using the Solver function in Excel by minimise residuals. The only parameters that were floated in the model were zeta potential ζ and specific surface conductivity κ_s . The $\Delta h-t$ data were

Figure 4.5: (a) Plot Δh as a function of time (Δh - t graph). Filled circles represent experimental data collected using U-tube No 1 with QZ1B quartz capillary and 0.1 mM KCl (aq) at 500V. The solid line is the theoretical best-fit which gives a $\zeta = -87.7$ mV. The dotted line is Δh_{max} with a $\pm 20\%$ uncertainty. (b) I - t graph. Filled circles represent measured electrical currents flowing through the cylindrical capillary. Solid line is calculated total current I_{total} and the dotted line calculated I_{eof} . This gives a best-fit $\kappa_s = 12$ nS. For a further description of Figure 4.5, see main body of text.



used to calculate ζ and the current-time data was used to calculate κ_s . The best-fit values were $\zeta = -87.7$ mV and $\kappa_s = 12$ nS at 25 ± 1 °C.

Best-fit values of ζ and κ_s appear reasonable and within the range of reported literature values as described in Table 1.6 for 0.1 mM KCl (aq)-glass interface. Arulanandam and Li [5] reported $\zeta = -140$ mV and $\kappa_s = 20 - 70$ nS for 0.1 mM KCl (aq) for a range of glass capillaries with an internal radius between 50 and 100 μm . Johnson [6] reported $\zeta = -54$ mV for quartz sand grains in 0.1 mM KCl (aq).

The uncertainty in Δh shown by the ± 40 μm error bars in Figure 4.5 (a), gives an uncertainty of ± 10 % in the zeta potential which is better represented as -90 ± 9 mV, rather than -87.7 mV. As pointed out by Gu and Li [7], zeta potentials can be significantly underestimated by up to one order of magnitude if specific surface conductivity is not taken into account. The electrical current represented by the dotted line in Figure 4.5 (b) is the calculated electroosmotic current (i.e. current flowing through the liquid bulk). The total current I_{total} (represented by the solid line) is the sum of electroosmotic I_{eof} and surface I_{surf} current. The magnitude of I_{surf} is estimated by the fitting procedure. Using equation 1.15 (pg 40) and $I_{eof} = 0.85$ μA (Fig. 4.5 b) the electroosmotic volumetric flow rate was calculated to be 58 nl s^{-1} . The estimated uncertainty in the measured current shown in Figure 4.5 (b) is ± 0.03 μA for a 96 % confidence limit and that in I_{eof} is ± 15 %. The estimated uncertainty in I_{surf} is ± 120 % and hence is represented in the best-fit κ_s value as 12 ± 14 nS.

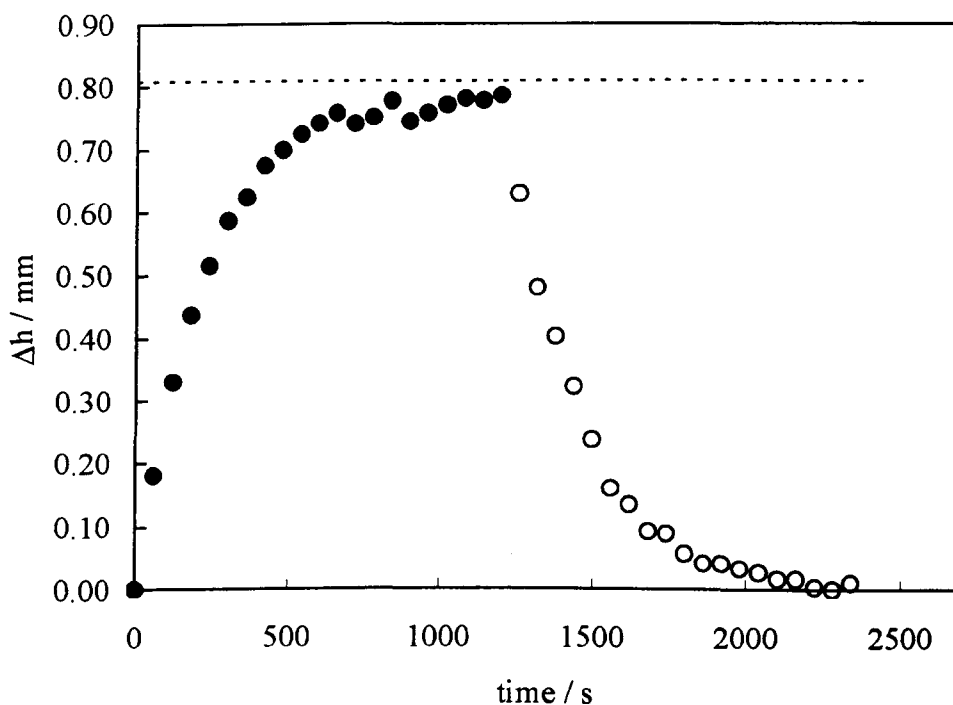
4.3.2 Steps in quality assurance for recorded data.

The accuracy and quality of recorded $\Delta h-t$ data must meet certain basic requirements before a data analysis procedure could be used to draw any meaningful conclusions.

These criteria are:

- The reservoir liquid meniscus should return to the starting point after a run (i.e. zero leakage).
- No precipitate should form in the electrode compartments during a run.
- The Δh values and electrical currents should not change erratically i.e. the electrical current must remain approximately constant during a run.
- The meniscus cap shapes in each reservoir should remain symmetrical and no contact angle pinning should occur throughout the run.

Figure 4.6: Full $\Delta h-t$ data set for Figure 4.5 (a). The filled circles indicate the cathode reservoir started filling when 500 V was applied to the electrodes. The open circles show the reservoir started emptying after the voltage was removed. The dotted line represents Δh_{max} .



Reservoir liquid levels return to their starting point

It was very important to establish that the change in liquid meniscus position brought about when a voltage was applied to the electrodes, actually returned to its starting point when the voltage was removed. This ensured that liquid mass and volume were conserved (i.e. zero leakage). Consider Figure 4.6, when 500 V was applied across the electrodes the cathode reservoir liquid level could be seen to rise. After the potential was removed at 1200 s, the liquid level decayed to the starting point at $\Delta h = 0$. Sometimes this did not happen and contact angle pinning fixed the liquid levels. In order to rule out contact angle pinning, it was necessary to continue recording data for at least the same amount of time as the voltage was initially applied. In the case of Figure 4.6, this was a further 1200 s. If this did not happen then the experiment was a null result.

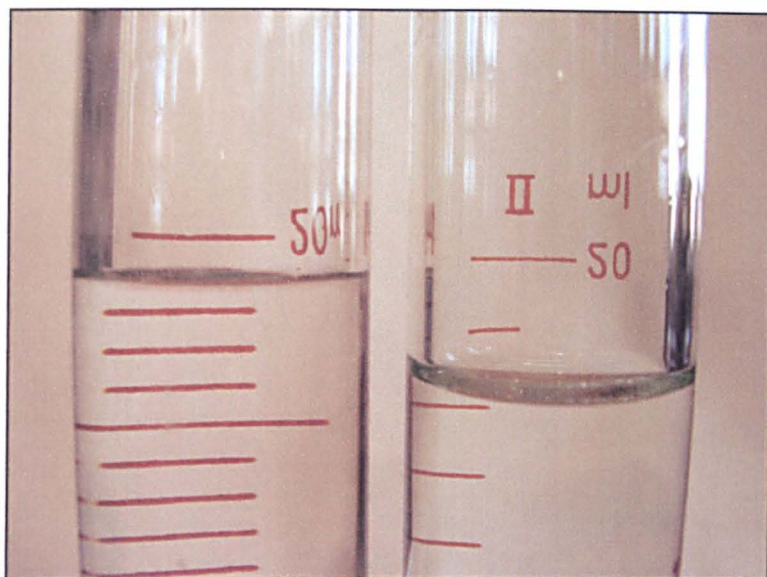
Precipitate formation and smooth changes in Δh and I_{total}

The production of any form of precipitate in the U-tube resulting from electrolysis could consistently give erroneous data if the source was not isolated. A clean experiment was one characterised by an almost constant electrical current and smooth changes in Δh over time. It was found that electrical current was a sensitive indicator for system disturbance. Gas pockets that were sometimes formed or migrated into the capillary could abruptly cut off the electrical current. If gas evolution was produced at the electrode surfaces in any significant quantity, varying and sometimes erratic currents could often be noted.

Symmetrical menisci and contact angle pinning

Since Laplace pressures can result in significant errors, it is also important to monitor them in some way throughout a run. The series of U-tube apparatus used for the flow

Figure 4.7: Meniscus shapes for dirty (left hand picture) and clean (right hand picture) glass reservoirs filled with 0.1 mM KCl (aq). The right hand reservoir was cleaned with a 5 min soak in alcoholic KOH and rinsing with pure water.



rate measurements were designed to have nearly matching internal radii reservoirs, so Laplace pressure differences could be minimised as far as possible. In addition, this was also achieved using the cleaning regimes outlined in Section 2.1.6. An example of a clean and a dirty reservoir can be seen in Figure 4.7. The dirty reservoir is characterised by the contact angle pinning, whereas the clean reservoir (alcoholic KOH) shows a symmetrical meniscus cap shape. Clean reservoirs such as the one on the right of Figure 4.7 with a symmetrical liquid meniscus shape helped reduce the possibility of Laplace pressures producing significant errors in ζ , κ_s and F_{eof} . Checking the meniscus shapes three or four times throughout each run with the cathetometer to measure the depth of the meniscus cap, was seen as a good safe guard against this possible error. It is estimated that there was about a 40 % net rejection of data resulting from the QA screening outlined in this Section.

4.3.3 Flow rate reproducibility.

To test the reproducibility of flow rate measurements made with a fresh solution, four separate runs (runs 2 to 5, Table 4.1) were recorded using the U-tube No 2 fitted with the QZ1B capillary. Before each run, the U-tube, chosen capillary and Pt electrodes were all given a 5 min soak in alcoholic KOH and then flushed with pure water (Section 2.1.6). The apparatus was then set up with all seals secured and filled from a stock solution of 0.1 mM aqueous KCl ($\kappa_o = 1.4889 \times 10^{-3} \text{ S m}^{-1}$). The fitted values of ζ and κ_s are summarised in Table 4.2. For all runs, including the original (run 1) given in Figure 4.5, it can be seen that the zeta potential values for 0.1 mM KCl (aq) and the quartz capillary QZ1B are adequately described by $-90 \pm 9 \text{ mV}$ (specified earlier). This demonstrates reproducibility in zeta potential of $\pm 10 \%$ for runs made using both U-tubes No 1 and No 2 with a new solution for each run. The specific surface conductivity values cover large range from 12 to 60 nS (i.e. about one order of magnitude of κ_s). Values currently available within the literature for 0.01 mM KCl (aq)-pure water cover approximately two orders of magnitude [8].

Table 4.2: List of runs made at an average temperature of 25.4 °C under identical experimental conditions (specified above) using new refill of 0.1 mM KCl from the aqueous stock solution for each measurement and Pt wire electrodes. The recorded $\Delta h-t$ and $I-t$ data sets were used to calculate best-fit values for ζ , κ_s . These were then used to find I_{eof} and hence F_{eof} .

Run	ζ / mV	κ_s / nS	I_{eof} / μm	F_{eof} / nl s ⁻¹	Electrode voltage / V	U-tube No
1	- 87.7	12	0.85	58	500	1
2	- 88.0	60	0.43	20	250	2
3	- 96.9	5	0.85	43	500	2
4	- 84.9	10	0.85	38	500	2
5	- 84.1	40	0.85	37	500	2

From Table 4.2, it can be seen that $F_{eof} \propto V$. As the electrode voltage doubles from

250 V (run 2) to 500 V (run 3), I_{eof} (Eqn 1.12) doubles and hence so does F_{eof} from approximately 20 to 40 nl s⁻¹. The simple capillary-electrode arrangement of the U-tube apparatus behaves as a DC circuit and obeys Ohm's law. As the electrode voltage is increased from 250 to 500 V in going from run 2 to 3, the total current approximately doubles from 0.7 to 1.2 μ A i.e. $I_{total} \propto V$.

To test the reproducibility of flow rate measurements made with the same solution, the clean U-tube No 1 was assembled and filled with an aqueous solution of 0.1 mM NaCl. Measurements were made at 500 V with the soldered Pt electrodes (Fig. 4.8) and the QZ1B capillary. The height changes for the initial run are indicated by the open circles in Figure 4.9. The calculated zeta potential for this first run was noted to be - 80 mV. Upon reversing the polarity and restarting the experiment (after the liquid levels had returned to their equilibrium position), the observed Δh values were much

Figure 4.8: 0.75 mm Pt electrodes used in the U-tube apparatus. The coiled wire electrode on the left gave reproducible data, whereas the soldered electrode on the right did not. The source of the irreproducibility was found to lie in the tin and lead ions migrating out of the solder.

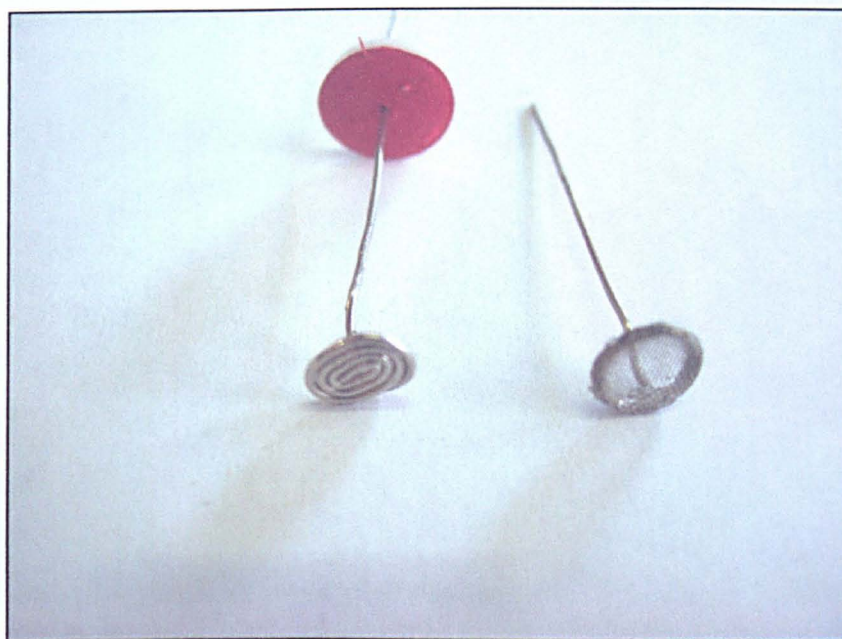


Figure 4.9: Two consecutive runs made using same solution of 0.1 mM NaCl (aq). The initial run (open circles) had a best-fit zeta potential of -80 mV. The second run under the same conditions of 500 V applied to the soldered Pt electrodes gave irreproducible results (filled circles) with a best-fit $\zeta = -185$ mV. A precipitate was seen to form during the second run.

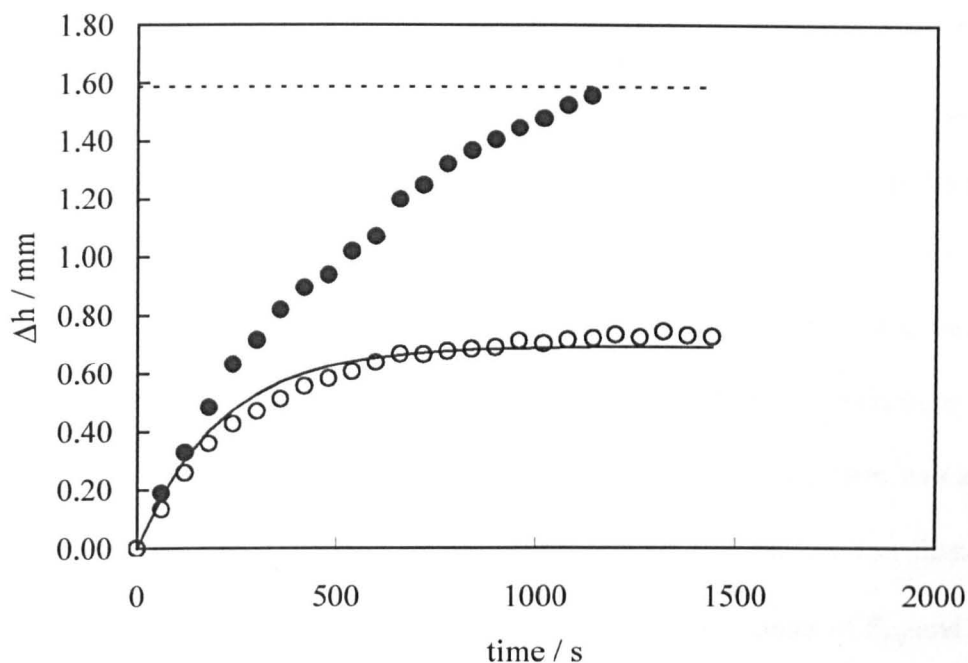
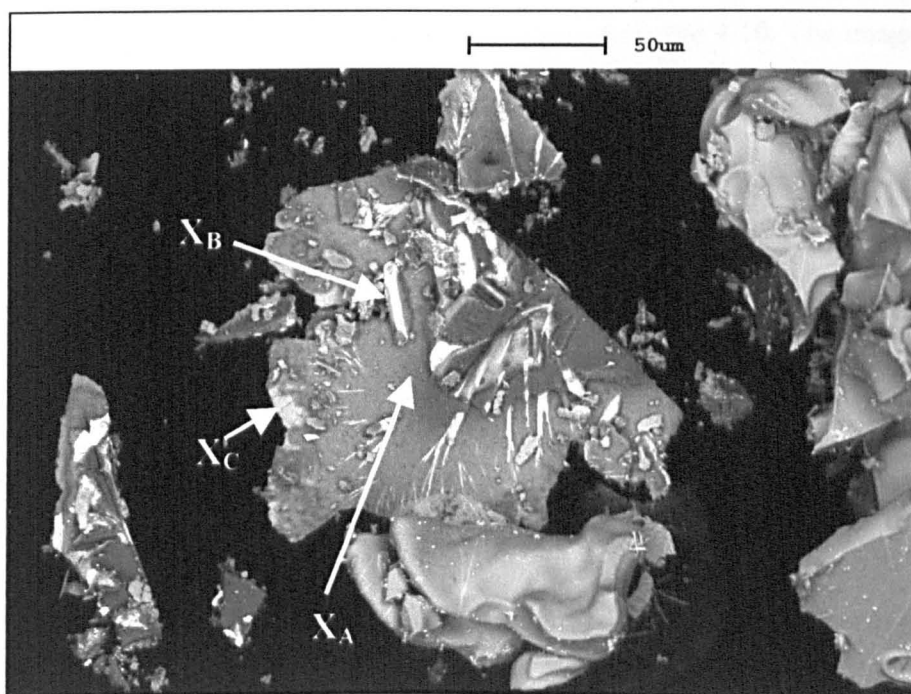


Figure 4.10: Scanning Electron Micrograph of evaporite grain formed in the electrode compartments of the U-tube, which was run overnight with 0.1 mM NaCl (aq) solution. Brighter areas indicate elements of higher atomic number. X_A is mostly NaCl, X_B is $PbCl_2$ with some Sn and X_C is $SnCl_2$.



greater than the first run. Later into the experiment a clouding of the electrode compartments was noticed. The filled circles in Figure 4.9 indicating the liquid level height changes for the second run, can be seen not to converge to Δh_{max} at approximately 1.6 mm. The best-fit zeta potential of -185 mV is clearly far higher than what would be expected and is in error for the NaCl solution outlined. Several repeat measurements using new fills of the 0.1 mM NaCl stock solution gave similar results.

An overnight run confirmed a precipitate had indeed formed and this could be clearly seen. This case serves as an example of how sensitive the flow rate technique was to changes in zeta potential. Well before the precipitate could be seen, there was a much greater $d\Delta h / dt$ for the first few Δh measurements of the second run than when compared to the first. This is indicative of a system with higher values of F_{eof} and ζ . The solution from the overnight run was evaporated in an oven for 24 hrs and the dry sample sent for Scanning Electron Microscopic analysis. Figure 4.10 shows the source of the irreproducibility. The electron micrograph of a single evaporite grain (mineral residue left over after evaporation) can be seen at the centre of Figure 4.10. The image shown is displayed in so-called 3D atomic number contrast mode. Lighter shades of grey (i.e. toward white), indicate elements of increasing atomic number. By using back-scattered X-ray data collected with the electron microscope, it was possible to perform pinpoint analysis of individual areas on the precipitate grain. The dark grey area marked X_A is mostly sodium chloride. X_B the lighter spot is mainly lead chloride with some tin and X_C is tin chloride. From this absolute method of analysis, it was certain that the precipitate was forming because of tin and lead ions, which were leaching from the soldered Pt electrodes. Cooler Pb soldering was chosen to secure the Pt mesh to the Pt wire frame, because hotter silver soldering was not possible on such a fragile structure.

The soldered Pt electrodes were replaced by the coiled Pt wire electrodes shown in Figure 4.8. U-tube No 1 was set up using these new wire electrodes and capillary QZ1B with a single filling of 0.1 mM KCl (aq) from the stock solution ($\kappa_0 = 1.4889 \times 10^{-3} \text{ S m}^{-1}$). The results for repeat flow measurements made using the same potassium chloride solution without change are shown in Table 4.3. The best-fit values of ζ , κ_s and F_{eof} were calculated in the same way as for Figure 4.5 using the published values for the physical properties of water at 25 °C. On initial inspection, the zeta potential seems to decrease with increasing run number, suggesting that the reproducibility is degrading the more the solution is used. This may arise from changes in the solution composition brought about by sequential electrolysis of impurities retained in the chemical compounds. Although this offers a possible explanation, the real cause remains largely unknown and requires further investigation. The average zeta potential for these three runs is $-74 \pm 7 \text{ mV}$ and the specific surface conductivity varies from 60 to 250 nS.

Table 4.3: List of three consecutive runs made under identical conditions (specified in text as for Fig 4.5) with the same solution of 0.1 mM KCl (aq) and Pt wire electrodes. The recorded $\Delta h-t$ and $I-t$ data sets were used to calculate best-fit values for ζ , κ_s and F_{eof} .

Run	ζ / mV	κ_s / nS	I_{eof} / μm	F_{eof} / nl s ⁻¹	Electrode voltage / V	U-tube No
Initial	-79.0	250	0.43	17.5	250	1
Repeat 1	-74.3	60	0.43	16.5	250	1
Repeat 2	-68.5	130	0.43	15.1	250	1

A statistical summary of ζ , κ_s and F_{eof} listed in Tables 4.2 and 4.3 is given in Table 4.4. For the limited sample sizes, it is difficult to draw any meaningful conclusions about the differences in reproducibility for runs made with a new solution and runs made consecutively with the same solution. Both ζ and F_{eof} have an estimated error of $\pm 10 \%$ (1 s.f.) and κ_s about an order of magnitude ($\pm 100 \%$). Using a new solution for

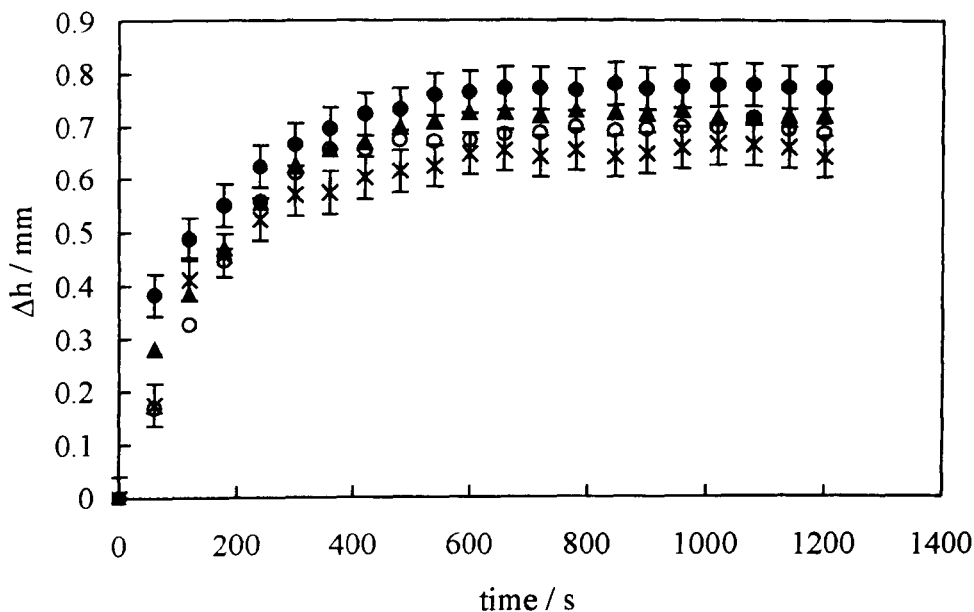
each run apparently produces a slightly higher zeta potential than that obtained when using the same solution for consecutive runs.

Table 4.4: Statistical summary of the average zeta potential, average specific surface conductivity and average electroosmotic volumetric flow rates for runs 2 – 5, Table 4.2 and all runs in Table 4.3.

Parameter	Table 4.1, runs 2 – 5	% error	Table 4.2, all runs	% error
ζ / mV	-89 ± 9	± 10	-74 ± 5	± 10
κ_s / nS	23 ± 20	± 70	155 ± 90	60
$F_{eof} / \text{nl s}^{-1}$	39 ± 4	± 10	16 ± 2	± 10

For a number of years certain analytical instruments such as capillary electrophoresis (CE) devices have relied on reproducible electroosmotic flow rates to perform routine chemical separations to a commercial standard. The surface conditioning and the methods used to clean the fused silica capillary separating columns have been seen as the key to this. Lauer and McManigill [9] first suggested washing the columns with a base such as 0.1 M KOH (aq). In conducting capillary zone electrophoresis (CZE) experiments using a cleaning method involving pre-soaking with 1 M KCl (aq) and flushing with water and running buffer, they found a day to day variation of less than 4 % in retention times. This cleaning method was said to: reduced the deleterious effects of capillary “ageing,” which can result in changes to the sample-wall interactions. As small neutral sample molecules do not have a tendency to interact with the capillary wall, washing between each injection is not usually necessary [10]. It was found that other publishing researchers also used similar CE and CZE column cleaning procedures. Culbertson and Jorgenson [11] pre-conditioned before runs by flushing at 20 bar for 1 hr with 75 % 1 M NaOH / 25 % methanol followed by a 1 hr flush with running buffer. Regnier *et al.* [12, 13] preferred using 1 M NaOH (aq) for 10 min followed by rinsing with buffer for a further 10 min prior to use.

Figure 4.11: Δh - t plots for different cleaning methods made in U-tube No 1 with 0.1 mM KCl (aq) at 500V using Pt wire electrodes. The filled circles represent alcoholic KOH cleaning for QZ1B capillary and the open circles alcoholic KOH cleaning for BORO1 capillary. The filled triangles and crosses represent 5M KOH (aq) for QZ1B and BORO1 capillaries respectively.



To test how cleaning technique and capillary material affected flow rate reproducibility, a simple experiment was devised. It was proposed that Δh - t data would be recorded in the U-tube No 1 for separate experiments using first the quartz capillary, QZ1B and then the borosilicate capillary, BORO1. The choice of these two capillaries was based on the need to have two capillaries made from slightly different glass types, but with a similar internal radius. This would ensure that each give an almost identical theoretical Δh_{max} values for the same aqueous 0.1 mM KCl solution. It was set as a requirement that if one cleaning method was superior to another, then the superior cleaner should demonstrate a higher electroosmotic flow rate and final Δh_{max} than all others. With this requirement, it was considered unnecessary to fit each individual data set and assign a zeta potential. Simple inspection of the Δh - t data should be enough to observe any superior cleaning method. The chosen cleaning procedures that were

compared were 2 M KOH in pure ethanol (i.e. alcoholic KOH described in Section 2.1.6) against aqueous 5 M KOH. U-tube No 1 and each capillary was prepared for use by giving them a 5 min flushing, with first the cleaner, and then with pure water.

It can be seen from Figure 4.11 that the filled circles and filled triangles representing the alcoholic KOH cleaning of the quartz and borosilicate capillaries lie outside the ± 40 μm error bars assigned to the filled circles. The same can also be said for the 5 M KOH (aq) cleaning method. Due to the limited data sets for each cleaning procedure, only limited deductions can be derived about the observed trends and no statistical data about the reproducibility. One such deduction is that the higher flow rates seem to be produced with alcoholic KOH cleaning than for 5 M KOH (aq). It is also appears that the quartz capillary produced a higher zeta potential and greater electroosmotic flow rate than the borosilicate capillary did. It should be remembered, this is a very limited data set and many more repeat measurements are required to make conclusions with confidence. Jednacak and Pravdic [2] reported for 1 mM NaCl (aq) at pH 6, that a zeta potential of -137 mV was noted for a quartz capillary containing 50 ppm Al_2O_3 and -127 mV for a borosilicate glass capillary. This slight difference in reported zeta potentials between the two glass types gives some credibility towards the data in Figure 4.11.

4.4 Summary.

In this Chapter, a simple model was derived which accurately predicted the combined effects of electroosmotic and pressure-driven flows through a cylindrical glass capillary. Data about the flowing liquid was measured by noting the liquid level height changes in a reservoir over time. This $\Delta h-t$ data along with electrical current

information was used to characterise the flow properties of solutions by assigning best-fit values to ζ and κ_s . The model was then verified with a test solution of 0.1 mM KCl (aq). It was found that this solution could be used repeatedly without renewing for at least three runs. Theoretical predictions and recorded experimental data were in good agreement. A variation in run-to-run repeatability of less than 10 % was found for ζ and F_{eof} . The repeatability of κ_s , as expected, was poor with values spread over about one order of magnitude of κ_s .

Laplace pressures were considered a potential and significant source of error in Δh . In practice, they actually never really presented much of a problem due to the high standards of cleaning equipment and data quality control. It was identified for a limited data set that the best cleaning compound was alcoholic KOH. This produced slightly higher electroosmotic flow rates than 5 M KOH (aq) for both quartz and borosilicate glass capillaries. The $\Delta h-t$ data sets also suggested that the quartz glass capillary had a higher zeta potential than the borosilicate glass capillary for the same cleaning method and 0.1 mM KCl (aq) solution.

The method presented here for characterising the flow properties of 0.1 mM KCl (aq) solution through ζ and κ_s , has been adequately demonstrated and can be effectively adapted for use in microreactors with a few minor modifications. This will then enable on-chip characterisation measurements to be made of a wide range of solvents of interest.

4.5 References.

- [1] P. D. Christensen, S. W. P. Johnson, T. McCreedy, V. Skelton & N. G. Wilson, *Chem. Commun.*, 1998, 35, 341. *Reports first use in Hull group of silica as a hydrodynamic restriction.*
- [2] J. Jednacak & V Pravdic, *J. Colloid Interface Sci.*, 1974, 49, 16.
- [3] P. D. I. Fletcher, S. J. Haswell & V. N. Paunov, *Analyst*, 1999, 124, 1273.
- [4] J. Timmermans, *Physico-Chemical Constants of Pure Organic Compounds*, vol. 1 (1950) and vol. 2 (1965) Elsevier, New York.
- [5] S. Arulanandam & D. Li, *J. Colloid Interface Sci.*, 2000, 225, 421.
- [6] P. R. Johnson, *J. Colloid Interface Sci.*, 1999, 209, 264.
- [7] Y. Gu & D. Li, *J. Colloid Interface Sci.*, 2000, 226, 328.
- [8] J. Th. G. Overbeek, *in Colloid Science*, Ed. H. R. Kruyt (1952) Elsevier, Amsterdam, Vol. 1, Ch. V, Table 6, p236.
- [9] H. Lauer & D. McManigill, *Anal. Chem.*, 1986, 58, 166.
- [10] M. J. Sepaniak, A. Craig Powell, D. F. Swaile & R. O. Cole, *Capillary Electrophoresis Theory and Practice*, Ed. P. D. Grossman & J. C. Colburn (1992) Academic Press, London, p176.
- [11] C. T. Culbertson & J. W. Jorgenson, *Anal. Chem.*, 1994, 66, 955.
- [12] B. J. Harmon, D. H. Patterson & F. E. Regnier, *Anal. Chem.*, 1993, 65, 2662.
- [13] B. J. Harmon, I. Leesong & F. E. Regnier, *Anal. Chem.*, 1994, 66, 3797.

5. PURE ELECTROOSMOTIC FLOW IN CHANNEL NETWORKS.

5.1 Introduction: *Flow rate measurements on-chip.*

The aim of the work outlined here was to characterize the microfluidic flow properties of solvents of interest within microreactors (i.e. on-chip). It was considered that the model outlined in Chapter 4 should be developed and be able to:

- Predict the voltage and current characteristics of solvents systems of interest within microreactor channel networks, using the 3D channel network information, the bulk solution conductivity and assigned specific surface conductivity.
- Predict the electroosmotic flow rates of solvents systems of interest using electrical current information and assigned zeta potential.

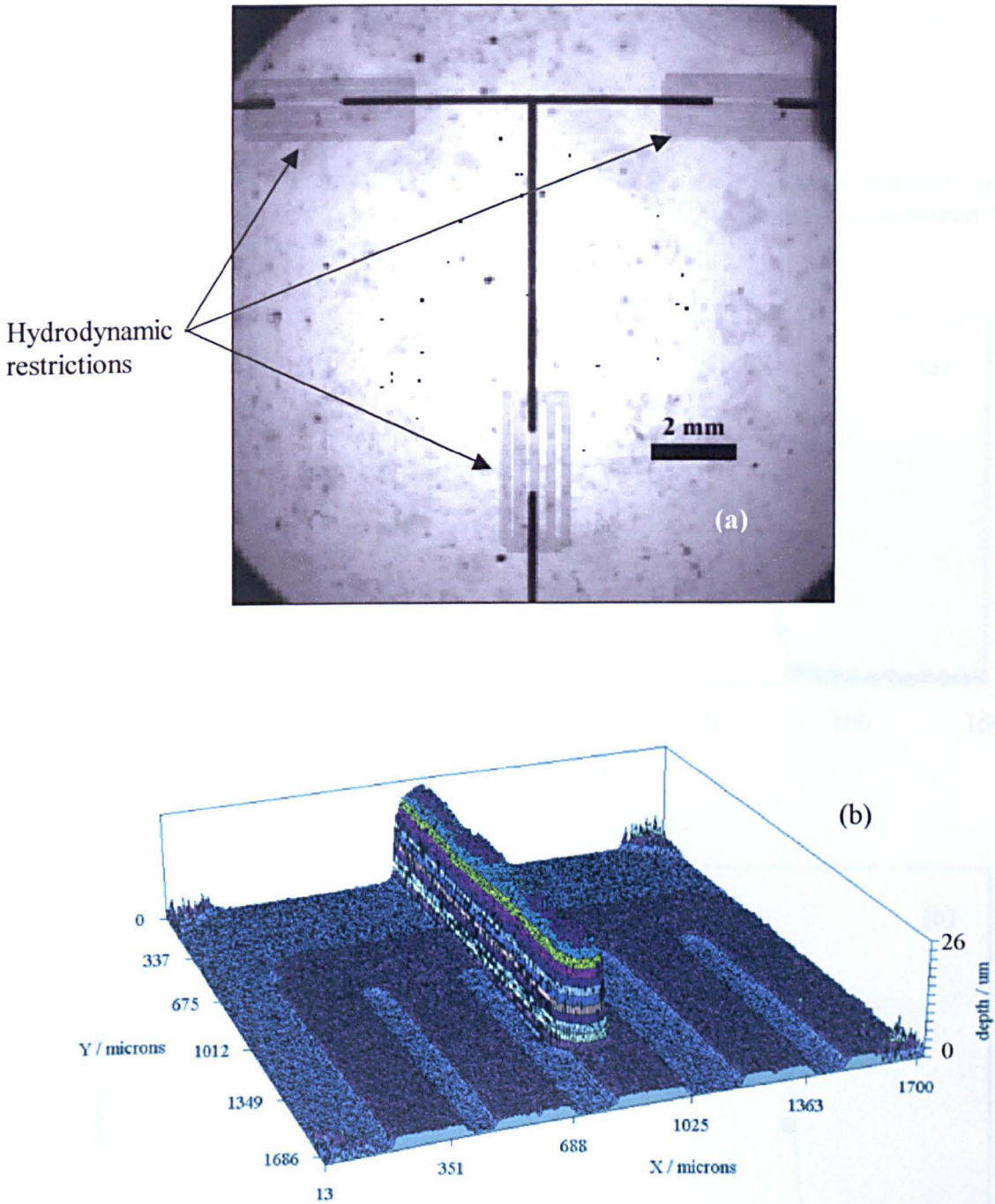
Success and validation of this revised model would then enable the microreactor user to be able to either dial up a voltage on a computer screen and obtain a accurate electroosmotic flow rate within a desired channel section or dial up an electroosmotic flow rate and have the computer automatically compute the voltage settings required.

5.2 Apparatus and theory.

5.2.1 *Microreactor dimensions and reservoir arrangement.*

The Chip 004, used for our investigations, was etched according to procedure 4 in Table 2.1 and bonded according to procedure 3 in Table 2.2. The two-stage bonding was necessary because the chip contained a series of hydrodynamic restrictions etched into a middle plate. The hydrodynamic restrictions were incorporated into this chip to directly control the pressure-driven flow component of the total flow within the channel

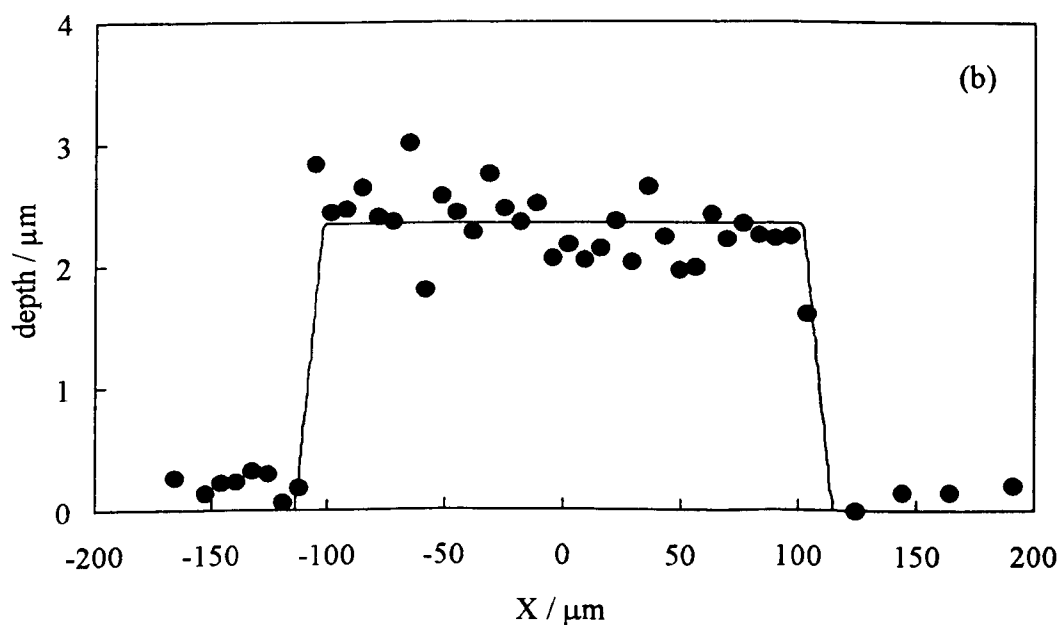
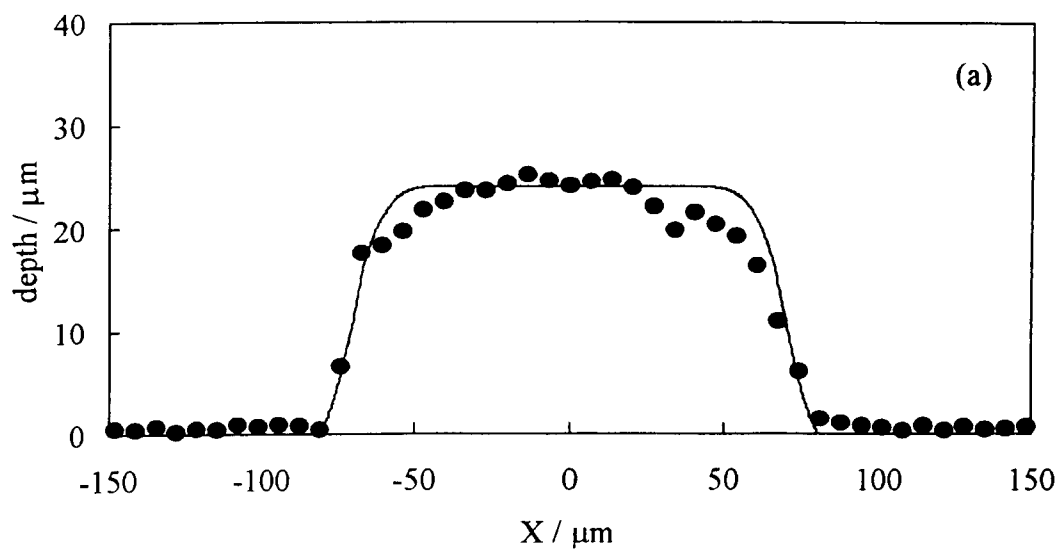
Figure 5.1: (a) Optical micrograph of chip 004 made with a 1.25X objective on the Axiovert S100 inverted microscope. (b) 3D depth profile made of a hydrodynamic restriction that was used to suppress pressure-driven flow in each channel section of chip 004. The depth colour coding represents $2\ \mu\text{m}$ per division.



network and therefore, allow reproducible and predictable EOF. An optical micrograph of the channel network layout of chip 004 can be seen in Figure 5.1 (a). From the

micrograph the hydrodynamic restrictions can be seen to consist of a grid containing a number of fine parallel channels. A 3D profile of a hydrodynamic restriction as determined by absorbance imaging is shown in Figure 5.1 (b). The plots shown in Figures 5.2 (a) and (b) typify cross-sectional profiles for the large central channel and the series of smaller hydrodynamic channels.

Figure 5.2: Cross-sectional profiles for chip 004 in region of large channel (a) and smaller channel (b). In each case the solid line shows the calculated best-fit to the isotropic etch model.



From Figure 3.16 it can be recalled that the cross-sectional shape for thermally bonded channels was defined in terms of the apparent mask line width m , channel depth d and smoothing length δ . The calculated best-fit values of m , d and δ according to the smoothed isotropic etch model for the large channel (Fig 5.2 a) are $m = 100 \pm 10 \mu\text{m}$, $d = 24 \pm 2 \mu\text{m}$ and $\delta = 13 \mu\text{m}$ and for the hydrodynamic resistance channels $m = 210 \pm 20 \mu\text{m}$, $d = 2.4 \pm 0.2 \mu\text{m}$ and $\delta = 11 \mu\text{m}$ respectively. These best-fit values indicate that there has been little distortion of the channels due to thermal bonding of chip 004.

The extended glass reservoir sets 1 – 3, listed in Table 2.5, were mounted into the top block of chip 004 by gluing using the procedures outlined in Section 2.1.4. Voltages were applied to the microreactor channel network via platinum wire electrodes mounted through the extended reservoirs. Voltage and current measurements were made using a Thurlby-Thandar 1906 digital multimeter with the Paragon computer controlled power supply as described in Section 2.1.8.

5.2.2 Theory for microreactor current-voltage characteristics.

For an isotropically etched microreactor channel of mask line width m and depth d the cross-sectional area A of the channel is given by:

$$A = (md) + \frac{\pi d^2}{2} \quad (5.1)$$

For a channel of length L , cross-sectional area A that is filled with a liquid of bulk conductivity κ_o , the electrical resistance of the bulk liquid R_{bulk} is:

$$R_{bulk} = \frac{L}{\kappa_o A} \quad (5.2)$$

For channels in which the ratio of surface area to volume is relatively high and the conductivity of the liquid is low, the surface conductivity of the channel wall-liquid interface becomes significant relative to that of the bulk liquid [1, 2]. It can be shown from equation 1.17 that for a resistance element with length L , cross-sectional area A , cross-sectional circumference C and specific surface conductivity κ_s , the surface component of the electrical resistance R_{surf} is given by:

$$R_{surf} = \frac{L}{\kappa_s C} \quad (5.3)$$

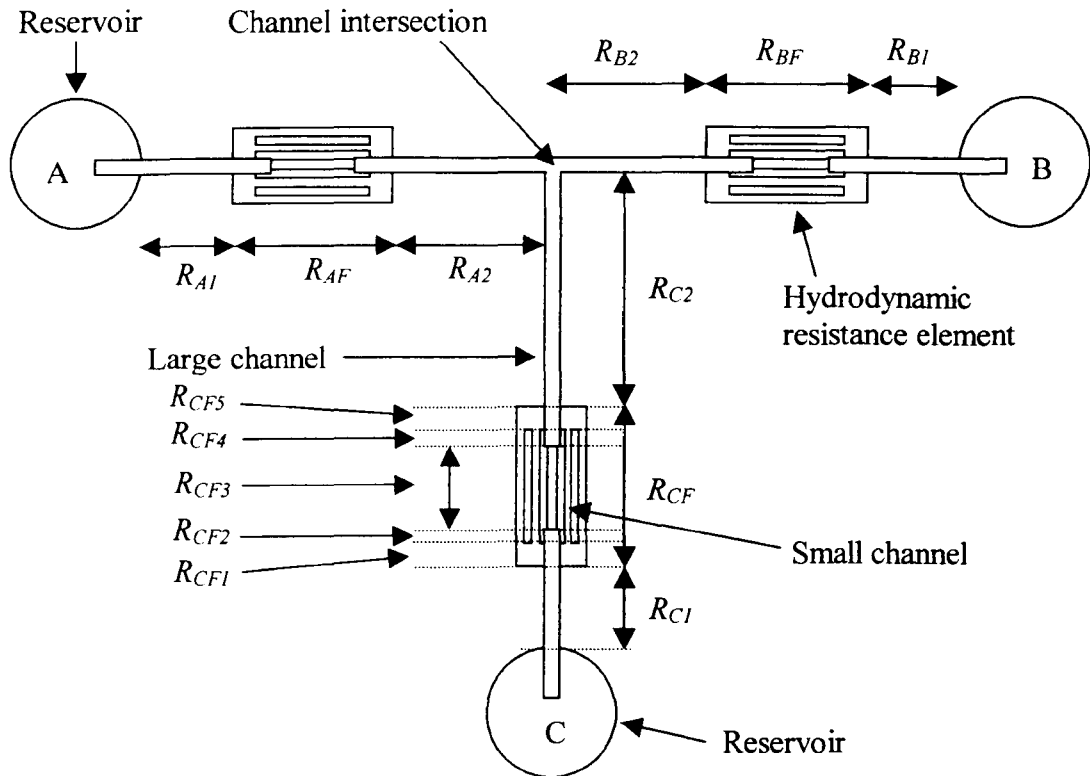
For each element of channel resistance, the components of the total electrical resistance R_{elec} arising from the bulk liquid and the surface act in parallel. Hence, the overall resistance of each element is given by:

$$R_{elec} = \left(\frac{R_{bulk} \cdot R_{surf}}{R_{bulk} + R_{surf}} \right) = \left(\frac{L}{\kappa A + \kappa_s C} \right) \quad (5.4)$$

(N.B. equation 5.4 is the corrected form of the equation printed in Ref. 3.) Using an independent measurement for the liquid conductivity κ_0 and the geometrical parameters of the channel network, equation 5.4 enables the calculation of the resistances of all the channel sections of the microreactor using only the specific surface conductivity κ_s as an adjustable parameter.

The microreactor channel network of chip 004 can be thought of as a network of electrical resistors. Each limb of the channel network can be subdivided into its individual lengths and cross-sectional areas. These can then be assigned an electrical resistance value for that channel element. In regions where there are narrow overlapping

Figure 5.3: Schematic diagram for the T-shaped channel network of chip 004 showing the correspondence between individual channel sections and their associated resistances elements.



channel regions such as at the hydrodynamic restrictions, there is an increased electrical resistance and these areas require additional consideration in their definition. It can be seen in Figure 5.3 how the individual resistance elements are assigned. For the simple sections of large straight channels, these are adequately defined by R_{A1} , R_{A2} and so on, but the hydrodynamic restrictions (i.e. R_{AF} , R_{BF} and R_{CF}) have to be subdivided further. Each hydrodynamic resistance can be seen to comprise five individual resistance elements: R_{CF1} , R_{CF2} , R_{CF3} , R_{CF4} and R_{CF5} . Sections 1 and 5 (i.e. R_{CF1} and R_{CF5}) correspond to the sections where the large channels overlap with the grid end borders. Sections 2 and 4 are the sections where the large channels overlap with the small channel zone. Section 3 contains only small channels. Values of the lengths and cross-sectional areas for R_{A1} , R_{A2} , R_{B1} , R_{B2} , R_{C1} , R_{CF} (sections 1 – 5) and R_{C2} were determined

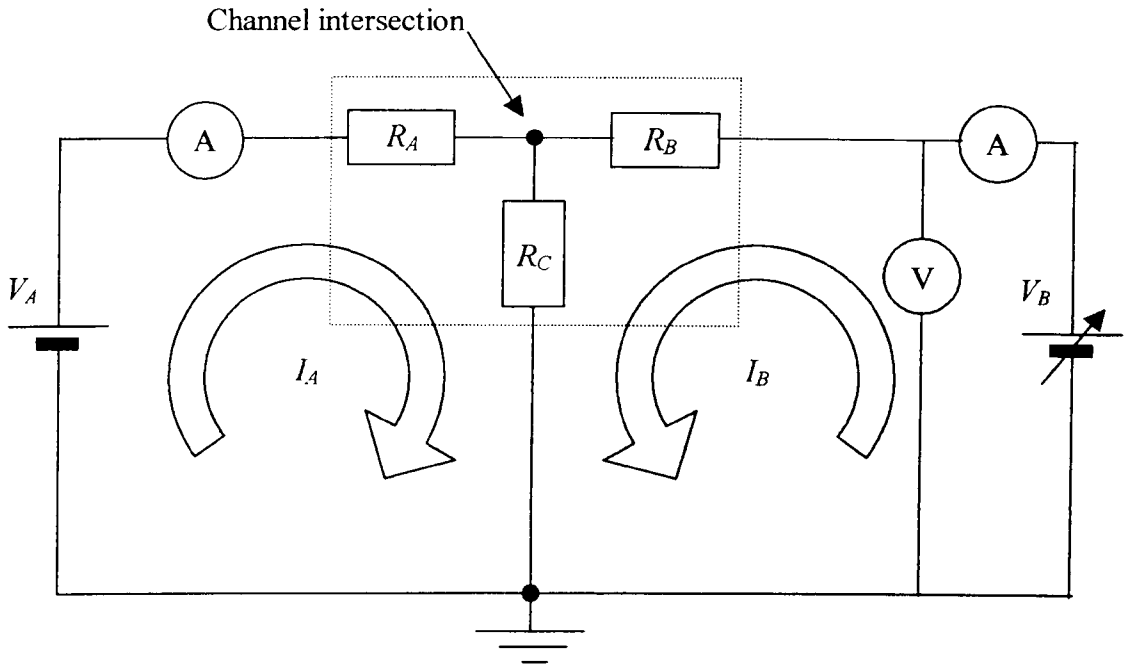
from a series of optical micrographs similar to that shown in Figure 5.1 (a) and 3D profiles as in Figure 5.2. The results are summarised in Table 5.1. Similar measurements were made on the other hydrodynamic resistances in chip 004 (i.e. R_{AF} and R_{BF} sections not listed in Table 5.1). Values of d were found to be within $1 \mu\text{m}$ of the corresponding R_{CF} sections and m values were within $10 \mu\text{m}$. The full set of lengths and cross-sectional areas of the channel elements was used in the data analysis.

Table 5.1: Lengths L and cross-sectional areas A of the different channel section types as defined by the subscripts on the R values in Figure 5.3. Cross-sectional areas for the large channels, small channels and the border region are indicated by A_l , A_s and A_b respectively. The dimensions of the R_{AF} and R_{BF} channel sections (not included here) were measured and found to be similar to the corresponding R_{CF} sections.

Channel section	Length / mm ± 0.05	Expression for A	$A / \mu\text{m}^2 \pm 20\%$
$A1$	1.53	A_l	3830
$A2$	2.74	A_l	3830
$B1$	0.81	A_l	4121
$B2$	3.06	A_l	4121
$C1$	7.18	A_l	3291
$C2$	7.02	A_l	3291
$CF1$	0.30	$A_l + A_b$	7263
$CF2$	0.83	$A_l + 5A_b$	5825
$CF3$	1.53	$5A_s$	2534
$CF4$	0.83	$A_l + 5A_s$	5825
$CF5$	0.30	$A_l + A_b$	7263

The relative uncertainties in the channel lengths (Table 5.1) are minor compared with those in d and m (approx. 10 % in each) for the different channel sections. The uncertainties in derived channel cross-sectional areas are approximately 20 %. The uncertainties in each of the channel dimensions, dominated by that in the area values, gives an approximate uncertainty of 20 % in each of the derived resistance values used in the subsequent current-voltage analysis described here.

Figure 5.4: The DC equivalent circuit for chip 004 within the dotted line and the external circuitry used for measuring voltage and currents.



Using the information listed in Table 5.1 and Figure 5.3, it was possible by application of Kirchoff's laws to draw a DC equivalent circuit for chip 004, as shown in Figure 5.4. It can be seen that the three limbs of the circuit can be considered as two independent circuits. The first consists of the channel sections from reservoir A to the ground at reservoir C and the second, channel sections from reservoir B to reservoir C. For each circuit, the applied voltage relative to ground is equal to the sum of the resistance multiplied by the respective current in the limb of the circuit. Hence:

$$V_A = (R_A + R_C)I_A + R_C I_B \quad (5.5)$$

and

$$V_B = (R_B + R_C)I_B + R_C I_A \quad (5.6)$$

where $R_A = (R_{A1} + R_{AF} + R_{A2})$, $R_{AF} = (R_{AF1} + R_{AF2} + R_{AF3} + R_{AF4} + R_{AF5})$ and R_B and R_C

refer to similar sums for the B and C limbs of the channel network. I_A corresponds to the electrical current flowing along the channel from reservoir A toward intersection. I_B is electrical current flowing along the channel from reservoir B to the intersection. The magnitude of the combined currents (i.e. sum) of I_A and I_B gives the current I_C . A positive I_C is defined as the current flowing along the channel away from the intersection toward reservoir C. Since I_A , I_B or I_C could be negative depending on the different combinations of V_A and V_B that were applied to the microreactor, it was important to be able to calculate the values of these currents. Solution of the two simultaneous equations 5.5 and 5.6, provide expressions for I_A and I_B :

$$I_A = \frac{(R_B V_A + R_C V_A - R_C V_B)}{(R_A R_B + R_A R_C + R_B R_C)} \quad (5.7)$$

and

$$I_B = \frac{-(R_C V_A - R_A V_B - R_C V_B)}{(R_A R_B + R_A R_C + R_B R_C)} \quad (5.8)$$

5.3 Results and discussion.

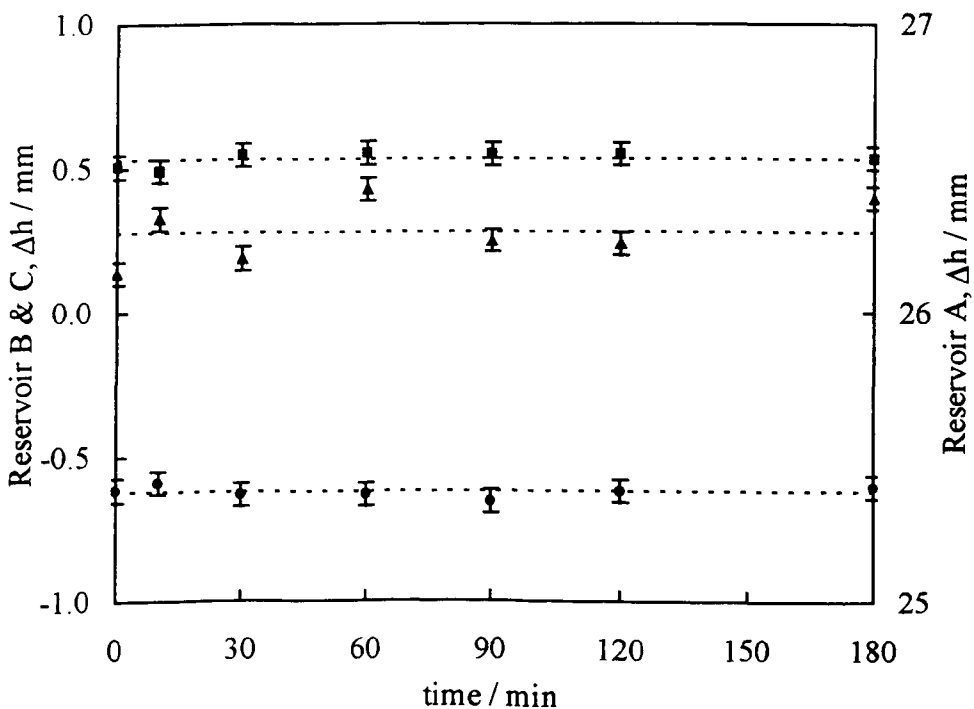
5.3.1 Verification that the pressure-driven flow is negligible within chip 004.

As discussed in Chapter 1, non-negligible pressure-driven flow can occur when non-zero liquid level height or Laplace pressure differences exist between reservoirs. For pressure-driven flow to be considered negligible, Fletcher *et al.* [4] specified that the pressure-driven volumetric flow rate should amount to less than 10 % of the total flow within a microreactor channel. For chip 004 used here, total volumetric flow rates of the order 2 nl s^{-1} were commonly measured. If the pressure-driven flow is to be considered negligible, this component of the total flow should be not greater than 0.2 nl s^{-1} and

should be insignificant within the margin of uncertainty. The uncertainty in the measured volumetric flow rate comprise: (1) the error in the radius of the extended reservoir and (2) the error in the gradient of the $\Delta h-t$ graph. The first uncertainty arising from a 1 % error in the radius of the reservoir translates into a 2 % error in the area and therefore a fixed percentage error of 2 % in the flow rate. The second uncertainty arising from the ability to measure the smallest possible Δh value produces a fixed error in the flow rate of approximately 0.3 nl s^{-1} . From this simple analysis, it is indicative that the pressure-driven flow in chip 004 is insignificant.

To test this hypothesis more thoroughly, chip 004 was filled with pure water such that the liquid level heights in each reservoir were approximately equal. A single

Figure 5.5: Plot of reservoir liquid levels for chip 004 when a water column of approximately 26 mm was added to reservoir A (filled triangles) with respect to the liquid levels in reservoirs B (filled circles) and C (filled squares). Pressure-driven flow in chip 004 is negligible within the error ($\pm 40 \mu\text{m}$ error bars) for a 26 mm high column of water. Data was recorded at average temperature of $24 \text{ }^\circ\text{C}$.

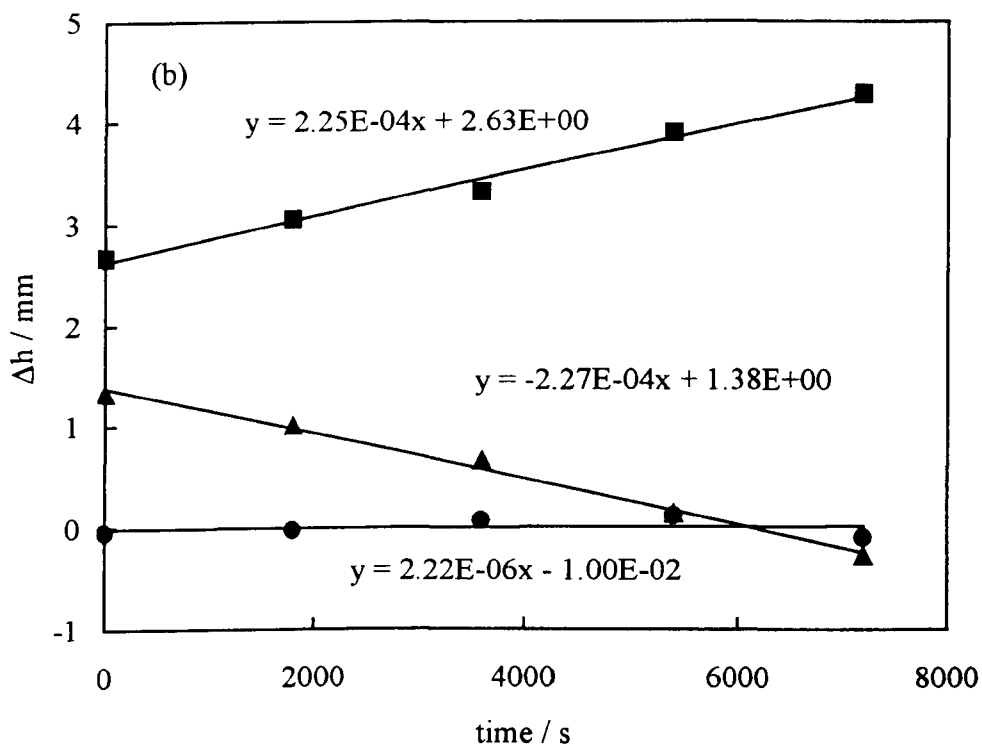
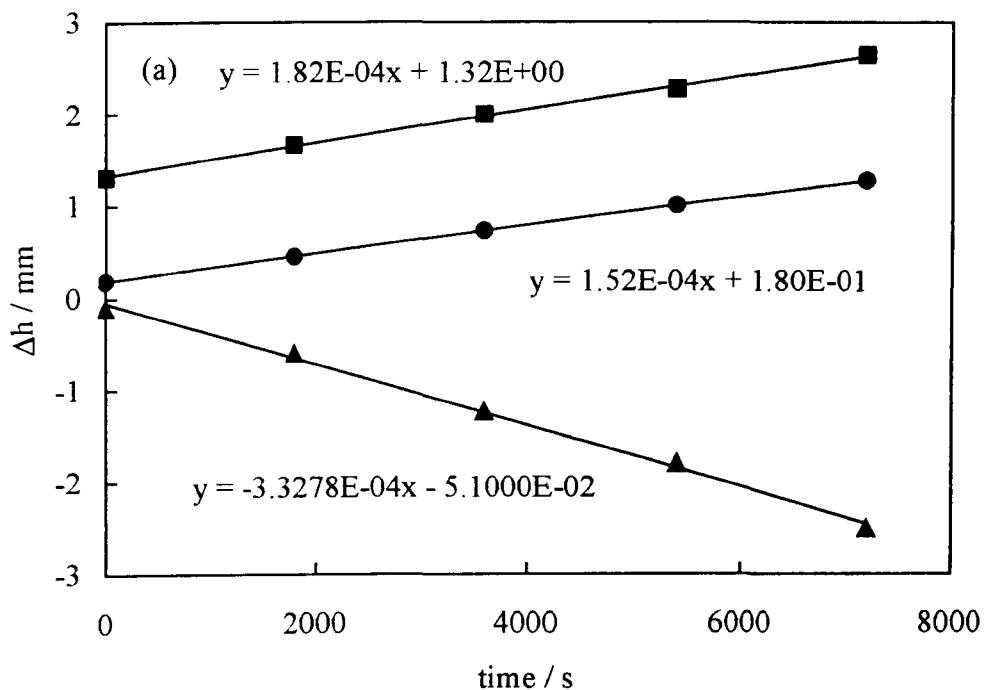


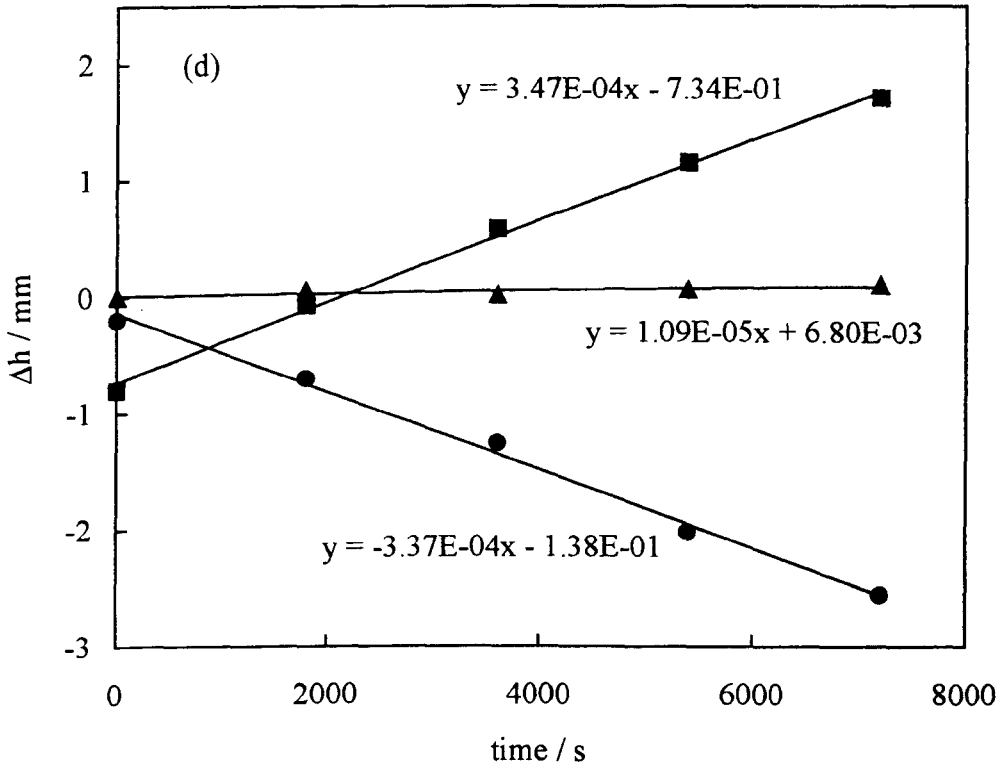
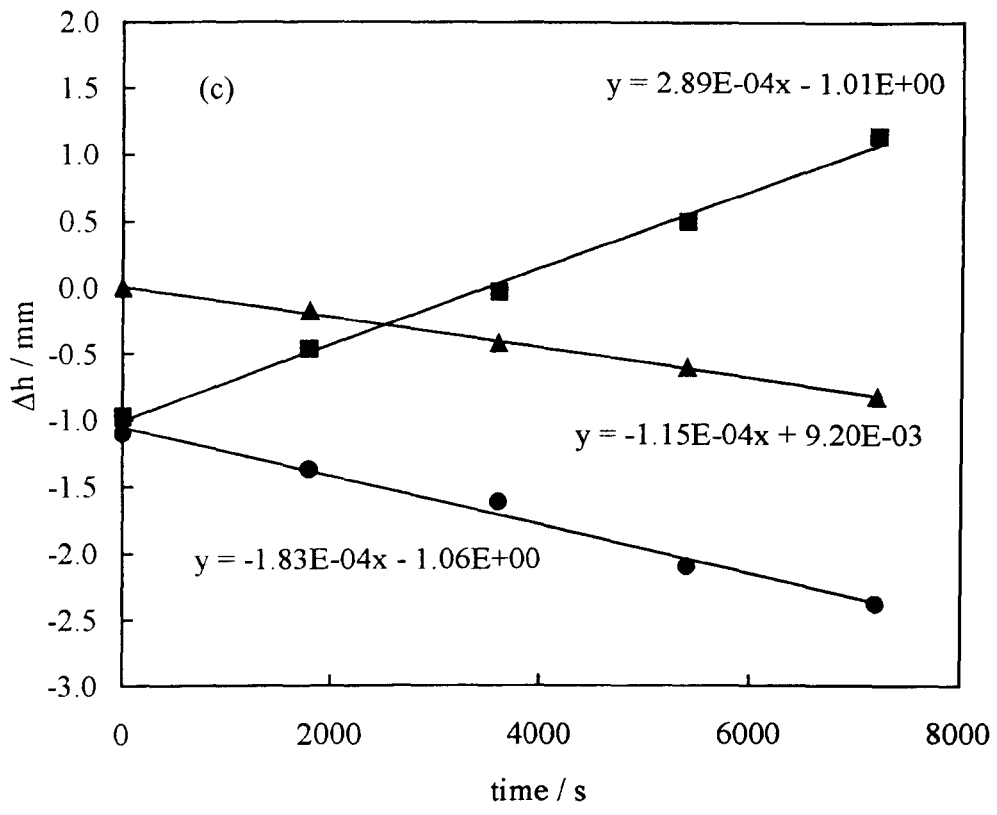
injection of pure water into reservoir A raised the liquid level height by approximately 26 mm above the other reservoirs. The liquid levels of the three reservoirs were monitored over a 3 hr period with the cathetometer; the data recorded is shown in Figure 5.5. From this plot, it is clear that the liquid levels in each reservoir remain constant within estimated uncertainty. This experimental result means that the initial liquid level height differences between reservoirs do not have to be zero at the start of a run, but can be anything up to approximately 26 mm apart. The result also indicates Laplace pressure differences no longer pose a problem.

5.3.2 Characterisation results for different solvent systems in chip 004.

In order to establish a better understanding of the methodology involved in making on-chip flow rate measurements, it was decided to try to reproduce the simple experimental results reported by Fletcher *et al.* [3] for sodium methoxide in methanol. A 10 mM solution of sodium methoxide (NaOMe) was prepared in methanol. The clean chip 004 was filled with this solution and liquid flow rates and electrical currents were measured as a function of applied voltage using the procedures established in Sections 2.1.4 and 2.1.8. For a constant V_A of + 300 V on reservoir A, the voltage applied to reservoir B (V_B) was varied from 0 – 600 V in 150 V increments. The corresponding $\Delta h-t$ data sets can be seen in Figures 5.6 (a) to (e). These linear plots further indicate that the volumetric flow rates are independent of the relative reservoir liquid level heights. (N.B. any $\Delta h-t$ data sets that deviated from a straight line were rejected because of either meniscus shape distortions from contact angle pinning or gas bubble formation). The gradients of each reservoir liquid level height change were used to calculate the volumetric flow rate of the liquid, into or out of, each reservoir from their cross-sectional areas. The measured flow from reservoir A to the channel intersection

Figure 5.6: Reservoir liquid level height changes recorded for 10 mM NaOMe in methanol in chip 004 using reservoir set 1 (Table 2.5). Reservoir A (filled triangles), reservoir B (filled circles) and reservoir C (filled squares). $V_A = +300$ V, $V_B =$ (a) 0 V, (b) 150 V, (c) 300 V, (d) 450 V and (e) 600 V.





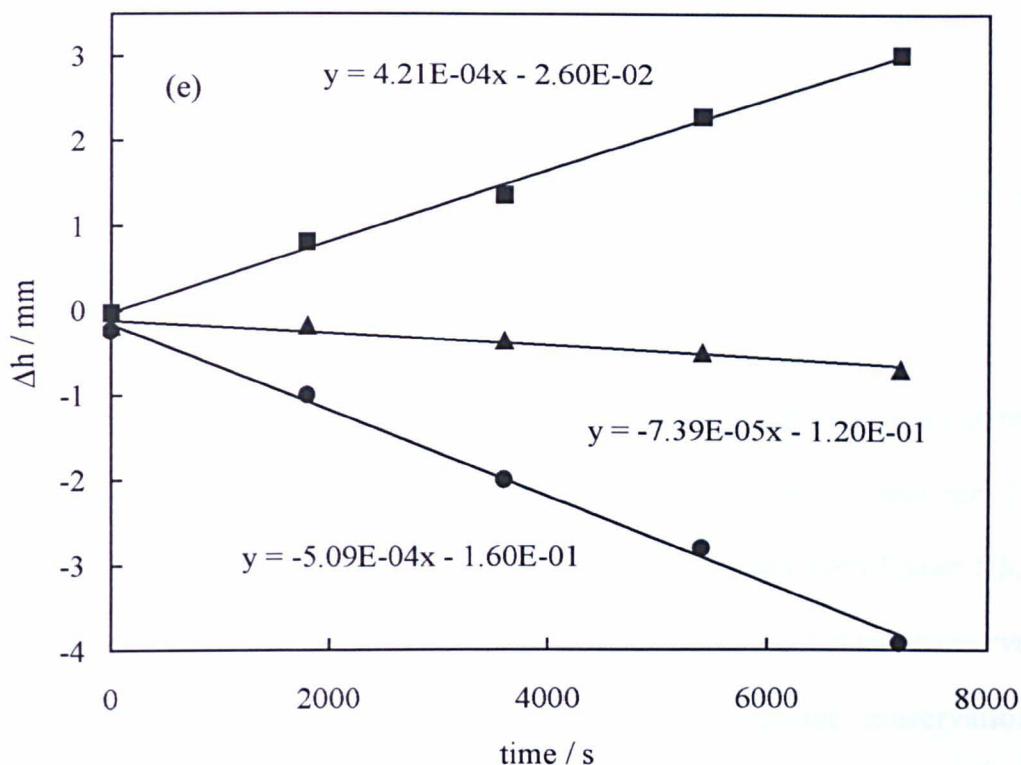
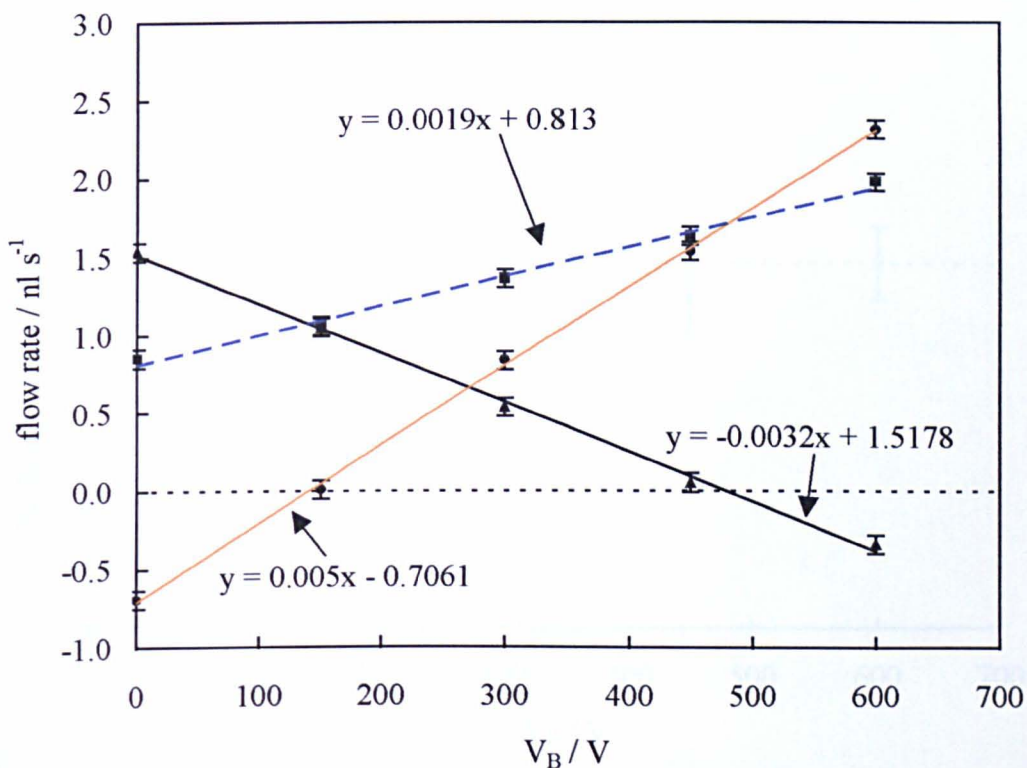


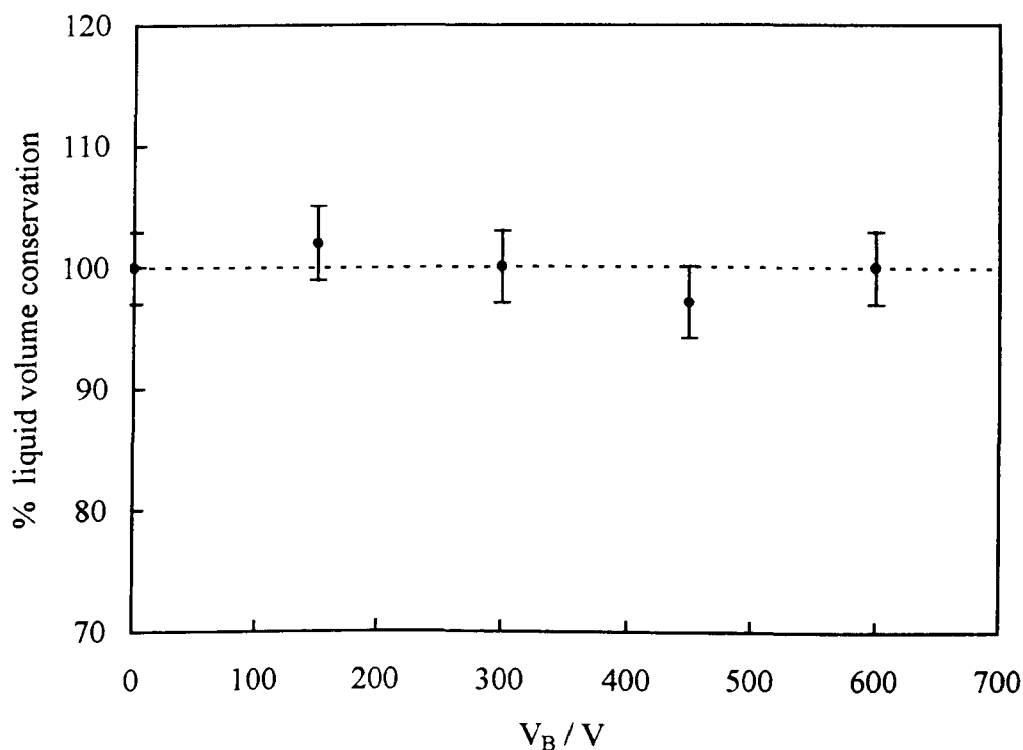
Figure 5.7: Plot of all measured flow rates versus varying V_B and constant $V_A = +300$ V for 10 mM NaOMe in methanol. Flow rates F_A (filled triangles), F_B (filled circles) and F_C (filled squares) are all directly proportional to V_B within an estimated uncertainty level of ± 0.06 nl s⁻¹ (see text for details of calculating uncertainties).



(Fig. 5.3) is denoted by F_A . Similarly, the flow from reservoir B to the channel intersection is F_B and F_C the flow from the channel intersection toward reservoir C. It can be seen from the plot of liquid flow rate versus applied voltage to reservoir B shown in Figure 5.7, that all the measured flow rates F_A , F_B and F_C vary linearly in response to changing V_B .

The sum of the flow rates F_A , F_B and F_C for each Δh - t data set was rigorously compared for a liquid volume conservation of at least 97 % or better for each run. Those runs that did not meet this criterion were rejected. It can be seen from Figure 5.8, that all the Δh - t runs made for 10 mM NaOMe in methanol met this volume conservation criterion. The 3 % uncertainty estimated for the liquid volume conservation, is

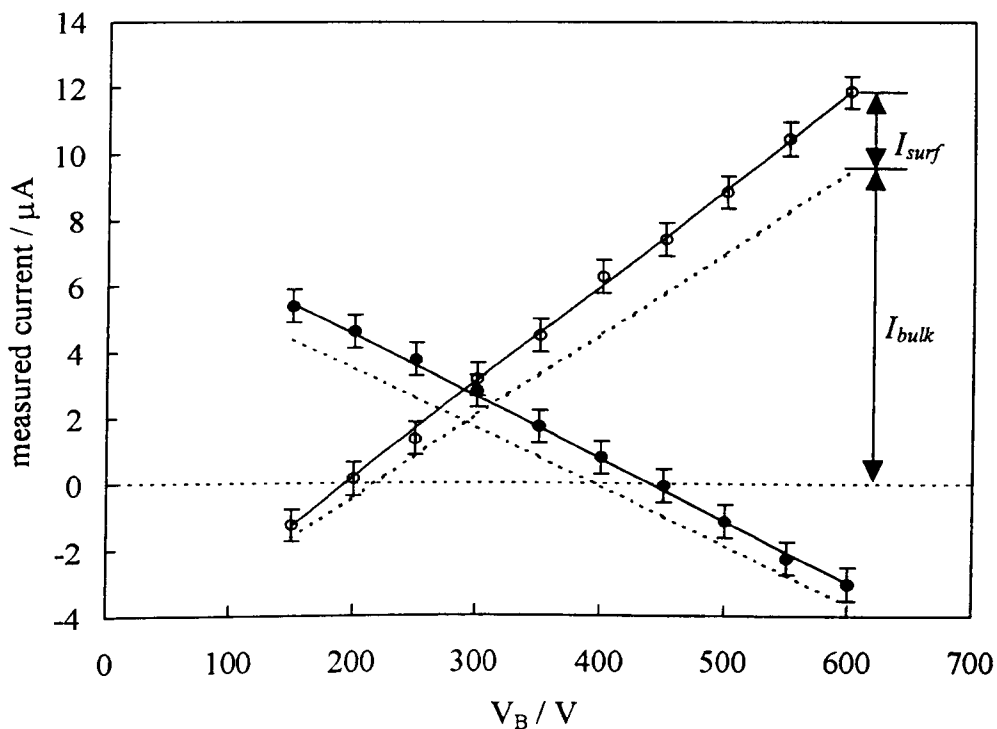
Figure 5.8: Plot of percentage volume conservation for each experimental Δh - t run made for 10 mM NaOMe in methanol versus voltage applied to reservoir B. All liquid flows between reservoirs were conserved as indicated by the level of estimated uncertainty in the measured flow rates. This was $\pm 0.06 \text{ nl s}^{-1}$ equivalent to an uncertainty of 3 %, hence the minimum acceptable volume conservation of 97 %.



equivalent to the uncertainty in the measured flow rate given in Figure 5.7 (i.e. error in flow rate of $2.30 \pm 0.06 \text{ nl s}^{-1}$).

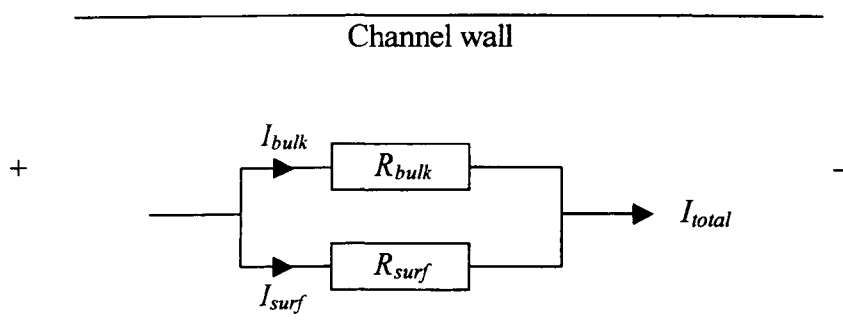
It was noted when performing the experiments that the flow rates varied in a linear way with measured currents I_A and I_B . Measurement of the current-voltage characteristics of chip 004 filled with 10 mM NaOMe in methanol indicates that the device behaved exactly as a purely resistive circuit over a limited range of applied voltages. Comparison of the current-voltage characteristics of chip 004 shown in Figure 5.9 with the measured flow rate data shown in Figure 5.7, confirms the observation that electroosmotic flow rate is proportional to electrical current exactly as theory predicts [3].

Figure 5.9: Measured currents I_A (filled circles) and I_B (open circles) as a function of applied voltage V_B at constant $V_A = 300 \text{ V}$. Chip 004 was filled with 10 mM NaOMe in methanol ($\kappa_0 = 785 \mu\text{S cm}^{-1}$ at 23.9°C). The black solid line indicates best-fit $\kappa_s = 0.039 \text{ nS}$. The dotted lines are for I_{bulk} without any I_{surf} present. Estimated uncertainty in measured current is $\pm 0.5 \mu\text{A}$.



To predict the electroosmotic (volumetric) flow rate for a given electrical current, the measured currents I_A and I_B shown in Figure 5.9, need to be resolved into their components of electroosmotic (bulk) and surface currents. This process was briefly outlined in Section 1.3.9. Once the microreactor current-voltage characteristics are known along with the 3D channel network information and the bulk solution conductivity, separation is a relatively simple step. It can be seen from Figure 5.9 that the circles represent the measured currents I_A and I_B . These measured currents can both be represented as the total current I_{total} in a particular circuit limb (Fig. 5.4). Consider the equivalent circuit for a microreactor channel as shown in Figure 5.10. When the surface current I_{surf} is zero as occurs when $R_{surf} \rightarrow \infty$, $I_{total} = I_{bulk}$. This condition is represented by the dotted lines in Figure 5.9. When I_{surf} is non-zero as occurs when R_{surf} is finite, the surface contribution to the total current must be taken into account by inclusion of a non-zero specific surface conductivity. For the data shown in Figure 5.9, the solid lines fitted to the circles (measured current) were obtained when a best-fit $\kappa_s = 0.039$ nS with a bulk solution conductivity $\kappa_o = 785$ $\mu\text{S cm}^{-1}$ at 24°C was used. This value of specific surface conductivity was found to be in excellent agreement with

Figure 5.10: The equivalent circuit for a microreactor channel carrying a measured current I_{total} , which consists of the bulk current I_{bulk} flowing through the bulk resistor R_{bulk} and the surface current I_{surf} flowing through the surface resistor R_{surf} .



the data reported by Fletcher *et al.* [3] for 10 mM NaOMe in methanol. They reported $\kappa_s = 0.048$ nS for $\kappa_o = 740$ $\mu\text{S cm}^{-1}$ at 25 °C.

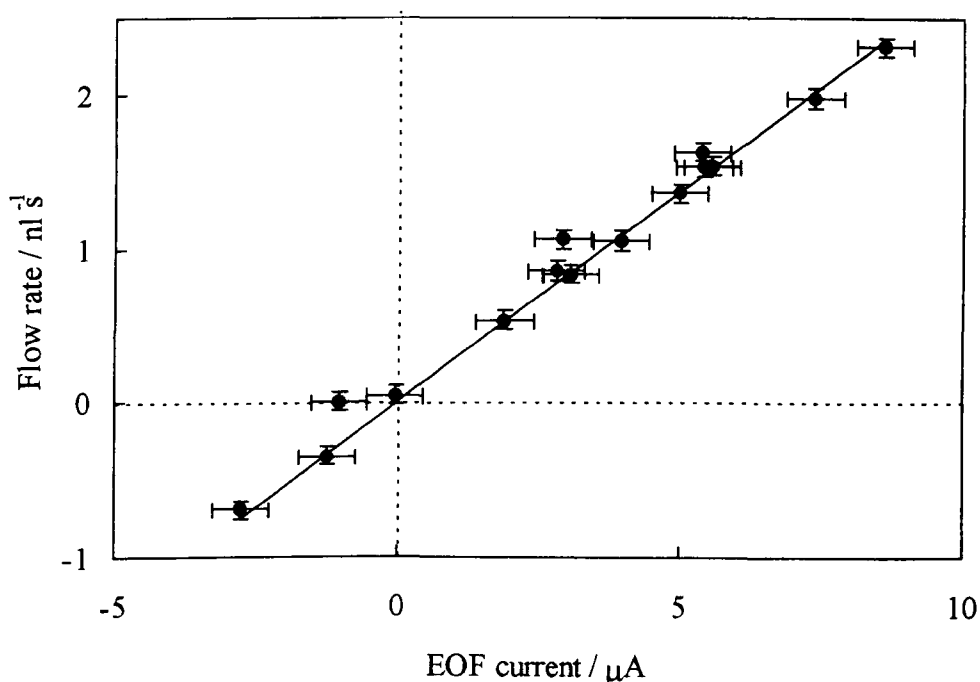
To fit the theoretical and predicted currents shown in Figure 5.9, the resistors R_A , R_B and R_C , typically of the order 20 – 60 M Ω , were floated along with the specific surface conductivity using the solver function in Excel. It was noted that reductions in R_A , R_B and R_C of 12, 10 and 38 % respectively were required for the optimal fit. This can be understood in terms of reducing the total resistance by changing R_{surf} in Figure 5.10. The required decrease in these resistance values compares favourably with those reported by Fletcher *et al.* [3]. They noted that for the chip 004 (same microreactor and solution of 10 mM NaOMe in methanol) reductions in R_A , R_B and R_C of 28, 13 and 46 % were required to achieve a fit to the measured currents. This indicates that similar changes in the surface resistance were necessary for both of these independent data sets (Fig. 5.9 and Ref. 3).

The conclusion from Figure 5.9 that it is necessary to include a non-zero specific surface conductivity term to correctly predict the current-voltage characteristics of microreactors is also reiterated by Fletcher *et al.* [3]. In principle, any non-zero surface current requires a non-zero specific surface conductivity to correctly predict the microreactor current-voltage characteristics. The basis for this conclusion requires some discussion of the experimental uncertainties. The major uncertainty in the comparison of measured and predicted currents arises from the uncertainties of ± 20 % in the channel cross-sectional areas, which translate into approximately 20 % uncertainties in R_{bulk} and I_{bulk} . The uncertainty in the measured current I_{total} (estimated from Fig 5.9) is approximately 5 %, which translates into an uncertainty in I_{surf} equal to 15 % of I_{total} .

This indicates that I_{surf} is a source of large relative error if its contribution to the total current is greater than 15 % (i.e. non-zero within the error). Consider the measured current I_B in Figure 5.9; at $V_B = 600$ V the actual contribution of I_{surf} to I_{total} is 15 %. This is approximately equivalent to $I_{total} = 10 \pm 0.5 \mu\text{A}$ and $I_{surf} = 1.5 \pm 1.5 \mu\text{A}$, which shows the uncertainty arising from surface conduction in the actual data is on the boundary of being significant. It can be seen from the 100 % uncertainty in I_{surf} that the surface current is zero within the error (i.e. range of possible currents 0 – 3 μA). This translates into an uncertainty of 40 – 80 % in the calculated specific surface conductivity. Hence a specific surface conductivity for the fitted data in Figure 5.9 of 0.04 ± 0.03 nS is a good approximation.

The final part in gaining an understanding of this characterisation methodology was to be able to predict the electroosmotic flow rates for 10 mM NaOMe in methanol,

Figure 5.11: Measured liquid flow rates (F_A , F_B and F_C) versus calculated EOF currents ($I_{A,eof}$, $I_{B,eof}$ and $I_{C,eof}$) for 10 mM NaOMe at 24 °C. The solid theory line gives a best-fit value for the zeta potential of -41 mV. The error bars represent a $\pm 0.5 \mu\text{A}$ uncertainty in I_{eof} and $\pm 0.06 \text{ nl s}^{-1}$ random uncertainty in measured flow rates.



using electrical current information and assigned zeta potential. All values of flow rate shown graphically in Figure 5.7 (i.e. F_A , F_B and F_C) along with the calculated electroosmotic (bulk) currents for each associated flow (shown graphically in Fig 5.9) were summarised in a plot of F_{eof} vs. I_{eof} . The resulting plot shown in Figure 5.11, confirms a linear relationship between flow rate and electroosmotic current. The black solid line fitted to the data was calculated with equation 1.15 (pg 40) and gives a best-fit zeta potential of -41 ± 4 mV. The input parameters were either taken from the literature [5, 6] or measured independently; $\epsilon_r = 32.6$, $\epsilon_0 = 8.854 \times 10^{-12}$ F m⁻¹, $\eta = 0.547$ cP and $\kappa_0 = 785$ μ S cm⁻¹. The value of ζ agrees with the result of Fletcher *et al.* [3] for 10 mM NaOMe in methanol of $\zeta = -46$ mV.

To summarize, the method outlined here has been successfully repeated for 10 mM NaOMe in methanol. The relatively high accuracy of measured values for κ_s and ζ , shows the viability of this method for characterising further solvent systems of interest directly on-chip.

Those solvent systems that were relevant to catalytic reaction studies in microreactors included: water, methanol, dimethylacetamide (DMA), formamide, tetrahydrofuran (THF) and acetonitrile. Due to the limited time and the slow process of gathering the required $\Delta h-t$ data only water, methanol, DMA and DMA (aq) solvent systems were examined. The values for κ_s and ζ along with independently measured κ_0 for each solvent system are given in Table 5.2. The linearity of the plot of F_{eof} versus I_{eof} , such as was noted for 10 mM NaOMe in methanol, can be seen for 10 mM NaBr in water and 10 mM NaBr in methanol in Figure 5.10. The best-fit zeta potentials for 10 mM NaBr in water was $\zeta = -15$ mV ($\epsilon_r = 78.304$ and $\eta = 0.8904$ cP at 25 °C) and

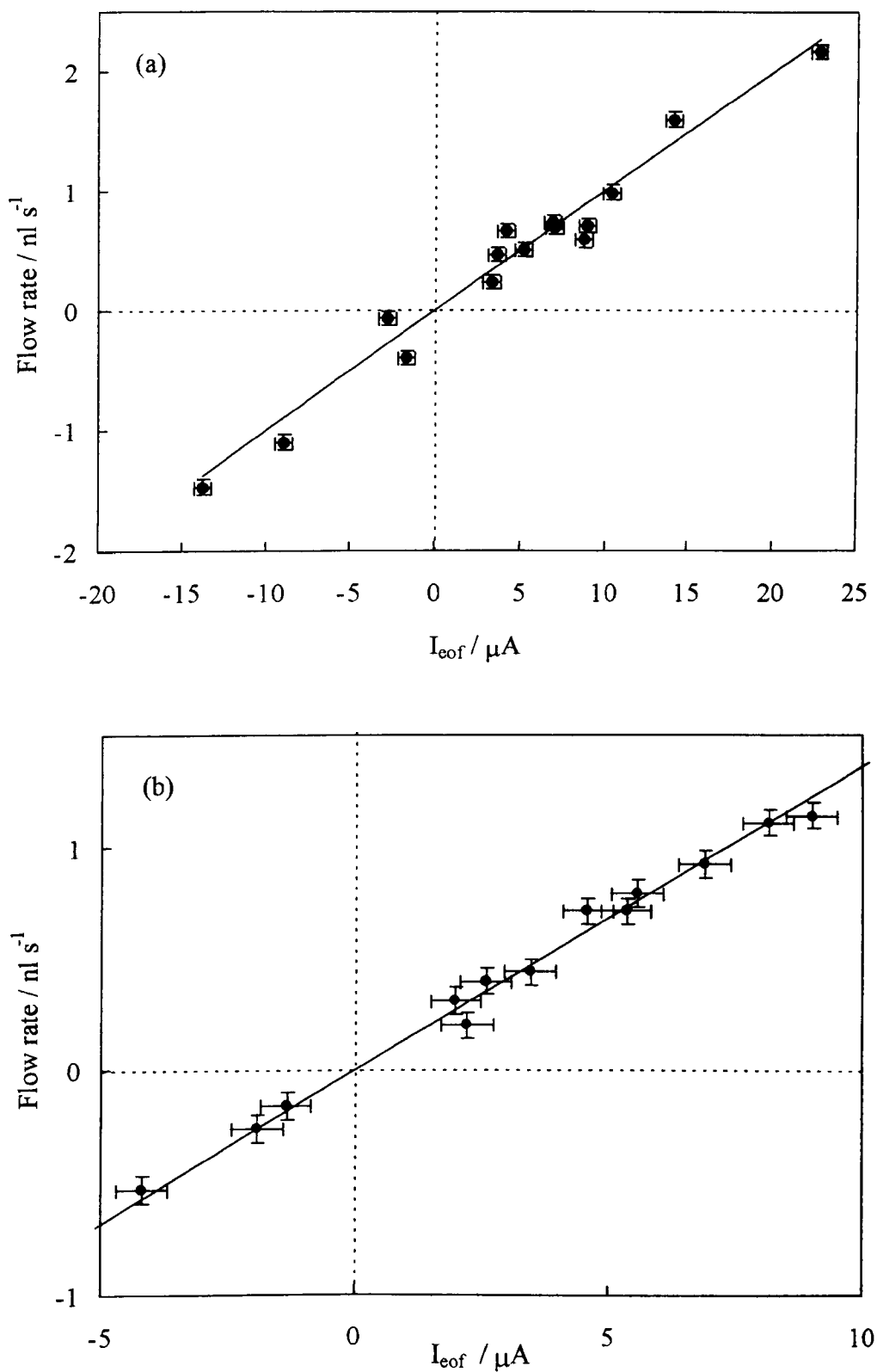
for 10 mM NaBr in methanol was $\zeta = -25$ mV ($\epsilon_r = 32.63$ and $\eta = 0.0547$ cP at 25 °C). Given higher relative permittivity solvents usually exhibit the largest zeta potentials (Section 1.3.8), it was not expected that 10 mM NaBr in water would have a lower zeta potential than 10 mM NaBr in methanol. Although no reference for zeta potential in the literature was found for NaBr in water, 10 mM KI (aq) and 1 mM NaCl (aq) for a glass-water interface were found to be $\zeta = -65$ mV for KI [7] and $\zeta = -21$ mV NaCl [8], so $\zeta = -15$ mV for 10 mM NaBr (aq) may be a respectable figure. Similarly, no literature references were found for NaBr in methanol. The closest solution was 10 mM KI in methanol which had $\zeta = -50$ mV for a glass-solution interface [7].

Table 5.2: Solvent system characterisation results for a fixed V_A of 300 V and varying V_B (150 – 600 V) applied to shiny Pt metal electrodes. ζ – zeta potential, κ_s – specific surface conductivity, κ_o – bulk solution conductivity and pH measured with standard pH electrode. * no available best-fit

Solvent system	ζ / mV	κ_s / nS	κ_o / $\mu\text{S cm}^{-1}$	pH
10 mM NaOMe in methanol	-41	0.039	785	
10 mM NaBr in water	-15	0.059	1170	6.42
10 mM NaBr in methanol	-25	0.062	978	
40 mM NaBr in methanol		2.255	3310	
10 mM NaBr in DMA		*	994	
45 mM NaBr in 80 vol.% DMA (aq)	-4	0.035	922	6.37

The specific surface conductivities for 10 mM NaBr in water and 10 mM NaBr in methanol are very similar. Both values are approximately 0.06 nS. The values of κ_s estimated here are smaller than many experimental values determined for a range of glass-solvent surfaces, but are similar in magnitude to theoretical estimates [1]. The best-fit κ_s value for 40 mM NaBr in methanol was significantly larger than that for 10 mM NaBr in methanol and indicates there was comparatively more surface conduction occurring for this 40 mM NaBr system. This difference in specific surface conductivity

Figure 5.12: Flow rate vs. EOF current for (a) 10 mM NaBr in water and (b) 10 mM NaBr in methanol. The calculated best-fit zeta potentials are -15 and -25 mV respectively for the microreactor channel glass / solution interfaces. The estimated uncertainty in I_{eof} is $\pm 0.5 \mu\text{A}$ and in measured flow rates is $\pm 0.06 \text{ nl s}^{-1}$.



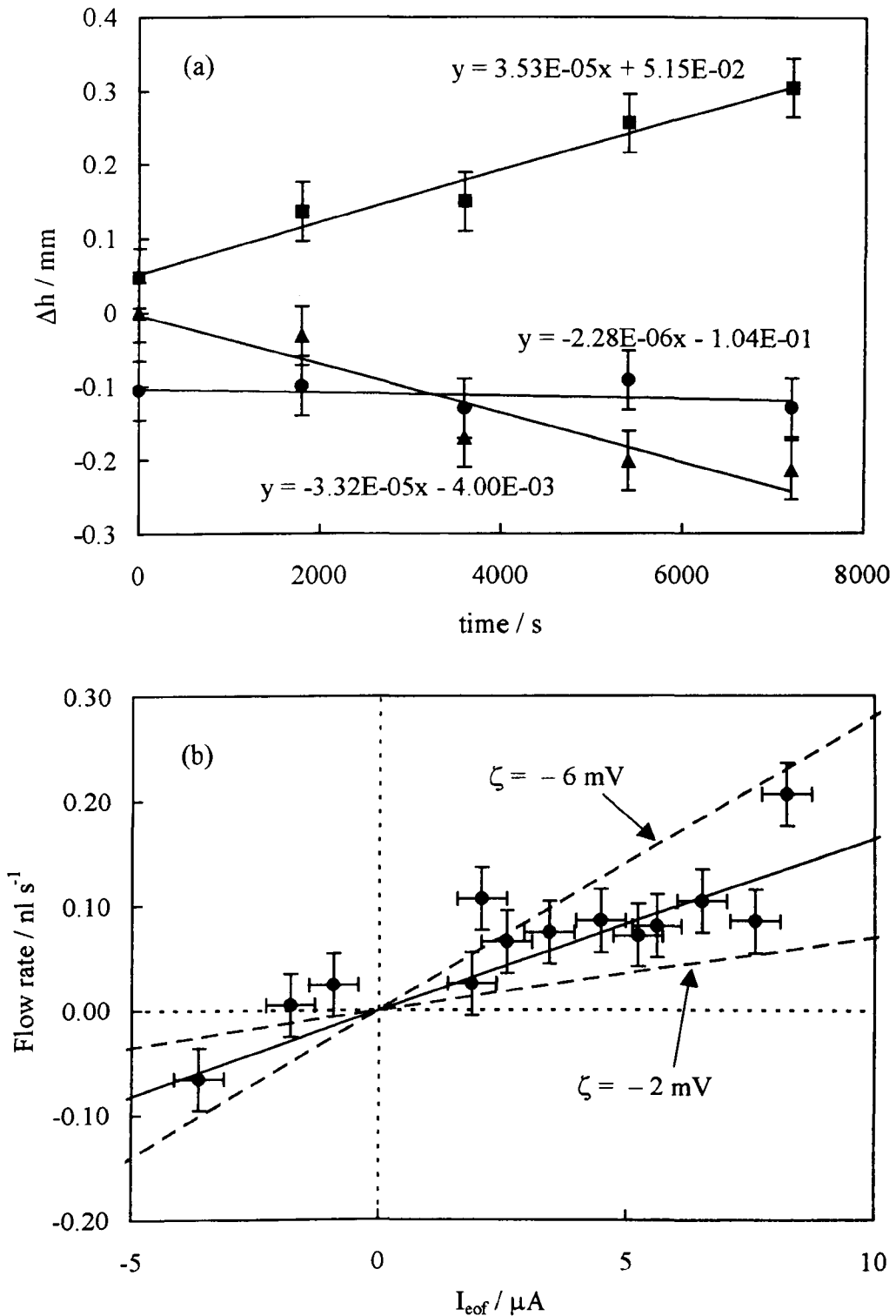
values is probably due to the increased electrolyte concentration. κ_s is after all, dependent on the square root of electrolyte concentration as well as the fixed geometry of the microreactor.

The apparent wide variation in κ_s values spanning two orders of magnitude for similar glass-solvent interfaces such as Pyrex glass-KCl (aq) as listed in Table 1.6, can be explained in terms of the different geometries of capillaries used for these reported experiments. From the previous discussion on page 42 about the dependence of the bulk and surface currents on the geometry of the capillary tubes, it should be understood that I_{bulk} increases more rapidly than I_{surf} with increasing capillary radius, because of its r_{cap}^2 dependence. The result of this is that experiments performed in larger bore tubes using solutions with a constant electrolyte concentration and glass type yield larger κ_s values [9].

For the 10 mM NaBr in DMA listed in Table 5.2, it was impossible to obtain any reasonable $\Delta h-t$ data because of the very low electroosmotic mobility. Even at high $V_B \sim 600$ V the measured liquid level height changes over a 2 hr period were approximately zero within the error. Significant gas pocket production was noted even at low V_B s, which also hampered measurements. The current-voltage characteristic for 10 mM NaBr in DMA was successfully determined, but because the current did not scale linearly with applied voltage, it was impossible to fit the measured and predicted currents for any value of specific surface conductivity.

The best-fit zeta potential calculated for 45 mM NaBr in 80 vol. % DMA (aq) was also difficult to determine because of its low electroosmotic mobility. It can be seen

Figure 5.13: (a) Typical Δh - t plot for 45 mM NaBr in 80 vol. % DMA (aq) with constant $V_A = 300$ V and $V_B = 150$ V. The estimated uncertainty Δh is ± 40 μm . (b) Liquid flow rate versus calculated EOF current for 45 mM NaBr in 80 vol. % DMA (aq). Solid line indicates a best-fit zeta potential of approximately -4 ± 2 mV. The estimated uncertainty in F_{eof} is ± 0.03 nl s^{-1} and that in I_{eof} is ± 0.5 μA .



from the example of a $\Delta h-t$ data set for 45 mM NaBr in 80 vol. % DMA (aq) shown in Figure 5.13 (a), that the liquid level height changes over 2 hrs were quite small in comparison to the estimated uncertainty. The summarised flow rates for the 45 mM NaBr in 80 vol. % DMA (aq) are shown in Figure 5.13 (b). It can be seen that the scatter of the data points gives a best-fit zeta potential of -4 ± 2 mV (assuming a volume weighted fraction mean is taken to calculate all solvent parameters at 21.5 °C i.e. $\eta = 0.9593$ cP as shown in Appendix F¹ and $\epsilon_r = 46.788$ in Appendix G²). The margin of uncertainty in calculated ζ suggests that the lower limit of resolution for this characterisation methodology has been found. Later work published by Fletcher *et al.* [17], reports a calculated best-fit zeta potential using the same characterisation methodology, to be -7 ± 2 mV (assuming $\epsilon_r = 64$, $\eta = 0.975$ cP and $\kappa_0 = 1028 \mu\text{S cm}^{-1}$ at 24 °C) for 30 vol. % ethanol in water with 50 mM Tris buffer. They measured flow rates below 0.8 nl s^{-1} for this low electroosmotic mobility solvent system. For a solution of 2.1 mM Ni^{2+} ions in the same solvent mixture a best-fit $\zeta = 0 \pm 2$ mV was obtained (assuming the same calculation values for the solvent parameters and a $\kappa_0 = 1194 \mu\text{S cm}^{-1}$). Clearly there is a minimum uncertainty in ζ of ± 2 or 3 mV and only zeta potentials bigger in magnitude than about 20 or 30 mV can be determined with an uncertainty of 10 %.

The current-voltage characteristic for 45 mM NaBr in 80 vol. % DMA (aq) required a best-fit specific surface conductivity of 0.035 nS to fit the measured and predicted currents. The fitting procedure for 45 mM NaBr in 80 vol. % DMA (aq) accompanied

¹ Beilstein database (Web of Science) was searched for the viscosity and dielectric properties of pure DMA. Dynamic viscosity values over the temperature range 20 – 35 °C are given in Refs 10-12. The dynamic viscosities of pure water over the same temperature range are given in Ref 13.

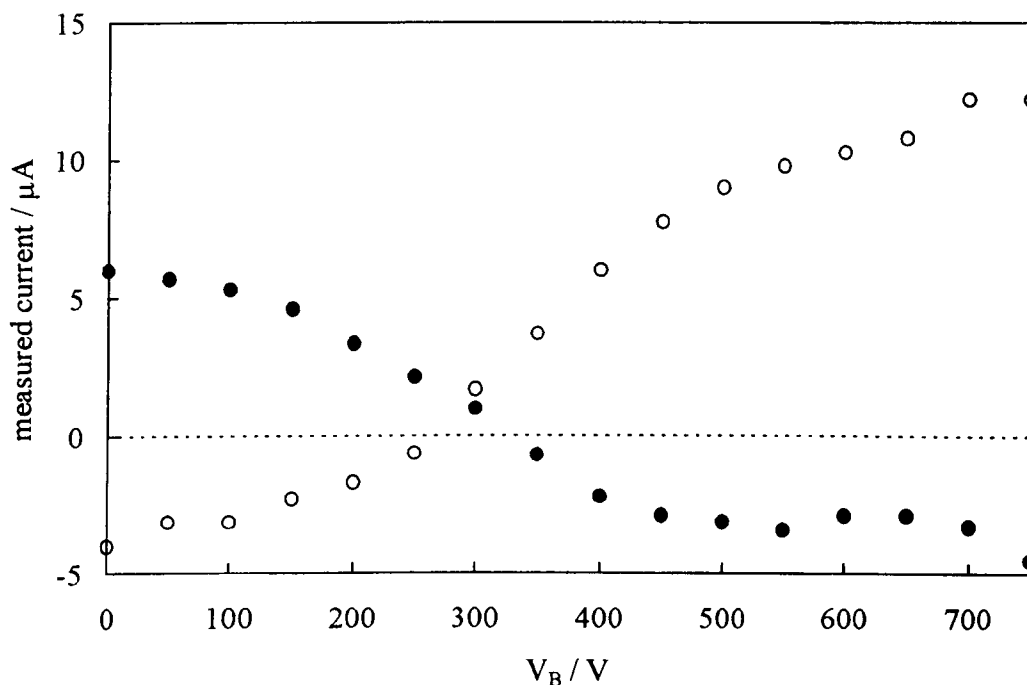
² The static dielectric constant (relative permittivity) for pure DMA over the temperature range 15 – 30 °C is given in refs 14 and 15. The static dielectric constant for pure water over 5 – 30 °C is given in ref 16.

reductions in the values of R_A , R_B and R_C of 10, 8 and 33 % respectively. Both the value of κ_s and reductions in the resistances R_A , R_B and R_C are all within the expected range when compared to other values determined for different solvent systems explored in this investigation.

5.3.3 Choice of electrode material for on-chip flow rate measurements.

To correctly predict the current-voltage characteristic for a fixed geometry microreactor containing a solution with a known bulk and specific surface conductivity, there should exist a linear relationship between applied voltage and measured current.

Figure 5.14: The current-voltage characteristic for chip 004 filled with 10 mM NaBr in DMA and using Pt electrodes. Filled circles represent the measured current I_A and the open circles the measured current I_B . The overall graph is dominated by converging currents indicating a deviation from Ohm's law.



For the solution of 10 mM NaBr in DMA, shown in Figure 5.14, this is clearly not the case. The overall feature of the data is to converge to some limiting current. Between

$V_B = 200 - 400$ V the graph is approximately linear and outside this range it deviates from a straight line. The deviation from the straight line indicates that significant solution polarisation is occurring [18]. The degree of polarisation that occurs depends on a number of variables, but the most significant of these are the electrical properties of the electrode and the surrounding solution.

For nearly every zeta potential investigation reported in the literature, platinum has been adopted as the standard fabrication material for electrodes. The physical properties of platinum which favour its use as an electrode material are:

- The low reactivity that allows metallic Pt to remain shiny, when submerged in liquids for long periods or subjected to harsh cleaning.
- The high exchange current densities and fast rate of charge transfer from the solution to the electrode surface, helps to prevent the formation of concentration polarisation within the microreactor channel by rapid discharge of the ions in solution.
- Malleable and is easily made into different shaped electrodes.

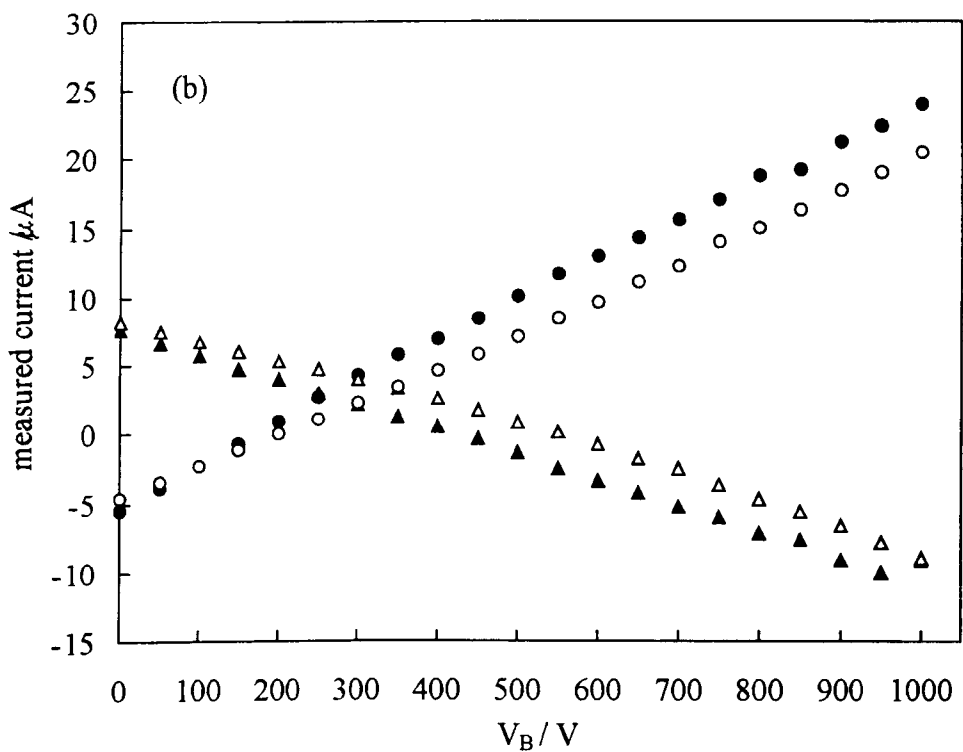
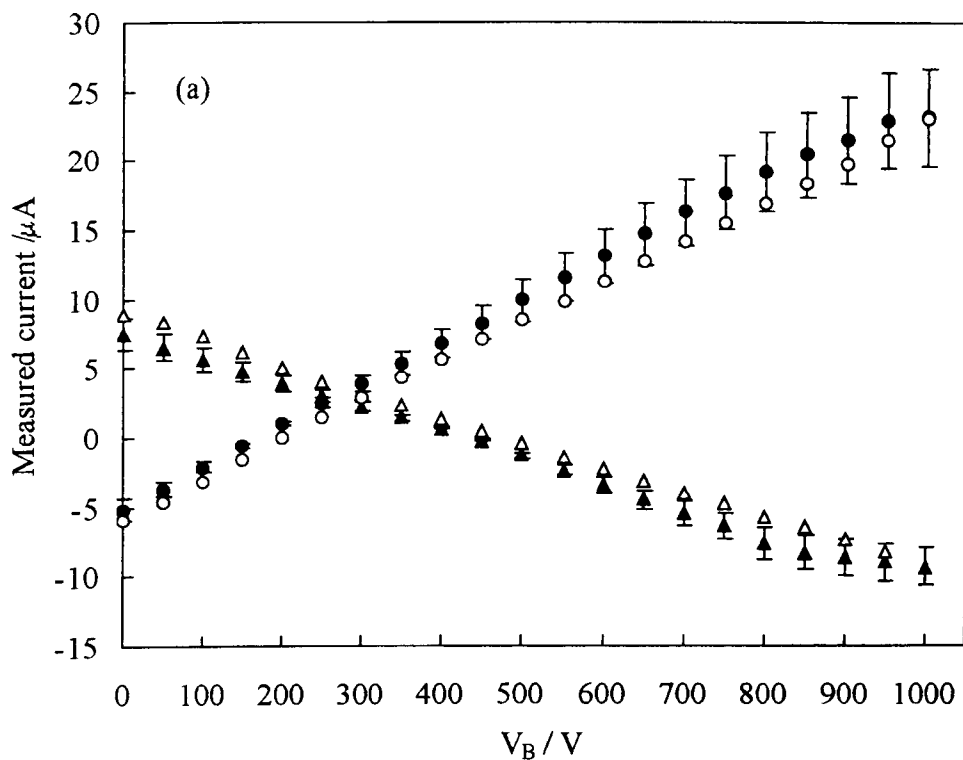
The important feature of platinum to act as a non-polarizable electrode (and so reduce solution polarisation) is evident from the current-voltage characteristics of different solvent systems. The aqueous and mixed aqueous-organic solvent systems listed in Table 5.2, exhibit a wide range of linearity for measured current as a function of applied voltage. For the organic solvent systems such as DMA, these were not so well behaved and resulted in unpredictable currents. Since we now know for a constant electrode material (i.e. Pt), that the electrical properties of the solution surrounding the electrode can drastically alter the measured current-voltage characteristic for a given

solvent system, it was decided to investigate whether different electrode materials would also produce any effects.

The chip 004 was cleaned and filled with a solution of 10 mM NaBr in methanol. The currents I_A and I_B were measured as a function of voltage as applied to the electrodes. V_A was set to + 300 V while V_B was cycled from 0 – 1000 V and back to zero again in 50 V increments. This cycling was made to see if there was any hysteresis occurring in the measured current-voltage characteristics. The first run was made with Pt electrodes and this was used as the control data set. The observed trend in measured currents shown in Figure 5.15 (a) for the Pt electrodes shows good agreement with Ohm's law. This level of linearity noted for the Pt electrodes is also similar to that for the silver, gold and tungsten electrode systems shown in Figures 5.15 (b) to (d). From this, it can be concluded that polarisation effects were insignificant for the electrode materials and solutions outlined here. It can be seen that there is some level of hysteresis for the different electrodes. The variation between the initial rise and fall of the currents are approximately the same within the estimated uncertainty for the Pt electrodes. This maybe also true for the other electrode materials, but it is worth pointing out that silver and gold can be seen to change their current-voltage gradients between the rise and fall parts of the cycle. Tungsten appears to be the most consistent electrode for producing the least apparent hysteresis.

The level of estimated uncertainty in the measured currents for the Pt electrodes, given in Figure 5.15 (a), was considered relatively high compared to those estimated earlier in this Chapter. It was decided to repeat the experiment of cycling the applied voltage to reservoir B using a different solvent system. Measurements were made at the

Figure 5.15: I-V data recorded using chip 004 with a solution of 10 mM NaBr in methanol and (a) Pt (b) Ag (c) Au (d) W electrodes. $V_A = 300$ V, V_B was cycled from 0 – 1000 V (rise) and back to zero (fall) again in 50 V increments. Rise I_A (filled triangles), fall I_A (open triangles) and rise I_B (filled circles), fall I_B (open circles). The random uncertainty in measured current is $\pm 15\%$ for the Pt electrode data set.



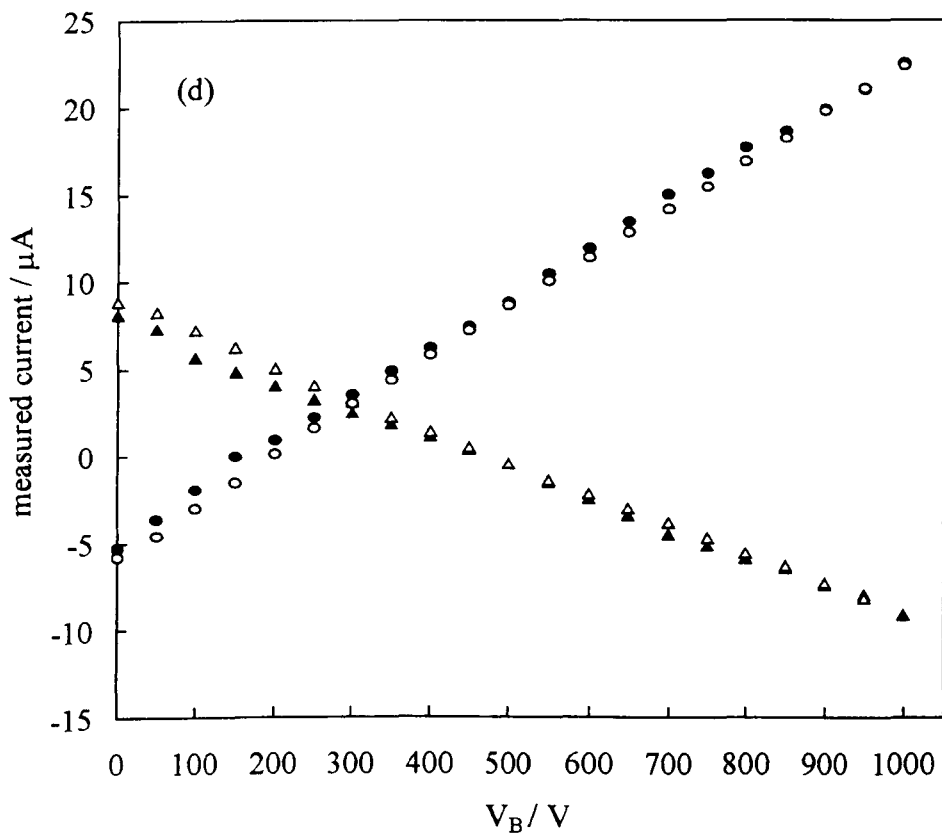
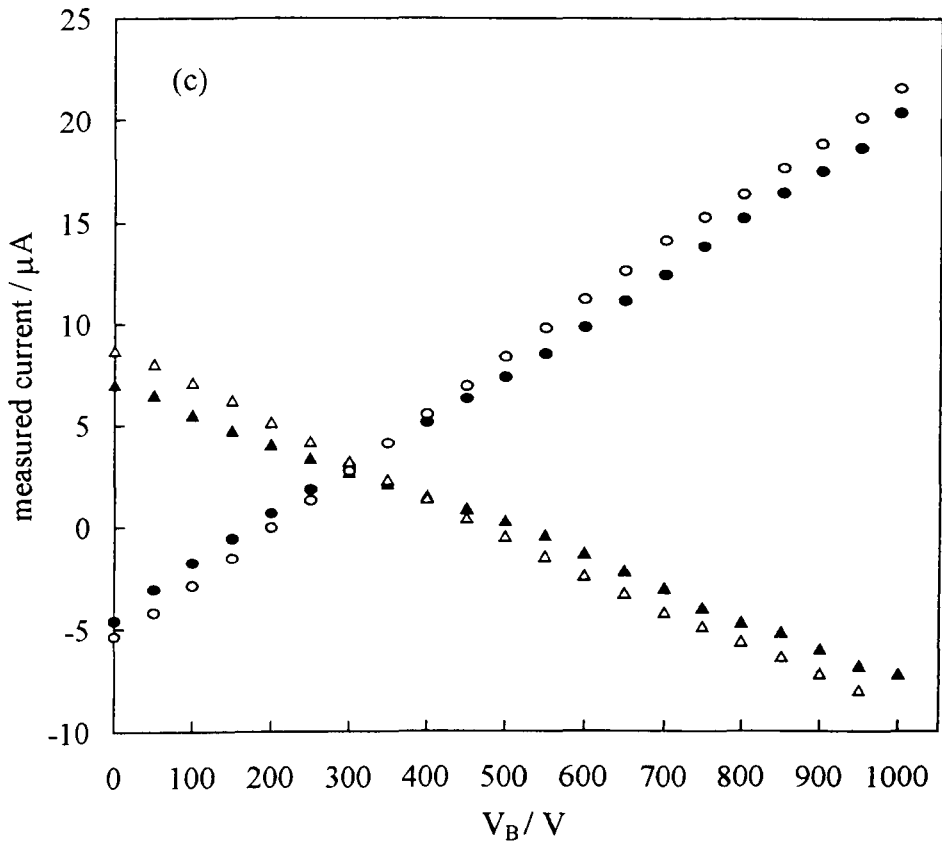
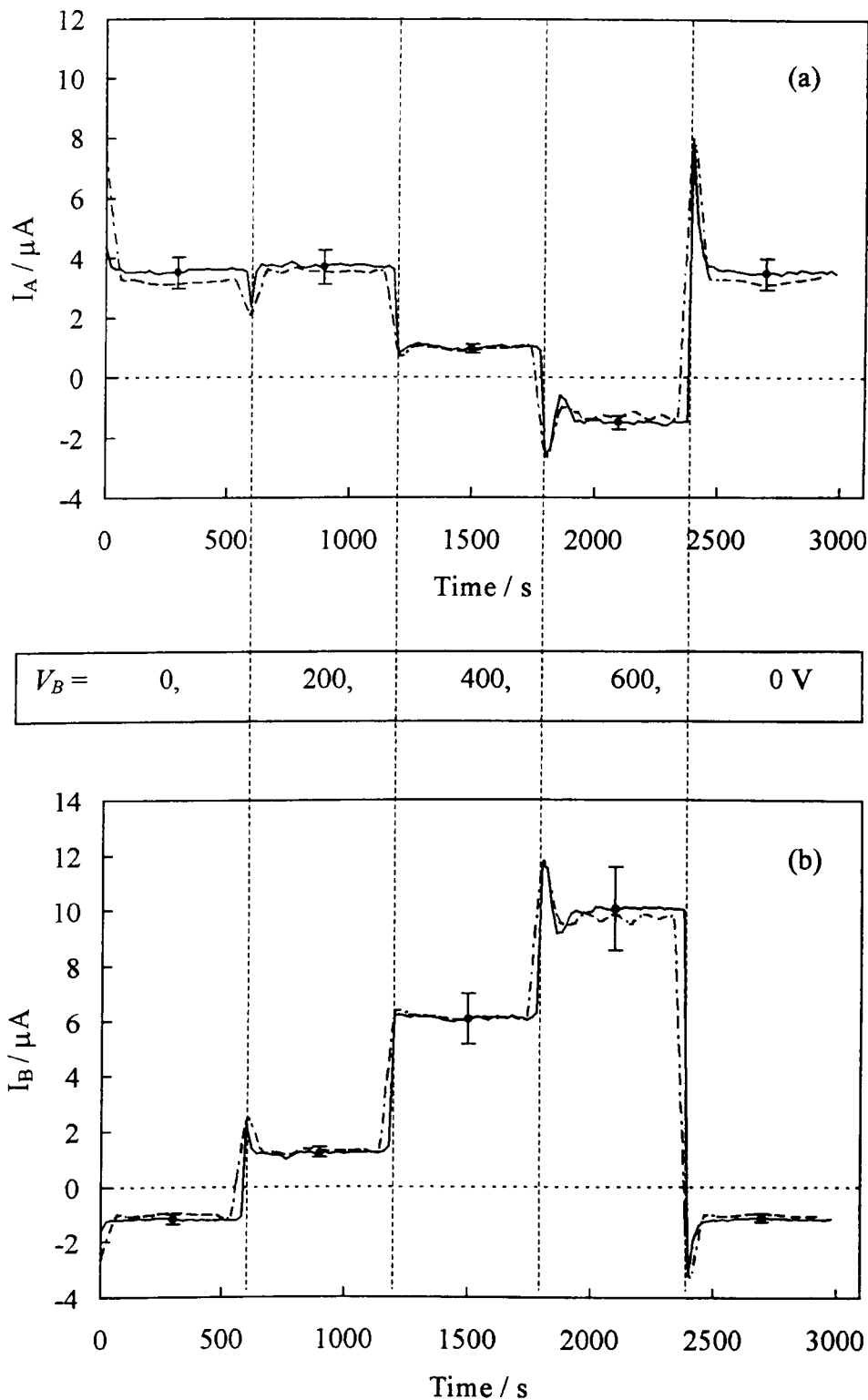


Figure 5.16: I-V measurements made at 23.4 °C using chip 004 filled and Pt electrodes with a solution of 10 mM NaOMe in methanol. The data was recorded at 20 s intervals using the LabVIEW set up that automatically logged the values. The plots show the change in measured current I_A and I_B for (a) a new solution (solid line) and (b) the same solution after being left in the chip for 2 days (dashed line). With a constant $V_A = +300$ V, V_B was cycled through 0, 200, 400, 600, 0 V at 10 min intervals. The reproducibility in the measured current was estimated to be $\pm 15\%$.



start and end of a 2 day period using 10 mM NaOMe in methanol with the same set up of chip 004 and Pt electrodes as for Figure 5.15 (a). It can be seen from Figure 5.16 that the measured currents are approximately constant for each V_B and respond to change within a few seconds. In conclusion, these currents can be reliably reproducible to a similar level of uncertainty of $\pm 15\%$ using the same solution over a 2 day period. Hence, the apparent electrode hysteresis occurring for the Pt electrodes in Figure 5.15 (a) is insignificant within the error.

5.4 Summary.

We have demonstrated here that the voltage-current characteristics of solvent systems of interest within microreactor channel networks can be predicted to an accuracy of between 10 and 20 %, using the complete set of 3D channel network information, the bulk solution conductivity and channel wall-solution specific surface conductivity as the only adjustable parameter. Values for specific surface conductivity were in good agreement with other published values for a test solution of 10 mM sodium methoxide in methanol.

The electrical currents due to EOF in the different limbs of the channel network are proportional to the corresponding volumetric liquid flow rates with the constant of proportionality dependent on the relative permittivity, viscosity and conductivity of the liquid and the zeta potential of the channel wall-liquid interface. Measurement of the volumetric flow rates within the channel network as a function of electrical current, proved to be a simple and effective method of characterising the microfluidic flow properties of solvent systems of interest. The uncertainty in each calculated zeta potential was estimated to be about 10 % and that in the measured flow rates, to be

approximately between 10 to 20 %. It was found for a solution of 45 mM NaBr in 80 vol. % DMA (aq), that the measured zeta potential of -4 ± 2 mV was at the limit of resolution of this $\Delta h-t$ characterisation method and that a new more sensitive technique must be sought if lower electroosmotic mobility solvent systems are to be investigated.

An analysis of the current-voltage characteristics of different electrode materials was made for silver, gold and tungsten to determine if they had different electrical properties to platinum. Experimental runs made under identical conditions with each electrode material indicated that there were no conclusive differences between them and platinum, given a random error in measured currents of approximately ± 15 %. This level of random error appeared to be independent of time or solvent system used.

5.5 References.

- [1] J. Th. G. Overbeek, *In Colloid Science*, ed. H. R. Kruyt (1952) Elsevier, Amsterdam and London, vol. 1, p194.
- [2] R. J. Hunter, *Zeta Potential in Colloid Science* (1981) Academic Press, London, p63.
- [3] P. D. I. Fletcher, S. J. Haswell & X. Zhang, *Lab on a Chip*, 2001, 1, 115.
- [4] P. D. I. Fletcher, S. J. Haswell & V. N. Paunov, *Analyst*, 1999, 124, 1273.
- [5] *Handbook of Chemistry and Physics*, 62nd edn. (1981) CRC Press, Boca Raton.
- [6] J. Timmermans, *Physico-Chemical Constants of Pure Organic Compounds*, vol. 1 (1950) and vol. 2 (1965) Elsevier, New York.
- [7] J. Th. G. Overbeek, *In Colloid Science*, ed. H. R. Kruyt (1952) Elsevier, Amsterdam and London, vol. 1, p230.
- [8] Y. Gu & D. Li, *J. Colloid Interface Sci.*, 2000, 226, 328.
- [9] S. Arulanandam & D. Li, *J. Colloid Interface Sci.*, 2000, 225, 421.
- [10] T. M. Aminabhavi & V. B. Patil, *J. Chem. Eng. Data*, 1998, 43, 497.
- [11] L. Pikkarainen, *J. Chem. Eng. Data*, 1983, 28, 344.
- [12] B. S. Krumgalz, *J. Chem. Soc. Faraday Trans. 1*, 1982, 78, 437.
- [13] *Handbook of Chemistry and Physics*, 62nd edn. (1981) CRC Press, Boca Raton, pF-38.
- [14] Leader & Gormley (Handbook), *J. Amer. Chem. Soc.*, 1951, 73, 5731.
- [15] O. W. Kolling, *Anal. Chem.*, 1987, 59, 674.
- [16] R. Parsons, *Handbook of electrochemical constants* (1959) Butterworth Scientific Publications, London, p8
- [17] P. D. I. Fletcher, S. J. Haswell & X. Zhang, *Lab on a Chip*, 2002, 2, 102.
- [18] D. A. Skoog, F. J. Holler & T. A. Nieman, *Principles of Instrument Analysis* (1998) Saunders College Publishing, Florida, p584.

6. ABSORBANCE IMAGING OF REAGENT MOBILITIES.

6.1 Introduction: *The necessity to measure lower flow rates.*

Having highlighted the need to measure lower volumetric flow rates more precisely than was possible with the $\Delta h-t$ method outlined in Chapters 4 and 5, the aims of the work discussed in this Chapter were two fold. The first investigation was to determine the feasibility of using the absorbance-imaging microscope, described in Chapter 3, to track a moving front of a dye solution that has been mobilised in a microreactor channel. The recorded electrical current, voltage and front velocity data will be used to calculate the relevant solvent characteristics such as zeta potential and so on. Particular attention will be given to demonstrating the self-consistency between this new and the previously outlined flow rate method. The second aspect involves using the absorbance-imaging technique to characterise the microfluidic properties of a colloidal palladium catalyst sample introduced into a flowing liquid stream within a microreactor channel. The aim here was to determine the electrophoretic mobility and the zeta potential of the colloidal particles.

6.2 Apparatus and theory.

6.2.1 *Microreactor dimensions, I-V characteristics and electrical set up.*

For all the investigations described in this Chapter the double T-chip 301 was used. The reason for this choice was primarily that it possessed etched hydrodynamic restrictions that have been shown to suppress pressure-driven flow to insignificant levels for a 25 mm high column of water. Chip 301 was etched according to procedure 4, listed in Table 2.1 (pg 72) and thermally bonded in two stages according to procedure 3, in Table 2.2 (pg 73). A schematic diagram of the internal channel network of chip 301

with the relevant electrical connections can be seen in Figure 6.1. The channel region xy marked on the schematic diagram was used to make flow rate measurements. The region xy can be seen more clearly in an actual optical micrograph of the area shown in Figure 6.2. The length of the channel xy is approximately 5.8 mm. This was sufficiently long to allow front monitoring over about 6 minutes for a dye front moving with a velocity of $16 \mu\text{m s}^{-1}$.

Absorbance images taken of chip 301 (similar to those in Figure 5.1) were used to find best-fit values of the apparent mask width m and channel depth d according to the isotropic etch model. It was found that the best-fit values for m and d were common of channels that had slight distortion arising from thermal bonding. The large channels have best-fit values for m of $146 \pm 5 \mu\text{m}$ and d of $38 \pm 2 \mu\text{m}$. The small channels used in the hydrodynamic restrictions have $m = 183 \pm 5 \mu\text{m}$ and $d = 3.1 \pm 0.5 \mu\text{m}$ respectively.

Extended glass reservoirs were not required for the series of experiments outlined here. Solutions were simply added via a clean syringe to the top block holes as shown in Figure 1.1 (a). Chip 301 was routinely cleaned after each run with alcoholic KOH (Section 2.1.6). Particular attention was given to filling the channel network with solvent so that it was free from air pockets. This was best achieved by using a syringe to draw the liquid through the network from a reservoir opposite to the ones containing solvent. Reservoir electrodes were made of 0.26 mm diameter shiny Pt wire. One electrode was inserted into each reservoir at the start of the experiment. Care was taken to ensure that the depth each electrode was inserted into the liquid was about the same.

Microreactor current-voltage relationships for chip 301 were greatly simplified by

Figure 6.1: Schematic diagram of the channel network in the double T-chip 301. As the name implies, the channel network contains two T-junctions. Flow rate experiments were made in the straight channel region xy and the potential difference was applied across reservoir electrodes A and C.

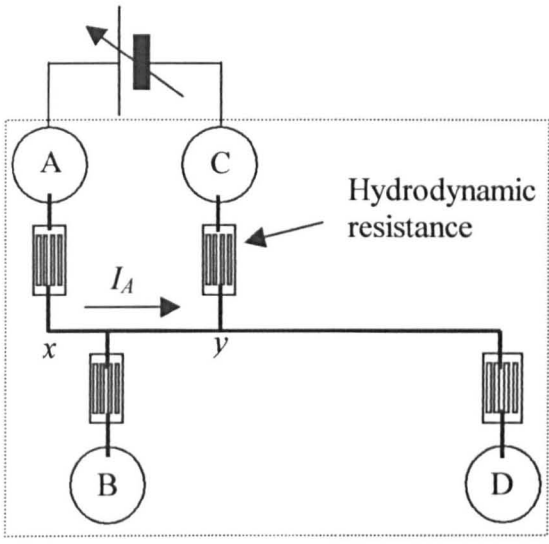
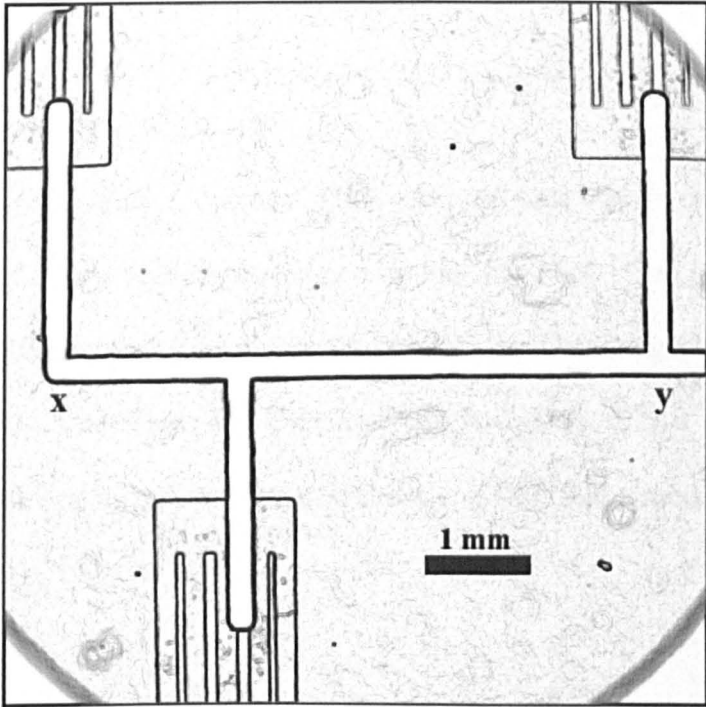


Figure 6.2: Optical micrograph of chip 301 showing the hydrodynamic restrictions and the channel section xy . Images were made using the X2.5 objective lens.



using only one power supply. Consider Figure 6.1, a current I_A flowing from reservoir A to reservoir C gives rise to a series of voltages because of the resistance of each channel section. In some regions such as the hydrodynamic restrictions, the resistance will be higher across this part of the channel network than across the channel length xy . The significance of this varying channel resistance is not evident in the device current-voltage profiles, but could be for moving fronts encountering non-uniform electric fields when moving between different channel sections. If the resistance of the channel section Ax is R_{Ax} , xy is R_{xy} and yC is R_{yC} , then the potential difference between reservoir A and C (i.e. V_{AC} arising from this flow of current) is given by:

$$V_{AC} = I_A (R_{Ax} + R_{xy} + R_{yC}) \quad (6.1)$$

It is possible to determine the values of R_{Ax} , R_{xy} and R_{yC} for solutions of different bulk conductivity, using a modified version of the spreadsheet that was used for the published calculations described in Ref. 1. This contains all the relevant chip dimensions and solution variables.

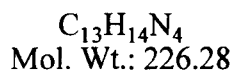
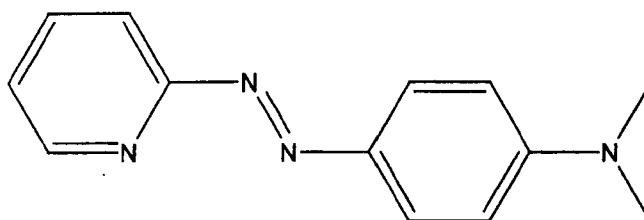
6.2.2 Concentration-imaging theory.

The absorbance-imaging (Axiovert S100 inverted Carl Zeiss) microscope set up shown in Figure 3.3, was recently confirmed by Fletcher *et al.* [1] to be a viable way of performing *in situ* monitoring of chemical reactions by observing changes in reagent concentration over time. From the Beer-Lambert law (Eqn. 6.2) it can be seen that absorbance measurements can be used to determine d (if C and ε are known) or C (if d and ε are known):

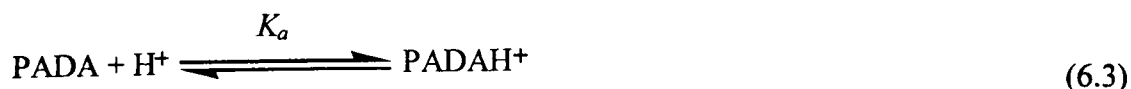
$$A_M = \log \left\{ \frac{I_{solvent} - I_{dark}}{I_{dye} - I_{dark}} \right\} = Cd\varepsilon \quad (6.2)$$

where $I_{solvent}$ and I_{dye} are the transmitted light intensities recorded separately through the solvent filled and the dye filled channel respectively. I_{dark} is the detector signal recorded in the absence of incident light with the microreactor still in position. These intensities can be measured as a function of channel position and time, and used to extract the relevant dye front velocities for the given set of electrokinetic conditions.

Figure 6.3: The structure of the dye PADA (pyridine-2-azo-p-dimethylaniline). PADA is a red-brown crystalline compound at room temperature that is sparingly soluble in water and much more soluble in some organic solvents.



For convenience, the same dye (PADA) used in the study by Fletcher *et al.* [1] was used here. The structure of PADA (pyridine-2-azo-p-dimethylaniline) is shown in Figure 6.3. PADA can be used as a pH indicator according to the following reaction:



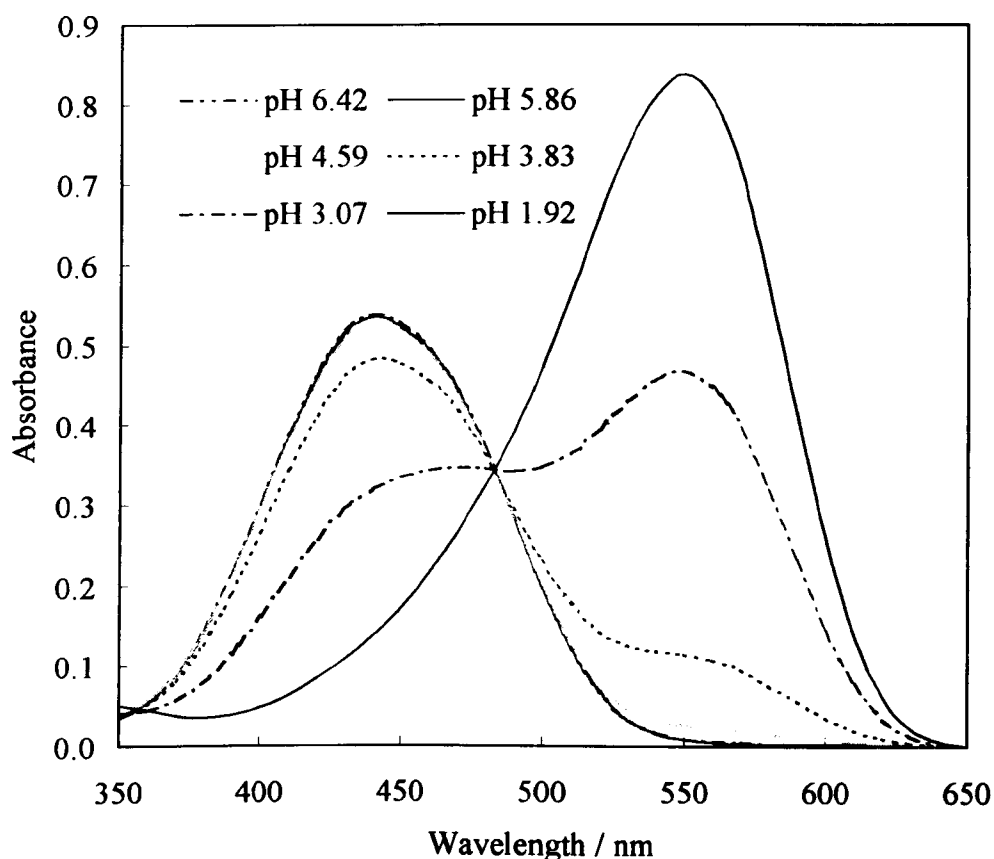
At about pH 2 dye solutions containing PADA are almost entirely composed of the protonated form PADAH^+ . At pH 7 the dye solutions are predominantly PADA. A dye front consisting of predominantly uncharged PADA will move along a microreactor channel at the electroosmotic velocity v_{eof} of the bulk solvent. Similarly a dye front consisting of predominantly the charged PADAH^+ species will move along at a

combined velocity of the bulk solvent movement plus the electrophoretic velocity i.e.

$$v_{eof} + v_{eph}$$

PADA solutions containing 4 mM PADA in 80 vol. % DMA (aq) with 45 mM NaBr were made up from an original stock solution containing 5 mM PADA with 56 mM NaBr in DMA. 20 ml of the stock solution was pipetted into a 25 ml volumetric flask. HCl and / or NaOH was then added to adjust the pH before each solution was finally made up to the mark with pure water. 10 min ultrasonication ensured each solution was completely mixed and free of dissolved gasses. Before use, each solution was filtered through a 0.2 μm Anisotop filter to reduce the chance of particulate blockage of chip 301.

Figure 6.4: A plot of absorbance versus wavelength recorded in a 50 μm path length cell for solutions containing 4 mM PADA with 45 mM NaBr in 80 vol. % DMA (aq). Solutions were pH adjusted using NaOH and HCl. All absorbances were measured at 25 $^{\circ}\text{C}$.



The absorbance spectra for PADA and PDAH⁺ can be seen in Figure 6.4. The spectral peak at 450 nm corresponds to the absorption maximum of the PADA. The spectral peak at 550 nm corresponds to the absorption maximum for PDAH⁺. Clearly, the spectra of PADA and PDAH⁺ share significant overlap. The concentrations of PADA and PDAH⁺ can be determined from measurements of absorbance at 450 and 550 nm. From the Beer-Lambert law:

$$A_{450} = d(\epsilon_{450}^{PADA} [PADA] + \epsilon_{450}^{PDAH^+} [PDAH^+]) \quad (6.4)$$

and

$$A_{550} = d(\epsilon_{550}^{PADA} [PADA] + \epsilon_{550}^{PDAH^+} [PDAH^+]) \quad (6.5)$$

where d is the optical path length, ϵ is the extinction coefficient of the superscripted species at the subscripted wavelength (i.e. 450 or 550 nm) and the square brackets denote concentrations. Solution of the two equations 6.4 and 6.5 yields:

$$[PADA] = \frac{\left(\frac{A_{550}}{\epsilon_{550}^{PDAH^+}} - \frac{A_{450}}{\epsilon_{450}^{PDAH^+}} \right)}{d \left(\frac{\epsilon_{550}^{PADA}}{\epsilon_{550}^{PDAH^+}} - \frac{\epsilon_{450}^{PADA}}{\epsilon_{450}^{PDAH^+}} \right)} \quad (6.6)$$

$$[PDAH^+] = \frac{\left(\frac{A_{550}}{\epsilon_{550}^{PADA}} - \frac{A_{450}}{\epsilon_{450}^{PADA}} \right)}{d \left(\frac{\epsilon_{550}^{PDAH^+}}{\epsilon_{550}^{PADA}} - \frac{\epsilon_{450}^{PDAH^+}}{\epsilon_{450}^{PADA}} \right)} \quad (6.7)$$

For equilibrium 6.3, we can also write an expression for the equilibrium or acidity constant for this proton transfer reaction:

$$K_a = \frac{[PADA][H^+]}{[PADAH^+]} \quad (6.8)$$

pH and pK_a are related to the concentrations of PADA and $PADAH^+$ through the expression known as the Henderson-Hasselbalch equation [2]:

$$pH = pK_a - \log_{10} \left\{ \frac{[PADAH^+]}{[PADA]} \right\} \quad (6.9)$$

As it is one of our objectives to show a self-consistency between different flow rate methods (i.e. results of Chapter 5), it was decided to use 45 mM NaBr in 80 vol. % DMA (aq) as the base solvent for the PADA dye solutions. Since the values of the extinction coefficients for PADA and $PADAH^+$ in 45 mM NaBr in 80 vol. % DMA (aq) are unknown, it was necessary to define equations 6.8 and 6.9 in terms of known quantities. All solutions were made up to contain 4 mM PADA. We therefore know that $[PADA] + [PADAH^+] = 4$ mM which can be denoted as $[PADA]_o$. From the measured pH it is possible to calculate $[H^+]$ and so eliminate $[PADAH^+]$ from the set of equations as described in Appendix H. This enables calculation of the absorbance of PADA at 450 or 550 nm (i.e. A_λ) from the initial PADA concentration and measured extinction coefficients:

$$A_\lambda = d(\varepsilon_\lambda^{PADA} [PADA] + \varepsilon_\lambda^{PADAH^+} ([PADA]_o - [PADA])) \quad (6.10)$$

and

$$[PADA] = \frac{\left(\frac{K_a [PADA]_o}{[H^+]} \right)}{\left(1 + \frac{K_a}{[H^+]} \right)} \quad (6.11)$$

where A_λ denotes the calculated absorbance of the solution at the subscript wavelength, ϵ^{PADA} and ϵ^{PADAH^+} are the extinction coefficients at the subscript wavelengths.

Optical wavelengths that coincided with the maximum absorbances of PADA and $PADAH^+$ were selected for the concentration-imaging using two narrow band pass filters. These were the Edmund Scientific N43-111 (peak 450 nm, full width at half maximum 10 nm) and the Edmund Scientific N43-126 (peak 550 nm, full width at half maximum 10 nm). A series of digital images were recorded at predefined intervals using a digital monochrome CCD camera (Hamamatsu C4742-95-12NRB) as described in Chapter 3. The 256 x 256 array of pixels coupled with a X2.5 objective lens gave a field of view of 6.88 x 6.88 mm, which corresponds to a resolution of 26.9 μm / pixel. The channel section xy shown in Figure 6.2 is 222 μm or approximately 8 pixels wide. This requires accurate positioning of the microreactor channel in the microscope field of view. For each captured frame of the moving dye front, the single line of pixels (with their associated intensities) running along the centre of the channel xy , across the micrograph (Fig. 6.2) was noted. These values formed the array of values for I_{dye} . The values for $I_{solvent}$ and I_{dark} were recorded by capturing the respective images of solvent filled channels and the same image with the microscope lighting removed. The combined arrays of transmitted light intensities were used to determine the on-chip absorbances A_{chip} . Clearly, given this method of data gathering, the positioning of the microreactor channel in the microscope field of view is critical to minimising data wastage. If the axis of the channel region xy was not parallel with the bottom edge of the optical micrograph shown in Figure 6.2, there would be a resulting loss of information.

6.2.3 *Imaging experiments with colloidal catalyst in suspension.*

Solutions of colloidal palladium stabilized with polyvinylpyrrolidone (PVP) were prepared over a range of concentrations from 1 to 12 % wt. / vol. (or % w/v) colloid to solvent in (1) 80 vol.% DMA (aq) with 45 mM NaBr and (2) methanol with 10 mM NaBr. Spectrophotometric calibrations were made for each solution as outlined in Section 2.1.3. The clean chip 301 was filled with carrier solvent in the channel region xy then the solvent in reservoir C was replaced with colloid solution. With 500 V applied between reservoirs A and C in Figure 6.1, concentration-imaging measurements were made using the microscope set up shown in Figure 3.3. To fully characterise the properties of each colloid solution, additional independent measurements of the particle size distribution and zeta potential were made using a Malvern 3000HS Zetasizer as described in Section 2.1.10.

6.3 **Results and discussion.**

6.3.1 *The pK_a of PADA in solutions containing 80 vol. % DMA (aq) and 45 mM NaBr.*

Equations 6.4 – 6.11 were implemented in an Excel worksheet. The measured absorbances at 450 and 550 nm for PADA and PADAH^+ given in Figure 6.4, were entered into the worksheet as can be seen in Appendix I. The spectrophotometer data for solutions A to F is listed toward the upper part of Appendix I. This was used as the calibration dataset to calculate the pK_a , K_a and extinction coefficients at 450 and 550 nm for PADA and PADAH^+ in 80 vol. % DMA (aq) with 45 mM NaBr. Fitting of the measured spectrophotometer absorbances to those predicted by equations 6.4 and 6.5 involved minimising the residuals between these two quantities for all solutions. The results of floating K_a and all four extinction coefficients to minimise the total residuals are given in the second column of Table 6.1. For these data (Figure 6.5), the best-fit pK_a

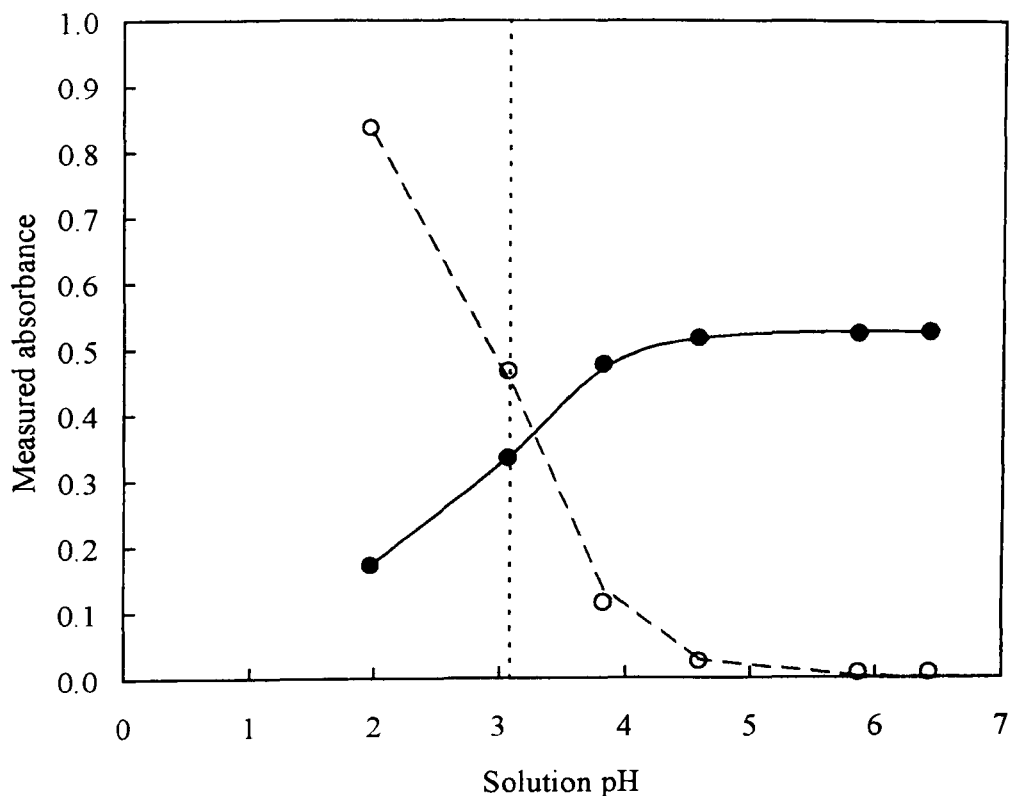
was 3.08. James and Robinson [3] report extinction coefficients for PADA and PDAH⁺ in water, which are listed in the third column of Table 6.1. They note a pK_a for PDAH⁺ in water with 25 mM SLS (sodium dodecylsulphate) of about pH 4.5. These extinction coefficients show good agreement with our calculations for 4 mM PADA in 80 vol. % DMA (aq) with 45 mM NaBr. Lastly, Fletcher *et al.* [1] reported extinction coefficients for 2.1 mM PADA in 30 vol. % ethanol (aq) with 50 mM tris buffer at pH 7.5. These values are listed in the fourth column of Table 6.1 and are very close to the extinction coefficients reported by James and Robinson [3].

Table 6.1: A comparison of calculated extinction coefficients at 450 and 550 nm for PADA and PDAH⁺ in 80 vol. % DMA (aq) with 45 mM NaBr denoted by *, to other solvent systems. Ref. 3 data is based on PADA and PDAH⁺ in water with 25 mM sodium dodecylsulphate. Ref 1 data is for PADA and PDAH⁺ in 30 vol. % ethanol (aq) with 50 mM tris buffer at pH 7.5.

Parameter	Fitted data in DMA(aq)*	Ref. 3 in water	Ref. 1 in 30 vol. % ethanol (aq)
K_a / M	8.4×10^{-4}	-	-
$\epsilon_{450}^{PADA} / M^{-1} cm^{-1}$	26309	24000	24000
$\epsilon_{550}^{PADA} / M^{-1} cm^{-1}$	64	1400	1000
$\epsilon_{450}^{PDAH^+} / M^{-1} cm^{-1}$	7218	6800	-
$\epsilon_{550}^{PDAH^+} / M^{-1} cm^{-1}$	45125	46000	-

The measured and calculated absorbances given in Appendix I are shown graphically in Figure 6.5. The vertical dashed line represents the $pK_a = 3.08$. The significance of pK_a is that at $pH = 3.08$, the PADA and PDAH⁺ concentrations are equal in the dye solution. It should be noted that the crossover point for the calculated absorbances of PADA and PDAH⁺ in Figure 6.5 only signifies the pH where both PADA and PDAH⁺ share the same absorbance value. The concentrations are not equal at this pH, like for the pK_a .

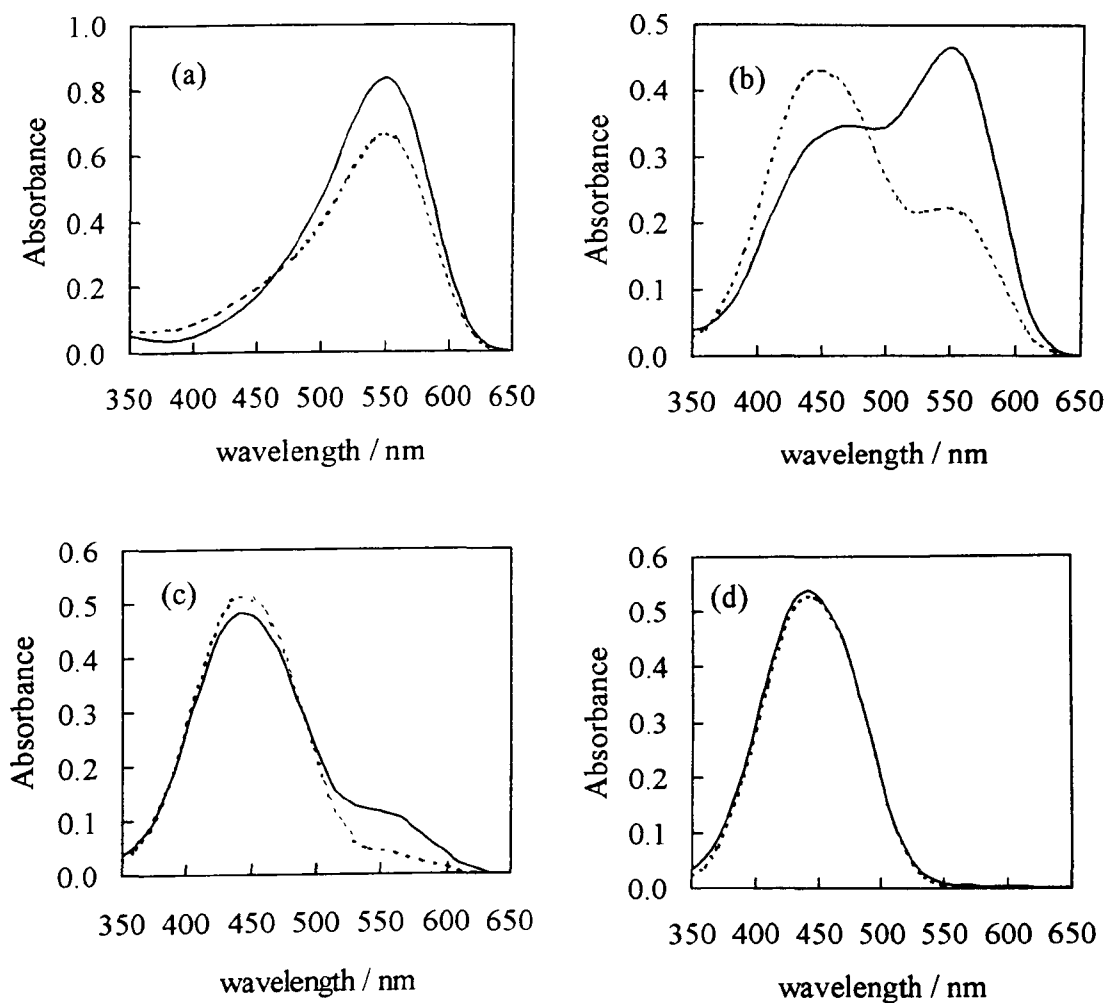
Figure 6.5: The maximum measured spectrophotometer absorbances in a 50 μm path length cuvette at 450 nm (filled circles) and 550 nm (open circles) for the solutions with varying pH listed in Figure 6.4. The vertical dashed line indicates the dye solution $pK_a = 3.08$. The theoretical absorbances for 450 nm (solid line) and 550 nm (heavy dashed line) are as calculated in Appendix I.



6.3.2 Time dependent changes of pH in the PADA dye solutions.

As a routine method of reducing experimental uncertainties, spectrophotometer calibrations were made for each dye solution on the day of use. It was noticed that the spectra of these non-buffered dye solutions changed over time and was particularly striking at pH's around the pK_a . For the experiments described in the preceding Section, solutions were chosen to cover a wide range of pH and hence PADA:PADAH⁺ ratios. The freshly prepared solutions A, B, C and F with the corresponding pH values 1.97, 3.07, 3.83 and 6.42, as listed in Appendix I, were each used for on-chip absorbance experiments. The solutions D and E were not used because the PADA:PADAH⁺ ratios were considered not significantly different to that

Figure 6.6: Time dependent changes in the absorbance spectra of dye solutions (A, B, C and F) containing 4 mM PADA in 80 vol. % DMA (aq) with 45 mM NaBr. All solid lines represent the original spectra of the freshly prepared solution. The dotted lines represent the spectra of the solution on the day each experiment was made. (a) corresponds to the dye solution with an original pH of 1.97, and the spectral change after after 18 days. Similary (b) pH 3.07 and change after 21 days, (c) pH 3.83 and change after 24 days (d) pH 6.42 and change after 25 days.



of solution F. The spectra for each of these dye solutions recorded when freshly prepared and then when used for the on-chip experiments, were seen to show varying degrees of spectral shift over time as shown in Figure 6.6. The corresponding measured pH of solutions A, B, C and F on the day each on-chip experiment was performed were 2.40, 3.55, 4.43 and 6.48. The largest spectral shift and pH change occurred for the dye solution with the starting pH closest to the pK_a , which was solution B (Fig.6.6 b). In

these non-buffered dye solutions the change in pH was always toward higher values. Calculated pH values based on the absorbance data in Figure 6.6 yield pHs of 2.43, 3.56, 4.39 and 5.45 for the “aged” solutions A, B, C, and F respectively. This shows that the observed dye solution pH change is not driven by the dye species reacting with the solvent, but in fact could be the constituents of the solvent reacting with one another. Similar time dependent changes in the pH of the solvent solutions containing only 80 vol. % DMA (aq) with 45 mM NaBr were also noticed. For the concentration-imaging experiments described in the next Section, the aqueous DMA carrier solvent was matched for conductivity and pH to the dye solutions. The maximum measured difference in each of these quantities on the day of the on-chip experiment was no greater than $\pm 100 \mu\text{S cm}^{-1}$ and ± 0.2 pH. In conclusion, this time dependent change in the pH of the dye solutions was not a problem when independent spectrophotometric calibrations were made before each experiment.

6.3.3 Concentration-imaging of PADA dye solutions.

For dye solutions containing comparable concentrations of both PADA and PADAH^+ (such as solutions A, B and C), it was expected that there might be two moving dye fronts formed because of the different mobilities of PADA and PADAH^+ . Due to the relative extinction coefficients for PADA and PADAH^+ at 450 and 550 nm, it was considered more likely to see two fronts at a wavelength of 450 nm. A series of micrographs recorded in the channel section xy (Fig. 6.2), for solution C at 450 nm, indeed reveals the presence of two fronts (Figure. 6.7). This observation is enough to obtain a simple qualitative understanding of the production of two fronts, but is not sufficient to demonstrate the measurement of on-chip concentrations using the microscope set up given in Figure 3.3. It was chosen to compare the measured

Figure 6.7: A series of micrographs recorded at 450 nm in chip 301 for the dye solution C, which has a pH of 4.43. 500 V was applied across reservoir electrodes A and C (Fig 6.1). The first frame (a) was taken approximately 5 minutes after application of the voltage. Subsequent frames (b), (c), (d), (e) and (f) are consecutive micrographs taken at 2 min intervals.

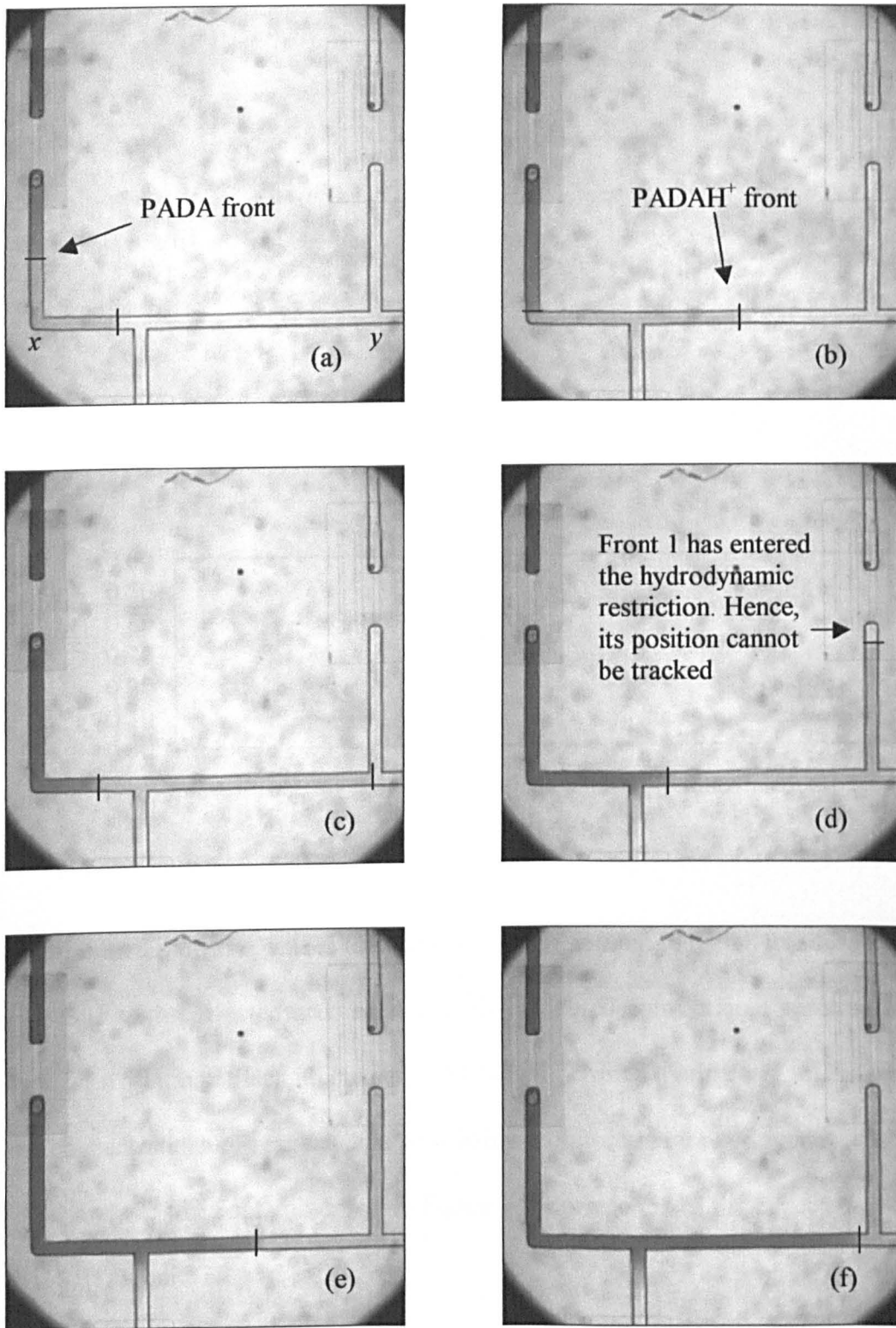
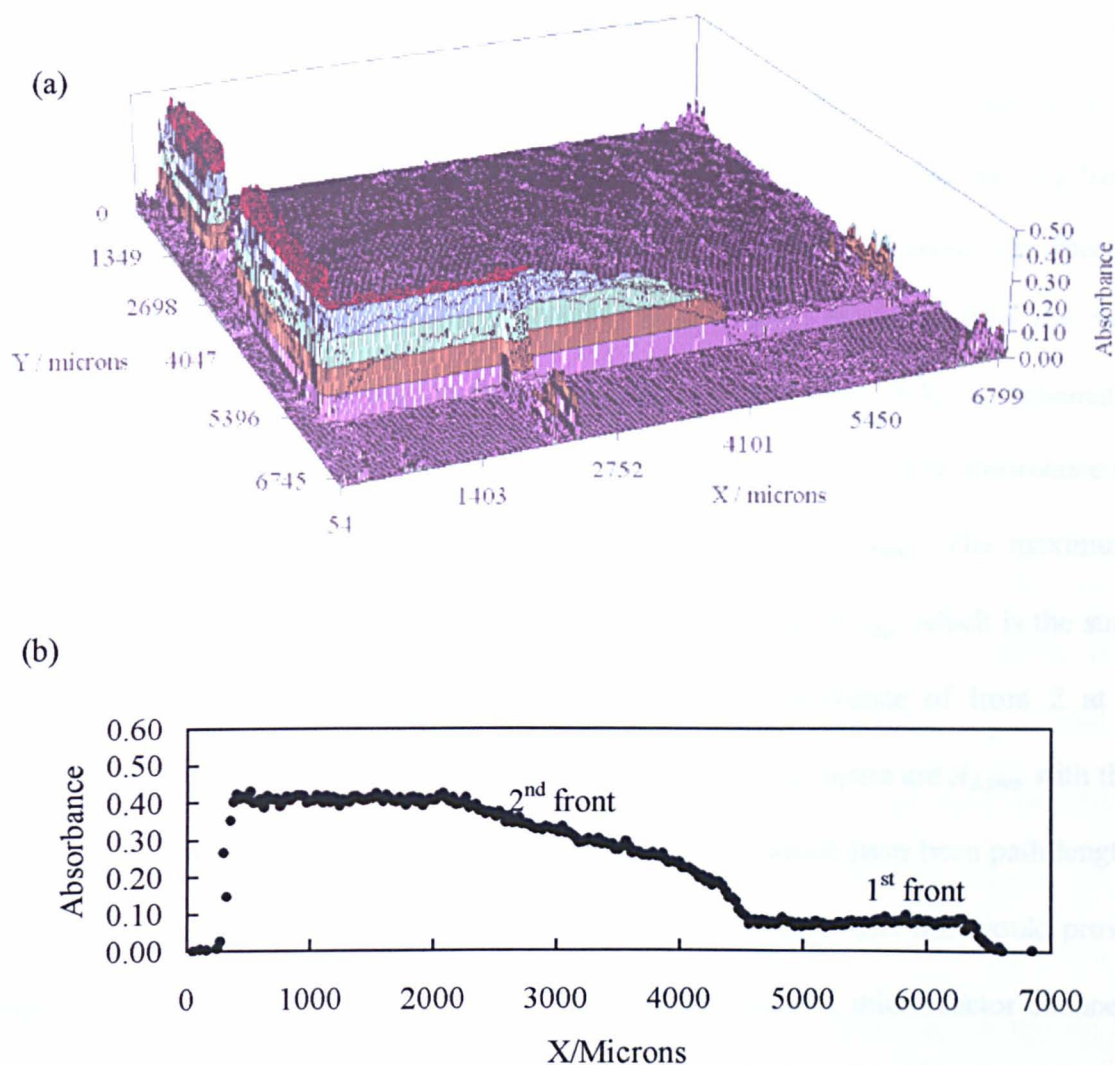


Figure 6.8: (a) An absorbance image derived from the optical micrograph shown in Figure 6.7 (c) for dye solution C. (b) Slice of data taken along the X-axis from Figure 6.8 (a) at Y = 5396 microns. This corresponds to channel section xy in Figure 6.2.

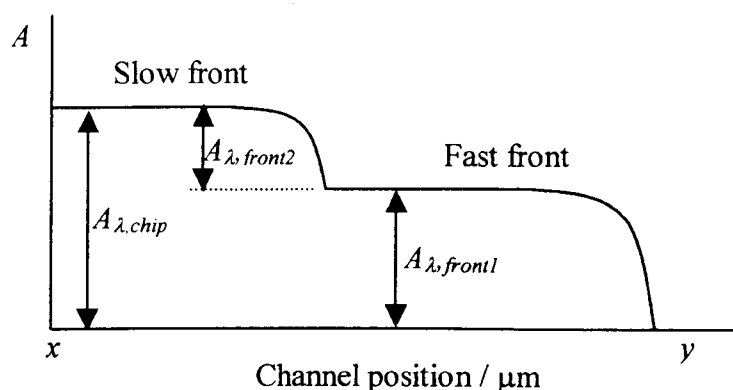


microscope absorption values obtained at 450 and 550 nm in the 38 μm deep channel of chip 301 with corrected and independently measured conventional spectrophotometer data for a 50 μm path length cuvette. This would permit experimental validation that (1) the concentrations of reagents can be reliably monitored in a microreactor channel ($A_M \propto C$) and (2) the fronts observed in Figure 6.7 correspond to the expected PADA and PDAH⁺ species.

For the micrograph shown in Figure 6.7 (c) a 3D absorbance plot can be produced as shown in Figure 6.8 (a). A further absorbance profile that lies along the central axis of channel length xy can be selected as shown in Figure 6.8 (b). Consider the absorbance plot given in Figure 6.8 (b); the microscope camera monitoring this moving front is only able to distinguish between absolute values of absorbance, such as those that occur at each plateau of constant absorbance, after a front has passed. The first fast moving front that we believe to be composed of PADAH^+ is straightforward to measure. The second front with the lower velocity (probably arising from PADA) is obscured by the first front and therefore requires further clarification. In Figure 6.9, a schematic representation of the front scenario given in Figure 6.8 (b) is shown. The absorbance of the first front at a given wavelength λ is simply defined as $A_{\lambda,front1}$. The maximum absorbance measured via the microscope camera is defined as $A_{\lambda,chip}$, which is the sum of the absorbance of front 1 and front 2. Hence, the absorbance of front 2 at a wavelength λ is given by $A_{\lambda,front2}$. The important variables to compare are $A_{\lambda,chip}$ with the maximum measured spectrophotometer absorbance values which have been path length corrected i.e. $A_{\lambda,38\mu m}$. These values in theory should be the same and this would prove that concentrations of reagents could be reliably monitored in a microreactor channel. Comparison of $A_{\lambda,front1}$ with calculated absorbances for PADAH^+ at 450 and 550 nm (which were derived from measured spectrophotometer data), would prove that the fronts observed in Figure 6.7 (and particularly the first front) are actually the predicted PADA species.

The moving front data recorded in chip 301 for solutions A, B, C and F is shown in Figures 6.10 – 6.13. The abrupt rise in the absorbance values at about $X = 0.5$ mm

Figure 6.9: Schematic representation of the fronts shown in Figure 6.8 (b) with the associated absorbances A defined in terms of wavelength λ and front number.



for Figures 6.10 – 6.13, corresponds to the start of the channel section xy and the position from where absorbance data was recorded for the moving front analysis. The average absorbance value A_{ave} reported for each plot was calculated from the largest possible data range. Frequently level absorbance plateaus of at least 50 data points were used. The summarised A_{ave} values are sorted according to the definition given in Figure 6.9, into measured on-chip absorbances $A_{450,chip}$ and $A_{550,chip}$ and measured spectrophotometer absorbances that have been path length corrected i.e. $A_{450,38\mu m}$ and $A_{550,38\mu m}$. These absorbance values are shown graphically in Figure 6.14. It can be seen that for each solution, the absorbances measured on-chip at 450 nm and 550 nm are in good agreement with those measured independently with a conventional spectrophotometer. The relatively high uncertainty in the measured absorbances arises from a combination of imperfect reservoir emptying into the channel, dilution of the dye solution when filling the reservoirs and front distortion from going around the right-angled channel geometry [4]. This demonstrates that concentrations of PADA can be reliably monitored in a microreactor channel.

The on-chip absorbance data recorded for front 1 in Figures 6.10 – 6.13 is

Figure 6.10: Plots of dye front absorbance vs. channel position for solution A at pH 2.40. Runs were made at 500 V in 38 μm channel depth at a wavelength of (a) 450 nm (b) 550 nm. A_{ave} is the average front absorbance and σ is the standard deviation.

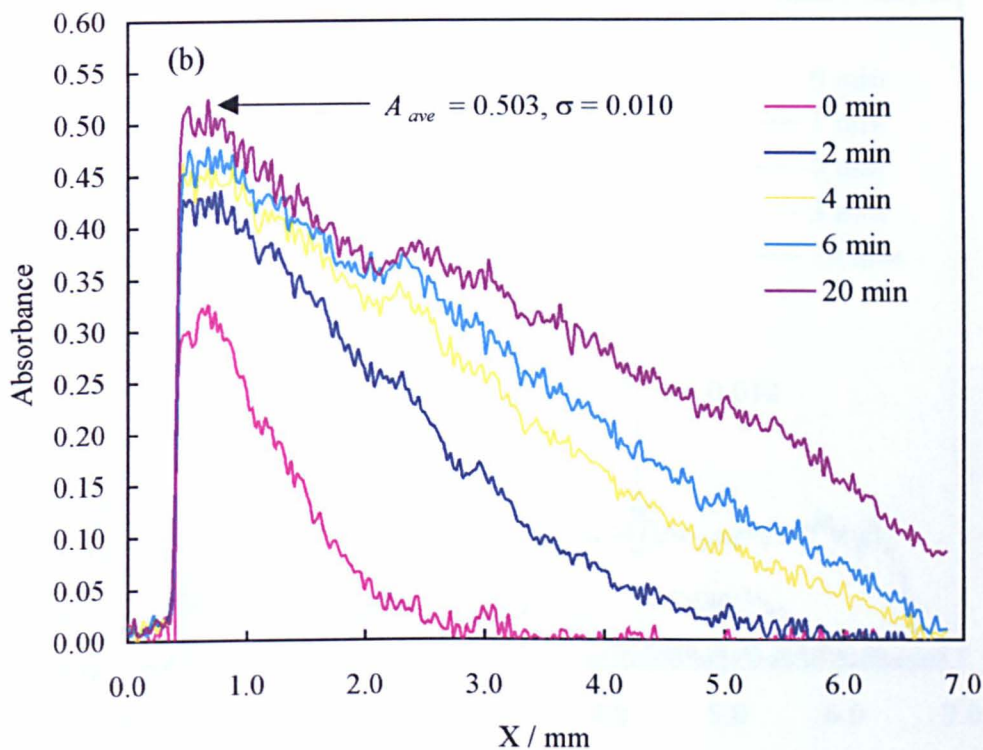
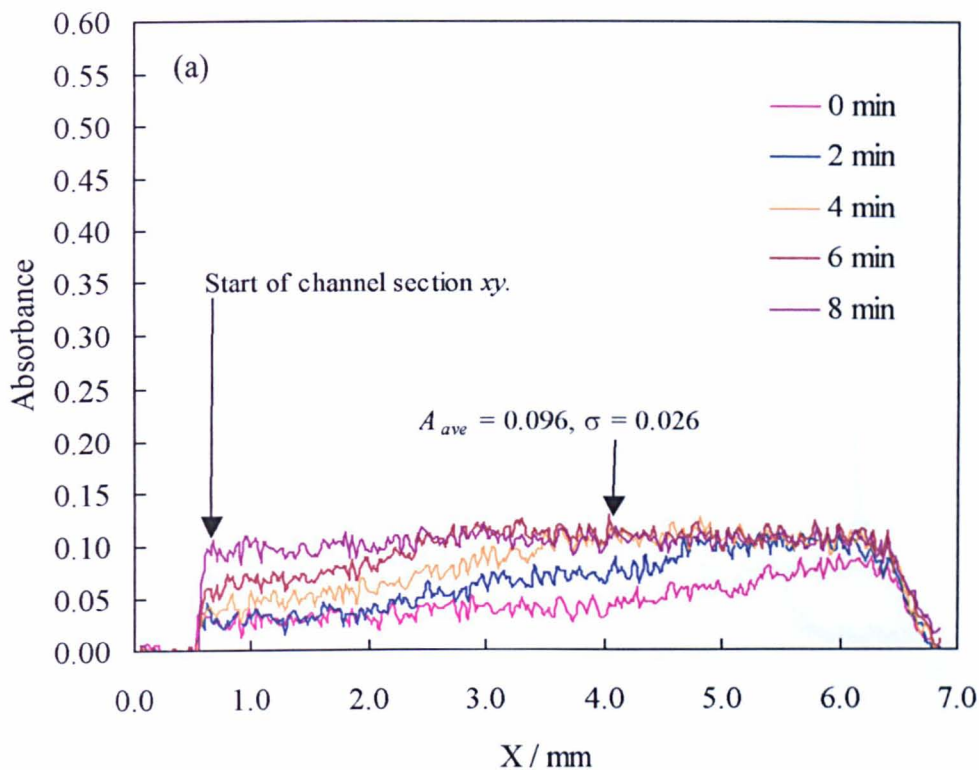


Figure 6.11: Plots of dye front absorbance vs. channel position for solution B at pH 3.55. Runs were made at 500 V in 38 μm channel depth at a wavelength of (a) 450 nm (b) 550 nm.

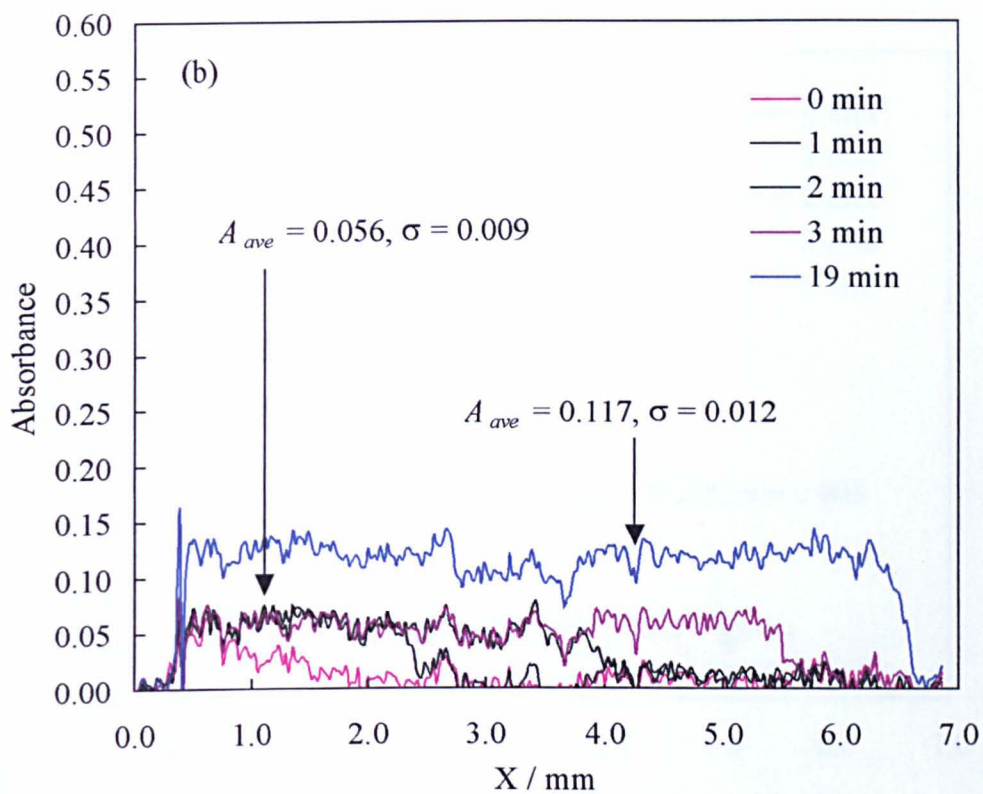
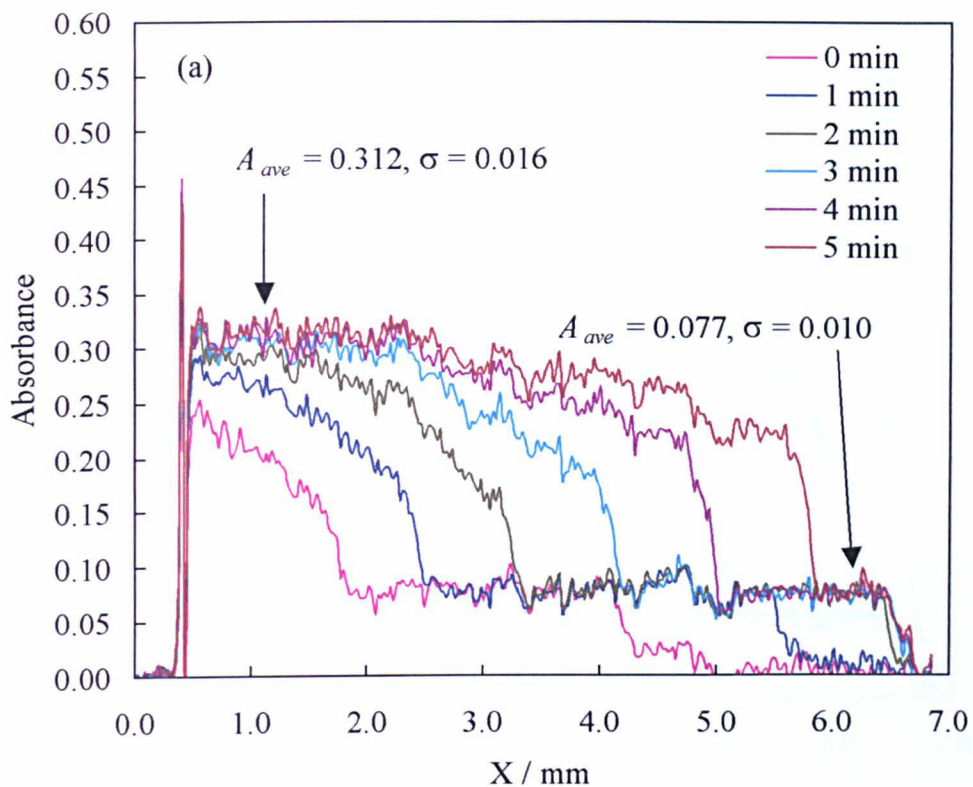


Figure 6.12: Plots of dye front absorbance vs. channel position for solution B at pH 4.43. Runs were made at 500 V in 38 μm channel depth at a wavelength of (a) 450 nm (b) 550 nm.

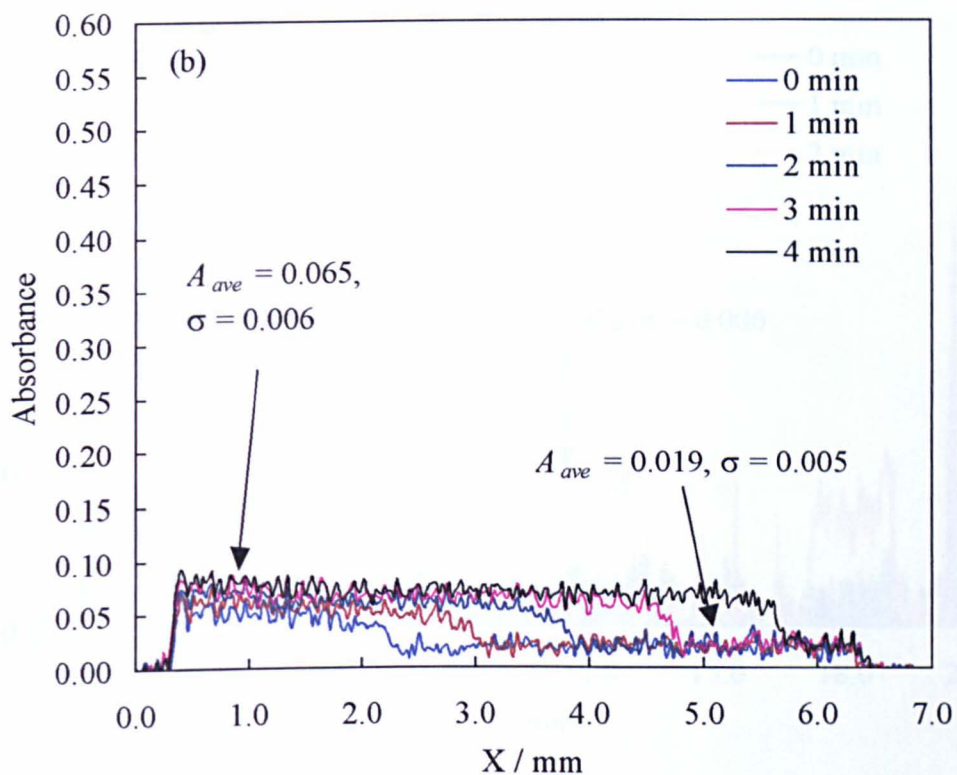
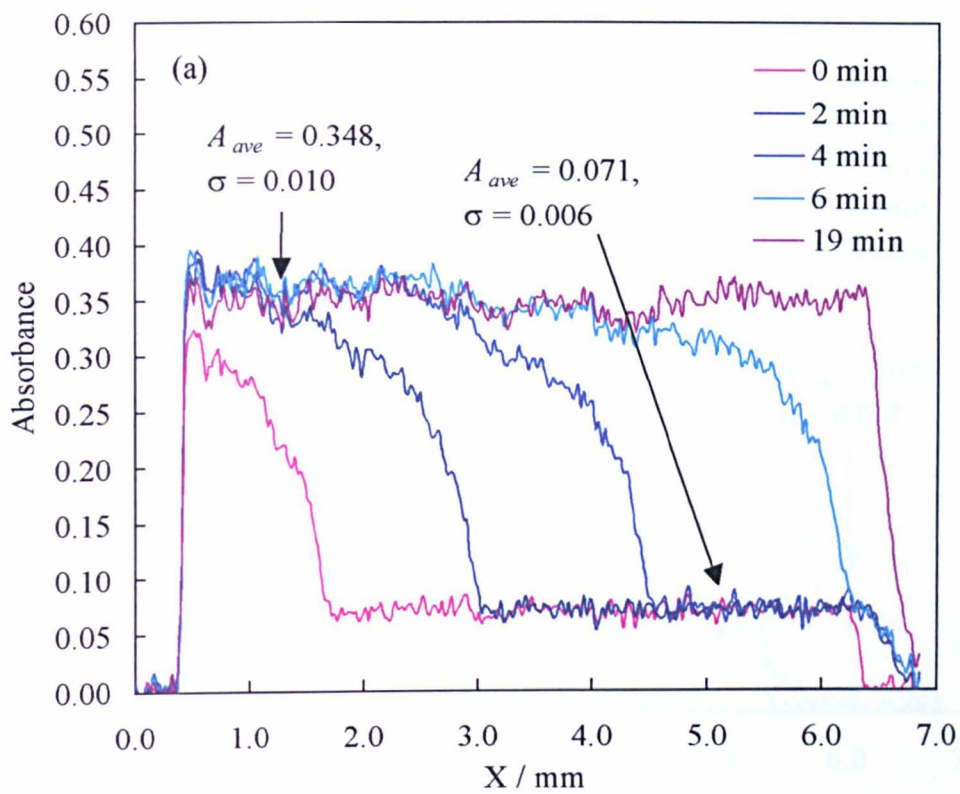


Figure 6.13: Plots of dye front absorbance vs. channel position for solution B at pH 6.48. Runs were made at 500 V in 38 μm channel depth at a wavelength of (a) 450 nm (b) 550 nm.

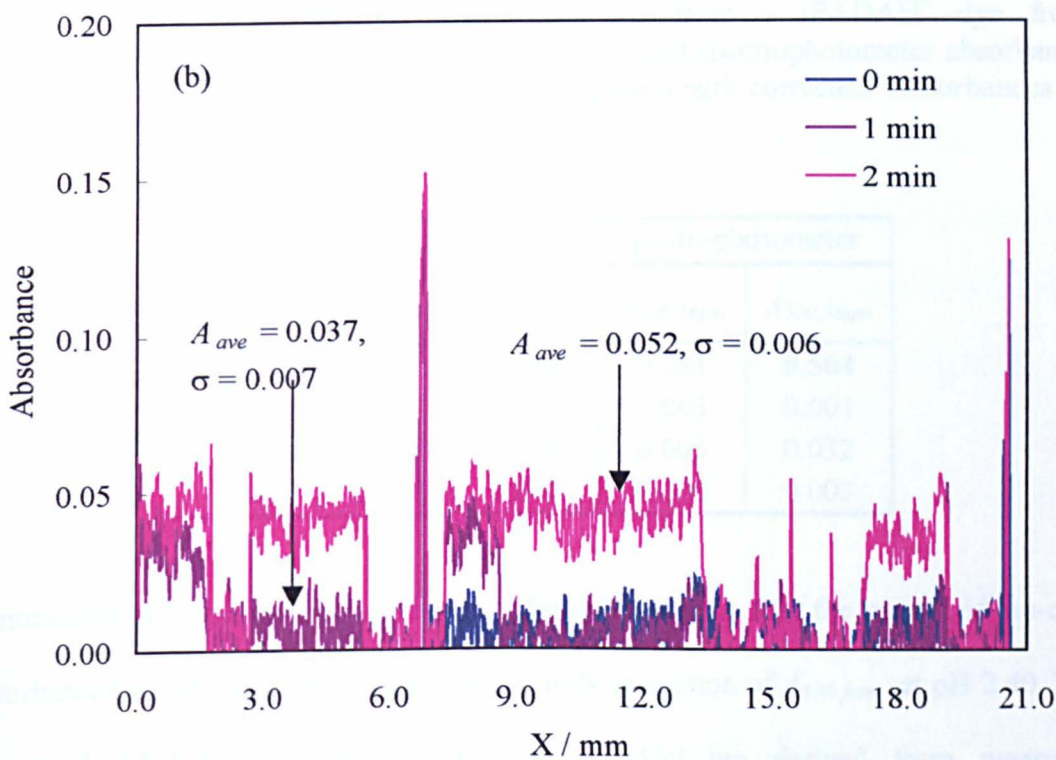
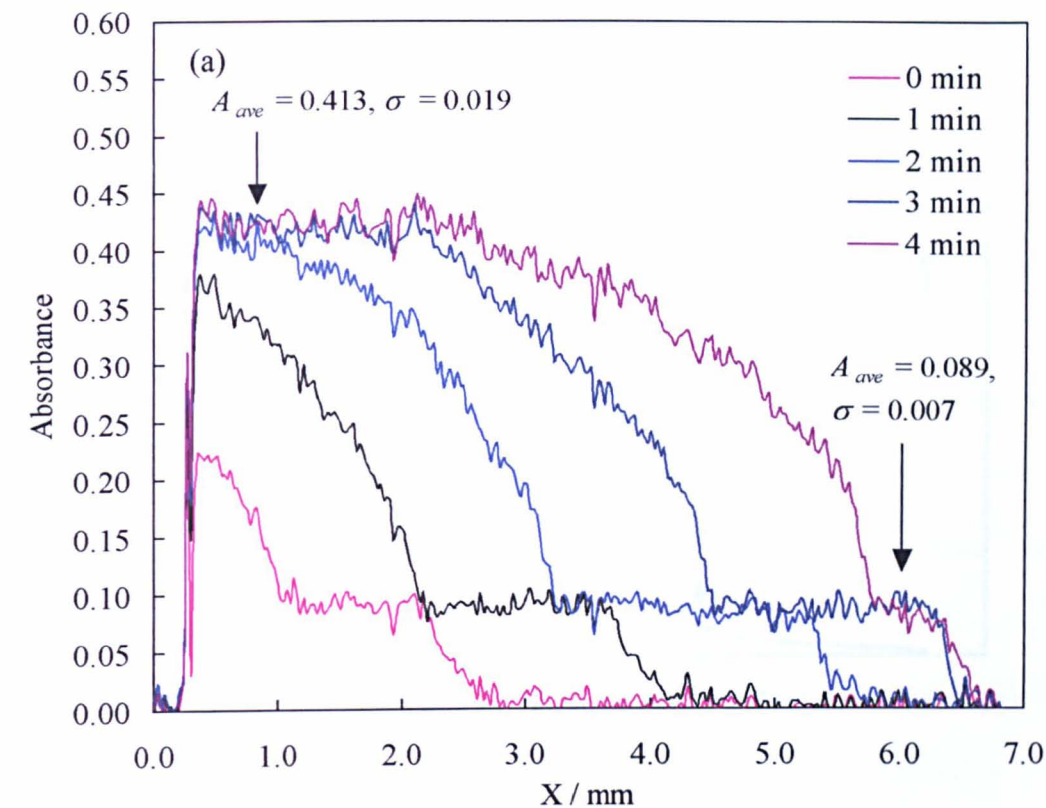


Figure 6.14: Plot of measured on-chip absorbances and spectrophotometer absorbances as a function of dye solution pH. The dotted line represents $A_{450,38\mu\text{m}}$ and the solid line $A_{550,38\mu\text{m}}$. The open circles represent $A_{450,\text{chip}}$ and the filled circles $A_{550,\text{chip}}$. The estimated uncertainty in measured absorbances is ± 0.04 .

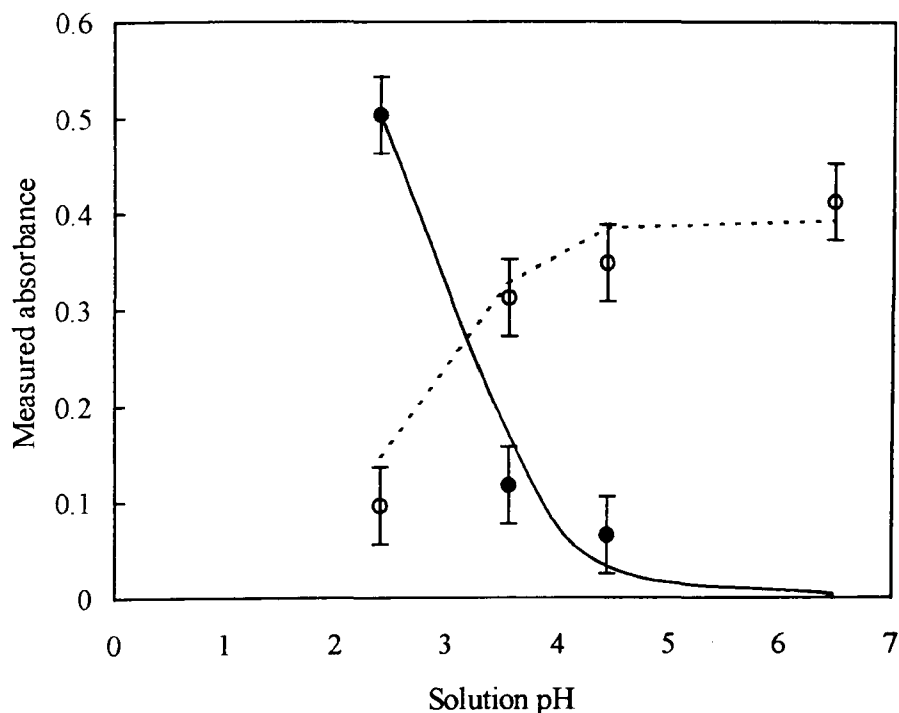


Table 6.2: Tabulated on-chip absorbances for front 1 (PADAH⁺ dye front) determined from Figures 6.10 – 6.13 and spectrophotometer absorbances values for front 1 that have been path length corrected. Absorbances are defined in Figure 6.9.

Solution pH	On-chip		Spectrophotometer	
	$A_{450,\text{front1}}$	$A_{550,\text{front1}}$	$A_{450,38\mu\text{m}}$	$A_{550,38\mu\text{m}}$
2.40	-	0.503	0.081	0.504
3.55	0.077	0.056	0.003	0.001
4.43	0.071	0.019	0.005	0.032
6.48	0.089	0.052	0.000	0.003

summarised in Table 6.2. It can be seen from Table 6.2, that the measured on-chip absorbances are all extremely small with the only exception of $A_{550,\text{front1}}$ at pH 2.40. The calculated PADAH⁺ absorbances at 450 and 550 nm derived from measured

spectrophotometer absorbances, are listed in the last two columns of Table 6.2. These values are also extremely small with the exception of $A_{550,38\mu\text{m}}$ at pH 2.40. The on-chip and spectrophotometer absorbances for PADAH^+ are effectively the same within an estimated level of uncertainty of ± 0.04 . The results of this investigation strongly suggest that front 1 consists of only PADAH^+ species.

6.3.4 *PADA and PADAH^+ dye front velocities in 80 vol. % DMA (aq) with 45 mM NaBr as a function of applied voltage and pH.*

To complete the investigation of how mobilised dye fronts behave in a microreactor channel under voltage-driven flow conditions, it was decided to monitor the velocity of dye fronts (composed entirely of PADA or PADAH^+) as a function of applied voltage. Two solutions containing 4 mM PADA in 80 vol. % DMA (aq) with 45 mM NaBr were adjusted to a pH of 6.54 and 2.47 for this purpose. The solution with the higher pH consisting predominantly of PADA, had a bulk solution conductivity of 0.120 S m^{-1} and corresponding channel section resistances R_{Ax} , R_{xy} and R_{yC} of 7.51, 2.33, and 7.36 $\text{M}\Omega$ respectively. The solution with the lower pH, consisting predominantly of PADAH^+ had a conductivity of 0.233 S m^{-1} and channel section resistances of 3.87, 1.20 and 3.79 $\text{M}\Omega$ respectively. The choice of pH for the dye solution was based on the pH dependent ratio of PADA: PADAH^+ concentrations. At extremes of pH, one PADA species will always be present in excess. This situation helps simplify the experiment by presenting only one moving front for examination.

Front velocity profiles of PADA and PADAH^+ were recorded over time as shown in Figures 6.15 and 6.16. It can be seen from Figures 6.15 (e) and 6.16 (e) that the front velocities increase with increasing voltage. Recalling from Section 1.3.5, the dye front moves with a total velocity v_{total} equal to the vector sum of the electroosmotic and

electrophoretic velocities. For the uncharged PADA dye front, we would expect this to move along at the electroosmotic velocity of the bulk solvent given by:

$$v_{eof} = -\frac{E\varepsilon_0\varepsilon_r\zeta}{\eta} \quad (6.12)$$

where E is the electric field strength, ε_0 is the permittivity of free space, ε_r is the relative permittivity of the liquid, ζ is the zeta potential of the solid-liquid interface and η is the liquid viscosity. Similarly, we would also expect the electrophoretic velocity of the PADAH^+ front relative to the bulk solvent movement to be given by:

$$v_{eph} = \frac{zeED}{kT} \quad (6.12)$$

where z is the integer charge number, e is the electronic charge, E is the electric field strength, D is the diffusion coefficient, k is the Boltzmann constant and T is the absolute temperature. The dye front velocities as a function of electric field strength are shown in Figure 6.17. From this Figure, as expected, it can be seen the velocity of the PADAH^+ front is higher than that of the PADA for a given value of E . The gradient of the trend line fitted to the open triangles gives the electroosmotic mobility μ_{eof} of the 80 vol. % DMA (aq) with 45 mM NaBr. The (dynamic) viscosity and relative permittivity of 80 vol. % DMA (aq) was calculated to be 0.9268 cP and 46.183 at 24 °C (Appendix F and G). The best-fit zeta potential for the microreactor glass-80 vol. % DMA (aq) with 45 mM NaBr was found to be -4 ± 1 mV. This zeta potential is in excellent agreement to that of -4 ± 2 mV for the same solvent system which was determined in Chapter 5 and demonstrates reproducible self-consistency between two independent flow rate methods.

Figure 6.15: Plots of front position versus time for PADA front moving along channel section xy . Measurements were made at pH 6.54 in chip 301 at 450 nm and with an applied voltage of (a) 150, (b) 300, (c) 450 and (d) 600 V. The velocity profiles for these dataset are summarised in (e).

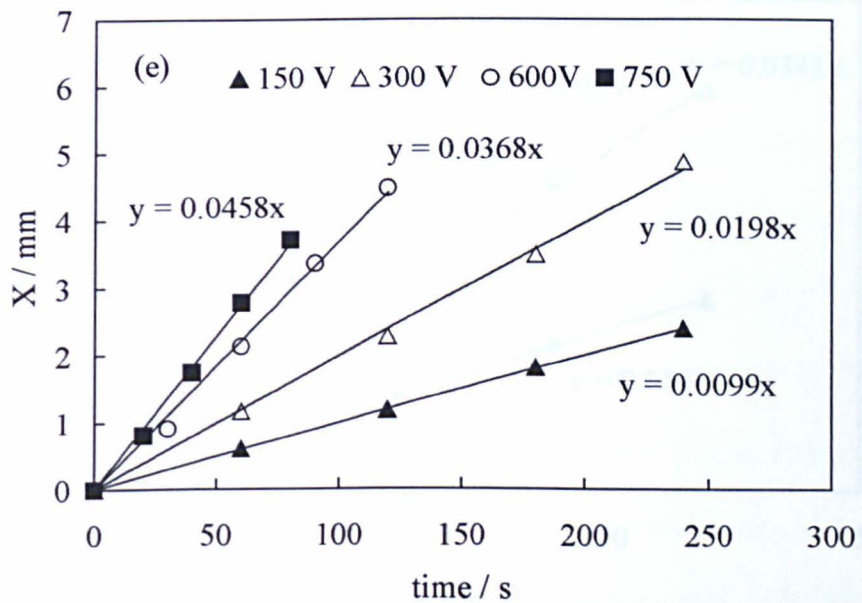
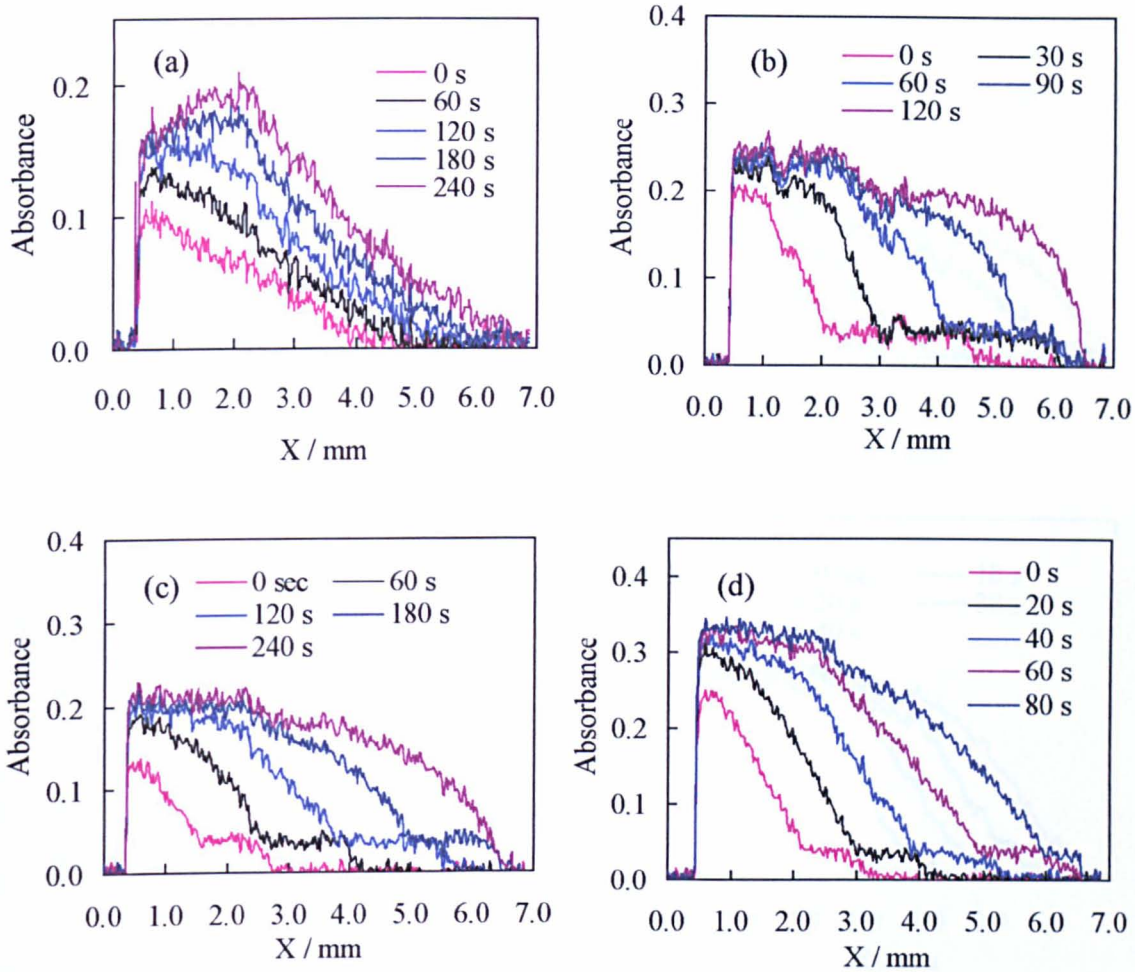


Figure 6.16: Plots of front position versus time for PADAH^+ front moving along channel section xy . Measurements were made at pH 2.47 in chip 301 at 550 nm and with an applied voltage of (a) 150, (b) 300, (c) 450 and (d) 600 V. The velocity profiles for these dataset are summarised in (e).

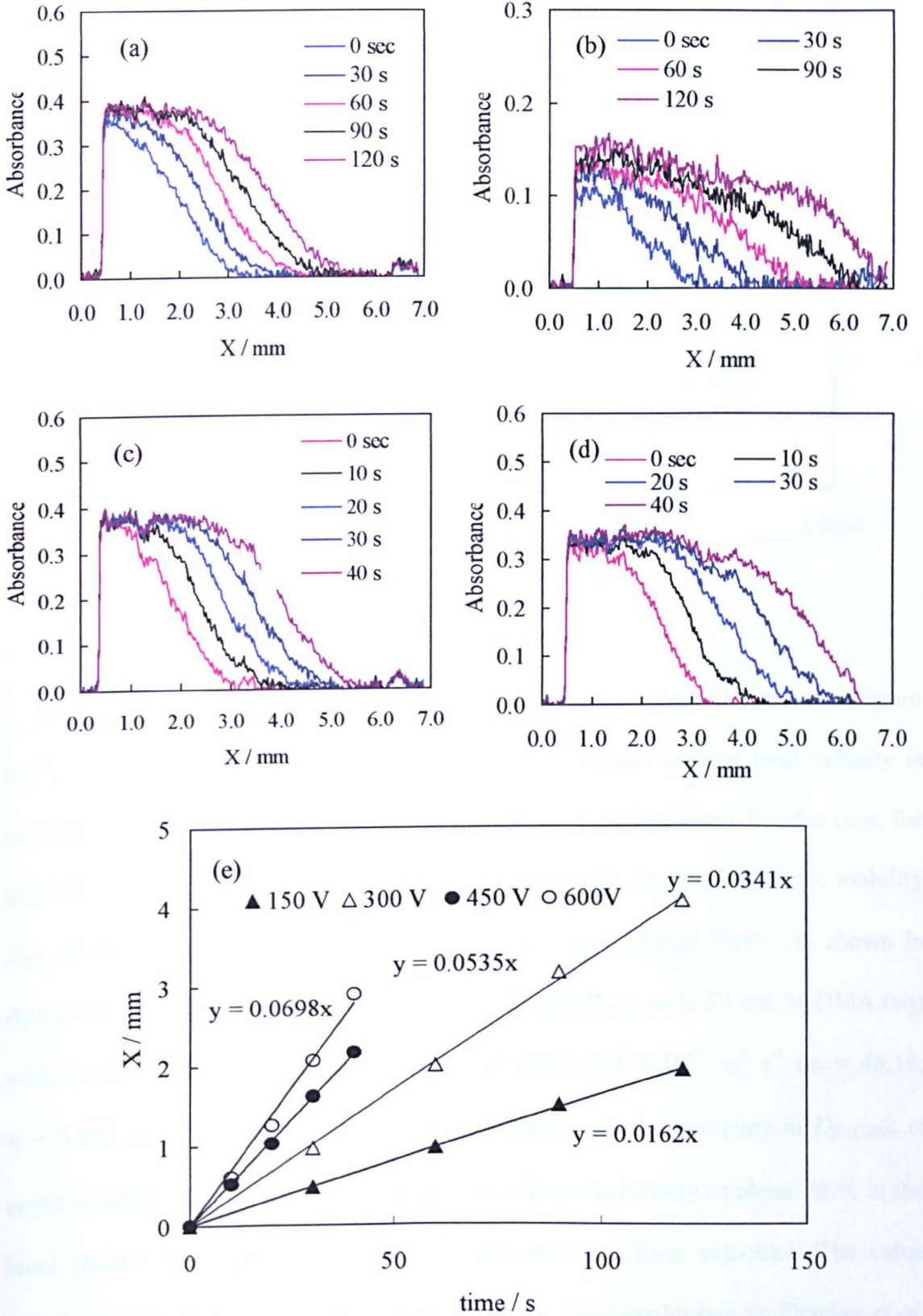
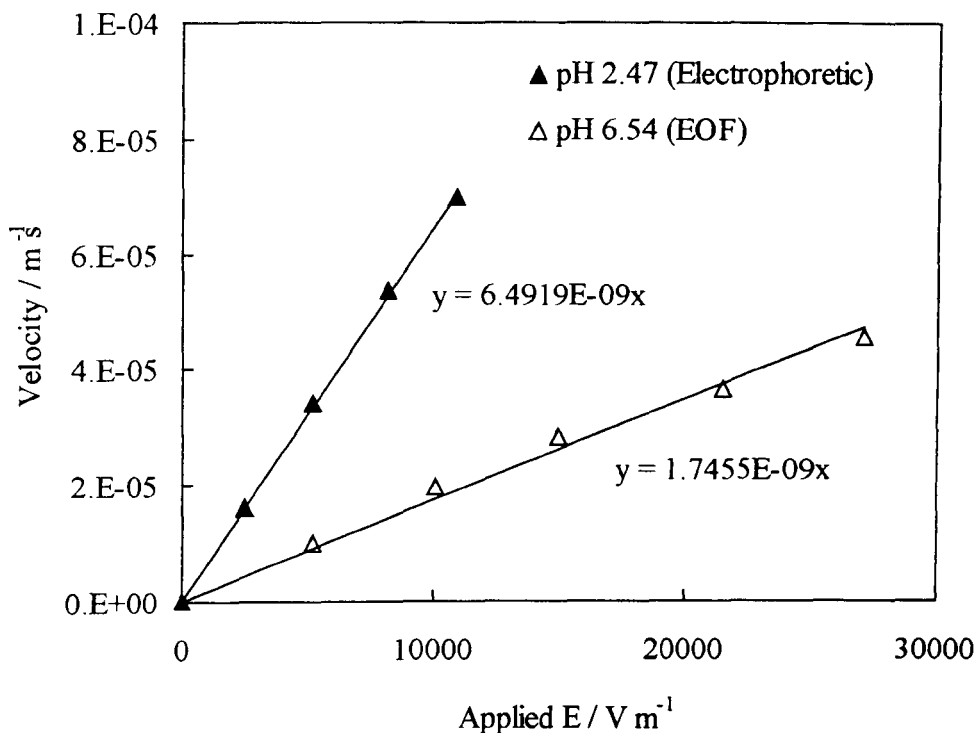


Figure 6.17: Plot of front velocity versus electric field strength. The filled triangles with the greater slope represent the electrophoretic velocity of the moving PADAH^+ front. The open triangles represent the slower moving electroosmotic PADA front.

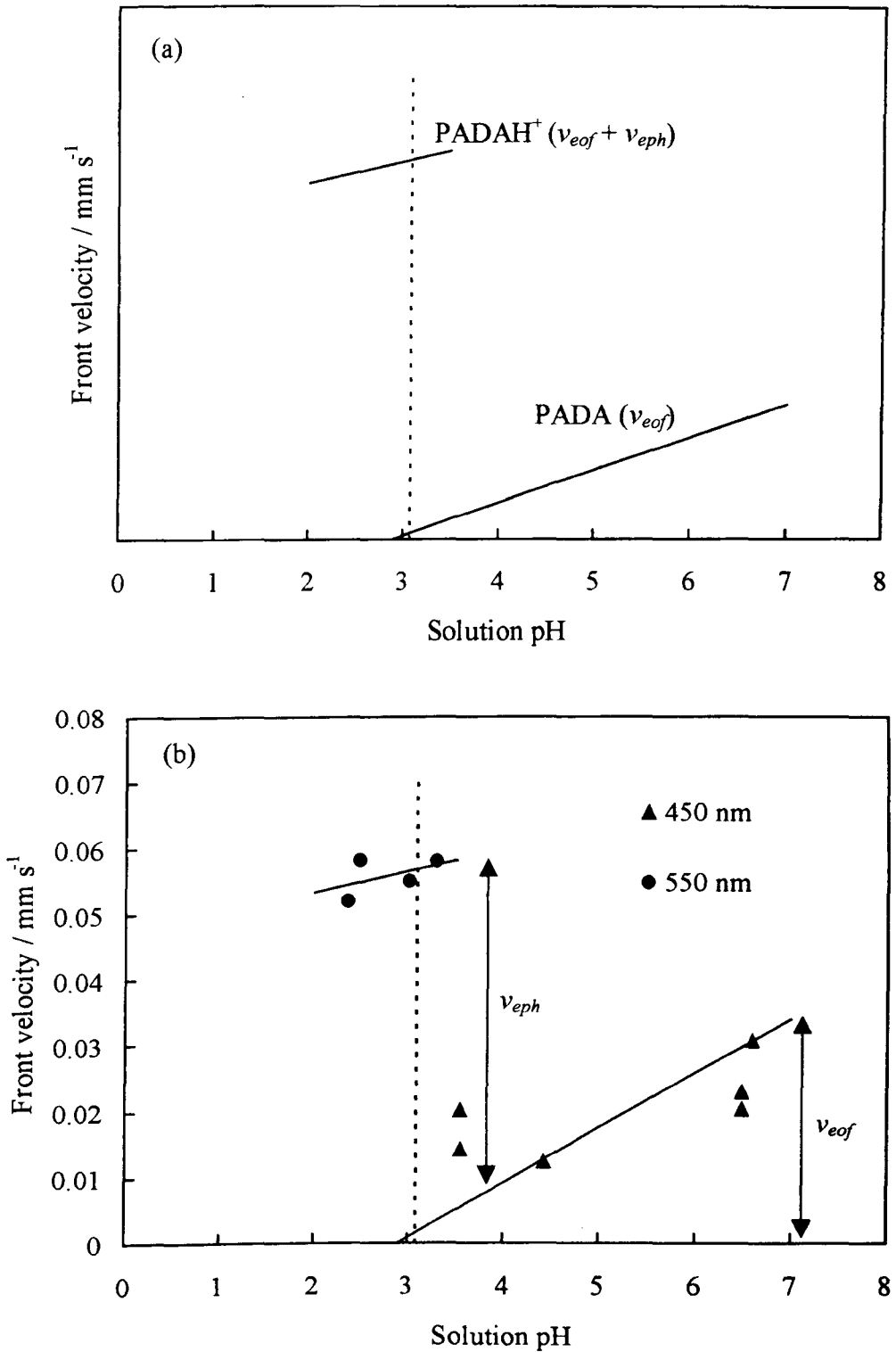


In order to determine the electrophoretic velocity of the PADAH^+ front in Figure 6.17, it must be assumed that the electroosmotic component of total front velocity is negligibly small relative to the electrophoretic velocity (justified later). For this case, the gradient of the trend line fitted to the filled triangles gives the electrophoretic mobility μ_{eph} of the PADAH^+ ions in 80 vol. % DMA (aq) with 45 mM NaBr. As shown in Appendix J the diffusion coefficient for PADAH^+ ions D_{PADAH^+} in 80 vol. % DMA (aq) with 45 mM NaBr was calculated to be approximately $2 \times 10^{-10} \text{ m}^2 \text{ s}^{-1}$ ($\epsilon_r = 46.18$, $\eta = 0.927 \text{ cP}$, $\kappa_o = 2.33 \text{ mS cm}^{-1}$ at $24 \text{ }^\circ\text{C}$). The estimated uncertainty in D_{PADAH^+} is approximately $\pm 30 \%$ which primarily arises from an uncertainty of about 20% in the local electric field strengths and 10% in the measured front velocities. The value calculated here for D_{PADAH^+} compares well with the results published by Fletcher *et al.*

[1] for 2 mM PADA in 30 vol. % ethanol (aq) with 50 mM Tris buffer. A full understanding of the comparisons made here requires some discussion of the theory. Fletcher *et al.* [1] report a diffusion coefficient for PADA of $4 \times 10^{-10} \text{ m}^2 \text{ s}^{-1}$ at pH 7.5 ($\epsilon_r = 64$, $\eta = 0.975 \text{ cP}$, $\kappa_o \approx 1 \text{ mS cm}^{-1}$). Due to a combination of ionic relaxation and electrophoretic retardation effects as described by Debye-Huckel-Onsager theory [5] and the small increase in molecular volume from additional atoms in the molecule (i.e. PDAH⁺ in comparison to PADA), Fletcher *et al.* [1] estimated that the diffusion coefficient of NiPADA²⁺ is approximately 50 % lower than for PADA. Considering η is approximately the same and κ_o for 30 vol. % ethanol (aq) with 50 mM Tris buffer (pH 7.5) is about half of that for 80 vol. % DMA (aq) the 45 mM NaBr (pH 2.5), an estimate of D for PDAH⁺ of $2 \times 10^{-10} \text{ m}^2 \text{ s}^{-1}$ in 80 vol. % DMA (aq) with 45 mM NaBr would not be unrealistic. In this analysis the effect of scaling for the volume change between PADA and PDAH⁺ on the estimated diffusion coefficient is less than that estimated by Fletcher *et al.* [1] in scaling from NiPADA²⁺ to PADA. The electrophoretic retardation effects on the estimated diffusion coefficient of PDAH⁺ though, are likely to be much greater due to the higher dissolved electrolyte concentration.

As shown in Table 1.3, the zeta potential for a glass-aqueous solution interface varies widely with pH. On this basis, to determine the electrophoretic velocity of the PDAH⁺ front, it was assumed that the zeta potential at the interface between a glass channel and a solution of 80 vol. % DMA (aq) with 45 mM NaBr would also follow a similar trend. Given the zeta potential for the aqueous system in Table 1.3 was approximately zero mV at pH 2.5 and the zeta potential measured earlier for 80 vol. % DMA (aq) with 45 mM NaBr was -4 mV at pH 6.54, the assumption made for Figure 6.17, that the electroosmotic component of total front velocity is negligibly small appears justified. A

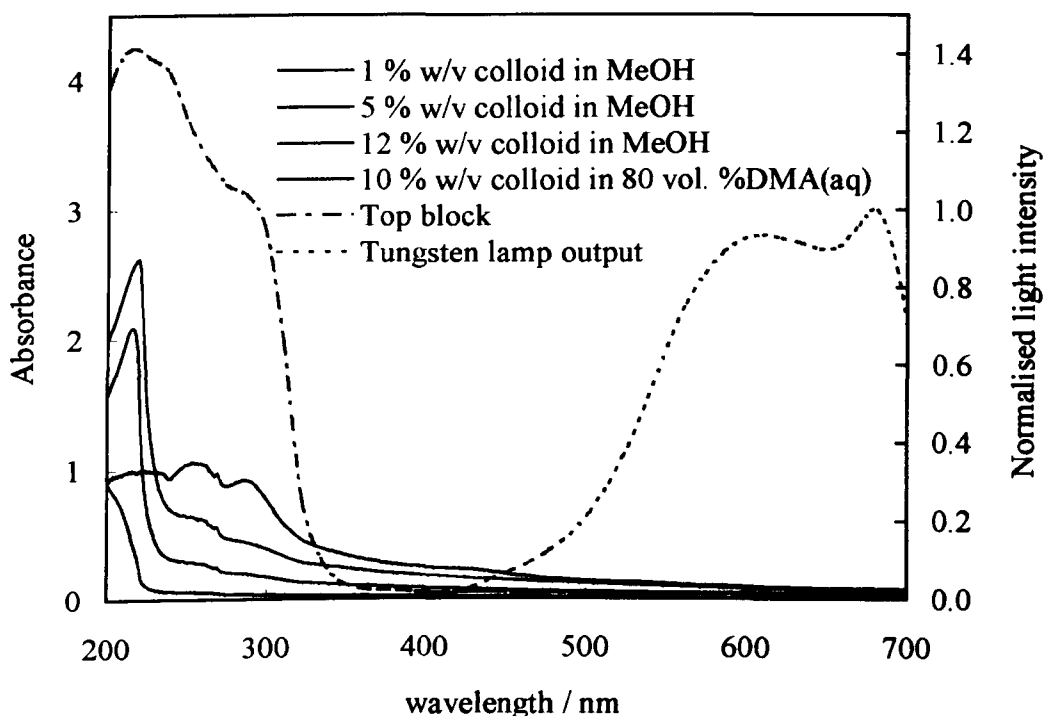
Figure 6.18: (a) Schematic plot of PADA and PADAH^+ front velocity profiles as a function of pH at fixed V_{AC} for solutions containing 80 vol. % DMA (aq) and 45 mM NaBr in chip 301. The vertical dashed line represents the pK_a of the PADA dye solutions. (b) Summary of all front velocities recorded at different pH and fixed $V_{AC} = 500$ V. The filled triangles represent bulk electroosmotic movement and the filled circles the bulk plus the electrophoretic movement of the charged PADAH^+ dye species.



schematic plot of how the dye front velocities are expected to change with pH is shown in Figure 6.18 (a). Both the PADA and PADAH^+ fronts are expected to be pH dependent because of the electroosmotic movement of the solvent bulk. The pH range covered by each line in Figure 6.18 (a) shows the pH range over which PADA and PADAH^+ dominate. A comprehensive summary of all the front velocity data sets for PADA and PADAH^+ work described here is shown in Figure 6.18 (b). It can be seen that the measured front velocities vary with pH. The important feature of the graph which validates the assumption for the diffusion calculations made earlier, is that the electroosmotic velocity of the bulk solvent is approximately zero at pH 2.5 relative to the electrophoretic velocity of the PADAH^+ .

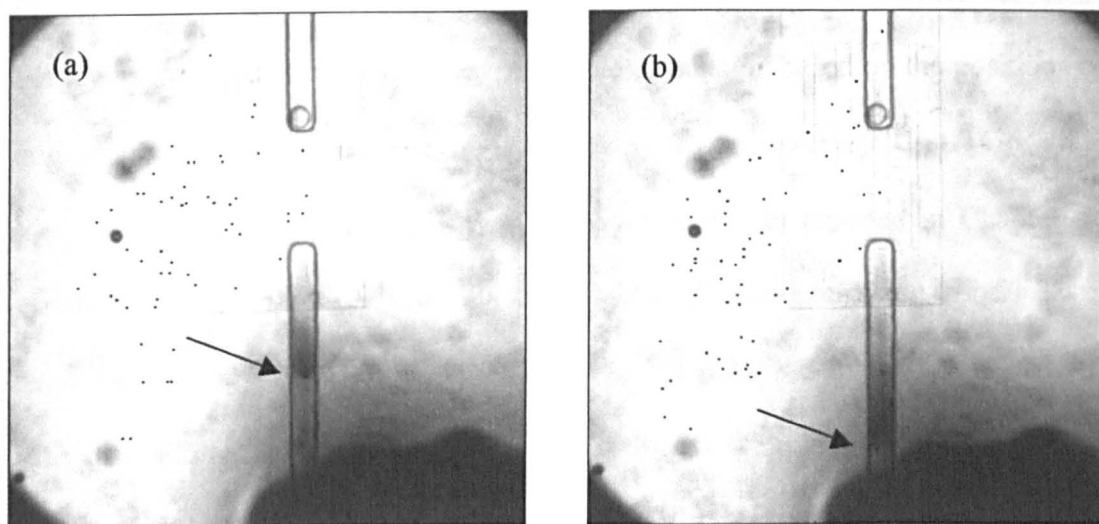
6.3.5 Absorbance-imaging of colloidal catalyst in a microreactor.

Figure 6.19: A plot of measured absorbance of the Pd colloid in solutions of methanol and 80 vol. % DMA (aq) for a 50 μm path length cuvette. The absorbance of a 12 mm thick piece of Crown glass top block is added to illustrate the limiting practicalities of the absorbance imaging technique. On-chip measurements cannot be made using the absorbance-imaging technique for wavelengths below 400 nm with a tungsten lamp.



The final aspect of this work involves using absorbance imaging to characterise the microfluidic properties of a colloidal palladium catalyst sample introduced into a microreactor channel. The aim here was to monitor the velocity of a colloid front migrating along the channel section C_y in Figure 6.2 and to also determine the local concentration, electrophoretic mobility and the zeta potential of the colloidal particles.

Figure 6.20: Time lapse optical micrographs of 12 % w/v colloid in methanol with 10 mM NaBr. The dark cylindrical region at the bottom of the images is reservoir C. Initially reservoir C was set to -500 V and the colloids migrated towards the anode off the top of the image. After reversing the polarity and making reservoir C equal to -500 V, micrograph (a) was taken followed by (b) 45 s later. The field of view for these optical micrographs is 4.3×4.3 mm.



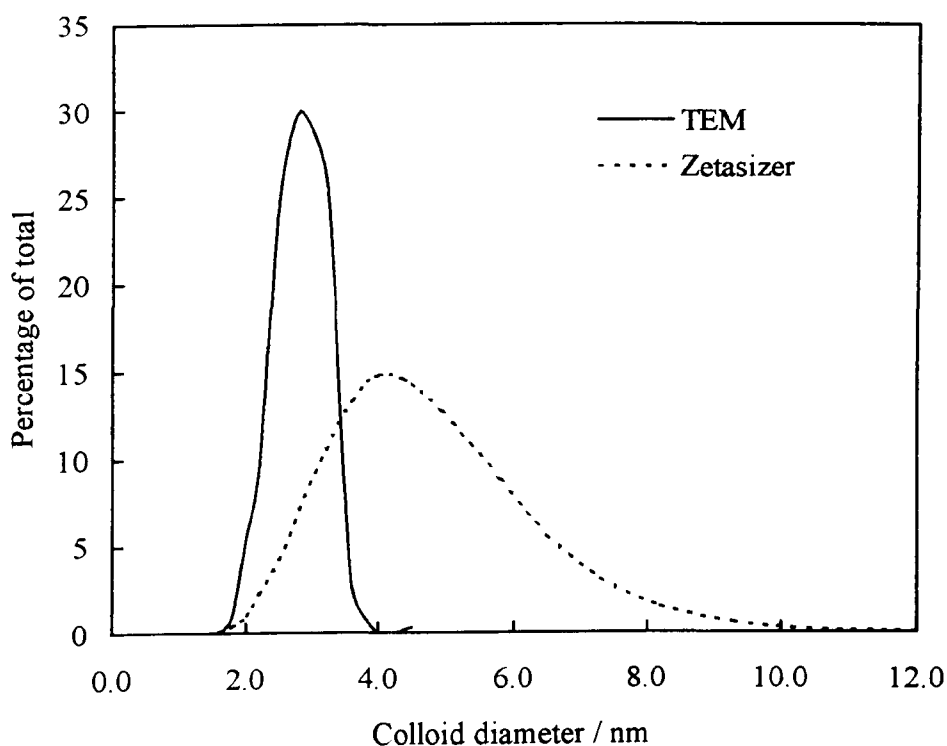
The results of spectrophotometric calibrations made in a $50 \mu\text{m}$ path length cuvette for different concentrations of colloid in (1) 80 vol.% DMA (aq) with 45 mM NaBr and (2) methanol with 10 mM NaBr are shown in Figure 6.19. It can be seen that the colloid solutions only exhibit useful levels of absorbance at wavelengths below 350 nm. In practice, this region is not accessible for the microscope optics because of the significant absorbance of the microreactor glass and the poor spectral output of the tungsten lamp. Given this, it was decided to pursue only a limited experimental investigation with colloids.

The 12 % w/v colloidal solution in methanol was chosen for concentration-imaging experiments because of its relatively high absorbance (~ 0.2 in 50 μm path length cuvette) over the wavelength range 400 – 500 nm. It was found by alternating the polarity of the electrodes and making reservoir C initially – 500 V, then + 500 V, that the colloid moved toward the anode. This observation confirmed the colloids (colloidal particles) possessed both a negative surface charge and zeta potential. It can be seen from the optical micrographs of this moving slug of colloid shown in Figure 6.20 (a) and (b), that it actually elongates (i.e. becomes longer in length) with time. This suggests that the colloid particles have a range of electrophoretic mobilities. The front of the slug indicated by the arrows in Figure 6.20, probably comprises the particles with the higher electrophoretic mobilities. A simple calculation based on the positions of the colloid front in Figure 6.20, shows it is moving toward reservoir C at $14 \mu\text{m s}^{-1}$ in a local electric field of $3.1 \times 10^4 \text{ V m}^{-1}$. From the results reported in Chapter 5, the electroosmotic mobility of 10 mM NaBr in methanol was determined to be $1.33 \times 10^{-8} \text{ m}^2 \text{ s}^{-1} \text{ V}^{-1}$ (for $\epsilon_r = 32.6$, $\eta = 5.45 \times 10^{-4} \text{ Pa s}$, $\kappa_o = 0.0978 \text{ S m}^{-1}$ and $\zeta = -25.4 \text{ mV}$). This data can be used to calculate the electroosmotic velocity of the bulk solvent i.e. 0.410 mm s^{-1} away from reservoir C. The actual electrophoretic velocity of the colloid particles is therefore 0.424 mm s^{-1} toward reservoir C.

A solution containing 1 % w/v of colloid in methanol and 10 mM NaBr was examined using the Malvern 3000HS Zetasizer. It was found that the average zeta potential for the colloidal particles was – 140 mV ($\epsilon_r = 32.6$, $\eta = 0.545 \text{ cP}$, $\kappa_o = 0.0861 \text{ S m}^{-1}$ and $\mu_{eph} = 7.39 \times 10^{-8} \text{ m}^2 \text{ s}^{-1} \text{ V}^{-1}$). Using this independent measure of the electrophoretic mobility of the colloid particles, the electrophoretic velocity of the front in Figure 6.20 was estimated to be 2.3 mm s^{-1} . Clearly, discrepancies exist between the

measured electrophoretic velocities of the colloid front, obtained using concentration-imaging and calculated from the Malvern Zetasizer data. The reason for this probably lies with the high concentration of colloid particles used in the concentration-imaging experiment and their close proximity reducing the observed zeta potentials.

Figure 6.21: The Pd colloid has an average dry core diameter of 3.7 nm which was determined by TEM (Transmission Electron Microscopy) and a mean hydrodynamic diameter of 4.2 nm in methanol. This hydrodynamic diameter was measured using a Malvern 3000HS Zetasizer and a 1 % w/v colloid solution concentration (see Section 2.1.10).



Size distribution measurements were made of a solution containing 1 % w/v of colloid in methanol and 10 mM NaBr using the Malvern 3000HS Zetasizer (Section 2.1.10). The reported size distribution for the colloids in methanol and the dehydrated particles are shown in Figure 6.21. The mean hydrodynamic diameter of colloidal particles in methanol was found to be 4.4 nm, whereas the average dry core diameter established using TEM (Transmission Electron Microscopy) and reported by Blackmond *et al.* [6], was noted to be 3.7 nm. These measured size distributions shown

in Figure 6.21, are valid for the 1 % w/v colloid sample but probably not at higher colloid concentrations (such as 12 % w/v) where particle aggregates can form.

Based on the limitations of the concentration-imaging technique to access useful colloid absorbances in a microreactor channel and the high colloid concentrations required to perform even the most basic moving front investigation, concentration-imaging is obviously not the best way of determining the electrophoretic mobility of colloidal particles. From the limited investigations performed here, a more sensitive technique is required to monitor colloid movement in a channel at much lower concentrations. An upgrade of the existing concentration-imaging technique is possible by using it in conjunction with another analytical technique such as fluorescence microscopy. The idea of tagging colloid particles with a fluorescent dye so they could be tracked in a microreactor channel at much lower concentrations is one possible area for future investigation.

6.4 Summary.

It has been demonstrated in this Chapter that concentration-imaging is a viable way of tracking a moving front of dye solution, which has been mobilised in a microreactor channel under voltage-driven flow conditions. Recorded electrical current, voltage and front velocity data has been used to calculate the relevant solvent characteristics such as zeta potential and diffusion coefficients. A demonstration of the self-consistency between absorbance-imaging and previously outlined flow rate methods has been shown for 80 vol. % DMA (aq) with 45 mM NaBr by obtaining a zeta potential of -4 ± 2 mV.

An investigation using the concentration-imaging technique to characterise the microfluidic properties of a colloidal palladium catalyst was made with some limited success. It was found that there was a range of electrophoretic mobilities for colloid samples in methanol. Due to the high colloid concentrations required to obtain the necessary absorbance for on-chip measurements, reduced electrophoretic mobilities were noted. Independent measurements made using a Malvern Zetasiser showed that at low colloidal concentrations the particles in methanol had a zeta potential of -140 mV. Due to the microreactor glass absorbing at specific wavelengths (Fig. 6.19), it was not possible to use concentration-imaging to determine further quantitative data. Through moving front observations, the colloidal particles were concluded to have a negative zeta potential.

6.5 References.

- [1] P. D. I. Fletcher, S. J. Haswell & X. Zhang, *Lab on a Chip*, 2002, 2, 102.
- [2] P. W. Atkins, *The elements of physical chemistry*, 2nd edn. (1996) Oxford University Press, Oxford, p182.
- [3] A. D. James & B. H. Robinson, *J. Chem. Soc. Faraday Trans. 1*, 1978, 74, 10.
- [4] J. M. MacInnes, *Chem. Eng. Sci.*, 2002, 57, 4539.
- [5] P. W. Atkins, *Physical Chemistry* (1990) Oxford University Press, p760.
- [6] J. Le Bars, U. Specht, J. S. Bradley & D. G. Blackmond, *Langmuir*, 1999, 15, 7621.

7. COMBINED ELECTROOSMOTIC AND PRESSURE-DRIVEN FLOWS IN CHANNEL NETWORKS.

7.1 Introduction: *The necessity to model and measure combined flows on-chip.*

In previous chapters, the effects of various combinations of Laplace, hydrostatic and electroosmotic pressures have all been successfully modelled by using the approach of considering the least number of variables as possible to simplify the modelling. The final thrust of this project is to consider all these pressures as a combined entity and incorporate them into a theoretical framework combining electrical and hydrodynamic resistances. Previous studies of flow in micro-channel networks have mainly employed computational fluid dynamic methods to understand the microscopic details of flow patterns on a micron length scale, particularly in the region of a single channel junction [1-7]. Although yielding valuable microscopic information, these highly computer intensive methods do not currently yield the overall relationships between applied pressures and voltages and the macroscopic flow patterns within a total channel network of even moderate complexity. With a view to “bridging the gap” between fluid dynamic specialists and the end-users of microreactors, the aim is to provide an accessible analysis methodology for the quantitative prediction of the overall voltage / pressure / flow pattern relationships for entire microreactor channel networks. With such a tool, microreactors could be designed to have the correct geometries to give the required electroosmotic and hydrodynamic flow rate characteristics. This would avoid the spoilage associated with the previously hit and miss fabrication process [8].

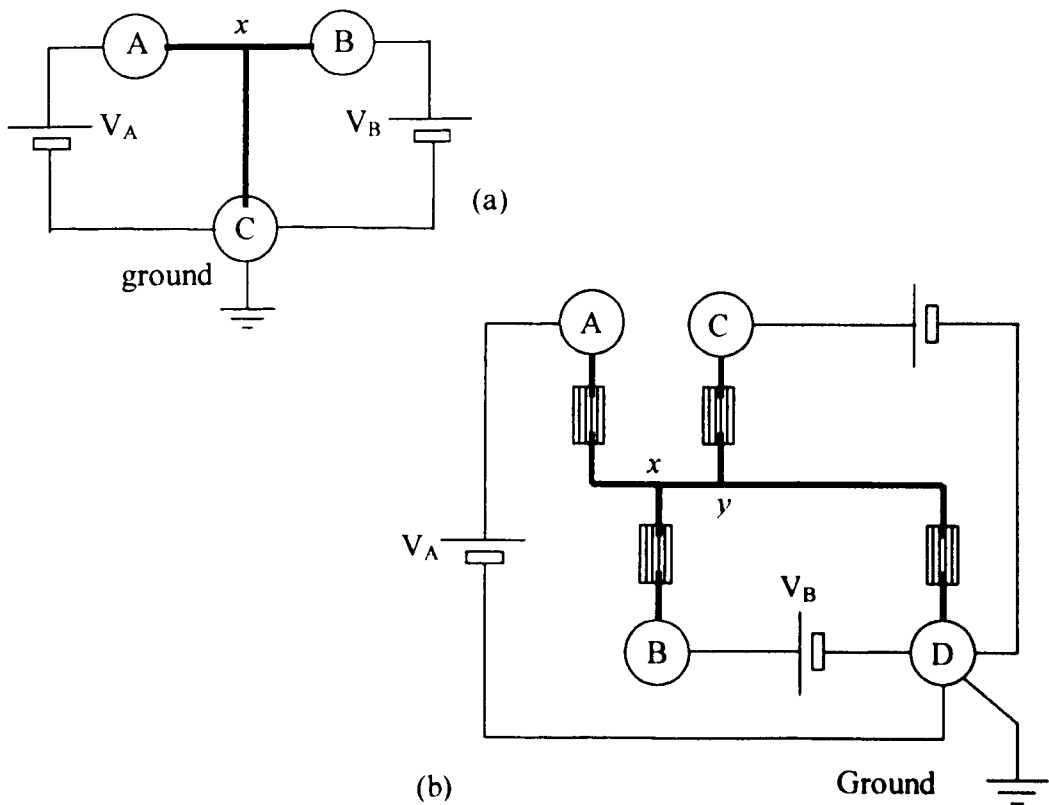
7.2 Apparatus and theory.

7.2.1 Microreactor dimensions and reservoir arrangements.

To investigate the combined electroosmotic and pressure-driven flows on-chip, two

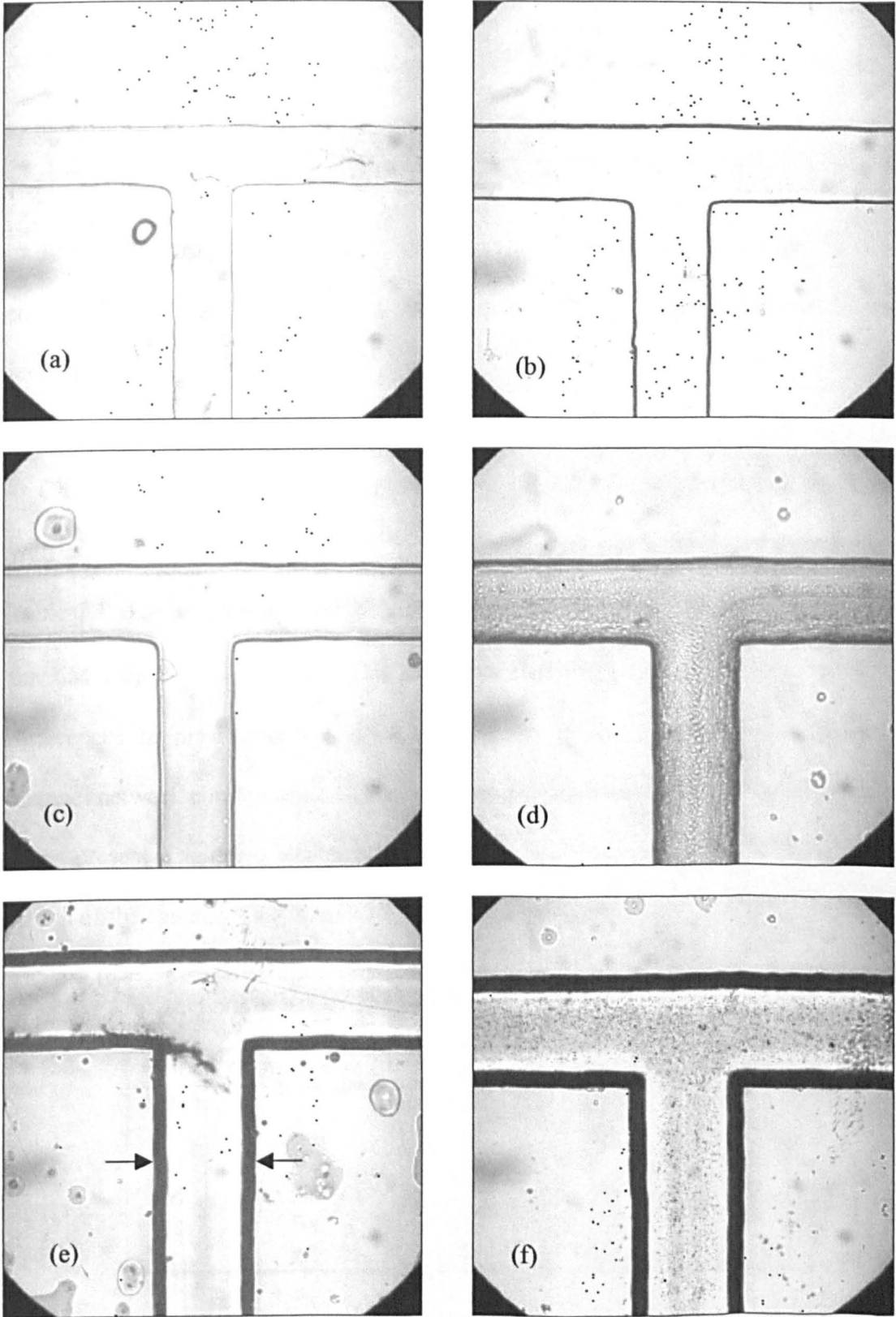
simple T-chip networks shown in Figure 7.1 (a) of different channel dimensions were chosen to compare against a double T-chip shown in Figure 7.1 (b) with hydrodynamic restrictions. The two T-chips (designated 6M and 12M) were etched according to procedure 5, listed in Table 2.1 (pg 72) and the double T-chip (designated chip 303), was etched according to procedure 6 listed in Table 2.1. All chips used in this study were thermally bonded according to procedure 3 listed in Table 2.2.

Figure 7.1: Channel network configurations and external electrical connections for (a) T-chip design with no hydrodynamic restrictions and (b) double T-chip with hydrodynamic restrictions as used in combined analysis.



Actual micrographs of chips 6M and 12M can be seen in Figure 7.2 (d) and (f). This series of micrographs is for a run of chips that were etched for between 1 and 12 min as outlined in Section 2.1.1. They were all made using a common channel mask line width of $107.5 \mu\text{m}$. When compared, the micrographs show an increasingly thick black line that outlines the edge of the channel. This line originates from the steep channel

Figure 7.2: Micrographs of a series of thermally bonded T-chips made using an Axiovert S100 inverted microscope with X20 objective lens. The base plates of these chips were etched for (a) 1 min (b) 2 min (c) 4 min (d) 6 min (e) 10 min and (f) 12 min etch. The arrows in (e) indicate true width of channel. Each micrograph shows a $860 \times 860 \mu\text{m}$ field of view.



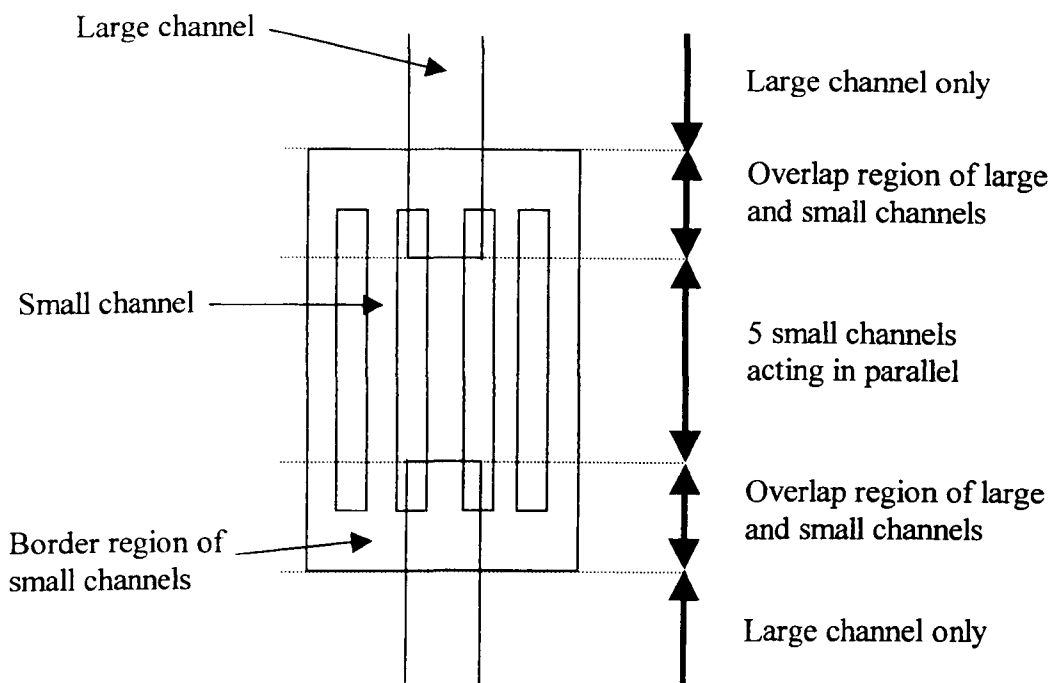
side being viewed at grazing incidence from above which prevent the transmission of light in this region. The true edge and width of the channel w , is indicated by the arrows shown on Figure 7.2 (e). The reason for choosing chips 6M and 12M for this investigation was two fold: firstly, the chips were required to be repeatedly used and remain free from particulate blockage; secondly, the internal geometry of the chips had to be sufficiently different in order to observe differences in pressure-driven flow. Chips 1M to 4M became blocked with fine grade Jeweller's Rouge polish (particulates $\sim 1 \mu\text{m}$ in diameter) shortly after thermally bonding. The remaining chips 10M and 12M were considered but due to our second requirement 12M was chosen for the flow rate investigations.

Chips 6M and 12M were depth profiled using the 3D method developed in Chapter 3 with an aqueous solution of 2.1 g dm^{-3} Rose Bengal, with results as summarised in Table 7.1. The channel depth d for chip 12M is approximately $46 \mu\text{m}$ whereas that for the 6M chip is $23 \mu\text{m}$ deep. This indicates that there should be some observable differences in pressure-driven flow components of the measured total flows. The channel network configuration of the T-chips with constant channel cross-sectional area helps present a uniform electrical and hydrodynamic resistance to the flows per unit length of the channel. This is useful for modelling purposes.

Table 7.1: Measured dimensions depth d , width w and length L) for the channel sections of chips 12M and 6M.

Chip	channel section	$d / \mu\text{m}$	$w / \mu\text{m}$	L / mm
12M	Ax	47	205	6.360
	Bx	48	205	4.514
	xC	45	205	11.90
6M	Ax	24	199	5.232
	Bx	22	193	4.924
	xC	23	195	13.258

Figure 7.3: A schematic representation of a hydrodynamic restriction present in chip 303 with the different channel regions.



Since chip 303 possesses the hydrodynamic restrictions, it is the more structurally complex device of the three chips and so does not have a uniform electrical and hydrodynamic resistance to flow per unit length of channel. Indeed the hydrodynamic restrictions of chip 303 demands that the dimensional information be known for the modelling as was outlined in Chapter 5. Consider Figure 7.3; the dimensions of the large, small and overlapping regions of the hydrodynamic resistance were determined using 3D absorbance imaging with aqueous solutions of Rose Bengal. The results of this characterisation are listed in Table 7.2. As can be seen the depth of the small channels in each hydrodynamic restriction is between 10 – 13 μm . The channel depths of chip 303 are smaller than 12M or 6M and so are especially susceptible to blockage from particulate matter. Consequently as a precaution, all solutions were filtered through 200 μm Anotop 10 inorganic membrane filters (Whatman, Maidstone, England).

Table 7.2: Measured dimensions for the channel sections of chip 303. Each hydrodynamic resistance / grid contains 5 small channels. N.B. ^a The lengths refer to the sum of channel sections containing only large channels. ^b The lengths refer to the grid sections containing only small channels (Fig. 7.3). ^c The lengths refer to the sum of the grid region lengths which contain both large and small channels (shown in Fig. 7.3).

Chip	channel section	$d / \mu\text{m}$	$w / \mu\text{m}$	L / mm	L / mm (overlap)
303	Ax (large)	53	218	6.227 ^a	
	Bx (large)	50	211	5.213 ^a	
	xy (large)	53	218	3.378 ^a	
	Cy (large)	53	205	4.054 ^a	
	yD (large)	50	218	7.626 ^a	
	Ax (grid)	12	173	0.56 ^b	2.124 ^c
	Bx (grid)	12	168	0.502 ^b	2.123 ^c
	Cy (grid)	10	161	0.386 ^b	2.192 ^c
	yD (grid)	13	173	0.386 ^b	2.268 ^c

The extended glass reservoir sets 1 – 3, listed in Table 2.5, were mounted into the top block of chip 003 by gluing using the procedures outlined in Section 2.1.4. Voltages were applied to the microreactor channel network via platinum wire electrodes mounted through the extended reservoirs. Voltage and current measurements were made using a Thurlby-Thandar 1906 digital multimeter with the Paragon computer controlled power supply as described in Section 2.1.8. Liquid conductivity measurements of the solutions used in these investigations were also performed as outlined in Section 2.1.9.

7.2.2 *The analogies between electrical and pressure driven flows in microreactors.*

To define the analogies between the flow of electrical current and of liquid in a microreactor, we first consider the relationship between channel cross-sectional area and the hydrodynamic resistance to pressure driven flow. For isotropic etching of glass by HF, the etched channel cross-section shape consist of a rectangle of mask line width m flanked by two-quarter circles of radius and channel depth d , as shown in Figure 3.16 (pg 112). The maximum channel width w is equal to $(m + 2d)$. As discussed in Section

3.3.3, thermal bonding of the microreactors can lead to a slight distortion from the idealised profile. Neglecting this minor distortion, the channel cross-sectional area A is given by:

$$A = (dm) + \frac{\pi d^2}{2} \quad (7.1)$$

The channel cross-sectional perimeter length C (required for the estimation of surface conduction effects, see later) is:

$$C = 2(m + d) + \pi d \quad (7.2)$$

As discussed by MacInnes *et al.* [7], the general relationship between pressure-driven volumetric flow rate F_{press} and pressure gradient involves the fluid viscosity η , channel size (for which the depth d is selected) and channel cross-sectional area according to:

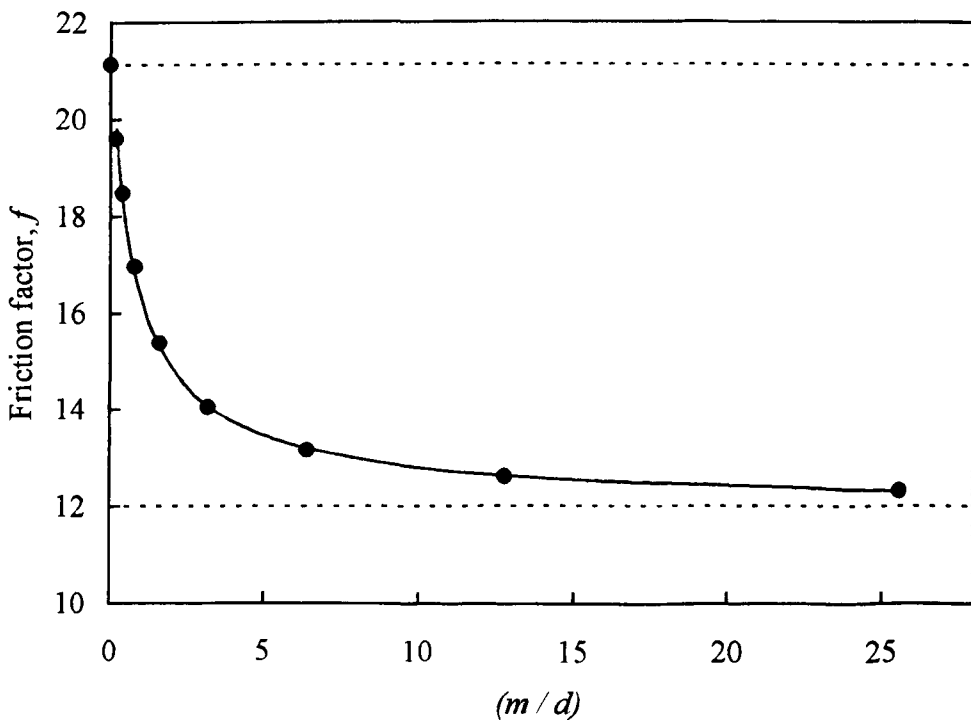
$$F_{press} = \frac{\Delta P A d^2}{L f \eta} \quad (7.3)$$

where ΔP is the pressure drop between the ends of a uniform channel section of length L and cross-sectional area A . The friction coefficient f is a dimensionless number depending only on the channel cross-sectional shape. For the isotropic etched channels considered here, the shape is parameterised in terms of the aspect ratio (m/d) . The value of f for the two limiting cases of $(m/d) = 0$ (corresponding to a semicircle) and $(m/d) = \infty$ (corresponding to infinite parallel plates) are $f = 21.115$ and 12 respectively. Values of f at intermediate values of (m/d) have been determined numerically [7] and, as shown in Figure 7.4, are described with good precision by equation 7.4, which enables the calculation of f within 1 % for any isotropically etched channel with $(m/d) > 0.2$:

$$f = 12 + \exp\left(-0.09340962(\ln(m/d))^2 - 0.5186174(\ln(m/d)) + 1.459567\right) \quad (7.4)$$

Within any channel network, the fluid flows driven by either pressure or voltage and electrical currents within individual channel sections are determined by the overall driving pressures, voltages and corresponding resistances of the different sections. For the case of electrical currents, standard methods of DC circuit analysis are used to derive the channel section currents in terms of the applied voltages and electrical resistances of the different sections. Analysis of pressure-driven fluid flows can be analysed similarly in terms of the driving pressures and hydrodynamic resistances of the channel sections [9]. Voltage-driven electroosmotic flows can also be derived using the same analysis. In this section, expressions for pressure and voltage driven flows and electrical currents are derived using related equations in terms of the corresponding

Figure 7.4: Friction factor f for an isotropic etch channel plotted as a function of the aspect ratio m/d . The horizontal dashed lines show the values of f for the limiting cases of $m/d = 0$ (semi-circle) and $m/d = \infty$ (parallel plates). Data points were taken from numerical calculations and the solid line corresponds to the fitting function described in the text.



resistance values. This procedure enables full advantage to be taken of the similarities in channel network analysis for the cases of pressure and voltage driven flows and electrical currents.

We consider the i th section of a channel network which has a length L , uniform cross-sectional area A , zeta potential ζ and is filled with a liquid of uniform electrical conductivity κ_o , relative permittivity ε_r and viscosity η . The developed volumetric flow rate F_{total} in the channel section due to pressure driven flow and electroosmosis is expressed as the sum of two terms, each involving a driving variable (i.e. pressure ΔP or voltage drop ΔV) divided by the corresponding resistance:

$$F_{total} = \frac{\Delta P}{R_{press}} + \frac{\Delta V}{R_{eof}} \quad (7.5)$$

The resistance to pressure driven flow R_{press} is (from Equation 7.2):

$$R_{press} = \frac{fL\eta}{d^2 A} \quad (7.6)$$

where f is the friction factor for a channel of depth d and mask width m and is obtained using Equation 7.4. The resistance to electroosmosis R_{eof} [10, 11] is given by:

$$R_{eof} = \frac{L\eta}{\varepsilon_r \varepsilon_o \zeta A} \quad (7.7)$$

where ε_r is the relative permittivity of the liquid, ε_o is the permittivity of free space and ζ is the zeta potential of the channel wall-solution interface. Analogously to the flow rates, the electrical current I in the i th channel section is given by:

$$I = \frac{\Delta V}{R_{elec}} \quad (7.8)$$

where the electrical resistance R_{elec} of the section is a function of the channel dimensions, the liquid (bulk) conductivity κ_o and the specific surface conductivity κ_s according to [11]:

$$R_{elec} = \left(\frac{L}{\kappa_o A + \kappa_s C} \right) \quad (7.9)$$

where C is the cross-sectional perimeter length (Equation 7.1). (Note. This equation corrects an error in the previously published work, Equation 4 of Ref. 12)

In the analysis presented here, we neglect the fact that pressure-driven flow down a channel creates a voltage difference (the streaming potential) which acts to oppose the pressure-driven flow [10]. Calculations show that the streaming potentials generated under the experimental conditions used here are of the order of mV and hence negligible. In principle, imposing a pressure-driven flow and measuring the streaming potential offers an alternative method of determining the zeta potential.

For a T-chip channel network (i.e. chips 6M and 12M), the total pressure differences P_A and P_B (relative to the pressure at reservoir C) and total voltage differences V_A and V_B (relative to ground at reservoir C), are equal to the sum of the pressure and voltage drops in the relevant channel sections (indicated by the subscripts relating to the microreactor diagram in Figure 7.1 a):

$$P_A = \Delta P_{Ax} + \Delta P_{xC} \quad (7.10)$$

$$P_B = \Delta P_{Bx} + \Delta P_{xC} \quad (7.11)$$

$$V_A = \Delta V_{Ax} + \Delta V_{xC} \quad (7.12)$$

$$V_B = \Delta V_{Bx} + \Delta V_{xC} \quad (7.13)$$

At the channel junction x, mass conservation requires that the volume of liquid flowing into the junction is equal to that flowing out. Hence

$$\frac{\Delta P_{Ax}}{R_{press,Ax}} + \frac{\Delta P_{Bx}}{R_{press,Bx}} - \frac{\Delta P_{xC}}{R_{press,xC}} + \frac{\Delta V_{Ax}}{R_{eof,Ax}} + \frac{\Delta V_{Bx}}{R_{eof,Bx}} - \frac{\Delta V_{xC}}{R_{eof,xC}} = 0 \quad (7.14)$$

Conservation of electrical charge (i.e. flow of charge corresponding to current) yields the final equation

$$\frac{\Delta V_{Ax}}{R_{elec,Ax}} + \frac{\Delta V_{Bx}}{R_{elec,Bx}} - \frac{\Delta V_{xC}}{R_{elec,xC}} = 0 \quad (7.15)$$

Solution of the six simultaneous equations 7.10 – 7.15 yields analytical expressions for the six unknown pressure and voltage drops in terms of the reservoir voltages and pressures plus the set of resistance values. These solutions, although overlong to be reproduced here, are easily obtained using a software package such as MathCAD. Combination of these equations with equation 7.5 then enables the calculation of the volumetric flow rates.

In the total set of simultaneous equations, analytical expressions for the voltage drops across each channel section can be obtained without consideration of the pressure terms by solution of the independent sub-set of equations (7.12, 7.13 and 7.15). These solutions can then be used to obtain the pressure drops by solution of equations 7.10,

7.11 and 7.14. For this latter sub-set of equations, some simplification of this analysis is possible when the pressure and voltage driven flows are decoupled. This occurs when the combination of voltage terms $\frac{\Delta V_{Ax}}{R_{eof,Ax}} + \frac{\Delta V_{Bx}}{R_{eof,Bx}} - \frac{\Delta V_{xC}}{R_{eof,xC}}$ in the mass conservation equation 7.14 is equal to zero. By comparison with equation 7.14, this is true when the ratios of corresponding voltage terms in the mass and charge conservation equations (7.14 and 7.15 respectively) are equal, i.e.

$$\frac{R_{eof,Ax}}{R_{elec,Ax}} = \frac{R_{eof,Bx}}{R_{elec,Bx}} = \frac{R_{eof,xC}}{R_{elec,xC}} \quad (7.16)$$

These conditions (equation 7.16) are fulfilled for a channel network with uniform surface properties when filled with a single liquid (i.e. η , κ_o , κ_s , ε and ζ are constant) and the cross-sectional dimensions (i.e. C and A) of all channel sections are identical. When η , κ , κ_s , ε and ζ are constant but the C and A differ between the different channel sections, then the conditions of equation 7.16 are fulfilled when

$$\kappa + \kappa_s \frac{C_{Ax}}{A_{Ax}} = \kappa + \kappa_s \frac{C_{Bx}}{A_{Bx}} = \kappa + \kappa_s \frac{C_{xC}}{A_{xC}} \quad (7.17)$$

That is, the perimeter to area ratio must be the same for all channel sections in order that the pressure and voltage driven flows are decoupled. This condition is met within a few % for both T-chips in which the dimensions of the individual channel sections are similar (Table 7.1). It is not true for the 303 chip, which contains hydrodynamic restriction grids of fine channels (Table 7.2).

Equations 7.18 – 7.20 show the solutions for the pressure drops in the channel sections of a T-chip in which the pressure and voltage driven flows are decoupled. The

R terms refer to R_{press} of the channel section indicated by the subscript:

$$\Delta P_{Ax} = \frac{R_{Ax}(-P_B R_{xC} + R_{xC} P_A + R_{Bx} P_A)}{(R_{Bx} R_{xC} + R_{Ax} R_{xC} + R_{Ax} R_{Bx})} \quad (7.18)$$

$$\Delta P_{Bx} = \frac{-R_{Bx}(P_A R_{xC} - R_{xC} P_B - R_{Ax} P_B)}{(R_{Bx} R_{xC} + R_{Ax} R_{xC} + R_{Ax} R_{Bx})} \quad (7.19)$$

$$\Delta P_{xC} = \frac{R_{xC}(P_A R_{Bx} + R_{Ax} P_B)}{(R_{Bx} R_{xC} + R_{Ax} R_{xC} + R_{Ax} R_{Bx})} \quad (7.20)$$

The corresponding solution set for the voltage drops is simply obtained by substituting corresponding values of V for P and R_{elec} for R_{press} . Knowledge of the pressure and voltage drops across the different channel sections enables the calculation of both F_{total} deriving from pressure and EOF (from Eqns. 7.5 – 7.7) and the electrical current (using Eqns 7.8 and 7.9).

The network analysis of the more complex channel network in the 303 microreactor is made similarly with some additional considerations. The first step is to derive the overall resistance values of the Ax , Bx , xy , Cy and yD channel sections. For the hydrodynamic resistances comprising of a grid of 5 small parallel channels, the resistance of this section was obtained using the combining rules for resistors in series and parallel. For the sections in which the large channel overlaps with the grid of 5 small channels, the total resistance was obtained by using the combining rule for resistances of the large channel plus five small channels acting in parallel. The overall resistances of network sections containing a grid (Ax , Bx , Cy and yD) were then derived by summing the resistances of the large channel sections, the overlap regions, and the sections of 5 small channels which combine according to the rule for resistors placed in

series. This separation of the grid section into three regions ((i) large channels only, (ii) large + small channels and (iii) small channels only, Figure 7.3) is an approximation since it ignores the border region of the grid of small channels. However, taking full account of the border regions (as detailed in Ref. 12 for the case of electrical resistances) makes only a minor difference to the calculated resistances. Consequently, the simplified approach shown in Figure 7.3 was used here. Having obtained the overall resistances of all channel sections (Tables 7.3 and 7.4), the following sets of simultaneous equations is obtained by equating the total pressures and voltages at each reservoir with the sums of the pressure and voltage drops across each corresponding channel section:

$$P_A = \Delta P_{Ax} + \Delta P_{xy} + \Delta P_{yD} \quad (7.21)$$

$$P_B = \Delta P_{Bx} + \Delta P_{xy} + \Delta P_{yD} \quad (7.22)$$

$$P_C = \Delta P_{Cy} + \Delta P_{yD} \quad (7.23)$$

$$V_A = \Delta V_{Ax} + \Delta V_{xy} + \Delta V_{yD} \quad (7.24)$$

$$V_B = \Delta V_{Bx} + \Delta V_{xy} + \Delta V_{yD} \quad (7.25)$$

$$V_C = \Delta V_{Cy} + \Delta V_{yD} \quad (7.26)$$

Four additional equations are obtained by considering mass and charge conservation at each of the channel network junctions x and y :

$$\frac{\Delta P_{Ax}}{R_{press,Ax}} + \frac{\Delta P_{Bx}}{R_{press,Bx}} - \frac{\Delta P_{xy}}{R_{press,xy}} + \frac{\Delta V_{Ax}}{R_{eof,Ax}} + \frac{\Delta V_{Bx}}{R_{eof,Bx}} - \frac{\Delta V_{xy}}{R_{eof,xy}} = 0 \quad (7.27)$$

$$\frac{\Delta P_{xy}}{R_{press,xy}} + \frac{\Delta P_{Cy}}{R_{press,Cy}} - \frac{\Delta P_{yD}}{R_{press,yD}} + \frac{\Delta V_{xy}}{R_{eof,xy}} + \frac{\Delta V_{Cy}}{R_{eof,Cy}} - \frac{\Delta V_{yD}}{R_{eof,yD}} = 0 \quad (7.28)$$

$$\frac{\Delta V_{Ax}}{R_{elec.Ax}} + \frac{\Delta V_{Bx}}{R_{elec.Bx}} - \frac{\Delta V_{xy}}{R_{elec.xy}} = 0 \quad (7.29)$$

$$\frac{\Delta V_{xy}}{R_{elec.xy}} + \frac{\Delta V_{Cy}}{R_{elec.Cy}} - \frac{\Delta V_{yD}}{R_{elec.yD}} = 0 \quad (7.30)$$

Solution of equations 7.20 – 7.30 is most easily achieved in two stages. First, the independent sub-set of equations (7.24 – 7.26, 7.29 and 7.30) is solved to obtain the voltage drops. These solutions are then used to solve equations 7.20 – 7.23, 7.27 and 7.28. As noted earlier, for chip 303 the pressure and voltage driven flows could not be decoupled as for the T-chips, since chip 303 did not satisfy the condition specified by equation 7.17. The final solution set, obtained using MathCAD, is given in Appendix K.

Tables 7.1 and 7.2 list all the channel dimensions of the three chips. Tables 7.3 and 7.4 give the calculated channel section resistances relating to pressure and voltage driven flows and electrical currents for the case of each channel network filled with the

Table 7.3: Measured channel network dimensions of the two T-chips used in this work. Bracketed values of the depths are the adjusted values used in the calculation of flow rates and electrical resistances. The resistances are calculated for 1 mM aqueous KCl at 24 °C using the dimensions listed and a best-fit zeta potential of – 43 mV and specific surface conductivity of 220 nS.

Channel section	$d / \mu\text{m}$	$w / \mu\text{m}$	L / mm	$R_{press} / \text{Pa m}^{-3} \text{s}$	$R_{eof} / \text{V m}^{-3} \text{s}$	$R_{elec} / \text{M}\Omega$
Chip 12M						
Ax	47 (45)	205	6.360	4.7×10^{12}	-2.2×10^{13}	31
Bx	48 (48)	205	4.514	2.9×10^{12}	-1.5×10^{13}	22
xC	45 (42)	205	11.90	1.1×10^{13}	-4.5×10^{13}	60
Chip 6M						
Ax	24 (20)	199	5.232	4.1×10^{13}	-4.1×10^{13}	38
Bx	22 (21)	193	4.924	3.4×10^{13}	-3.8×10^{13}	36
xC	23 (22)	195	13.258	7.6×10^{13}	-9.6×10^{13}	94

test solution. This was 1 mM KCl (aq), unbuffered with a pH \approx 6. The solution at ambient temperature was found to have $\eta = 8.8 \times 10^{-4}$ Pa s, $\kappa_o = 0.0146$ S m⁻¹ and $\epsilon_r = 78$ [13].

Table 7.4: The calculated resistances for each channel section of chip 303. Each hydrodynamic resistance grid contains 5 small channels. The channel dimensions are listed in Table 7.2.

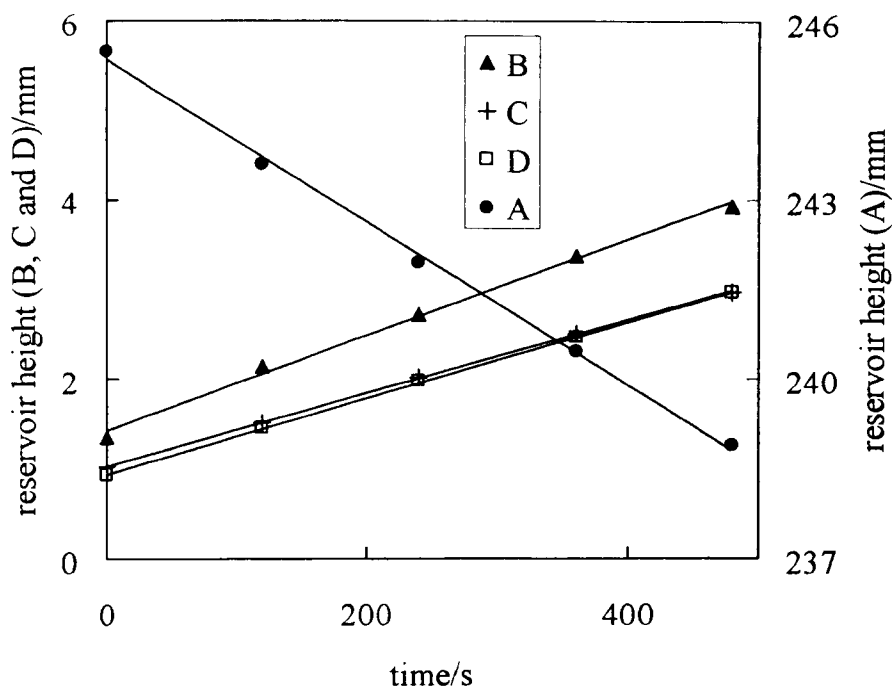
Channel section	R_{press} / Pa m ⁻³ s	R_{eof} / V m ⁻³ s	R_{elec} / M Ω
Ax (overall)	8.4×10^{12}	-2.1×10^{13}	29
Bx (overall)	8.4×10^{12}	-1.9×10^{13}	26
xy (overall)	1.5×10^{12}	-9.6×10^{12}	14
Cy (overall)	7.8×10^{12}	-1.5×10^{13}	20
yD (overall)	7.6×10^{13}	-2.5×10^{13}	35

7.3 Results and discussion.

7.3.1 Comparison of the combined flow theory with experiment.

For the microreactor design process to be effective, the pressure and voltage driven flow relations have to be experimentally validated. For each chip, the flow rates in or out of each reservoir were determined by measurement of the liquid height changes in extended reservoirs attached to the chip. Figure 7.5 shows an example of a Δh - t plot for chip 303 with a pressure of 780 Pa on reservoir A and zero pressure on reservoirs B and C (all relative to the pressure on reservoir D). The pressure differences set by the liquid heights, changed slightly as the heights changed because of the flows. Time averaged values of the pressures were used in all calculations. As expected, the liquid flows from reservoir A toward junction x and from either x or y toward reservoirs B, C and D. The measured flow rates of Figure 7.5 are compared with values calculated using the measured channel dimensions (Table 7.2) in Figure 7.6. It can be seen that the measured flow rates agree with the calculated flow rates to an estimated uncertainty of 10 % using

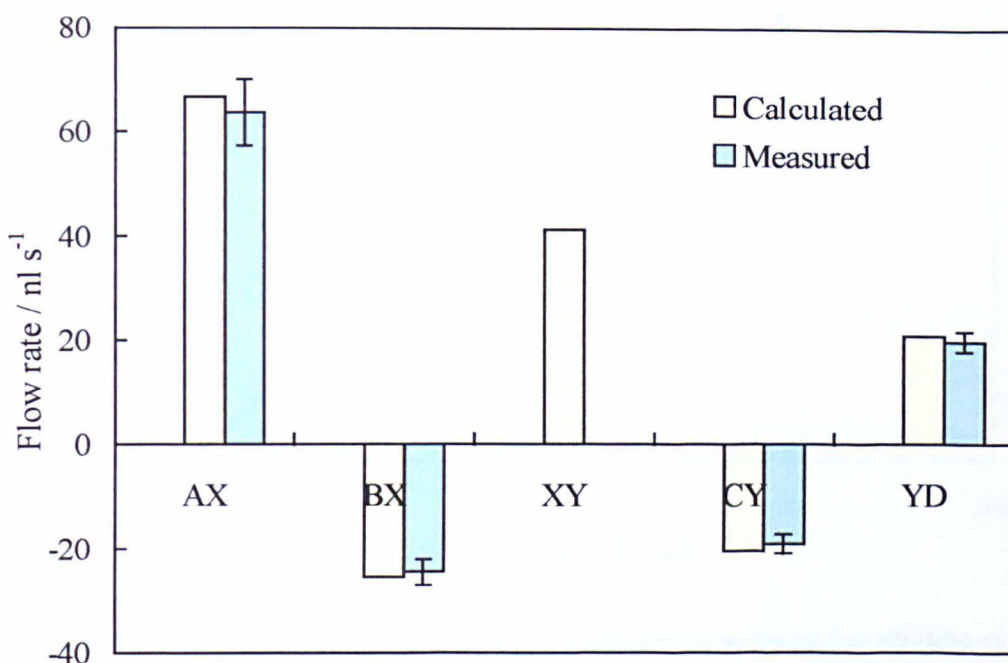
Figure 7.5: Measured reservoir liquid height changes for chip 303 containing 1 mM KCl(aq) with 780 Pa pressure applied to reservoir A relative to zero at reservoir D. No external voltages were applied to reservoir electrodes A, B or C. The zero positions for the height scales of the two ordinates in the plot are arbitrary; absolute average height differences used to determine the mean pressure differences were measured separately.



no adjustable parameters for this case of flow driven entirely by pressure.

Similar flow data was obtained for the 6M, 12M and 303 chips over other pressure and voltage ranges applied to the different reservoirs. Typically, ten data sets were obtained for each microreactor covering pressure ranges of -1000 to $+1000$ Pa and voltage ranges from -600 to $+600$ V. The electrical resistance between each pair of reservoirs was also measured. Global fitting of the entire data set required knowledge of all channel dimensions (Tables 7.1 and 7.2), bulk solution properties (relative permittivity, viscosity and bulk conductivity) of the test solution plus the zeta potential and specific surface conductivity. Best-fit values of these latter two parameters were obtained by globally fitting the entire data set. In addition, optimisation of the global fit

Figure 7.6: Comparison of calculated and measured flow rates in the different channel sections of chip 303. Measured flow rates were derived from the slopes of the plots in Figure 7.5. No measured flow rate for channel section xy is shown since this cannot be accessed using the reservoir height change method. According to the sign convention used, a positive flow indicates the liquid flows in the direction indicated by the order of the 2 letter subscript, i.e. for section Ax , positive flow signifies flow from reservoir A to position x .



required slight adjustment of the channel depths within the range of experimental uncertainty in the independently measured values, as noted in Table 7.3. All other parameters were measured independently. No adjustments to the measured channel dimensions were made for chip 303. The aim was to obtain a stringent validation of the analysis procedure, which requires that all flow rates; electrical currents and resistances are correctly predicted for the different channel geometries using the same values of the two unknown surface parameters i.e. zeta potential and specific surface conductivity. In this context, it is worth noting that flow rates driven solely by pressure do not depend on the unknown surface parameters (i.e. disconnected electrodes are equivalent to an open circuit and do not interfere with streaming currents).

Figure 7.7: Comparison of measured and calculated electrical currents for all data sets in all three chips. The best-fit values of the zeta potential and surface conductivity were -43 mV and 220 nS respectively.

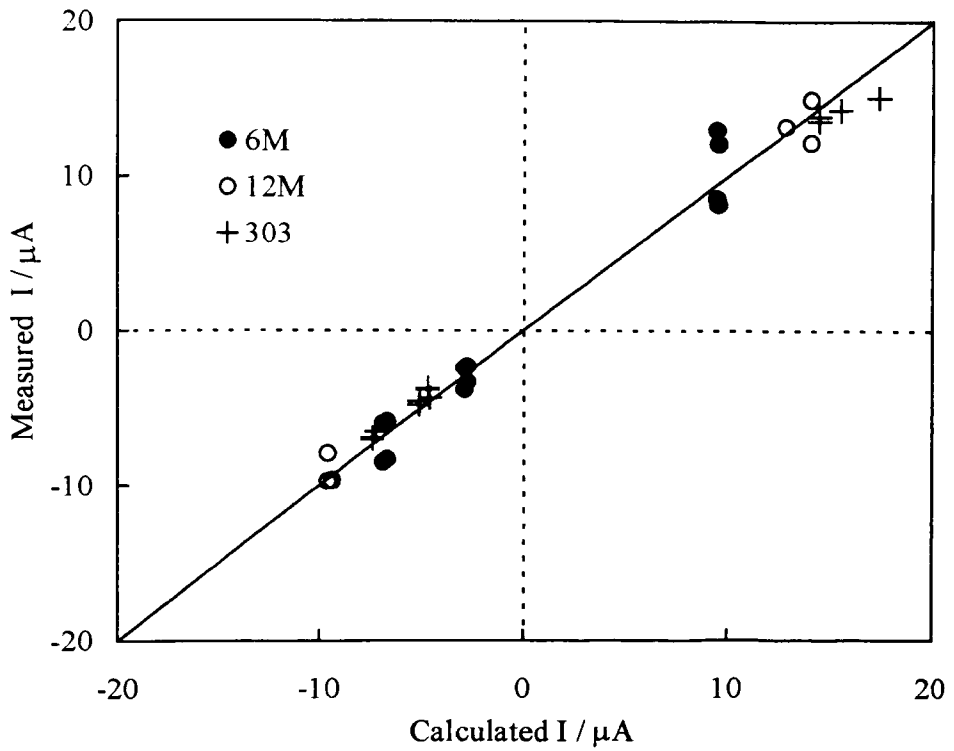


Figure 7.8: Comparison of measured and calculated flow rates for all data sets in all three chips. The best-fit value of the zeta potential was -43 mV.

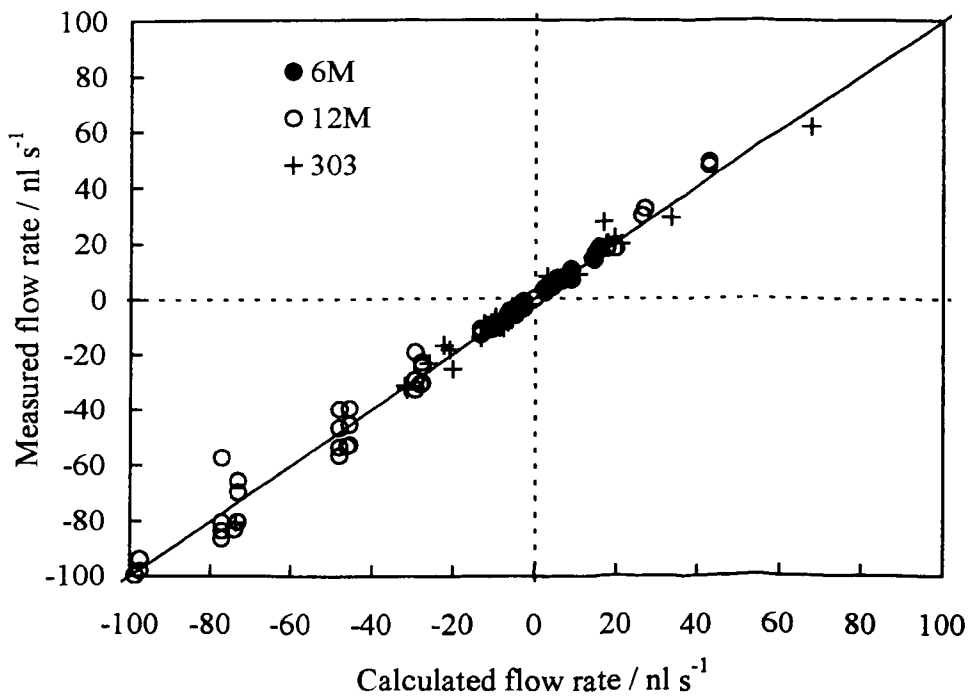
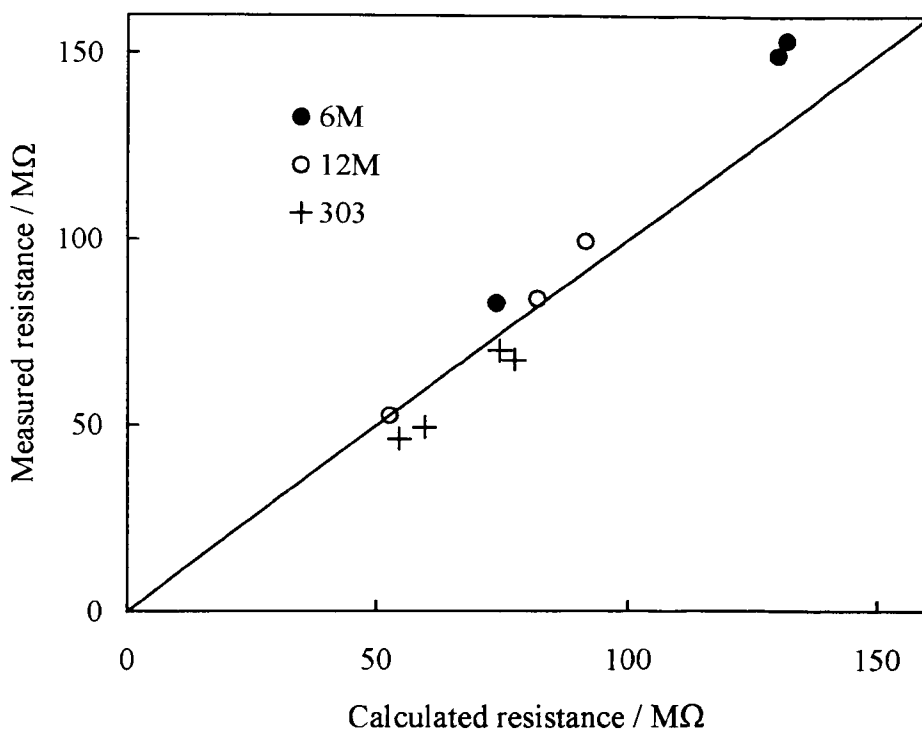


Figure 7.9: Comparison of measured and calculated electrical resistances between all reservoir pairs in all three chips. The best-fit value of the surface conductivity was 220 nS.



Figures 7.7 – 7.9 show comparisons of measured and calculated values of the electrical currents flow rates, and electrical resistances using best-fit values of zeta potential – 43 mV and surface conductivity 220 nS. Both values are within the wide range of published values for the glass / aqueous solution interface [12, 10, 14 – 21]. For the two T-chips (6M and 12M), a slight reduction in the observed deviations between theory and experiment was achieved by slight adjustment of the channel depth values (within the measurement uncertainty). As seen from Figures 7.7 – 7.9, the data sets for chip 303, for which no such adjustments were made, shows a similar level of “scatter”. Overall for the constant test liquid of 1 mM KCl (aq) the entire data set relating to 6M, 12M and 303 chips with different channel depths and network geometries is correctly predicted within a precision of approximately 20 %. Fitting the zeta potential and specific surface conductivity using the separate data sets for the three

chips, yielded values ranging from -36 to -45 mV for ζ and 180 to 250 nS for κ_s . The observed deviation between experiment and theory has to be compared with estimates of the overall uncertainties in the entire procedure for which the following considerations are relevant:

1. The uncertainties in the measured flow rates and currents were estimated by repeated measurements to be approximately 10 %. Electrical resistance values were accurate to 10 % for resistances less than 100 M Ω but were less accurate for values >100 M Ω .
2. Pressures, derived from the relative reservoir heights, were subject to Laplace pressure effects arising from the curvatures of the liquid menisci within the reservoirs. As discussed in Ref. 25, such Laplace pressure effects cancel so long as the liquid menisci in all reservoirs have equal curvatures as determined by the reservoir internal diameters and contact angles between the liquid and reservoir wall. In a dynamic flow measurement when the liquids in different reservoirs are moving either up or down, the dynamic contact angles are expected to differ between reservoirs and hence give rise to non-cancelling Laplace pressures. This effect can give rise to an uncertainty in the pressure of the order of $2\gamma/r$ where γ is the liquid tension and r is the inner radius of the reservoir. For the reservoirs used in this study, $r \approx 1$ mm and hence the uncertainty in the pressure is approximately 140 Pa which corresponds to 10-20 % of the applied pressures.
3. The channel depth is the least accurate channel dimension used in the calculations. The measured values have an uncertainty of approximately 10 %, which corresponds to uncertainties in the calculated values of R_{eof} and R_{elec} of similar magnitude. R_{press} scales approximately as d^3 and hence has an uncertainty of the order of 30 %.
4. In addition to these random errors, we observed instances of larger deviations between experiment and prediction. In these cases, microscopic observation revealed partial channel blockage due to the presence of particulate matter in the

channel network. Such measurements were repeated following cleaning of the chip.

Consideration of the aggregated effects of these different uncertainties leads to the conclusion that the observed deviations are within the expected overall uncertainties.

7.4 Summary.

We describe a unified analysis of pressure and voltage driven flow rates and electrical currents in microreactor channel networks in terms of the appropriate resistances. The method exploits the similarities between the analysis of pressure / flow relationships in fluid networks and voltage / current relationships in DC electrical circuits and is easily applied to complex microfluidic networks. The analysis has been validated using measured pressure and voltage drive flow rates together with electrical currents and resistances for a single test liquid within three chips of differing geometries. All measurements are correctly predicted within the experimental uncertainties of approximately 20%.

The unified analysis of both pressure and electrokinetic mobilisation of reagents within micro-channel networks has a number of important applications relating to the exploitation of microreactor technology. Firstly, it opens up the possibility of exploiting *combined* pressure- and voltage control to achieve complex flow patterns required for particular applications. Secondly, the method forms a useful tool for the pre-fabrication design of microfluidic devices with particular desired flow and electrical operating characteristics. For example, for microreactors designed to be driven solely by voltage, liquid height differences between reservoirs can give rise to anomalous pressure-driven flows unless the hydrodynamic resistances of all channel sections is high enough to

suppress pressure-driven flow to negligible levels. This can be achieved by incorporation of grids of fine channels within a network of large channels (as in chip 303) but designs require careful and quantitative optimisation to ensure maximisation of voltage-driven flow whilst simultaneously suppressing unwanted pressure-driven flow to acceptably low levels. For microreactors driven solely by pressure, a channel network is commonly required to produce a predefined range of volumetric flow rates and residence times of reagents within particular sections. In order to achieve this, it is essential to know the maximum safe working pressure of the device, which obviously lies somewhere below that pressure which brings about mechanical failure. Again, the analysis outlined here enables this type of quantitative design optimisation before chip fabrication. Thirdly, comparison of measured flow with prediction provides a simple and reliable routine diagnostic test that a chip is operating correctly, i.e. that no blockages are present and that all channel dimensions have been measured correctly.

The analysis described here is valid for a channel network with uniform surface properties (zeta potential and specific surface conductivity) filled with a single liquid of uniform bulk properties i.e. constant viscosity, bulk conductivity and relative permittivity. In this situation, the properties of each channel section are time independent. For most microreactor applications, different reagent solutions are mixed within a channel network producing a system in which the properties of each channel section are non-uniform and depend on the history of flow patterns within the network. Although the analysis given here provides a starting point, a full theoretical description of the much more complex flow patterns in networks which are non-uniform and time (i.e. flow history) dependent remains an important future challenge.

7.5 References.

- [1] S. C. Jacobson, R. Hergenroder, L. B. Koutny, R. J. Warmack and J. M. Ramsey, *Anal. Chem.*, 1994, 66, 1107.
- [2] S. V. Ermakov, S.C. Jacobson and J. M. Ramsey in *Micro Total Analysis Systems '98*, Eds. D. J. Harrison and A. Van den Berg, Kluwer, Dordrecht, 1998, p149.
- [3] J.B. Knight, A. Vishwanath, J.P. Brody and R.H. Austin, *Phys. Rev. Lett.*, 1998, 80, 3863.
- [4] N.A. Patankar and H.H. Hu, *Anal. Chem.*, 1998, 70, 1870.
- [5] S. V. Ermakov, S.C. Jacobson and J. M. Ramsey, *Anal. Chem.*, 2000, 72, 3512.
- [6] J. M. MacInnes, *Chem. Eng. Sci.*, 2002, 57, 4539.
- [7] J. M. MacInnes, X. Du and R. W. K. Allen, *Physics of Fluids*, 2002, *in press*.
- [8] I. Broadwell, P. D. I. Fletcher, S. J. Haswell, X. Zhang, R. W. K. Allen, J. M. MacInnes and X. Du, *Lab on a Chip*, 2003, *Awaiting permission for publication*.
- [9] Reference Data for Radio Engineers, 6th edition (1975) Howard W. Sams & Co., Inc., Indianapolis, USA, pg. 37-10.
- [10] J. Th. G. Overbeek, in *Colloid Science*, Ed. H. R. Kruyt (1952) Elsevier, Amsterdam, Vol. 1, Ch. V, p194.
- [11] R. J. Hunter, *Zeta Potential in Colloid Science*, Academic Press, London 1981.
- [12] P. D. I. Fletcher, S.J. Haswell and X. Zhang, *Lab on a Chip*, 2001, 1, 115.
- [13] *Handbook of Chemistry and Physics*, CRC Press, 62nd Edition, Boca Raton, 1981.
- [14] M. Kosmulski and E. Matijevic, *Colloid Polym. Sci.*, 1992, 270, 1046.
- [15] I. E. Valko, H. Siren and M. L. Riekkola, *J. Microcolumn Separations*, 1999, 11, 199.
- [16] C. Schwer and E. Kenndler, *Anal. Chem.*, 1991, 63, 1801.
- [17] P. B. Wright, A. S. Lister and J. G. Dorsey, *Anal. Chem.*, 1997, 69, 3251.
- [18] G. R. Wiese, R. O. James and T. W. Healy, *Disc. Faraday Soc.*, 1971, 52, 302.
- [19] J. Jednacak, V. Pravdic and W. Haller, *J. Colloid Interface Sci.*, 1974, 49, 16.
- [20] R. A. Van Wagenen and J. D. Andrade, *J. Colloid Interface Sci.*, 1980, 76, 305.

- [21] P. J. Scales, F. Grieser, T. W. Healy, L. R. White and D. Y. C. Chan, *Langmuir*, 1992, 8, 965.

8. CONCLUSIONS AND SUGGESTIONS FOR FUTURE WORK.

The main objectives of the work described in this thesis are listed in Section 1.5. The methods used to achieve these objectives and the theoretical basis for the work has been presented in Chapters 3 to 7.

In Chapter 3, we have successfully shown that 3D profiles of microreactor channel networks can be produced using optical imaging of dye filled channels. These profiles can be used to determine local and overall channel depth to an accuracy of a few percent and a lateral resolution of less than 1 μm . It has also been established that distortion effects of the measured channel profiles resulting from a refractive index mismatch of ± 0.2 between the dye solution and the glass of the microreactor is insignificant. The imaging technique has been used to demonstrate the effects of thermal bonding and etch time on channel profiles. Channel cross-sectional profiles determined by absorbance-imaging show good agreement to those independently measured using optical microscopy.

In Chapter 4, a simple model was derived to accurately predict the combined effects of electroosmotic and pressure-driven flow through a cylindrical capillary. It was found that for a 0.1 mM KCl (aq) test solution, runs could be made many times over without refreshing. The observed repeatability was excellent, with the values of zeta potential and electroosmotic flow rate varying by less than 10 % from run to run. Associated specific surface conductivity values were, as expected, less repeatable with values spread over about one order of magnitude.

High standards of equipment cleaning and data quality control eliminated most

sources of potential error, such as those associated with Laplace pressure differences. It was identified (limited data) that alcoholic KOH was a better cleaner than 5 M KOH (aq) when used to degrease quartz and borosilicate glass capillaries. Quartz glass capillaries displayed slightly higher electroosmotic flow rates and zeta potentials than the borosilicate capillaries.

It has been successfully demonstrated in Chapter 5 that voltage-current characteristics for a simple T-chip microreactor filled with conducting organic solvent can be predicted to an accuracy of between 10 – 20 %, using the complete set of 3D channel network information, the bulk solution conductivity and channel wall-solution specific surface conductivity. Values of specific surface conductivity for a test solution of 10 mM sodium methoxide in methanol were in good agreement with other literature values. Measurement of the volumetric flow rates within the channel networks as a function of electrical current, proved to be a simple and effective method of characterising the microfluidic flow properties of the solvent systems of interest. The uncertainty in each calculated zeta potential was estimated to be approximately 10 % and that in the measured flow rates, to be between 10 and 20 %. It was found for a solution of 45 mM NaBr in 80 vol. % DMA (aq), that the measured zeta potential of -4 ± 2 mV was at the lower limit of resolution for this technique. Voltage-current profiles made with silver, gold and tungsten showed no conclusive differences in electrical properties between them and the standard platinum wire electrodes used for all other experiments.

The content of Chapter 6 experimentally validates the use of concentration-imaging as a method of measuring electroosmotic flow rate in a microreactor channel network

by simply monitoring the position of a moving dye front over time. Recorded electrical current, voltage and front velocity data were used to calculate solvent properties such as zeta potential and diffusion coefficient. These solvent properties further constitute the origins of a database of useful solvents that can be used for performing chemical reactions in microreactors. A demonstration of the self-consistency between concentration-imaging and the previously outlined flow rate methods has been shown for 80 vol. % DMA (aq) with 45 mM NaBr by obtaining a zeta potential of -4 ± 2 mV.

Concentration-imaging measurements made using colloidal palladium catalyst achieved limited success. A range of electrophoretic mobilities for the colloid samples in methanol was observed. The high colloid concentrations necessary for the success of the concentration-imaging technique apparently reduced the electrophoretic mobility of the particles. Independent measurements made with a Malvern Zetasizer showed that at low colloid concentrations, the particles in methanol had a zeta potential of -140 mV.

The final part of the work outlined in this thesis, describes a unified analysis of pressure and voltage-driven flow rates and electrical currents in microreactor channel networks in terms of resistances. The method exploits the similarities between the analysis of pressure / flow relationships in fluid networks and the voltage / current relationships in DC electrical circuits. By applying the principle of reciprocity such that each dynamic system has its own type of resistance, it was possible to fully analyse each aspect of microreactors. The analysis was validated using measured pressure and voltage-driven flow rates together with electrical currents and resistances for a single test solution. All measurements are correctly predicted within the experimental uncertainties to approximately 20 %.

Overall it has been demonstrated that:

- Microreactor channel dimensions can be determined using optical absorbance-imaging to an accuracy of a few percent and a spatial resolution of less than 1 μm .
- The voltage- and pressure-driven flows in glass microreactors can be predicted from the measured electrical currents, channel dimensions and applied voltages to a level of accuracy of approximately 20 %.
- The microreactor current-voltage characteristics can be reliably predicted from the measured channel dimensions, bulk solution conductivity and electrical resistances to a level of accuracy of approximately 20 %.
- The mobility of dye species and colloidal particles can be determined using absorbance-imaging to monitor the position of a moving front which is propelled by voltage-driven flow in a microreactor channel.

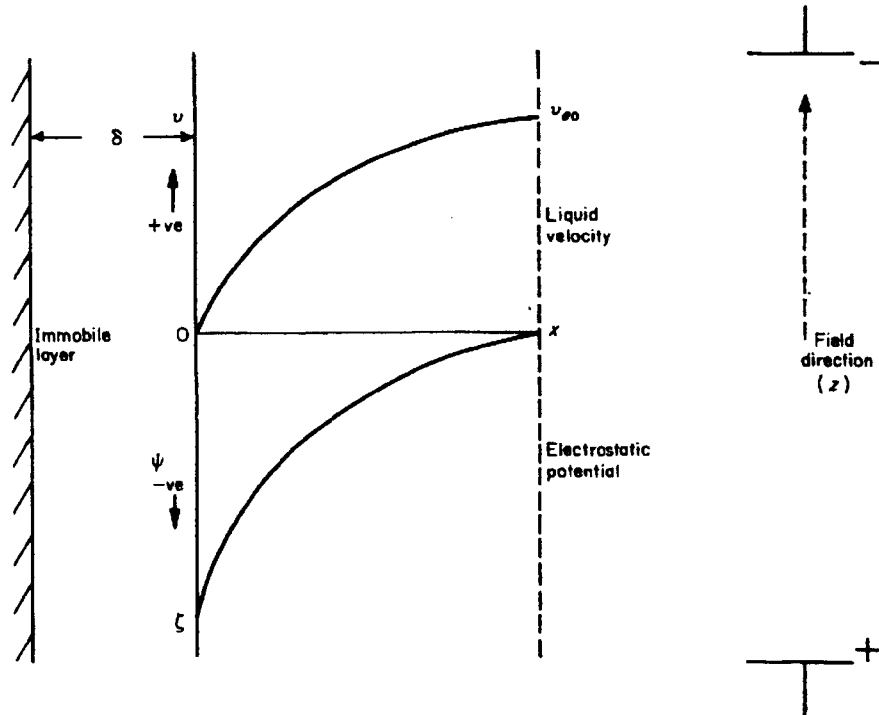
Suggestions for future work include:

- To use concentration-imaging to monitor *in situ* chemical reactions in a microreactor channel where non-homogeneous electrical (specific surface and bulk) conductivities, viscosities and temperatures exist. Then to produce a theoretical framework for the prediction of voltage- and pressure-driven flows from the measured electrical currents, channel dimensions and applied voltages
- To use concentration-imaging in conjunction with another technique such as fluorescence microscopy, to monitor the electrophoretic movement of colloidal particles in a microreactor channel at a low concentrations (i.e. where no surface charge interactions exist).
- To make pressure-driven flow and streaming potential measurements in a microreactor channel for determining the glass wall-solution interface zeta potential.

APPENDIX (A): MATHEMATICAL TREATMENT OF ELECTROOSMOSIS.

Consider a negatively charged solid surface. If positive charges exist in the adjacent liquid, there would be a net excess of ions at or near the solid-liquid interface. Any ionic movement of this region would drag the liquid along. A surface of shear can be defined for this case. It may be taken as a plane parallel to the surface which is located at a distance δ from it.

Figure A1: Distribution of electrostatic potential near a charged surface and the resulting electroosmotic velocity under applied electric field.



The velocity of the liquid in the direction parallel to the wall v_z , rises from zero in the plane of shear to a maximum value v_{eof} , at some distance from the wall (Fig. A1). v_{eof} is called the electroosmotic velocity of the liquid. The forces acting on a volume element of the liquid sample of charge density ρ in the channel are shown in Figure A2.

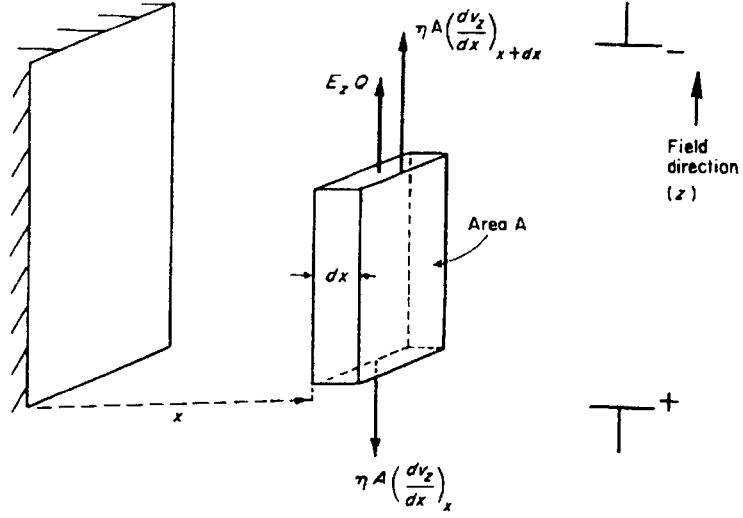
Evidently:

$$E_z \cdot Q = E_z \rho A dx = \eta A \left(\frac{dv_z}{dx} \right)_x - \eta A \left(\frac{dv_z}{dx} \right)_{x+dx} \quad (A1)$$

or

$$E_x \cdot \rho dx = -\eta \frac{d^2 v_z}{dx^2} dx \quad (A2)$$

Figure A2: Forces acting on a volume element $A \cdot dx$ of the liquid of area A and containing charge Q .



Substituting for ρ using Poisson's equation gives:

$$E_z = (4\pi\epsilon_0) \frac{D}{4\pi} \frac{d^2\Psi}{dx^2} dx = \eta \left(\frac{d^2 v_z}{dx^2} \right) dx \quad (\text{A3})$$

By integration from a point far from the solid where $\Psi = 0$ and $v_z = v_{eo}$; up to the shear plane where $v_z = 0$ and $\Psi = \zeta$, and using the fact that $d\Psi/dx = dv_z/dx = 0$ far from the surface. The result is:

$$\frac{v_{eof}}{E_z} = u_{eof} = 4\pi\epsilon_0 \frac{D\zeta}{4\pi\eta} \quad (\text{A4})$$

Hence electroosmotic velocity is given by;

$$v_{eof} = -\frac{E_z \epsilon_0 \epsilon_r \zeta}{\eta} \quad \text{Smoluchowski's equation} \quad (\text{A5})$$

Where u_{eof} is electroosmotic mobility, D the electric displacement vector ($D = \epsilon_0 \epsilon_r E$) and η the viscosity. E and E_z both represent the same electric field along the channel axis. The negative sign in equations A4 and A5 indicates that when ζ is negative the space charge is positive and so the liquid flow is towards the negative electrode (i.e. bottom to top Fig. A2. $\epsilon = \epsilon_r$ is relative permittivity.

APPENDIX (B): DYE SPECIES ADSORPTION CALCULATIONS.

pair of parallel plates 100 um long and 100 um wide
 dye molecules are 0.94 x 1.1 nm and lay with head towards channel wall and tail into the bulk solution
 calculations assume that filling with dye solution fills bulk of channel and places a coating of dye as a monolayer on the surface

absorbance	conc/ mol dm ⁻³	path length/um	ext coeff./mol ⁻¹ dm ³ cm ⁻¹	dye molecule area/nm ²
0.6	6.05449E-08	100	9.91E+04	1.034

Area/um ²	area /m ²	dye mol area /m ²	sample vol/m ³	no of dye mol in vol	no of mol on 2 plates
10000	1.00E-08	1.034E-18	1.00E-06	3.6448032E+13	1.93E+10

% extra molecules	effective path length/um	new conc/mol dm ⁻³
100.0530683	100.0530683	6.05770E-08

path length/um	% difference in molecules	effective path length/um	% error	sum of dye molecules
50	100.0531	50.0265	0.05304	3.65E+13
5	100.0531	5.0027	0.05304	
20	100.0531	20.0106	0.05304	new absorbance
100	100.0531	100.0531	0.05304	6.00318E-01
250	100.0531	250.1327	0.05304	

no of dye molecules in volume does not change because A is fixed at 0.6. This requires the conc to change for a changing path length.

APPENDIX (C): VISUAL BASIC CODE FOR ISOTROPIC ETCH PROFILES.

Function 1

function profiley(x, m, d)

'This function calculates the value of channel depth in microns

'x is position from channel centre in microns

'm is mask width in microns

'd is channel depth in microns

If x < (-m / 2 - d) Or x > (m / 2 + d) Then y = 0: GoTo 10

If x <= (-m / 2) And x >= (-m / 2 - d) Then y = (d ^ 2 - (x + m / 2) ^ 2) ^ (1 / 2): GoTo 10

If x > (-m / 2) And x < (m / 2) Then y = d: GoTo 10

If x >= (m / 2) And x <= (m / 2 + d) Then y = (d ^ 2 - (x - m / 2) ^ 2) ^ (1 / 2)

10 profiley = y

End Function

Function 2

Private Function profileave(x1, m2, d2, s2)

'This function calculates the value of smoothed channel depth in microns

'x2 is position from channel centre in microns

'm2 is mask width in microns

'd2 is channel depth in microns

's2 is the distance over which the y average is taken

nstep = 10

ysum = 0

For x2 = (x1 - s2 / 2) To (x1 + 1.00000001 * s2 / 2) Step (s2 / nstep)

If x2 < (-m2 / 2 - d2) Or x2 > (m2 / 2 + d2) Then y2 = 0: GoTo 10

If x2 <= (-m2 / 2) And x2 >= (-m2 / 2 - d2) Then y2 = (d2 ^ 2 - (x2 + m2 / 2) ^ 2) ^ (1 / 2): GoTo 10

If x2 > (-m2 / 2) And x2 < (m2 / 2) Then y2 = d2: GoTo 10

If x2 >= (m2 / 2) And x2 <= (m2 / 2 + d2) Then y2 = (d2 ^ 2 - (x2 - m2 / 2) ^ 2) ^ (1 / 2)

10 ysum = ysum + y2

Next x2

profileave = ysum / (nstep + 1)

APPENDIX (D): EOF CALCULATIONS 1.

The rate of change of reservoir height is given by:

$$\frac{d\Delta h}{dt} = \underbrace{\frac{E\varepsilon_o\varepsilon_r\zeta.A_{cap}}{\eta.A_{res}}}_X - \underbrace{\frac{\pi.\Delta\rho.g.r_{cap}^4}{4.\eta.L.A_{res}}}_Y \Delta h \quad (D1)$$

This can be represented as the following:

$$\frac{d\Delta h}{dt} = X - Y\Delta h \quad (D2)$$

Standard integrals for this form of differential equation can be solved using:

$$\int \left(\frac{d\Delta h}{X - Y\Delta h} \right) = \int dt + C \quad C = \text{constant of integration} \quad (D3)$$

hence

$$-\frac{1}{Y} \ln(X - Y\Delta h) = t + C \quad (D4)$$

When $t = 0$ and $\Delta h = 0$, $C = -\frac{1}{Y} \ln X$, the final result is:

$$\underline{t = -\frac{1}{Y} \ln(X - Y.\Delta h) + \frac{1}{Y} \ln X} \quad (D5)$$

APPENDIX (E): EOF CALCULATIONS 2.

Re-writing Eqn. D5 (Appendix D) gives:

$$t = -\frac{l}{Y} \left\{ \ln \left[\frac{(X - Y\Delta h)}{X} \right] \right\} \quad (\text{E1})$$

Consider equation 4.3, when $\frac{d\Delta h}{dt} = 0$ for a single reservoir, the liquid level $\Delta h = \Delta h_{max}$, therefore:

$$X = Y\Delta h = Y\Delta h_{max} \quad (\text{E2})$$

which gives the maximum possible height change in reservoir 1 to be:

$$\Delta h_{max} = \frac{X}{Y} \quad (\text{E3})$$

Substituting:

$$t = -\frac{l}{Y} \left\{ \ln \left(1 - \frac{\Delta h}{\Delta h_{max}} \right) \right\} \quad (\text{E4})$$

Rearranging:

$$\exp(-Y.t) = 1 - \frac{\Delta h}{\Delta h_{max}} \quad (\text{E5})$$

$$\frac{\Delta h}{\Delta h_{max}} = [1 - \exp(-Y.t)] \quad (\text{E6})$$

The final result is:

$$\underline{\Delta h = \Delta h_{max} [1 - \exp(-Y.t)]} \quad (\text{E7})$$

APPENDIX (F): THE VISCOSITY OF 80 VOL.% DMA IN WATER.

DMA Viscosity temp/oC	h/cP	(1/T)/K-1	ln(h/cP)
35	0.823	0.003245173	-0.194799
30	0.871	0.003298697	-0.138113
25	0.919	0.003354016	-0.084469

set temp/oC	h/cP
21.5	0.9576276

Water viscosity temp/oC	h/cP	(1/T)/K-1	ln(h/cP)
35	0.7194	0.003245173	-0.329338
30	0.7975	0.003298697	-0.226273
25	0.8904	0.003354016	-0.116084
20	1.002	0.003411223	0.001998

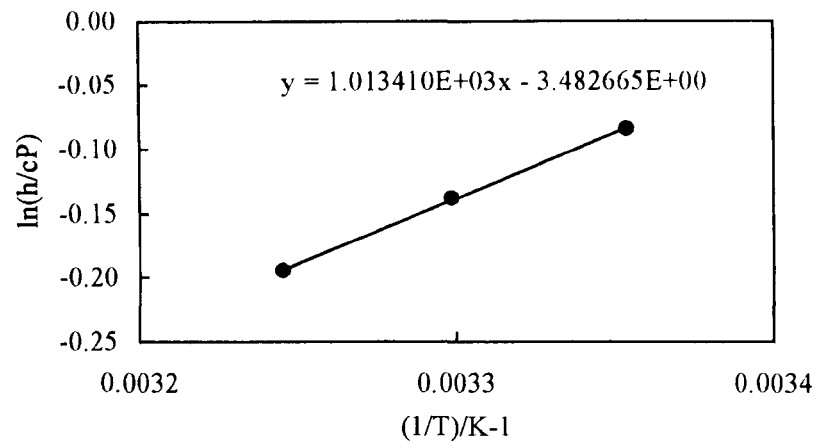
set temp/oC	h/cP
21.5	0.9660283

combined viscosity for 80 vol % DMA (aq)

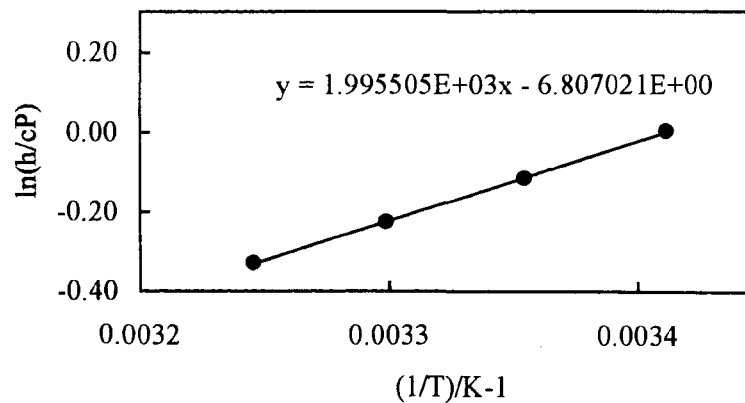
0.959307775 centipoise

set temp/oC
21.5

DMA viscosity (Beilstein ref 1,5&6) vs Temp.



Water viscosity (CRC handbook F-38) vs Temp.



APPENDIX (G): THE RELATIVE PERMITTIVITY OF 80 VOL.% DMA IN WATER.

DMA
dielectric constant

temp/oC	er	(1/T)/K-1	ln(epsilon)
30	36.81	0.0032987	3.6057695
25	37.78	0.00335402	3.6317799
20	38.93	0.00341122	3.6617652
15	40.09	0.00347041	3.6911269

set temp/oC	er
21.5	38.580357

from handbook of electrochemical constants

Water
viscosity

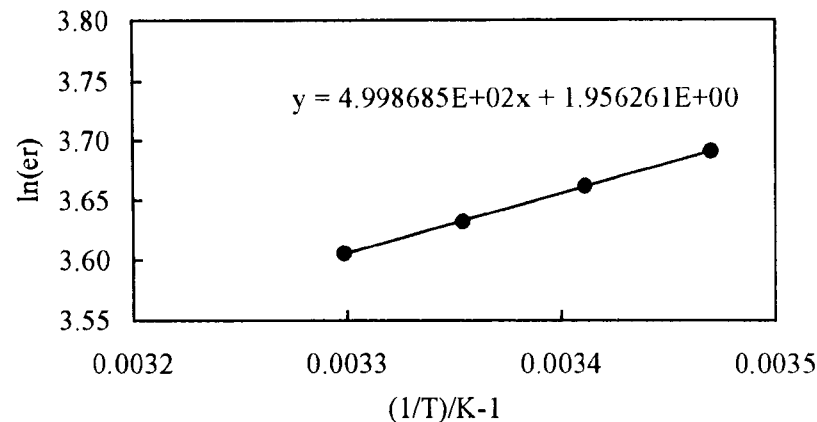
temp/oC	h/cP	(1/T)/K-1	ln(h/cP)
5	85.763	0.00359518	4.4515877
10	83.832	0.0035317	4.4288148
15	81.946	0.00347041	4.4060605
20	80.103	0.00341122	4.3833133
25	78.304	0.00335402	4.3605987
30	76.546	0.0032987	4.3378919

set temp/oC	h/cP
21.5	79.620261

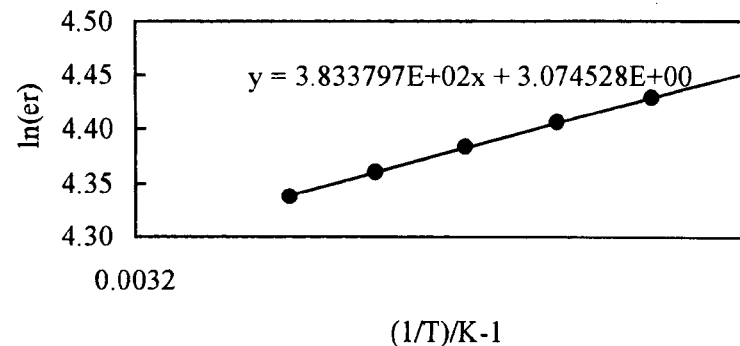
combined static dielectric constant for 80 vol % DMA (aq)

set temp/oC	
46.78833793	@ 21.5

DMA static dielectric constant (Beilstein REFS 7-10) vs Temp.



Water static dielectric constant (Handbook of electrochemical constants) vs Temp.



APPENDIX (H): RESOLVING PADA ABSORBANCES AT 450 AND 550 NM.

The absorbance of the PADA/PADAH⁺ solution for a known wavelength is given by:

$$A_{\lambda} = d(\varepsilon_{\lambda}^{PADA} [PADA] + \varepsilon_{\lambda}^{PADAH^{+}} [PADAH^{+}]) \quad (H1)$$

coupling this data with the acidity constant and the definition of pH and pK_a .

$$K_a = \frac{[PADA][H^{+}]}{[PADAH^{+}]} \quad (H2)$$

$$pH = pK_a - \log_{10} \left\{ \frac{[PADAH^{+}]}{[PADA]} \right\} \quad (H3)$$

An equation can be derived solely in terms of PADA concentrations.

$$pH = pK_a - \log_{10} \left\{ \frac{[PADA]_o - [PADA]}{[PADA]} \right\} \quad (H4)$$

where $[PADA]_o$ is the initial PADA concentration before any has been converted to PADAH⁺. Equation (A) can be rewritten in terms of initial PADA concentrations as shown below:

$$A_{\lambda} = d(E_{\lambda}^{PADA} [PADA] + E_{\lambda}^{PADAH^{+}} ([PADA]_o - [PADA])) \quad (H5)$$

The final PADA concentration of any solution which has been pH adjusted, can be calculated from the initial PADA concentration, the hydrogen ion concentration and the acidity constant:

$$[PADA] = \frac{K_a([PADA]_o - [PADA])}{[H^{+}]} = \frac{K_a[PADA]_o}{[H^{+}]} - \frac{K_a[PADA]}{[H^{+}]} \quad (H6)$$

Rearranging

$$[PADA] \left(1 + \frac{K_a}{[H^+]} \right) = \frac{K_a [PADA]_o}{[H^+]} \quad (\text{H7})$$

The final result is:

$$[PADA] = \frac{\left(\frac{K_a [PADA]_o}{[H^+]} \right)}{\left(1 + \frac{K_a}{[H^+]} \right)} \quad (\text{H8})$$

APPENDIX (I): CALCULATING THE pK_a FOR PADA IN 80 VOL. % DMA (AQ).

4 mM PADA in 80 vol%DMA with 45.4 mM NaBr, 50 micron path length at 23.6oC zeroed to 650 nm

[PADA]o/M	path length/cm	K _a /M	ePADA @ 450	ePADAH+ @ 450	ePADA @ 550	ePADAH+ @ 550	total resids	pK _a
0.004	0.005	8.40E-04	26308.95	7218.01	63.79	45125.41	5.88E-02	3.08

solutions as new (calibration set)			sum			sum			
Solution	[H+]/M	pH	expt Abs 450	calc Abs 450	resids Abs 450	expt Abs 550	calc Abs 550	resids Abs 550	[PADA]/M
F	3.80E-07	6.42	0.526	0.526	0.000	0.009	0.002	0.007	4.00E-03
E	1.38E-06	5.86	0.523	0.526	0.003	0.008	0.003	0.005	3.99E-03
D	2.57E-05	4.59	0.516	0.515	0.001	0.026	0.028	0.002	3.88E-03
C	1.48E-04	3.83	0.476	0.469	0.007	0.114	0.136	0.022	3.40E-03
B	8.51E-04	3.07	0.334	0.334	0.000	0.466	0.455	0.011	1.99E-03
A	1.07E-02	1.97	0.172	0.172	0.000	0.837	0.837	0.000	2.91E-04

256

aged solutions with pH change (calculating pH from spectrophotometer data)

	expt Abs 450	expt Abs 550	[PADA]	[PADAH ⁺]	from pK _a p and H ⁺ pH (calculated)	pH measured on day of experiment	10 ^{-(pHMEASURED)} [H ⁺]/M calc	K _a ([PADAH ⁺]) /[PADA] [H ⁺]/M calc	[PADA]/M
F	0.517	0.005	3.93E-03	1.66E-05	5.45	6.48	3.31E-07	3.55E-06	4.00E-03
C	0.506	0.043	3.80E-03	1.85E-04	4.39	4.43	3.72E-05	4.10E-05	3.83E-03
B	0.43	0.224	3.00E-03	9.89E-04	3.56	3.55	2.82E-04	2.77E-04	3.00E-03
A	0.193	0.663	6.61E-04	2.94E-03	2.43	2.40	3.98E-03	3.73E-03	6.97E-04

$$[PADA] = \frac{\left(\frac{A_{550}}{\epsilon_{550}^{PADAH^+}} - \frac{A_{450}}{\epsilon_{450}^{PADAH^+}} \right)}{d \left(\frac{\epsilon_{550}^{PADA}}{\epsilon_{550}^{PADAH^+}} - \frac{\epsilon_{450}^{PADA}}{\epsilon_{450}^{PADAH^+}} \right)}$$

$$[PADAH^+] = \frac{\left(\frac{A_{550}}{\epsilon_{550}^{PADA}} - \frac{A_{450}}{\epsilon_{450}^{PADA}} \right)}{d \left(\frac{\epsilon_{550}^{PADAH^+}}{\epsilon_{550}^{PADA}} - \frac{\epsilon_{450}^{PADAH^+}}{\epsilon_{450}^{PADA}} \right)}$$

$$pH = pK_a - \log_{10} \left\{ \frac{[PADAH^+]}{[PADA]} \right\}$$

$$[PADA] = \frac{\left(\frac{K_a [PADA]_o}{[H^+]} \right)}{\left(1 + \frac{K_a}{[H^+]} \right)}$$

APPENDIX (J): PADA ZETA POTENTIAL AND DIFFUSION COEFFICIENT CALCULATIONS.

channel cross sectional area calculated for channel with m and d of 146um and 38 um.

viscosity and permittivity is adjusted to 24 deg C and based on weighted volume ratios for water and DMA data

Valid for 4 mM PADA in 80 v% DMA(aq) with 45 mM NaBr background electrolyte

viscosity/Cp	epsilon r	epsilon vacuo/ Fm ⁻¹	Chan X /m ²	Z/PADAH+	e/C	k/JK ⁻¹	T/ K
0.92675647	46.183	8.85E-12	7.82E-09	1	1.60E-19	1.38E-23	297.15

viscosity/Pa s
9.268E-04

solution temps when freshly prepared

solution composition	pH	cond Sm ⁻¹	temp /C	ave pH	solution	ave_cond Sm ⁻¹
1 no PADA	2.54	0.2260	25.1	2.47	1&4	0.233
2 no PADA	6.66	0.1200	23.3	6.54	2&3	0.120
3 4mM PADA	6.43	0.1193	24.7			
4 4mM PADA	2.39	0.2390	25.6			

on-chip measurements made in a air conditioned room set to 24 deg C

pH 2.45 (Electrophoretic)				pH 6.6 (EOF)				
Voltage	mm/s	I start/uA	I finish /uA	average I/A	mm/s	I start/uA	I finish /uA	average I/A
0	0	0	0	0.00E+00	0	0	0	0.00E+00
150	0.0162	4.7	4.4	4.55E-06	0.0099	4.8	4.9	4.85E-06
300	0.0341	9.6	9.2	9.40E-06	0.0198	9.6	9.2	9.40E-06
450	0.0535	15.3	14.4	1.49E-05	0.0284	14.1	13.9	1.40E-05
600	0.0698	19.9	19.5	1.97E-05	0.0368	20.6	19.7	2.02E-05
750					0.0458	25.4	25.4	2.54E-05

diffusion coefficient calculations

Voltage	E Vm ⁻¹	v(electrophoretic)/ ms ⁻¹	diffusion D/ m2s ⁻¹
0	0.00E+00	0.00E+00	1.66326E-10
150	2.50E+03	1.75E-05	
300	5.17E+03	3.49E-05	
450	8.17E+03	5.24E-05	
600	1.08E+04	6.99E-05	
750			

zeta potential calculations

E Vm ⁻¹	veof/ ms ⁻¹	zeta potential/V
0.00E+00	0	3.96E-03
5.19E+03	9.2891E-06	
1.01E+04	1.8578E-05	
1.50E+04	2.7867E-05	
2.15E+04	3.7156E-05	
2.72E+04	4.6445E-05	

APPENDIX (K): PRESSURE EQUATIONS FOR CHIP 303.

$$\Delta P_{Ax} = \frac{-R_{Ax} \left(-P_B R_{xC} R_{vD} + R_{xy} P_B R_{Cy} + R_{Bx} P_C R_{yD} + P_B R_{Cy} R_{yD} - P_A R_{xy} R_{yD} - P_A R_{xy} R_{Cy} - R_{Bx} P_A R_{yD} - R_{Bx} P_A R_{Cy} - P_A R_{Cy} R_{yD} \right)}{\left(R_{Bx} R_{xy} R_{vD} + R_{Bx} R_{xy} R_{Cy} + R_{Ax} R_{xy} R_{yD} + R_{Ax} R_{xy} R_{Cy} + R_{Ax} R_{Bx} R_{yD} + R_{Ax} R_{Bx} R_{Cy} + R_{Bx} R_{Cy} R_{yD} + R_{Ax} R_{Cy} R_{yD} \right)} \quad (K1)$$

$$\Delta P_{Bx} = \frac{-R_{Bx} \left(P_A R_{xy} R_{vD} + R_{xy} P_A R_{Cy} + R_{Ax} P_C R_{yD} + P_A R_{Cy} R_{yD} - P_B R_{xy} R_{yD} - P_B R_{xy} R_{Cy} - R_{Ax} P_B R_{yD} - R_{Ax} P_B R_{Cy} - P_B R_{Cy} R_{yD} \right)}{\left(R_{Bx} R_{xy} R_{vD} + R_{Bx} R_{xy} R_{Cy} + R_{Ax} R_{xy} R_{yD} + R_{Ax} R_{xy} R_{Cy} + R_{Ax} R_{Bx} R_{yD} + R_{Ax} R_{Bx} R_{Cy} + R_{Bx} R_{Cy} R_{yD} + R_{Ax} R_{Cy} R_{yD} \right)} \quad (K2)$$

$$\Delta P_{xy} = \frac{-R_{xy} \left(-P_A R_{Bx} R_{vD} - R_{Ax} P_B R_{yD} + R_{Bx} P_C R_{yD} + P_C R_{Ax} R_{yD} - P_A R_{Bx} R_{Cy} - P_B R_{Ax} R_{Cy} \right)}{\left(R_{Bx} R_{xy} R_{vD} + R_{Bx} R_{xy} R_{Cy} + R_{Ax} R_{xy} R_{yD} + R_{Ax} R_{xy} R_{Cy} + R_{Ax} R_{Bx} R_{yD} + R_{Ax} R_{Bx} R_{Cy} + R_{Bx} R_{Cy} R_{yD} + R_{Ax} R_{Cy} R_{yD} \right)} \quad (K3)$$

$$\Delta P_{Cy} = \frac{R_{Cy} \left(-P_A R_{Bx} R_{vD} - R_{Ax} P_B R_{yD} + R_{Bx} P_C R_{yD} + P_C R_{Ax} R_{yD} - P_C R_{Ax} R_{Bx} - P_C R_{Bx} R_{yD} + R_{Ax} P_C R_{yD} \right)}{\left(R_{Bx} R_{xy} R_{vD} + R_{Bx} R_{xy} R_{Cy} + R_{Ax} R_{xy} R_{yD} + R_{Ax} R_{xy} R_{Cy} + R_{Ax} R_{Bx} R_{yD} + R_{Ax} R_{Bx} R_{Cy} + R_{Bx} R_{Cy} R_{yD} + R_{Ax} R_{Cy} R_{yD} \right)} \quad (K4)$$

$$\Delta P_{yD} = \frac{R_{yD} \left(P_C R_{Bx} R_{xy} + R_{Ax} P_C R_{xy} + R_{Ax} P_C R_{Bx} + P_A R_{Bx} R_{Cy} - P_B R_{Ax} R_{Cy} \right)}{\left(R_{Bx} R_{xy} R_{vD} + R_{Bx} R_{xy} R_{Cy} + R_{Ax} R_{xy} R_{yD} + R_{Ax} R_{xy} R_{Cy} + R_{Ax} R_{Bx} R_{yD} + R_{Ax} R_{Bx} R_{Cy} + R_{Bx} R_{Cy} R_{yD} + R_{Ax} R_{Cy} R_{yD} \right)} \quad (K5)$$